ABSTRACT

Title of dissertation: MEASUREMENT OF THE COSMIC-RAY PROTON SPECTRUM FROM 54 GEV TO 9.5 TEV WITH THE FERMI LARGE AREA TELESCOPE

David M. Green, Doctor of Philosophy, 2016

Dissertation directed by: Dr. Elizabeth A. Hays
NASA - Goddard Space Flight Center

Cosmic rays are a near-isotropic continuous flux of energetic particles of extraterrestrial origin. First discovered in 1912, cosmic rays span over 10 decades of energy and originate from Galactic and extragalactic sources. The *Fermi* Gamma-ray Space Telescope observations have recently confirmed supernova remnants (SNR) as a source class for Galactic cosmic-ray protons. Additionally, recent measurements made by *AMS-02* of the cosmic-ray proton spectrum to 1.8 TeV in kinetic energy have shown an unexpected spectral break at 415 ± 117 GeV with a primary spectral index of -2.794 ± 0.006 and a secondary spectral index of -2.702 ± 0.047. The *Fermi* Large Area Telescope (LAT), one of two instruments on *Fermi*, has an ideal energy range for confirming a spectral break and extending a space-based cosmic-ray proton spectrum measurement to overlap with higher energy balloon-borne measurements.

In this thesis, I present the measurement of the cosmic-ray proton spectrum from 54 GeV to 9.5 TeV with the *Fermi*-LAT. Using the LAT's anti-coincidence detector and tracker as two independent measures of charge, I estimated a residual contamination in our proton data set of less than 5% primarily from cosmic-ray electrons and positrons. The LAT calorimeter provides an energy estimation of the electromagnetic fraction of an induced cosmic-ray proton shower. I use the charge and energy measurements to build instrument response functions, such as acceptance and response for the LAT, and measure cosmic-ray proton flux. I estimate the systematic uncertainties associated with the acceptance and the energy measurement. Using a broken power-law spectrum, I find a primary spectral index of -2.80 ± 0.03, a secondary spectral index of -2.60 ± 0.04, and an energy break of 467 ± 144 GeV. I discuss possible astrophysical and cosmic-ray physics interpretations for the observed spectral break.

Measurement of the cosmic-ray proton spectrum from 54 GeV to 9.5 TeV with the *Fermi* Large Area Telescope

by

David Michael Green

Dissertation submitted to the Faculty of the Graduate School of the
University of Maryland, College Park in partial fulfillment
of the requirements for the degree of
Doctor of Philosophy
2016

Advisory Committee:
Professor Kara Hoffman, chair
Dr. Elizabeth A. Hays, co-chair
Professor Julie McEnery
Professor Jordan Goodman
Professor Cole Miller, Dean's Representative

For my grandparents.

Acknowledgments

Here we go, I always enjoy reading these because they are the rambling of a anxiety riddled person after six months of work. Like everything else in this thesis, this might be kind of long.

First thanks to all members of my committee for taking time out of their busy schedules. Thank you Liz, Julie, Kara, Jordan, and Cole.

I'd like to thank my advisor, Liz Hays. I learned so much not only from Liz but because of her. She was patient when I went down analysis rabbit holes which often resulted in nothing. She was encouraging of my research but critical when important and I'd like to think she passed that critical eye on to me. She has taught me how to be a good scientist by example. I am privileged to have such a wonderful and amazing advisor.

Everyone at Goddard has been encouraging and helpful over the years. Sylvia, thank you for putting up with me while exploring before and after collaboration meetings, the constant encouragement, and helping me with my continuing journey to being woke. Judy, thank you for letting me complain occasionally, being a great companion during collaboration meetings, the opportunity to travel Scotland, and the comments on this thesis. Jamie, thank your for being my Ph.D bro, letting me complain about graduate school, and letting play with Junie and Elliott at parties. Julie, thank you for your support and taking time out of your busy schedule to be on my committee. Jeremy and Donna, thank you for the dinners, game nights, whisky, and Scottish adventures. Alex, thank you for being critical of my analysis and driving me improve everything and dig deep into the underling physics of protons and the LAT detector. Terri, thank you for helping me work through the theory of cosmic-rays and to not accepting things on authority. I'd like to specifically thank Judy, Sylvia, Sara, and Jeff for all of the crazy cakes we baked. Judy, Sara, and Jeff you have to keep up the winning streak at Science is Food competition. I want to acknowledge how many people I know which their first name starts with 'J': Julie, Judy, Jeremy, Jamie, Jeff, Jack, Josh, Jordan, Jon... There are many others at Goddard I am forgetting and if I did consider your self thanked.

I'd also like to thank too many people in the *Fermi*-LAT collaboration that have helped me over the years through comments and ideas on my analysis, plots, talks, and papers.

Thank you to Jon, Kristen, Chris, and Matt for spending several hours in the early morning at my defense and being great friends. I'd also like to thank my parents and family for supporting me through graduate school and over the many years.

Finally, thank you Susannah. You've been there for years and on the front lines of this thesis, cooking dinners, cleaning the apartment, and spell checking the thesis over many many late nights. Oh, I can't forget the kitties: Scratch (RIP), Kitty (RIP), Juno, and Cricket.

Table of Contents

List of Tables

List of Figures

List of Abbreviations

ACD	Anti-coincidence Detector
ACE-CRIS	Advanced Composition Explorer – Cosmic Ray Isotope Spectrometer
ADC	Analog Digital Conversion
AGILE	Astro-Rivelatore Gamma a Immagini Leggero
AMS	Alpha Magnetic Spectrometer
ATIC	Advanced Thin Ionization Calorimeter
BESS	Balloon-borne Experiment with Superconducting Spectrometer
BKG	All-particle background simulation
BT	Beam-Test
CAL	Calorimeter
CALET	Calorimetric Electron Telescope
CDF	Cumulative Distribution Function
`CHIPS`	Chiral Invariant Phase Space
CME2K	Cascade-Exciton Model
CO	Carbon Monoxide
COBE	Cosmic Background Explorer
CREAM	Cosmic Ray Energetics and Mass
CsI	Cesium Iodide
CU	Calibration Unit
DAMPE	Dark Matter Particle Explorer
`DGN`	Diagnostic Events
DOCA	Distance of Closest Approach
DRAGON2	Diffusion Re-acceleration and Advection of Galactic cosmic rays
EM	Electromagnetic
FGST	*Fermi* Gamma-ray Space Telescope
FLUKA	Fluktuierende Kaskade
FOV	Field of View
FREE	Front End Electrons
`FTF`	Fritiof Model
GALPROP	Galactic Propagation Cosmic Ray Software
GBM	Gamma-ray Burst Monitor
GC	Galactic Clusters
GEANT	Geometry and Tracking
GeV	10^9 electronvolts
GSFC	Goddard Space Flight Center
GRL	Galactic Radio-lobes
H_1	Atomic hydrogen
H_2	Molecular hydrogen
HAWC	High Altitude Water Cerenkov Gamma-ray Observatory

`HI-PASS`	High Pass Filter
IC	Inverse Compton
IGM	Intergalactic medium
IGRF	International Geomagnetic Reference Field
IRF	Instrument Response Function
ISM	Interstellar Medium
ISS-CREAM	International Space Station Cosmic Ray Energetics and Mass
KASKADE	Karlsruhe Shower Core and Array Detector
LAT	Large Area Telescope
LAQGSM	The Los Alamos version of Quark Gluon String model
LHC	Large Hadron Collider
MAGIC	Major Atmospheric Gamma Imaging Cherenkov Telescopes
MC	Monte-Carlo
MeV	10^6 electronvolts
MIP	Minimum Ionizing Particle
MST	Minimum Spanning Tree
NASA	National Aeronautics and Space Administration
NS	Neutron Stars
PAMELA	Payload for Antimatter Matter Exploration and Light-nuclei Astrophysics
pc	Parsec
PeV	10^{15} electronvolts
PHA	Pulse Height Amplitude
PLC	Path Length Correction
PVT	Polyvinyltoluene
`QGS`	Quark Gluon String Model
SAT	Saturation
SNR	Supernova Remnant
SS	Sunspots
SSD	Silicon Strip Detector
TeV	10^{12} electronvolts
TKR	Tracker
ToT	Time over Threshold
VERITAS	Very Energetic Radiation Imaging Telescope Array System
WD	White Dwarfs
WMAP	Wilkinson Microwave Anisotropy Probe
X_0	Radiation Length
λ_i	Nuclear Interaction Length

Chapter 1: Introduction

In this thesis I present the measurement of the cosmic-ray proton spectrum from 54 GeV to 9.5 TeV with the *Fermi* Large Area Telescope (LAT). Chapter 2 presents a review of cosmic ray history, observations, acceleration methods and theory, possible cosmic-ray origins, and cosmic-ray propagation and transport. Chapter 3 describes the *Fermi* Large Area Telescope design, the Pass 8 reconstruction and simulation software, and the GEANT4 Monte-Carlo simulations used in this measurement. Chapter 4 presents the charge measurement for the proton spectrum analysis used for reduction of contamination sources from cosmic-ray ions and electrons and the associated residual contamination measurement. Chapter 5 presents the physics behind electromagnetic and hadronic showers and the energy measurement methods of Pass 8 and measuring the energy of cosmic-ray protons via the LAT's Calorimeter (CAL). Chapter 6 presents the spectral reconstruction methods, instrument response functions for the LAT from protons, and the measured cosmic-ray proton flux and discussion of results. Chapter 7 discusses possible astrophysical and cosmic-ray physics interpretations of the measured cosmic-ray proton spectrum. Chapter 8 presents how the cosmic-ray proton spectral analysis with the *Fermi*-LAT opens the door for possible additional cosmic-ray measurements.

Chapter 2: Cosmic Rays

Cosmic rays have a rich history spanning over 100 years of study. Despite a long history many mysteries still remain, but recent measurements paired with advancements in theory and modeling have resolved some important questions. The current paradigm for Galactic cosmic-ray physics is that Galactic cosmic-rays are accelerated through diffusive shock acceleration, or first order Fermi acceleration, occurring at the shock-waves of supernova remnants (SNRs). The origin of cosmic-rays is still not completely settled and open questions remain for sources: Are SNRs the only important site of acceleration? What are the maximum particle energies attained in SNRs? What is the impact of the local environment on cosmic-ray acceleration and escape?

Understanding cosmic-ray propagation is crucial to understanding the observed cosmic-ray populations at Earth. The freshly accelerated cosmic-rays are propagated through the Galaxy for several million years and their initial spectrum is modified predominantly by diffusive processes. The strength of every term in the cosmic-ray propagation equation is not known and terms like re-acceleration could prove to be stronger than currently thought. Standard ideas about cosmic-ray origins are built on several assumptions of homogeneity, isotropy, and temporal stability of both cosmic-ray accelerators and propagation. This paradigm has been challenged by an unmodeled spectral break at 100s of GeV in energy observed by *AMS-02* and by *Fermi*-LAT in the measurements presented in this thesis. We must first establish the current knowledge of cosmic-ray properties with the resulting ideas that explain them. In this chapter I will give a brief overview of the history, a review of acceleration physics, and some highlights of models for the origin and propagation of cosmic rays.

2.1 A Very Brief History

After the discovery of radiation and the invention of the electrometer in the late 19th century, it was widely believed that ionization present in the atmosphere was due to radioactive material in the atmosphere of the Earth. This idea was disproved by measurements of the increase of the ionization rate with increasing altitude via electrometer observations made by Domenico Pacini, Victor Hess, and Werner Kolhörster using the Eiffel Tower and hydrogen balloons respectively [12–14]. Hess was awarded the Nobel Prize in Physics in 1936 for his discovery of what would come to be known as cosmic rays. The only reasonable explanation for the altitude dependence of atmospheric ionization was a source of extraterrestrial radiation ionizing the atmosphere. The term 'cosmic ray' was coined by Millikan in 1928 to describe this extraterrestrial radiation [15]. Cosmic rays were first thought be due to gamma radiation, but measurements of the geomagnetic latitudinal dependence of the ionization showed that it was due to charged particles [16].

Using newly developed Geiger counters, extensive air showers were discovered using a large array of Geiger counters positioned in the Alps [17]. This lead to the conclusion that cosmic rays could be extremely high energy compared to terrestrial accelerators which were only just being developed. Later more dedicated experiments were developed to measure extensive air showers and discovered the first ultra-high-energy cosmic rays [18].

With the development of new detectors to study cosmic rays, such as cloud and emulsion chambers, cosmic rays drove several key discoveries in the early years of particle physics. The positron [19], the muon [20], the first mesons [21], and strangeness [22] were all discovered via cosmic-ray experiments. When multiple GeV energy cyclotrons and synchrotrons began operating in the 1950s, particle physicists were able to develop larger dedicated detectors and have greater control over particle beams and energy, after which cosmic ray use in particle physics died down.

At around the same time balloon-borne cosmic experiments began taking flight. The first such experiment was aptly named *Balloon*. *Balloon* discovered early composition of cosmic rays by distinguishing the light elements: H, He, Be, and B, at 100s of MeV per nucleon and measuring the inclusive electron positron spectrum above 15 GeV [23–25]. The earliest satellites also had cosmic-ray detectors but mostly to study solar cosmic rays [26, 27].

In the early 1970s fluorescence techniques were developed and first implemented in 1980 as *Fly's Eye*. Results from *Fly's Eye* in combination with those from several extensive air shower arrays revealed the ultra-high energy, above 10^8

GeV, cosmic-ray spectrum.

Despite over 100 years of cosmic-ray studies, mysteries still abound. Recent unexpected features were found in the proton and helium spectra from *AMS-02* [5,28]. Cosmic rays, which are expected to arrive isotropically due to interactions with Galactic magnetic fields, have been discovered to arrive anisotropically by *Milagro* with confirmation from *IceCube* and *HAWC* [29–31]. Supernova remnants (SRNs) have long been suspected to be the sources of Galactic cosmic rays. Observations from *Fermi*-LAT have now confirmed the presence of accelerated protons in several SNRs [32,33]. Questions remain about the total contribution of SNRs to the Galactic cosmic rays and the ability of SNRs to provide the highest observed energy of Galactic cosmic rays. In contrast, there is more uncertainty about the source of extragalactic cosmic rays. Along with the development of γ-ray astronomy, cosmic-ray physics plays a crucial role in understanding diffuse gamma-ray emission. Recent efforts in the field have produced a wealth of cosmic-ray observations with precise measurements of spectra for cosmic ray species, abundances, and anisotropies.

2.2 Observations

Cosmic rays are a near-isotropic continuous flux of energetic particles from extraterrestrial origin. They are further broken down according to their charge, particle type, and origin. Observed hadronic cosmic rays are composed of 79% protons, 14.7% helium, and 6.3% heavy cosmic rays [34]. In this analysis, we define heavy ions as cosmic rays with atomic charge, Z, greater than 3. Cosmic rays

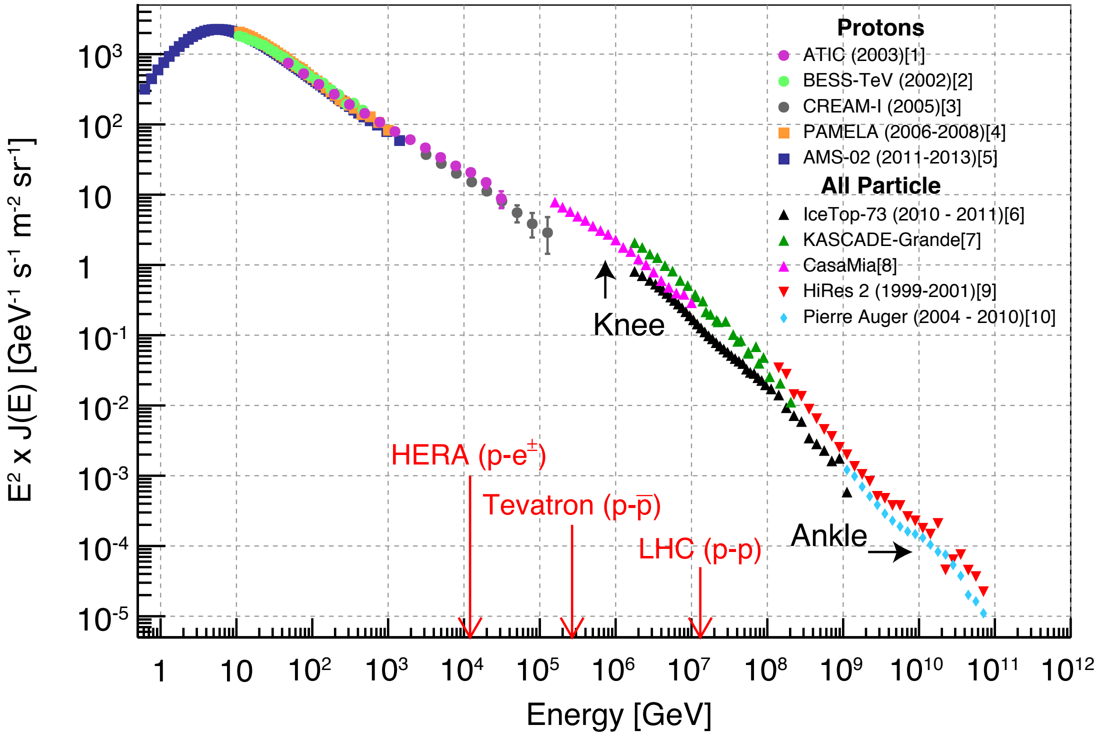

Figure 2.1: The proton and all-particle cosmic-ray energy flux spectrum in kinetic energy from 0.5 – 10^{12} GeV from various detectors: *ATIC* [1], *BESS-TeV* [2], *CREAM-1* [3], *PAMELA* [4], *AMS-02* [5], *IceTop-73* [6], *KASCADE-Grande* [7], *CasaMia* [8], *HiRes 2* [9], and *Pierre Auger* [10] and the time range of the datasets. Circles represent balloon-borne experiments, squares represent space-based experiments, upward point triangles represent air shower detectors, downward pointing triangles represent air fluorescence detectors, and diamonds represent hybrid air shower and air fluorescence detectors. The spectral inflections known as the knee and the ankle and the fixed target energy of terrestrial particle accelerators are indicated.

are highly relativistic, and their energies span from 1 GeV to 10^{11} GeV. Figure 2.1 shows the proton and all-particle energy flux spectrum multiplied by E^2 from several different types of experiments. There are several different types of detectors for cosmic rays, each examining different energy ranges.

Space-based observatories, *AMS-02*, *PAMELA*, and *Fermi*, are limited by their small effective area, on the order of 100 cm^2. Their typical energy range is from 1 GeV to 1 TeV and benefit from being able to directly measure the properties of the cosmic rays without atmospheric contamination. Additionally, space-based observatories have long times of flight on the order of years. Balloon-borne measurements, *ATIC*, *BESS*, and *CREAM-1*, range from a few TeV to 100 TeV and can have larger effective areas, on the order of 1 m^2, and more complex detector systems but are limited by statistics at the highest energies due to short time-of-flights usually on the order of a few weeks. Balloon-borne measurements also directly measure properties of the cosmic rays but have to account for atmospheric contamination from charge changing events of cosmic rays interacting higher in the atmosphere. This introduces a difficult to resolve contamination. Both space-based and balloon-borne measurements directly measure cosmic rays and are able to provide fluxes for individual species and even cosmic-ray isotopes and anti-particles if containing a powerful enough magnet.

Ground-based detectors measure the cosmic-ray shower in the atmosphere in order to measure the direction and energy of the incident cosmic ray. Two methods are: air shower detectors such as *IceTop*, *KASCADE-Grande*, and *CasaMia*, which are typically a sparse array of detectors measuring the extent, direction, and particle

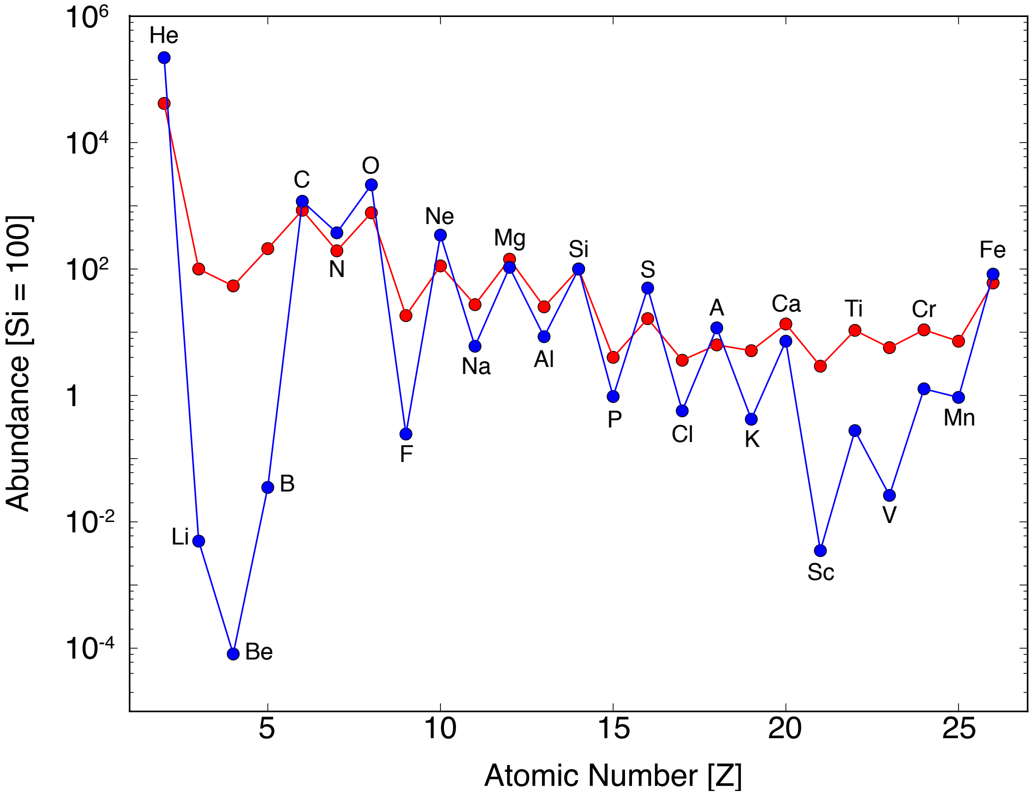

Figure 2.2: Relative elemental abundances for cosmic rays (red) and the solar system (blue) from helium to iron normalized such that Si = 100 [35, 36].

count of daughter particles from the air shower, and fluorescence detectors, *HiRes 2* and *Telescope Array*, which measure fluorescence photons from nitrogen atoms excited by high energy cosmic rays in the atmosphere. These two methods can be combined into a hybrid detector like *Pierre Auger*. Ground-based detectors typically measure the highest energy cosmic rays, 100 TeV and above, and therefore need a very large effective area usually on the order of km^2, but because of the indirect method the energy resolution can be limited. Ground-based detectors typically have no associated charge measurement and therefore measure the all-particle spectrum.

Cosmic rays possess a nearly featureless spectrum over 10 decades of energy.

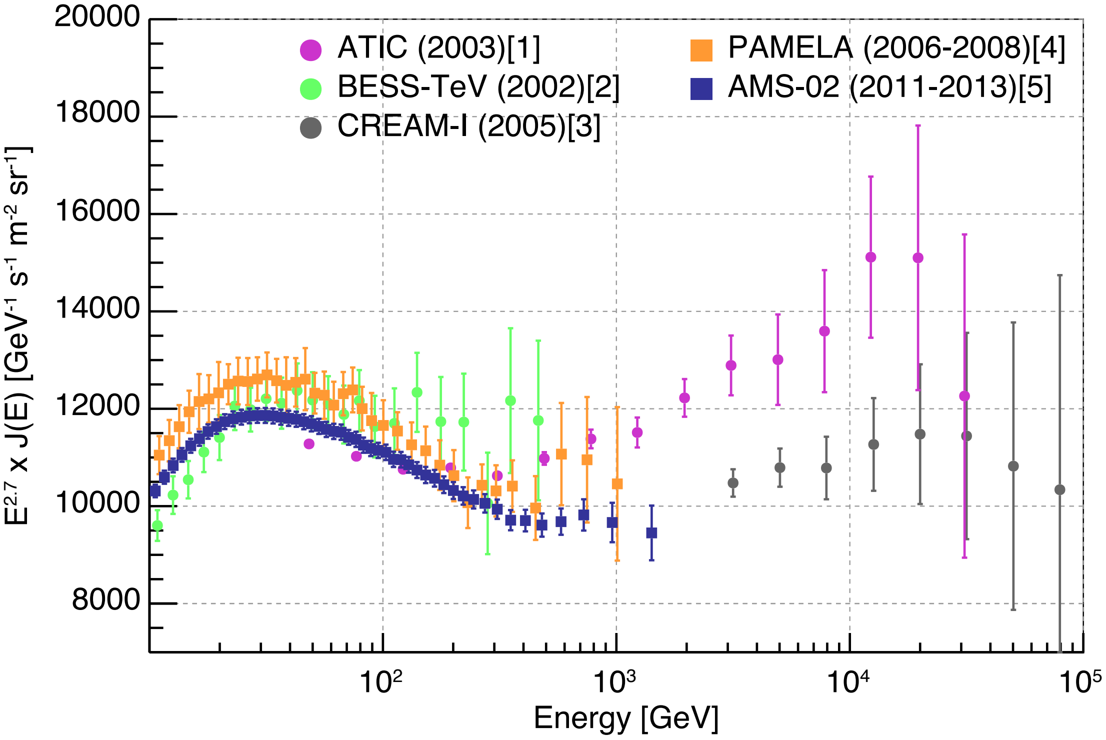

Figure 2.3: The cosmic-ray proton spectrum in kinetic energy from 10 GeV to 100 TeV multiplied by $E^{2.7}$ from *CREAM-1* [3], *AMS-02* [5], *PAMELA* [4], *BESS-TeV* [2], and *ATIC* [1].

From 10 GeV to 10^6 GeV the spectrum remains unchanged, with $dN/dE \propto E^{-2.7}$. At 10^6 GeV, the point known as the knee, the spectrum begins to steepen to $dN/dE \propto E^{-3.0}$ [37]. There is an additional slight steepening of the spectrum above $10^{8.3}$ GeV to 10^{11} GeV with $dN/dE \propto E^{3.07}$. This feature is known as the ankle [38]. The changes in the spectrum are believed to be caused by different cosmic-ray origins: Galactic versus extragalactic or different acceleration methods. Cosmic rays below a few GeV are solar in origin. Cosmic rays with energies above a few GeV and below the knee are considered Galactic in origin; energies above the knee and below the ankle are considered extragalactic; and the origin of cosmic rays above the ankle is not well understood.

Measurements of the chemical composition of Galactic cosmic rays, as seen in Figure 2.2, have a composition of similar form to solar and therefore stellar composition. This suggests that cosmic rays come from stellar objects. Elements that form as the end product of stellar nucleosynthesis, such as carbon or oxygen, have higher relative abundance and are known as ‘primary’ cosmic rays. The remaining elements have lower abundance and are called ‘secondary’ cosmic rays because they are the result of spallation of primary cosmic rays and not predominately stellar nucleosynthesis.

We can zoom in on Figure 2.1 to an energy range closer to the energy range of the analysis presented in this thesis in Figure 2.3. This energy range is covered by both space-based and balloon-borne cosmic-ray detectors. While there is decent agreement between space-based measurements, there are few measurements from 1 TeV to 100 TeV which is only covered by balloon-borne experiments. There is significant disagreement between fluxes found by balloon-borne experiments and extended spectral models from space-based observatories. Measurements from *AMS-02* at TeV energies suggest new, previously unmodeled spectral features [5]. Breaks and other spectral features can reveal possible new ideas about the cosmic-ray paradigm associated with cosmic-ray source populations, cosmic-ray propagation, and cosmic-ray acceleration.

AMS-02 and *PAMELA* have permanent magnets for matter anti-matter separation, charge measurement, and energy measurement, therefore they natively measure the particle rigidity, in units of voltage, instead of its kinetic energy. The relationship between kinetic energy and rigidity is:

$$E_K = \sqrt{R^2 + M^2} - M \tag{2.1}$$

where M is the rest mass of the particle, E_K is the kinetic energy of the particle, and R is the rigidity of the particle.

Next we determine the mechanism which can accelerate Galactic cosmic rays to such high energies.

2.3 Acceleration

What is evident from the near featureless spectrum of Galactic cosmic rays in Figure 2.1 is that cosmic rays below the knee are accelerated by the same mechanism over six decades of energy. Terrestrial particle accelerators use powerful electric and magnetic fields to accelerate protons to their desired energies. As seen in Figure 2.1, the LHC and Tevatron are able to reach the energy of the knee in the target frame for protons. In 1949, Enrico Fermi suggested an acceleration method whereby particles are accelerated by interactions with large Galactic magnetic fields in Galactic clouds [39]. This so-called second order Fermi acceleration, produces the wrong spectral index and therefore cannot account for the cosmic ray measurements. As discussed later in § 2.5.2, spectral index depends on the square of velocity of Galactic clouds. These velocities are very small, typically $V/c \lesssim 10^{-4}$, and produces a very large spectral index and does not reproduce the observed cosmic-ray spectra. In 1955, Davis proposed a modified version of second order Fermi acceleration whereby cosmic rays are accelerated by supersonic shocks instead of Galactic magnetic fields [40].

Known as first order Fermi acceleration, the theory suggests particles can gain energy by crossing a supersonic shock front and scattering on turbulent magnetic fields associated with the shock front. We now explore first order Fermi acceleration and its ramifications on cosmic-ray origins and propagation.

The following derivation is adapted from Cosmic Rays and Particle Physics by Gaisser [37]. Suppose a test particle increases its energy every time it crosses a shock front. If $\Delta E = \xi E$ per crossing, then after n crossings:

$$E_n = E_0(1+\xi)^n \tag{2.2}$$

where E_0 is the injection energy into the accelerators and n is the number of crossings. If the probability of escape from the acceleration region is P_{esc} the probability of remaining in the acceleration region after n crossings is $(1 - P_{esc})^n$.

The number of encounters to reach energy E is:

$$n = \ln\left(\frac{E}{E_0}\right) / \ln(1+\xi) \tag{2.3}$$

The number of particles accelerated to energies greater than E is:

$$N(\geq E) \propto \sum_{m=n}^{\infty}(1 - P_{esc})^m = \frac{(1 - P_{esc})^n}{P_{esc}}. \tag{2.4}$$

Substituting in n from Equation 2.3 yields the differential spectrum:

$$\frac{dN(\geq E)}{dE} \propto \frac{1}{P_{esc}}\left(\frac{E}{E_0}\right)^{-(1+\gamma)} \tag{2.5}$$

where

$$\gamma = \ln\left[\frac{1}{1 - P_{esc}}\right] / \ln[1+\xi] \approx \frac{P_{esc}}{\xi} = \frac{1}{\xi} \times \frac{T_{cycle}}{T_{esc}} \tag{2.6}$$

for small fractional energy gains. T_{cycle} is the time for the test particle to scatter off

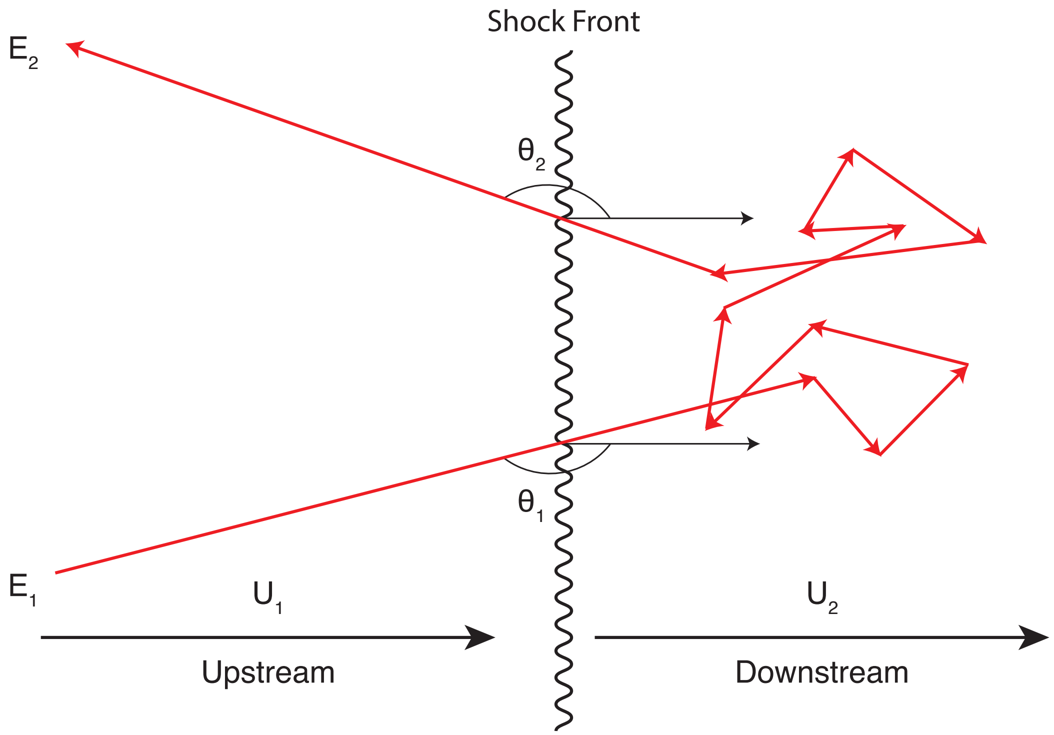

Figure 2.4: First order Fermi acceleration by a moving shock front. U_1 is the upstream gas velocity and U_2 is the downstream gas velocity [37].

of the shock front. T_{esc} is the time for the test particle to escape the acceleration region. The first important result of first order Fermi acceleration is its ability to recreate a power-law spectrum of similar form to that seen in nature.

Figure 2.4 shows a diagram of a test particle encountering a shock front. The test particle crosses the shock front and collisionlessly scatters off of turbulent magnetic fields and again crosses the shock front. In this process the test particle enters with energy E_1 and leaves with greater energy E_2. In the rest frame of the moving upstream gas, the cosmic ray has an energy:

$$E_1' = \Gamma E_1 (1 - \beta \cos\theta_1) \tag{2.7}$$

where β and Γ are the relative velocity of the shock and the Lorentz factor where primes are in the frame of the shock. We can also find the energy after the crossing the shock:

$$E_2 = \Gamma E_2'(1 + \beta \cos\theta_2'). \tag{2.8}$$

We also use the fact that just before leaving the shock, $E_2' = E_1'$ in the frame of the shock. Combining Equations 2.7 and 2.8 we find the change of energy to be:

$$\frac{\Delta E}{E_1} = \frac{1 - \beta\cos\theta_1 + \beta\cos\theta_2' - \beta^2\cos\theta_1\cos\theta_2'}{1 - \beta^2} - 1 \tag{2.9}$$

The fractional energy gain from the encounter is $\xi = \frac{E_2 - E_1}{E_1}$. To find the average fractional gain, ξ, we determine angular average of $\frac{\Delta E}{E_1}$.

Doing so we find:

$$\xi = \left\langle \frac{\Delta E}{E_1} \right\rangle = \frac{1 + \frac{4}{3}\beta + \frac{4}{9}\beta^2}{1 - \beta^2} - 1 \sim \frac{4}{3}\beta \sim \frac{4}{3}\frac{u_1 - u_2}{c} \tag{2.10}$$

where $u_1 - u_2$ is the relative velocity of the shocked gas and is not moving relativistically. Here is where first order Fermi acceleration gets its name, ξ is first order in the relative velocity of the shock. Using ξ and the kinetic theory of gases we arrive at:

$$\gamma \approx 1 + \frac{4}{\mathcal{M}^2} \tag{2.11}$$

where $\mathcal{M} = u_1/c_1$ is the Mach number in the downstream region and c_1 is the speed of sound in the downstream region. Supersonic shocks are expected in first order Fermi acceleration which means $\mathcal{M} > 1$ and typically on the order of $\sim 6 - 10$. This gives us a $\gamma \sim 1.1$. Galactic cosmic rays have an all-particle differential spectrum of $dN/dE \propto E^{-2.7}$ and first order Fermi acceleration produces a differential energy spectrum of $dN/dE \propto E^{-(\gamma+1)} \propto E^{-2.1}$. We can see that in the test particle case first order Fermi acceleration is able produce a power-law spectrum and a spectral index on the same order of the observed cosmic-ray spectral index. The discrepancy between the observed spectral index of 2.7 and first order Fermi acceleration spectral index of 2.1 should be noted.

We have a theory of cosmic-ray acceleration that can reproduce a power-law spectrum and approximately the observed power-law index, but is first order Fermi acceleration able to produce cosmic-ray energies up to or above the knee? To calculate the maximum energy of a test particle accelerated via first order Fermi acceleration, consider the upstream region with no net cosmic ray flow. The equilibrium condition is given by:

$$D_1 \frac{dN}{dz} = -u_1 N \tag{2.12}$$

where D_1 is the diffusion constant of the upstream region and N is the cosmic-ray density. D_1 describes the strength of cosmic-ray interactions with turbulent magnetic fields associated with a shock front. Solving for N in the upstream region by solving the differential Equation 2.12:

$$N(z) = \rho_{CR} \exp[-z u_1 / D_1] \tag{2.13}$$

where ρ_{CR} is the number density of cosmic rays at the shock. The mean time the test particle spends in the upstream region is:

$$(\rho_{CR}\ D_1/u_1)(c\ \rho_{CR}/4)^{-1} = 4\ D_1/(u_1\ c) \tag{2.14}$$

The same process applies to the downstream region. Thus, the total time of one cycle is:

$$T_{cycle} = \frac{4}{c}\left(\frac{D_1}{u_1} + \frac{D_2}{u_2}\right) \tag{2.15}$$

To find T_{cycle} we need an estimate of the diffusion coefficients for the downstream and upstream regions. The diffusion length should not be smaller than the gyroradius, $r_L = pc/(ZeB)$, where pc is the momentum of the test particle, Ze is the charge of the test particle, and B is the magnetic field of the environment. The gyroradius is a good approximation because particles cannot respond to irregularities in the magnetic field smaller than the gyroradius. Assuming the diffusion length is of order the gyroradius gives a lower limit on the diffusion constant,

$$D_{min} = \frac{r_L\ c}{3} \sim \frac{1}{3}\frac{E\ c}{Z\ e\ B}. \tag{2.16}$$

For strong shocks $u_2 = u_1/4$, and using $D_{min} = D_1 = D_2$, we find the time of the cycle to be $T_{cycle} \geq 20E/(3u_1 ZeB)$. The acceleration rate is:

$$\frac{dE}{dt} = \frac{\xi E}{T_{cycle}}. \tag{2.17}$$

By integrating Equation 2.17 and using Equation 2.10 we find:

$$E_{max} \leq \frac{3}{20}\frac{u_1^2}{c} Ze\ B\ T_A \tag{2.18}$$

where T_A is the lifetime of the accelerator [37]. Using values from a favored object, SNRs, we find the maximum energy predicted is about 10^{15} eV. First order Fermi acceleration is theoretically able to produce cosmic rays up to the energy of the knee. Non-linear magnetic field amplification through generation of Alfven waves of accelerated particles can increase the maximum energy to beyond the 10^{15} eV limit.

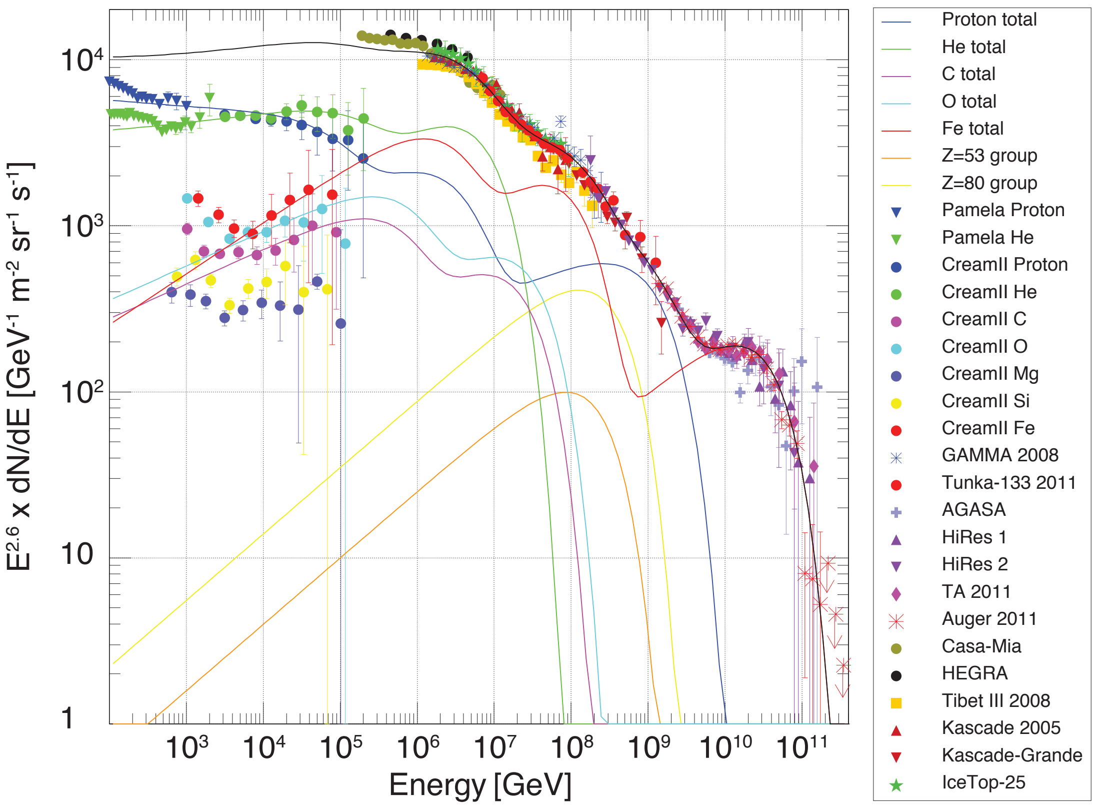

Figure 2.5: A fit of cosmic-ray species, proton, helium, carbon, oxygen, and iron, and all-particle spectra from different sources to data from *CREAM-1* and *PAMELA*. The figure shows one possible model how the charge of the cosmic-ray species affects the the all-particle spectrum to produce the cosmic-ray knee [41–43].

This requires a turbulent magnetic field in order to start the non-linear process, therefore turbulent magnetic fields are once again important for first order Fermi acceleration to occur.

It is important to know the role the charge of the test particle plays in Equation 2.18. As charge increases so does the maximum energy of first order Fermi acceleration. This change of maximum energy contributes to the cosmic-ray knee, where higher charged cosmic-rays will change the spectral index at their maximum acceleration energy. This effect can be seen in Figure 2.5, where different models of cosmic-ray species fit from lower energy data are extended out to higher energies and their cumulative contribution is fit to the all-particle cosmic-ray spectrum at PeV energies. Figure 2.5 also demonstrates the necessity of lower energy spectral measurements for individual species and how they are used to study the higher energy all-particle cosmic-ray spectrum.

First order Fermi acceleration is able to recreate a power-law spectrum and able to approximately recreate the observed power-law index. For these reasons first order Fermi acceleration is the preferred method of accelerating cosmic rays to the extreme energies of the cosmic-ray knee. Next we establish the best possible acceleration sites where Galactic cosmic rays originate.

2.4 Origins

First order Fermi acceleration is able to produce the necessary spectrum up to the maximum energy seen in Galactic cosmic rays, but the class of object with the necessary conditions and observations to provide a site for that acceleration is uncertain. Cosmic rays require a powerful Galactic source having stellar composition and frequent enough injections to meet the observed intensity.

Such a source should also satisfy the ‘Hillas criterion’, wherein the charged particle must be magnetically confined within the acceleration region [44]. We can use Equation 2.19, which defines the gyroradius, and find the required minimum magnetic field and size of acceleration region of several different sources.

$$E_{max} = qBr_g \tag{2.19}$$

We can see this relation for 10^6 GeV protons, near the maximum energy for Galactic protons which remain confined within the Galaxy, for various potential sources in Figure 2.6. Only a few sources satisfy the requirements: neutron stars (NS), white dwarfs (WD), and SNRs.

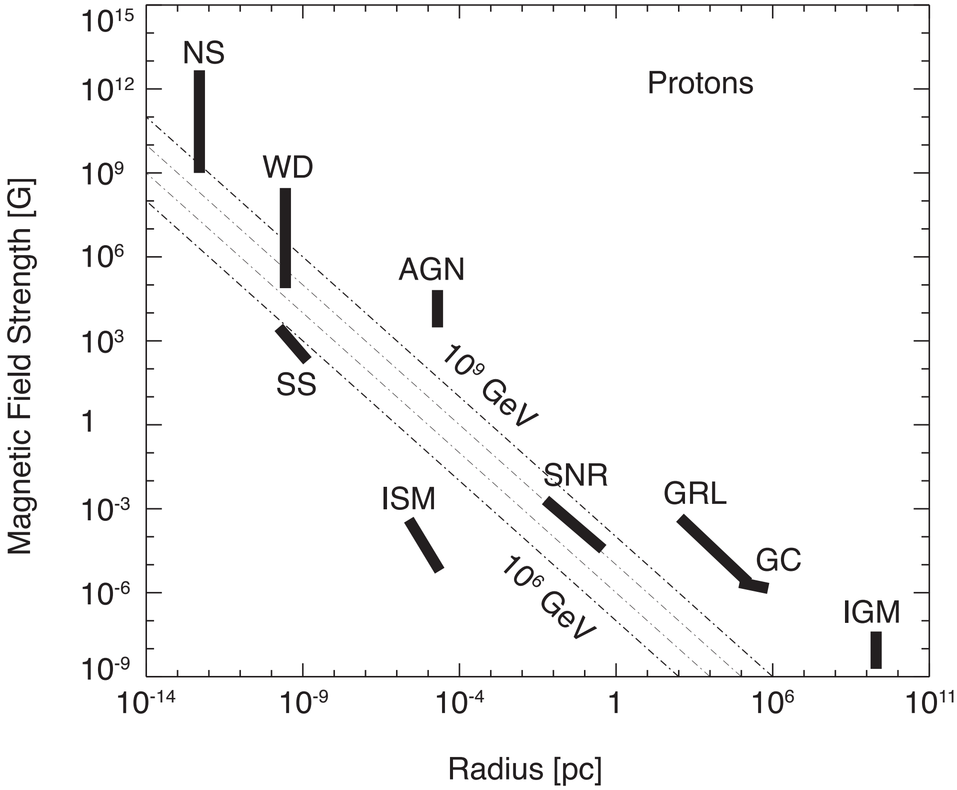

Figure 2.6: The Hillas plot showing magnetic field strength versus gyroradius for proton of momenta 10^6, 10^7, 10^8, and 10^9 GeV/c. Allowed regions for proton momenta are above the dashed lines. The range of sizes and magnetic field strengths for neutron stars (NS), white dwarfs (WD), sun spots (SS), AGN (active galactic nuclei), ISM (interstellar medium), SNR (supernova remnants), GRL (extra-galactic radio lobes), GC (galactic clusters), and IGM (intergalactic medium) [44, 45].

An additional constraint is the power requirement necessary to create the observed energy density of cosmic rays. The power requirement for cosmic rays can be estimated as:

$$P_{CR} = \frac{V_D\ \rho_{CR}}{\tau_{CR}} = \frac{(4 \times 10^{66}\ \text{cm}^3)(1\text{eV}/\text{cm}^3)}{6 \times 10^6\ \text{years}} \approx 5 \times 10^{40}\ \frac{\text{ergs}}{\text{s}} \tag{2.20}$$

where V_D is the volume of the Galactic disc, ρ_{CR} is the average energy density for Galactic cosmic rays, and τ_{CR} is the average lifetime of Galactic cosmic rays. WD fall under the power requirement necessary to recreate the observed cosmic-ray density but SN provide a possible explanation. The power output from a 10 $M_\odot$ supernova occurring every 30 years is:

$$P_{SN} = \frac{1}{2}(10M_\odot)(5 \times 10^8\ \text{cm/s})^2/(30\ \text{years}) \approx 3 \times 10^{42}\ \frac{\text{ergs}}{\text{s}}. \tag{2.21}$$

We can see that supernovae are powerful enough to accelerate Galactic cosmic rays with only a few percent efficiency [37]. Additionally, the aftermath of a supernova provides the necessary shock front and turbulent magnetic fields for first order Fermi acceleration. It should be noted that NS can have shock fronts but their magnetic fields are too ordered for first order Fermi acceleration. Therefore, NS can be ruled out as possible source for cosmic-ray acceleration. This leaves SNR as a possible source.

Ginzburg and Syrovatskii put forth the idea that SNRs could accelerate cosmic rays [46]. SNRs are hot plasma from a supernova expanding into the cold interstellar medium (ISM). Their temperature and pressure discontinuity provides the necessary supersonic shock front for first order Fermi acceleration. Additionally, X-ray observations of the shock front have shown the magnetic field associated with the shock front is turbulent enough to support first order Fermi acceleration [47].

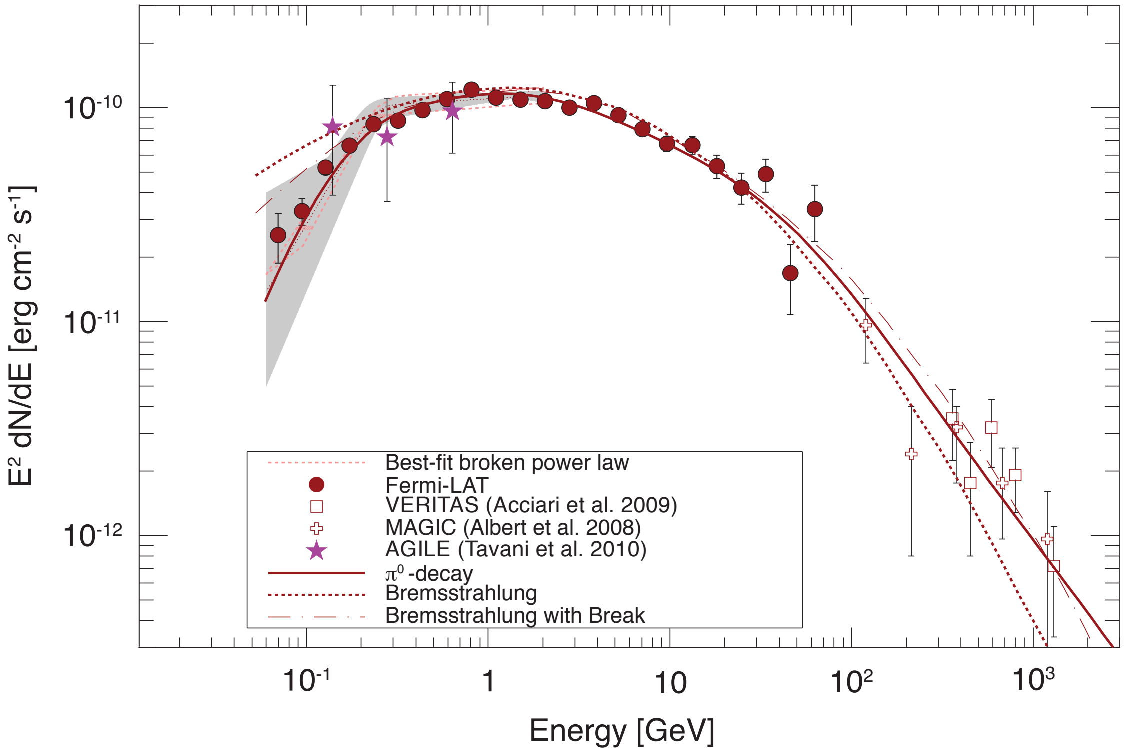

Figure 2.7: γ-ray spectrum for IC 443 measured with the *Fermi*-LAT, *VERITAS*, and *MAGIC* fit with a smoothly broken power-law. Solid lines show hadronic models of $\pi^0 \rightarrow \gamma\gamma$ decay spectra fits, and dotted and dashed lines show leptonic models using bremsstrahlung with and without a low energy break at 300 MeV. The best fit is produced by π^0 decay showing hadronic cosmic-ray acceleration [32].

γ-rays can be produced from cosmic-ray interactions and thus be used as a tracer for particle acceleration. SNRs will accelerate both leptons and hadrons but lepton production of γ-rays is much more efficient than hadronic production. Leptonic emission primarily comes from inverse Compton (IC) scattering, where high energy electrons up-scatter synchrotron produced X-rays to γ-ray energies. Hadronic emission comes from accelerated protons inelastically scattering with low energy ISM protons and dust and producing high energy π^0 daughter particles which

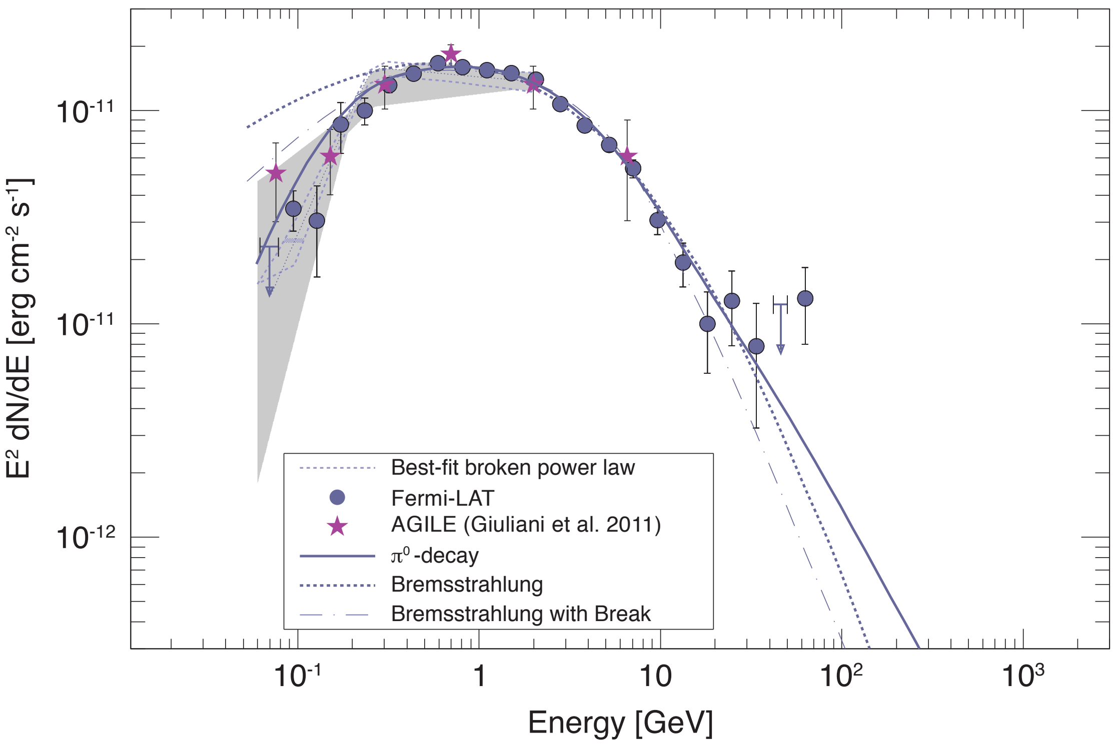

Figure 2.8: γ-ray spectrum for W44 measured with the *Fermi*-LAT, *VERITAS*, and *MAGIC* fit with a smoothly broken power-law. Solid lines show hadronic models of $\pi^0 \rightarrow \gamma\gamma$ decay spectra fits, and dotted and dashed lines show leptonic models using bremsstrahlung with and without a low energy break at 300 MeV. The best fit is produced by π^0 decay showing hadronic cosmic-ray acceleration [32].

then decay into two γ-rays. Hadronic-produced γ-rays show low energy spectral excesses of a minimum energy of half the mass of the π^0 or 70 MeV. The ratio of hadronic to leptonic emission is intrinsically dependent on SNR environment, age, mass, and observationally dependent on distance and brightness. It's difficult to link γ-ray observations of the few SNRs to the total population of SNRs in the Galaxy. Additionally, γ-ray observations do not give all of the information for proton acceleration and leave open questions such as the escape probability versus

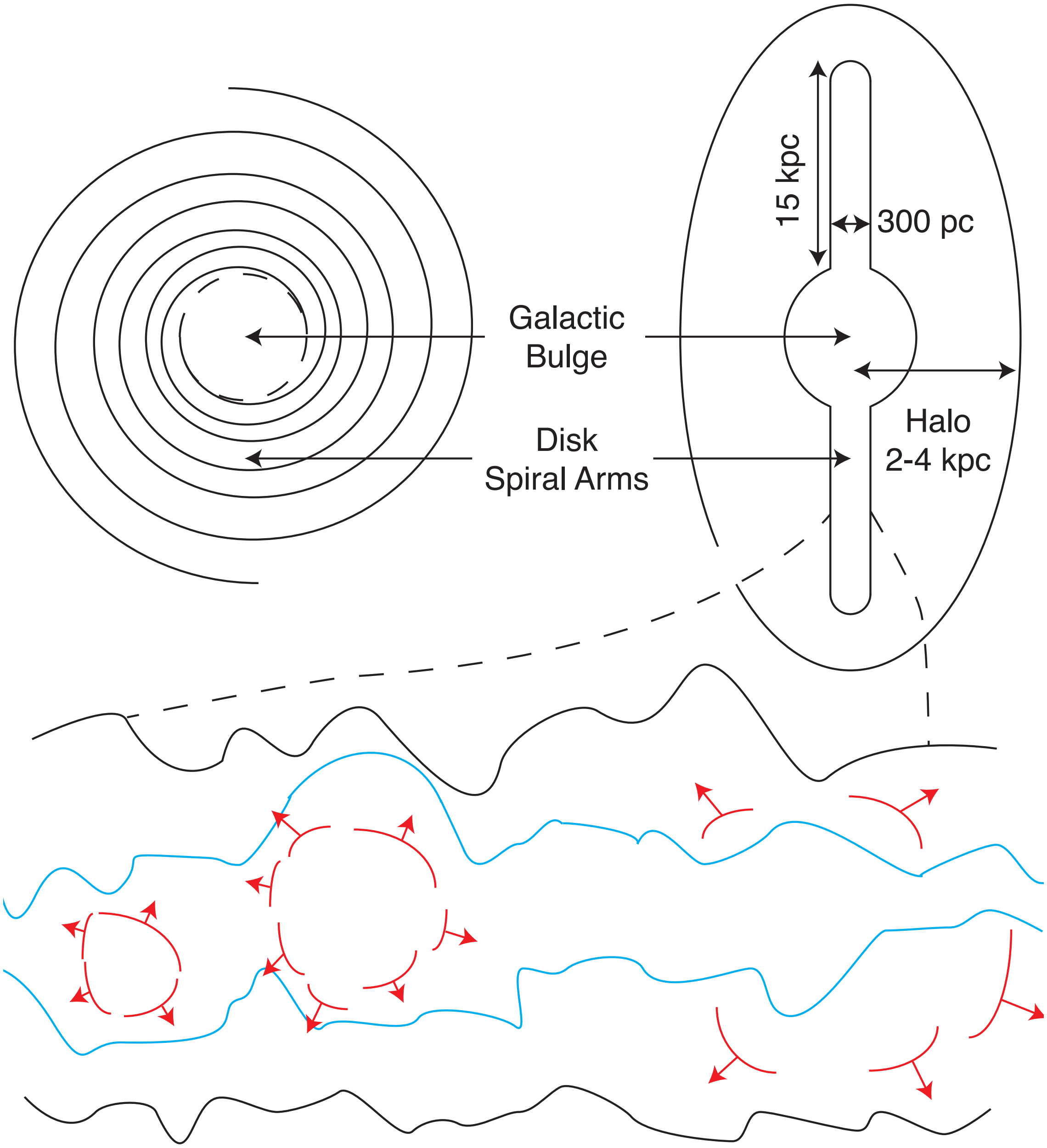

Figure 2.9: A cartoon of the basic structure of the Galaxy with an inset of the disc. The blue lines represent the interstellar medium (ISM) and the red lines are SNRs' hot plasma expanding into the ISM. From left to right show the expansion of the SNRs' shock-front into the ISM. The arrows represent areas of possible cosmic-ray acceleration

time, the maximum accelerated energy, and relative power of hadronic acceleration in different age SNRs.

Despite these difficulties, recent observations of IC 443, W44 and W51 fall within the observational constraints and have shown the characteristic π^0 spectrum indicating cosmic-ray proton acceleration as seen in Figures 2.7 and 2.8 [32, 33]. Clearly SNRs provide the necessary environment for first order Fermi acceleration and accelerate cosmic-ray protons.

Figure 2.9 shows a cartoon of cosmic-ray origins. A supernova explodes, producing a large cloud of hot plasma with stellar composition which slowly expands into the ISM, creating a supersonic shock front. Cosmic rays are accelerated in the supersonic shock front. This process repeats when another supernova explodes, injecting more cosmic rays into the Galaxy. This is not the end of the story for cosmic rays. Cosmic rays travel through our Galaxy full of magnetic fields, dust, gas, and winds before being observed. The journey noticeably changes the energy distribution, spectral index, and composition of cosmic rays. From measurements of different cosmic-ray elements we can learn about the physical processes that cosmic rays undergo during propagation and learn about the nature of the Galactic environment.

2.5 Propagation

Once these freshly accelerated cosmic rays leave their source, they travel through the Galaxy before finally being detected. We observe cosmic rays through the lens of propagation. The Galaxy is filled with magnetic fields, dust, and Galactic winds, which affect the composition and energy distribution of these freshly accelerated cosmic rays. The transport equation that sufficiently describes cosmic-ray propagation is:

$$\begin{aligned}\frac{\partial \mathcal{N}_i(E,\vec{x},t)}{\partial t} &= Q_i(E,t) + \nabla\cdot(D_i\nabla\mathcal{N}_i) - \frac{\partial}{\partial E}[b_i(E)\mathcal{N}_i(E)] - \frac{v\rho\sigma_i}{m}\mathcal{N}_i \\ &+ \frac{v\rho}{m}\sum_{k\geq i}\int\frac{d\sigma_{i,k}(E,E')}{dE}\mathcal{N}_k(E')dE' - \nabla\cdot\vec{u}\,\mathcal{N}_i(E) - \frac{1}{\Gamma\tau_{1/2}}\mathcal{N}_i \end{aligned} \tag{2.22}$$

where, $\mathcal{N}_i(E,\vec{x},t)$ is the density of particles of species i at position $\vec{x}$ with energy between E and $E+dE$. The source term is $Q_i(E,t)$ for particles of species i per interval dE. The second term represents diffusion. Energy loss or re-acceleration is described by the third term. The fourth and fifth terms represent particle loss from collisions and spallation. The spallation term includes both down fed cosmic rays from high energy cascades and nuclear fragmentation. The sixth term describes convection of cosmic rays due to Galactic winds. Loss of nuclei of type i from radioactive decay is represented by the final term [37].

2.5.1 Diffusion

The second term of Equation 2.22, $\nabla\cdot(D_i\nabla\mathcal{N}_i)$, describes diffusive processes. Understanding diffusion is an important factor to our understanding of cosmic-ray propagation. Using daughter to primary cosmic-ray ratios, like the Boron to Carbon ratio, and detection of radioactive cosmic-rays such as ^{60}Fe, we can determine that cosmic rays have an average lifetime of 2.6 MYr and travel through 5-10 g/cm^2 of matter during their lifetime [48,49]. The amount of matter in the line-of-sight of the

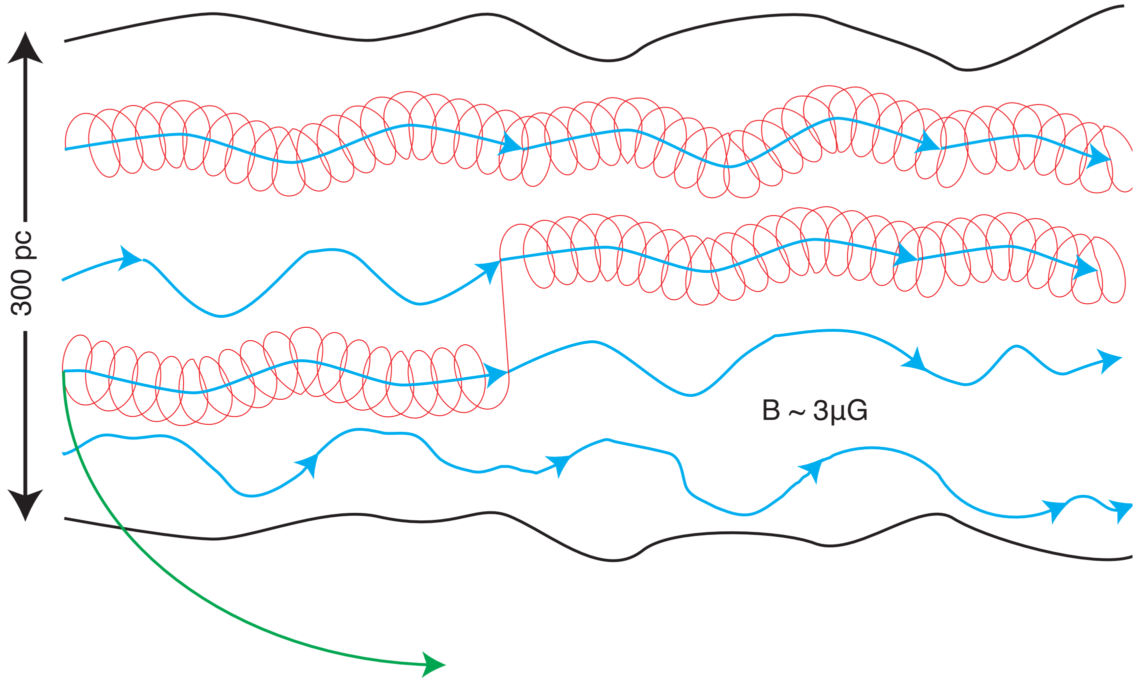

Figure 2.10: A cross-section of the Galactic disc that roughly shows how diffusion can affect cosmic-ray propagation. The black lines represent the boundary of the Galactic disc. The blue lines represent the magnetic field lines roughly parallel to the Galactic disc. The mean Galactic magnetic field is $\sim 3\mu$G. The red line represents the trajectory of a confined low energy cosmic ray as it interacts with the Galactic magnetic field. The green line represents the trajectory of an unconfined high energy cosmic ray as it interacts with the Galactic magnetic field.

Galactic disc is about 10^{-3} g/cm^2. This implies cosmic rays travel distances several thousand times greater than the thickness of the disc. Diffusion via collision-less interactions with interstellar magnetic fields show this implication is possible.

Figure 2.10 shows the process of diffusion due to the Galactic magnetic field. The Galaxy is full of magnetic fields associated with astrophysical objects like molecular clouds, nebulae, and large gas clouds. Since cosmic rays have charge, they spiral around Galactic magnetic field lines. If a magnetic field line has a kink, the cosmic ray can be diverted from the field line by the kink and travels until reaching a new magnetic field line as shown in Figure 2.10. Over their lifetime cosmic rays become completely disassociated with their source through diffusion. This produces a near-isotropic distribution of cosmic rays. We measure the mean Galactic magnetic field to be roughly 3 μG. We also measure the Galaxy to be roughly 300 parsecs thick [50]. Using the relativistic gyroradius from Equation 2.19, we can calculate the maximum energy of a particle confined to the Galaxy. We find a maximum proton energy of $\sim\ 10^{15}$ eV. Protons with energy less than this maximum energy will be confined to the Galaxy. Protons with energy greater than this will leave the Galaxy. Remember that combined with the different species of cosmic rays, this is a possible explanation of the knee; cosmic rays are no longer confined to the Galaxy with energies above the knee and therefore could undergo different acceleration process and have different spectral indices.

The proton spectral index is significantly affected by diffusion. The mean amount of matter traversed is dependent on the energy of the cosmic ray. Diffusion will effect the observed cosmic-ray spectral index. First order Fermi acceleration gave a source spectrum of $Q(E) \propto E^{-2.1}$. Including diffusion from the measured quantities of Galactic magnetic fields will reduce the spectral index by 0.6. Combining first order Fermi acceleration with diffusive processes will produce a cosmic ray spectral index of 2.7, which is much closer to the observed spectral index for Galactic cosmic-ray protons seen in Figure 2.3.

2.5.2 Energy Losses and Re-acceleration

The third term of Equation 2.22 is $-\frac{\partial}{\partial E}[b_i(E)\mathcal{N}_i(E)]$, where $b_i(E) \equiv dE/dt$ describes energy losses and re-acceleration. Energy losses are dominated by the same physical idea: a relativistic charged particle travels through a medium and interacts with lower energy electrons which are either unbound or bound to an atom. In the case of an unbound electron, the process is called Coulomb collision. The cosmic ray interacts with the electron via the Coulomb force and imparts a small amount of kinetic energy to the electron. As the interaction time is small, the cosmic ray's trajectory is unperturbed and the energy transfer is small. The accelerated electron radiates its gained energy via bremsstrahlung. The form of Coulomb energy loss is

$$\left(\frac{dE}{dt}\right)_{\text{Coul}} \approx -4\pi r_e^2 c m_e Z^2 n_e \ln\Lambda \frac{\beta}{x_m^3 + \beta^3} \tag{2.23}$$

where r_e is the classical electron radius, m_e is the electron mass, Z is the cosmic-ray charge, n_e is the plasma electron density, and

$$x_m \equiv [3\pi^{1/2}/4]^{1/3} \left(\frac{2kT_e}{m_e c^2}\right)^{1/2} \tag{2.24}$$

where T_e is the electron temperature, $n_e istheelectronnumberandis \sim 10^{-1} - 10^{-3} cm^{-3}$, and the Coulomb logarithm, $\ln\Lambda$, ranges from 40 - 50. Equation 2.23 shows Coulomb collisions depend on the thermal properties of the plasma [51]. The Coulomb cross-section for a 1 GeV proton as seen in Figure 5.10 is $\sim 2^{-26}$ cm^2. Interstellar particle density is ~ 1 cm^{-3} and traveling a the speed of light

$$n\sigma v \sim (1 \text{ cm}^{-3}) \times (2 \times 10^{-26} \text{ cm}^{-2}) \times (3 \times 10^{10} \text{ cm/s}) \sim 6 \times 10^{-16} \text{ s}^{-1}. \tag{2.25}$$

On average, every 53 MYr a 1 GeV cosmic-ray proton will Coulomb scatter in the ISM but as we established earlier the lifetime of Galactic cosmic-ray is 2.3 MYr. Therefore, energy losses to Coulomb scattering are negligible and the predominate term in energy losses is ionization.

Ionization losses occur when a cosmic ray interacts with an electron bound to an atom. The electron can only gain energy in discrete values according to the atom's ionization function. Ionization can be approximated by

$$\frac{dE}{dt}_I(\beta > \beta_0) = 2\pi r_e^2 m_e c^2 Z^2 \frac{1}{\beta} \sum_{s=H,H_e} n_s B_s \tag{2.26}$$

where n_s is the number density of the element s in the ISM, $\beta_0 = 1.4e^2/\hbar c = 0.01$ is the characteristic velocity of orbital electrons, and

$$B_S = \ln\left(\frac{s m_e c^2 \beta^2 \gamma^2}{\langle I_s \rangle^2}\right)\left(\frac{2 m_e c^2 \beta^2 \gamma^2}{1 + (2\gamma m_e/M)}\right) - 2\beta^2 \tag{2.27}$$

where M is the mass of the cosmic ray, and γ is the Lorentz factor, $\langle I_s \rangle$ is the geometric mean of all ionization and excitation potentials of the atom. For hydrogen $\langle I_H \rangle = 19$ eV and for helium $\langle I_{He} \rangle = 44$ eV [51].

Due to the large amount of material cosmic rays interact with during their lifetime, energy loss should occur via the methods described in this section. The amount of energy lost depends greatly on the Galactic environment. Note that both energy loss mechanisms depend on charge, and therefore ionization cannot be ignored when dealing with differently charged cosmic rays.

The term $-\frac{\partial}{\partial E}[b_i(E)\mathcal{N}_i(E)]$, where $b_i(E) \equiv dE/dt$ can also describe energy gains through re-acceleration. The most widely accepted form of re-acceleration is second order Fermi acceleration. Second order Fermi acceleration occurs when turbulent magnetic fields in large moving gas clouds impart a momentum kick to the cosmic ray along the gas cloud's motion shown in Figure 2.11. Each momentum kick increases the cosmic ray's energy.

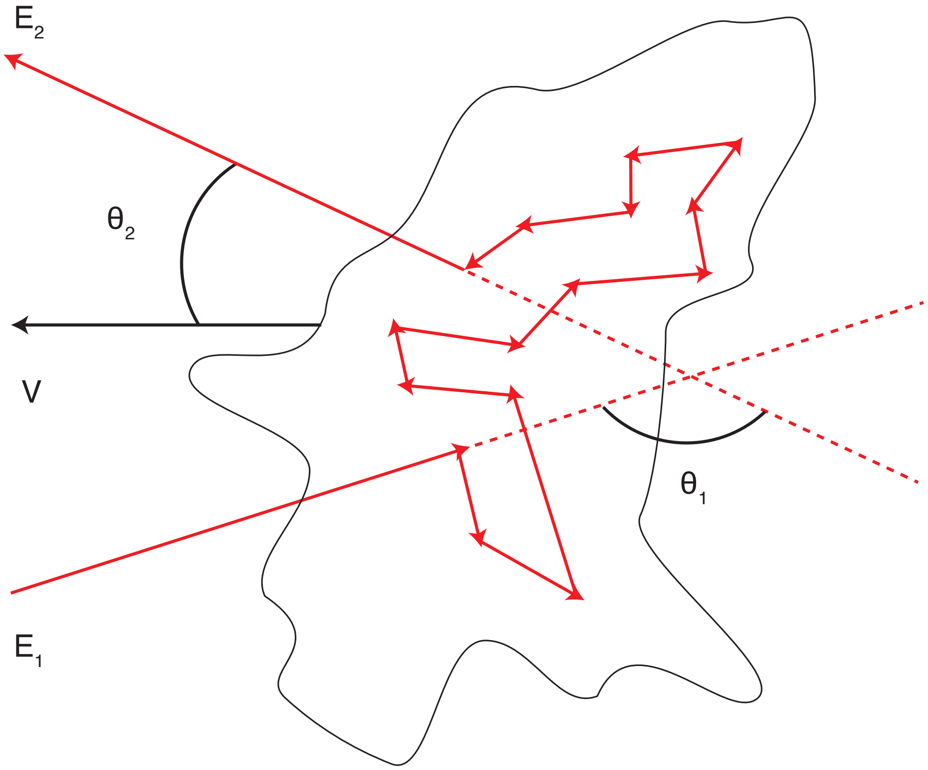

Figure 2.11: Second order Fermi acceleration of a moving gas cloud. V is the velocity of the gas cloud. θ_1 is the angle between the incoming and outgoing trajectories of the cosmic ray. θ_2 is the angle between the outgoing trajectory and the velocity of the gas cloud [37].

We can take the angular average of $\frac{\Delta E}{E_1}$ as we did for first order Fermi acceleration and find the average fractional energy gain per encounter to be

$$\left\langle \frac{\Delta E}{E_1} \right\rangle = \frac{1+\frac{1}{3}\beta^2}{1-\beta^2} - 1 \approx \frac{4}{3}\beta^2 \tag{2.28}$$

when the cloud's velocity is not relativistic. The fractional energy gain per encounter is second order in the velocity of the gas cloud. Secondary to primary measurements can put a limit on the strength of re-acceleration. If second order Fermi acceleration is the acceleration process, secondary cosmic rays will be accelerated at the same time as primary cosmic rays. A secondary to primary cosmic ray measurement allows us to put a limit on the strength of second order Fermi acceleration and therefore re-acceleration. Second order Fermi acceleration predicts that higher energy particles would spend a longer time being accelerated thus increasing the relative abundance of secondaries as energy increases. We can also learn about the ISM from secondary to primary measurements since re-acceleration is driven by magnetic fields in the ISM [52].

2.5.3 Interactions

The fourth and fifth terms of Equation 2.22, $-\frac{v\rho\sigma_i}{m}\mathcal{N}_i + \frac{v\rho}{m}\sum_{k\geq i}\int \frac{d\sigma_{i,k}(E,E')}{dE}\mathcal{N}_k(E')dE'$, are interactions and spallation of cosmic rays off of cold interstellar gas. These are purely nuclear interactions of cosmic rays with low energy protons and other cosmic rays. The two terms use the same physics but differ in their end products. The $-\frac{v\rho\sigma_i}{m}\mathcal{N}_i$ term produces hadronic showers through inelastic scattering of two protons. This has an effect on the proton spectrum since it leads to the depletion of cosmic-ray protons in particularly dense regions such as molecular clouds. This can also lead to an indirect measure of cosmic-ray protons through observations of diffuse γ-rays from molecular clouds near accelerators like SNRs which are then able to probe the strength of hadronic production of said accelerators [53,54]. The second term is a direct relation to the production of secondary cosmic rays through spallation.

The term $\frac{v\rho}{m}\sum_{k\geq i}\int\frac{d\sigma_{i,k}(E,E')}{dE}\mathcal{N}_{\|}(E')dE'$ describes spallation or nuclear fragmentation of heavier cosmic rays into lighter cosmic rays [37]. Primary cosmic rays are the result of stellar nucleosynthesis. As primary cosmic rays propagate through the Galaxy they spallate off of low energy protons. The result is a secondary cosmic ray that has most of the primary cosmic ray's energy. An example of this is carbon interacting with a proton and spallating into boron and two protons. Boron is not a final product of stellar nucleosynthesis; any boron cosmic rays are predominantly the result of spallation. Spallation explains the over abundance of cosmic ray secondaries like boron [55].

Spallation depends on the environment of the Galaxy. The longer a cosmic ray travels through the ISM, the larger the probability of interaction with the ISM. Spallation also depends on the cross-section of the nuclear interaction between the primary cosmic ray and the low energy proton. Cross-sections for these interactions are sources of error in understanding propagation. These interactions cannot be recreated on Earth; the energy required is far too high for current heavy ion accelerators. Cross-sections are measured at lower energies and extrapolated to higher energies using knowledge of nuclear interactions [56]. The energy dependence of these cross-sections is not completely understood and provides a source of error in our understanding of cosmic-ray propagation.

2.5.4 Convection

The sixth term of Equation 2.22, $\nabla \cdot \vec{u}\,\mathcal{N}_i(E)$, describes adiabatic momentum gains or losses in the Galactic wind, also known as convection [37]. Convection is an oft-forgotten term when models of cosmic-ray propagation are formulated [52]. Cosmic rays trapped in the magnetic field lines of Galactic winds adiabatically lose energy as the wind speed increases from the plane of the disc. The Galactic winds are driven by a pressure gradient from cosmic rays. These Galactic winds can create open field lines and can inflate field lines, both of which allow cosmic rays to escape into the Galactic halo [57]. This provides both a method of energy loss and cosmic ray escape from the Galactic disc.

The two most popular models for convection are one zone and two zone [52]. The one zone model assumes that convection and diffusion occur everywhere in the disc. The two zone model assumes that cosmic-ray propagation is diffusive in a zone where $|z| \leq 1$ kpc from the disc and diffusive and convective above 1 kpc where z is the distance above or below the disc.

The energy dependence of secondary to primary ratios is a good diagnostic for the strength of convection for cosmic-ray propagation. For convection dominated cosmic-ray transport with a constant Galactic wind velocity, there is no energy dependence for secondary to primary ratios [52]. Thus, convection alone cannot reproduce the observed energy dependence of secondary to primary ratios. Isotopes are used to constrain the Galactic wind speed to $\leq$ 10 km s^{-1} kpc^{-1} [52]. Most cosmic-ray propagation models include convection in their transport equations but support for convection requires direct observations of Galactic winds. Galactic winds are considered a small effect on the proton cosmic-ray spectrum mostly because of their small velocities but recent measurements of the Fermi Bubbles have shown that Galactic winds could have a larger contribution to cosmic-ray propagation than previously thought [58]. The Fermi Bubbles present an interesting situation where a potentially more active past state of the Galaxy could have effects on the current state of cosmic-ray propagation and therefore temporally dependent effects might need to be taken into account. This would have a much larger effect on cosmic-ray electrons than protons but the effect on cosmic-ray protons could change with further measurements [58]. Measurements of the local Galactic winds are poorly constrained outside of secondary to primary ratio measurements.

2.5.5 Radioactive Decay

The last term of Equation 2.22, $\frac{1}{\Gamma\tau_{1/2}}\mathcal{N}_i$, represents radioactive decay of unstable cosmic rays. $\Gamma\tau_{1/2}$ is the time dilated lifetime of the cosmic ray [37]. While protons are stable well beyond the lifetime of the Universe, other radioactive cosmic rays can decay into daughter particles which include protons [59]. Fortunately these unstable cosmic-ray isotopes are in such low abundance that they do not have a significant effect on the cosmic-ray proton spectrum.

2.6 Propagation Models

Because of the complexity of the differential Equation 2.22 and the many terms which involve energy, spatial, and temporal dependence, an analytical solution is often nearly impossible. Numerical solutions can be approximated but it is often easier to only model the dominant terms which affect the cosmic-ray spectra in simpler terms. The purpose of this section is not to describe in exacting details each cosmic-ray transport and propagation model, but to give a sense of the necessity cosmic-ray transport models in estimating astrophysical quantities from the cosmic-ray proton spectrum. One of the first and most prevalent models is the Leaky Box Model of cosmic-ray diffusion [60].

2.6.1 The Leaky Box Model

The Leaky Box Model assumes that cosmic rays propagate freely with a spatially constant time of escape, therefore the diffusion can be substituted with $\mathcal{N}_i/\tau_{esc}$. The diffusion coefficient, D_i, becomes a function of the distance away from the Galactic disc and the mean amount of material traversed becomes $\lambda_{esc} = \rho\beta c\tau_{esc}$ where βc is the speed of the cosmic ray [37, 60]. Substituting these values into Equation 2.22 results in:

$$\frac{\mathcal{N}_i(E)}{\tau_{esc}(E)} = Q_i(E) - \left(\frac{\beta\ c\ \rho}{\lambda_i}\right)\mathcal{N}_i(E) + \frac{\beta\ c\rho}{m}\sum_{k\geq i}\sigma_{i,k}\mathcal{N}_k(E) \tag{2.29}$$

ignoring radioactive decay, re-acceleration processes, convection, and interactions. For protons, the spallation term can also be ignored, giving a function for proton spectrum of:

$$\mathcal{N}_p(E) = \frac{Q_P(E)\tau_{esc}(E)}{1 + \lambda_{esc}(E)/\lambda_p} \tag{2.30}$$

We know for protons the interaction length is $\sim$ 55 g/cm^3, therefore $\lambda_{esc} \ll \lambda_p$ and Equation 2.30 reduces to:

$$\mathcal{N}_p(E) = Q_p(E)\tau_{esc}(E). \tag{2.31}$$

Therefore to model the cosmic-ray proton spectrum one has to measure τ_{esc} as a function of energy [37]. This can be done by examining primary to secondary ratios and detection of radioactively unstable isotopes as was seen in § 2.5.1 with [48] and [49].

The Leaky Box Model is a very simple way to describe cosmic-ray propagation. It has many limitations in not including more complicated interactions such as convection, energy losses, and re-acceleration. Additionally, assuming a spatially constant τ_{esc} is unfounded since we know that the density of the Galaxy is highly spatially dependent and does not include the Galactic halo which can affect cosmic-ray diffusion.

2.6.2 Numerical Diffusive Propagation Models

More complex and robust numerical codes of cosmic-ray transport and propagation exist using different measurements with proper accounting of Equation 2.22. We will discuss two codes: *GALPROP* and *DRAGON2*.

GALPROP is a software package which numerically solves Equation 2.22 by including data sources and constraints from various sources [52]. Cosmic-ray isotopes and secondaries are used for bounding of diffusion coefficients, lifetime of cosmic rays, and average Galactic properties like magnetic fields and interstellar medium densities. Direct measurements of isotopes and secondary cosmic rays from space-based instruments such as *ACE-CRIS* are used to bound these model parameters [61]. Direct observations of H_1, from 21 cm surveys, and H_2, from CO surveys, gas column densities gives accurate representations for cosmic-ray interactions and are critical to the understanding of the diffuse γ-ray emission observed by the *Fermi*-LAT and the development the LAT diffuse model [62]. Stellar populations and dust emission are taken from direct far infrared measured from *COBE* [61]. This is used for propagation of electrons and diffuse measurements from inverse-Compton scattering. Nuclear spallation cross-sections and isotope half-lives are measured via terrestrial accelerators simulated using CME2k and LAQGSM nuclear code [61]. This is critical for the understanding of the production of secondary cosmic rays. The last contribution is from the source distribution of cosmic ray primary from γ-ray observations of local SNRs. The energy injection spectrum from SNRs is assumed to be a power-law spectrum. The robustness of *GALPROP* is that all of these parameters are mutable, therefore you can set different diffusion properties and test source distributions of SNRs to recreate an observed cosmic-ray spectrum.

While *GALPROP* is the fundamental choice for many experiments to model cosmic-ray propagation and transport, alternatives do exist. One of the alternative cosmic-ray propagation and transport softwares is *DRAGON2* [63]. *DRAGON2* is fundamentally similar to *GALPROP* but has a few notable differences and incorporates updated data with more recent observations and measurements. *DRAGON2* uses several different gas density models including models based on *WMAP* data, new parameterizations and models of Galactic magnetic fields, additional impacts of spiral arm geometry, and new source density models [64, 65]. In addition to new astrophysical inputs, diffusion is modeled using a spatial dependence with a parallel and perpendicular diffusion coefficient, advective transport of cosmic-rays is included, and spallation is calculated using *FLUKA* particle simulation software [65, 66]. *DRAGON2* provides an alternative to *GALPROP* with updated astrophysical data and models and improved modeling of Galactic structure and transport physics.

The general difference between *GALPROP* and *DRAGON2* are the handling of local and distant cosmic-ray effects. *GALPROP* assumes uniform density and magnetic field distributions while *DRAGON2* allows for more degrees of freedom in local and non-local environments. Inclusion of additional physics, such as advective transport, produces small perturbations in cosmic-ray propagation. There is growing evidence of the effect of local and non-local environments on cosmic-ray physics from closer examination of the γ-ray diffuse models and cosmic-ray spectral modeling of *AMS-02* results [67, 68]. These local versus non-local effects could be evident in the cosmic-ray proton spectrum as a break energy where different populations begin to dominate. The *Fermi*-LAT energy range falls within the potential range for observing a spectral break and through interpretations discussed in § 6.9 can help reveal potential additional multi-component source distributions or the necessity for additional propagation physics. An additional possibility is different classes of accelerators such as SNRs or groups of SNRs called super-bubbles. We also note that since there are very few single species measurements above 100 TeV and in general few measurements around the cosmic-ray knee, that models and spectral fits at lower energies are extended to higher energies, as seen in Figure 2.5, necessitating a precise measurement of cosmic-ray spectra at lower energies.

It becomes evident that diffusion models and cosmic-ray transport software are necessary if one is to properly interpret any cosmic-ray spectral measurement. We can disentangle source population distributions and physical requirements for particle acceleration using *GALPROP* or *DRAGON2*. We can also search for changes in the cosmic-ray paradigm such as new cosmic-ray sources, changes in propagation, or local source distributions of cosmic-ray accelerators. This is performed by comparing cosmic-ray spectral measurements to models and interpretations of source distributions and modified cosmic-ray propagation. These interpretations can improve our understanding of the Galaxy.

Chapter 3: *Fermi* Large Area Telescope

Launched on June 11, 2008, the *Fermi Gamma-ray Space Telescope* operates in a low Earth orbit observing the entire sky every three hours and was designed to study γ-rays from 8 keV to 300 GeV. There are two instruments on *Fermi* to study γ-rays and cosmic rays called the Large Area Telescope (LAT) and Gamma-Ray Burst Monitor (GBM). The cosmic-ray proton spectral measurement is performed by the LAT and will be the focus of this chapter. We describe the subsystems of the LAT and their contribution to making the cosmic-ray proton spectral measurement. Additionally we describe the recent upgrade of the event reconstruction and simulation software called Pass 8 and describe the simulations used in this analysis.

3.1 Design

The LAT is a pair-conversion γ-ray telescope designed to measure the energy and incident direction of γ-rays from 20 MeV to > 300 GeV for events. The standard field of view for photons is very wide and ranges from normal incidence to the top of the LAT to 70° off axis. When a γ-ray enters the LAT it pair-converts into an electron-positron pair-converting in layers of tungsten foil in the tracker (TKR) as seen in Figure 3.1. These electron-positron pairs will then deposit energy via

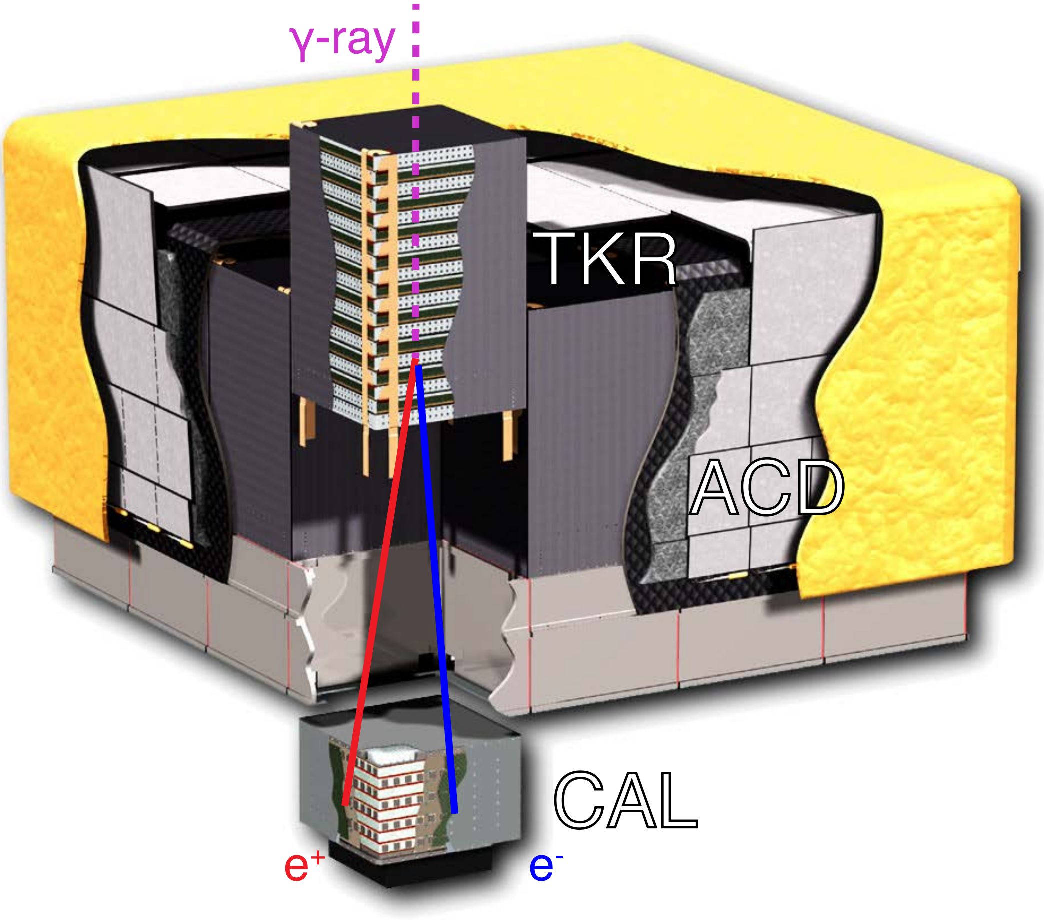

Figure 3.1: LAT cutaway showing a γ-ray converting into an electron-positron pair in reference to the ACD, TKR, and CAL.

ionization in the silicon strip detectors (SSD) of the TKR leaving a track pointing toward the original direction of the γ-ray. More information about ionization can be found later in § 4.1. The energy loss via ionization in the TKR is small and the resulting electron and positron pair travel to the CAL carrying almost all of their original energy. Entering the much denser CAL, the electron-positron pair undergoes an electromagnetic shower. More information about electromagnetic showers can be found later in § 5.1. The CAL measures energy deposition of the said electromagnetic shower to allow an estimate of the original energy of the incident γ-ray. On the

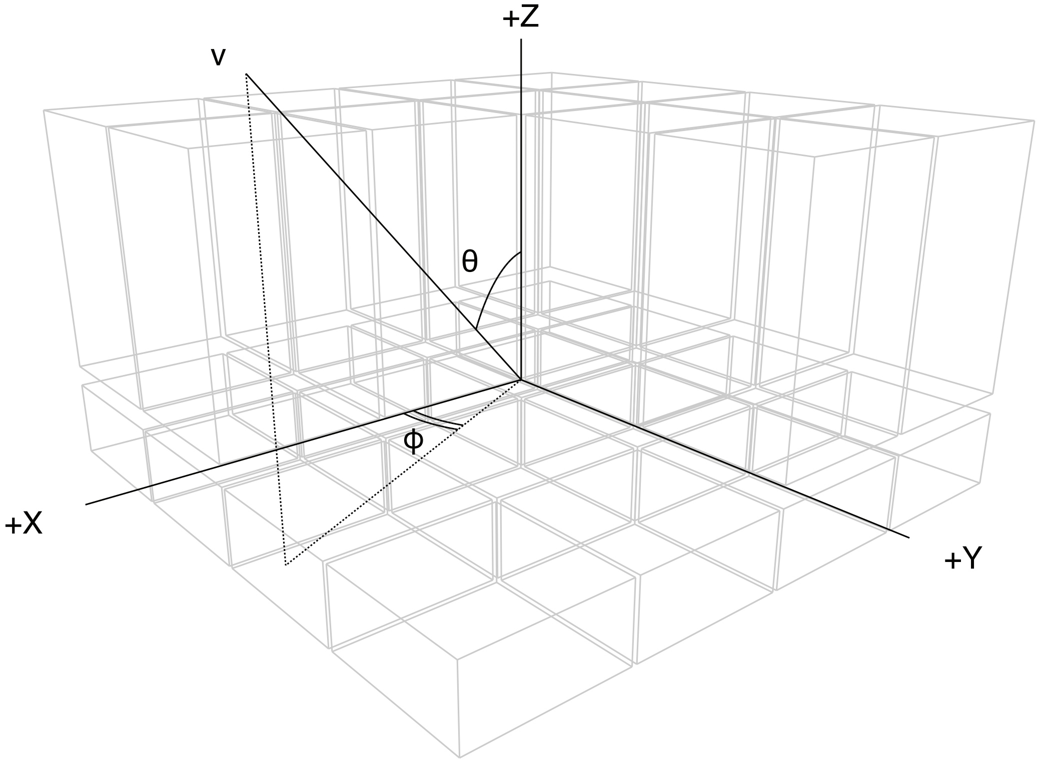

Figure 3.2: Definition of the LAT coordinate system in X,Y,Z and θ and ϕ directions overlaid on schematic of the LAT showing the 16 TKR-CAL modules [69].

Parameter	Value or Range
Energy Range	20 MeV - $>$ 300 GeV
Geometric area at normal incidence	0.95 m^2
γ-ray Energy Resolution	8% - 20%
γ-ray Angular Resolution	0.15° - 3.5°
Field of View	2.4 sr

Table 3.1: Summary of the LAT performance for γ-rays [69].

outside of the ± X, ± Y, and +Z sides, defined in Figure 3.2, of the LAT is the anti-coincidence detector (ACD). The ACD is used to detect the charge of an incoming particle. Because gamma rays are neutrally charged they deposit no signal in the ACD unlike charged cosmic-rays like protons, ions, and electrons. The ACD can then be used as a veto for charged cosmic rays which have much higher fluxes than many astrophysical γ-ray sources. The performance of the LAT for γ-rays is summarized in Table 3.1.

The LAT, as stated above, is composed of three subsystems: an anti-coincidence detector (ACD), a silicon strip tracker (TKR), and electromagnetic calorimeter (CAL). One CAL module and TKR module make a tower. The LAT consists of 16 towers in a 4 × 4 array for a total size 1.8 m × 1.8 meters × 0.72 m. We describe each subsystem in detail with a particular focus on cosmic-ray studies.

3.1.1 Anti-coincidence Detector

The ACD's primary mission is to veto charged cosmic rays with a high efficiency. Since the flux of cosmic rays, primarily protons, is significantly higher than any astrophysical γ-ray source, it is crucial to remove this background from the signal. To achieve this, the ACD consists of 89 plastic scintillator tiles and 8 plastic scintillator ribbons each with two photomultiplier tubes (PMT) to detect ionization photons produced when charged particles deposit energy in each ACD element. Since γ-rays are neutrally charged they will not deposit energy in the ACD. The arrangement of the tiles and ribbons can be seen in Figure 3.3. On the top of the

Property	Value
Number of tiles	89
Segmentation into tiles	< 0.1 m^2 each
Efficiency for MIP detection	> 0.9997
Top tile thickness	12.0 mm
Side tile thickness	10.0 mm
ACD tile material	Polyvinyltoluene

Table 3.2: Summary of the ACD detector properties [69].

LAT, ACD tiles have a thickness of 12 mm arranged in a 5 × 5 array. On each side, 16 tiles are arranged in 5 × 3 array with an additional large tile covering the entire bottom row. Ribbons are arranged to cover gaps between tiles on the top and sides of the LAT. The ACD has a 99.97% efficiency for charged particle detection. The performance and properties of the ACD are summarized in Table 3.2.

Segmentation of the ACD is designed to reduce false vetoes of $>$ 20GeV γ-ray events due to back-splash off of the CAL [70, 71]. Back-splash occurs when the electron or positron interact with the CAL and emits low energy electrons and positrons back and up into the TKR. These low energy electrons deposit energy in the ACD creating what would be a veto if the ACD were not segmented. Segmentation enables the LAT to ignore an ACD signal not adjacent to the best reconstructed track determined from the TKR.

When a charged particle passes through an ACD element it will deposit energy

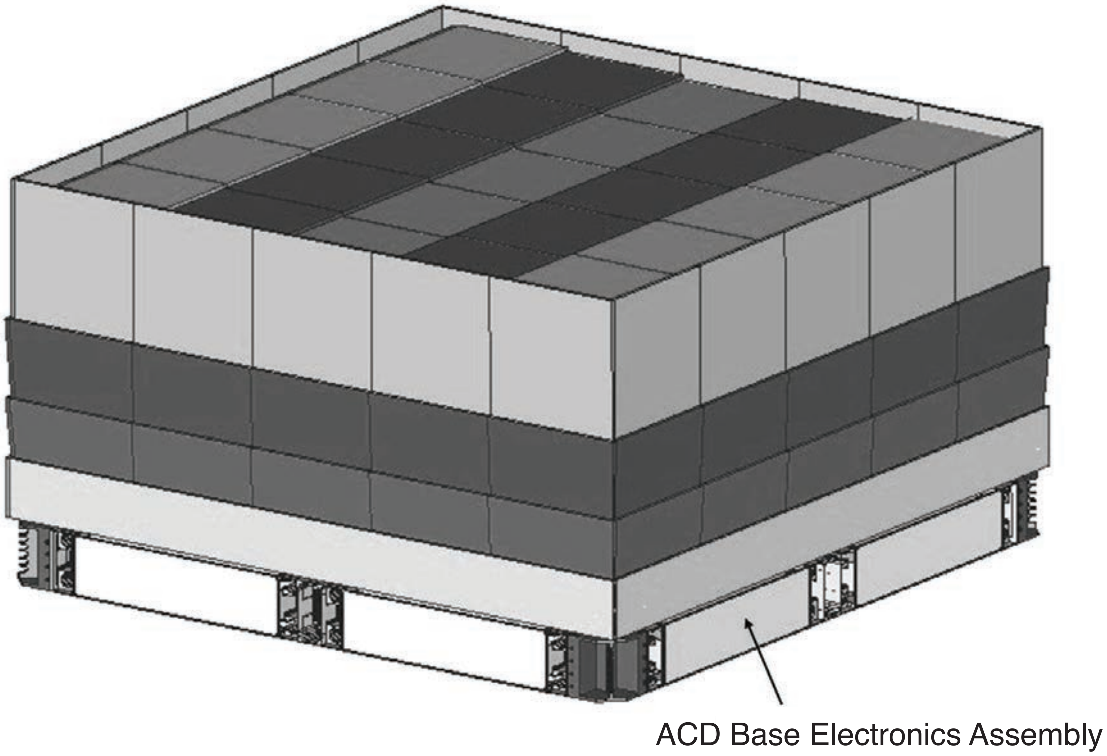

Figure 3.3: The LAT ACD design with 89 plastic scintillator tiles with a 5 × 5 array on the top and 3 × 5 array on the sides and one additional large tile on the bottom of each side for help with back-splash. Each tile has two PMTs for redundancy [69].

via ionization. The deposited energy is absorbed by the plastic scintillator and re-emitted as photons through florescence and phosphorescence transitions shown in Figure 3.6. These photons are then guided to PMTs through wavelength shifting fibers embedded in the ACD element where it is converted to photoelectrons and an analog signal. Each tile and ribbon have two PMTs. Each PTM has a low and high range readout. The dual readout is required because ionization deposits energy proportional to Z^2 of the charged particle therefore signal can quickly grow. The low range is set to detect minimum ionizing protons, defined in § 4.1, and the high range is set to detect higher charged particles like minimum ionizing carbon, nitrogen, and oxygen. Each PMT is attached to a fast shaping amplifier for triggering [72]. The dual readout allows for high efficiency for detecting protons through a linear low range response and higher charged Z particles through a non-linear high range response.

In the context of cosmic-ray measurements, the ACD is a powerful instrument for separation of cosmic-ray species. As stated previously, the ACD was not designed for high-precision measurements of the charge of cosmic-rays, but we can use the physics behind ionization to measure charge. Because of the charge dependence of ionization, higher charged cosmic rays will deposit more energy than protons or electrons. This allows for the removal of helium and other ions from the desired cosmic-ray sample. The ACD can also help in the removal of bottom entering events. Further details about the charge measurement for this analysis will be explained in Chapter 4.

3.1.2 Calorimeter

The CAL's main purpose is to measure the energy of incident γ-rays and to image showers for particle separation. Each CAL module is positioned under a TKR module and consists of 96 CsI(Tl) crystals which are arranged in 8 layers with 12 crystals in each layer [69, 73]. Figure 3.4 shows the diagram for an individual CAL module. Every CAL layer is arranged in an alternating X-Y direction creating a hodoscopic array of crystals, which allows for the ability to measure the particle's shower shape as well as deposited energy. Each CAL crystal has dimensions 326 mm

Property	Value
Depth including TKR in X_0	10.1
Longitudinal segmentation	8 segments
Lateral segmentation	$\sim$ Moliere radius (3.5 cm)
CAL crystal material	CsI(Tl)
Crystal size	326 mm × 26.7 mm × 19.9 mm
Number of crystals per module	96

Table 3.3: Summary of the CAL detector properties [34, 69].

× 26.7 mm × 19.9 mm with photo-diodes on each end with two ranges; a low range covering 2 MeV to 1.6 GeV, and a high range, 100 MeV to 70 GeV. A comparison between the energy deposition on each end of the crystal allows for a position measurement along the longitudinal direction of the crystal [69, 73]. Measuring shower shapes allows for the discrimination between electromagnetic and hadronic showers, which is a powerful tool for distinguishing γ-ray events from background protons.

The CAL at normal incidence is 8.6 X_0 (radiation lengths) deep, but for off axis events the maximum path-length is ~17.2 X_0. The CAL is therefore capable of measuring electromagnetic showers to TeV energies [69]. Using the longitudinal and transverse profile of electromagnetic showers measured by the CAL, the true energy of the incident γ-ray can be estimated as described more fully in § 5.2. CAL detector properties are summarized in Table 3.3.

In the context of cosmic-ray measurements, the CAL's imaging power can

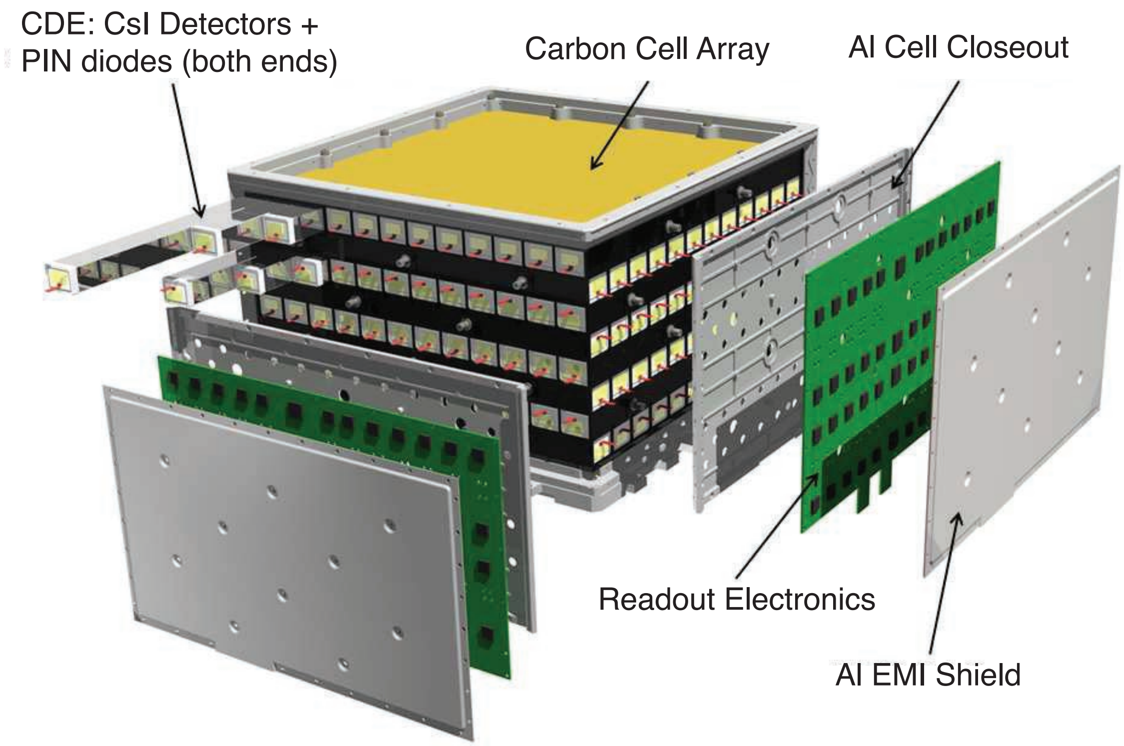

Figure 3.4: The design of a LAT CAL module. Each module has 96 CsI(Tl) crystals, where each crystal has high and low signal readouts on each end, in 8 layers with each layer rotated by 90° to create a hodoscopic array [69].

be used to separate purely electromagnetic showers induced by electrons from the hadronic showers induced by protons. By reconstructing the shower profile, the energy for electrons and the electromagnetic fraction of hadronic showers can be estimated. The CAL's shallow depth for hadronic showers becomes a major issue for energy estimation. The CAL's size and design result in an inability to constrain the hadronic component of a proton-induced shower. Despite these limitations, through careful event selection we can measure the incident energy of cosmic-ray protons with a reasonable accuracy. More details about energy reconstruction for γ-rays and protons are described in § 5.2 and § 5.4.

3.1.3 Tracker

Property	Value
Active area at normal incidence	1.96 m^2
γ-ray conversion probability	63%
Number of channels per tower	1536
SSD strip spacing	228 μm
SSD efficiency for MIPs	$> 99\%$
Aspect ratio (height/width)	0.4
Front convert foil thickness in X_0	$12 \times 0.03 = 0.36$
Back convert foil thickness in X_0	$4 \times 0.18 = 0.72$

Table 3.4: Summary of the TKR detector properties [69, 74].

The TKR consists of 16 layers of tungsten foil, used as conversion material for incident γ-rays, interleaved with 18 planes of X-Y oriented SSDs to detect the position of the photon conversion into an electron-positron pair. There are a total of 18 TKR planes where each plane consists of two layers of single sided SSD oriented in the X and Y direction [69]. Each SSD has a depth of $400\mu m$. To reduce multiple scattering of the electron-positron pair which would reduce the point spread function (PSF) of the LAT, the X-Y SSDs are placed directly underneath the thin tungsten foil. Photon pair production and multiple scattering of an electron-positron pair are shown in Figure 3.5.

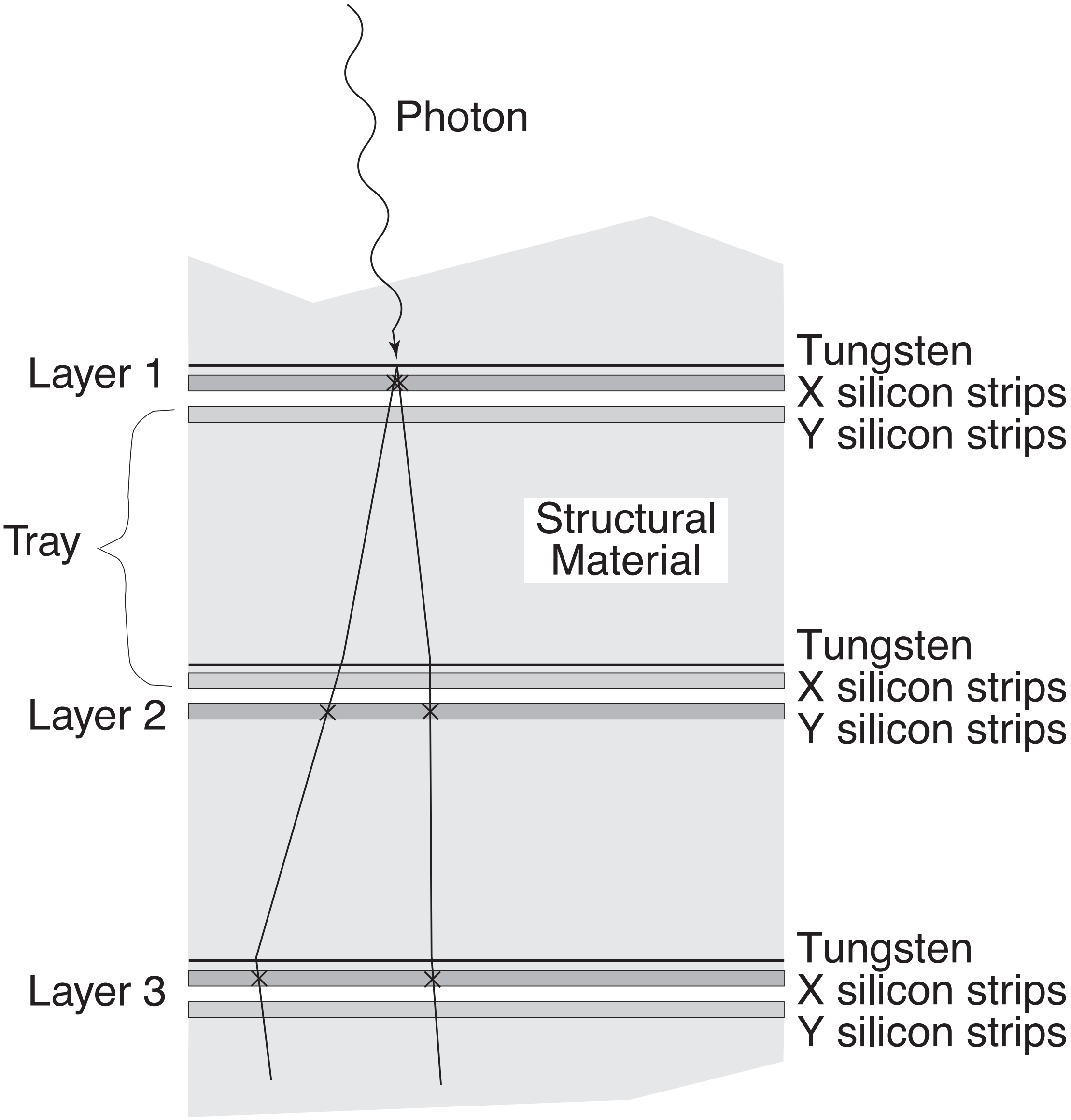

Figure 3.5: Simple representation of the TKR layer design with tungsten foil on top of the each X-Y SSD. Also shown is an ideal photon conversion event into an electron-positron pair and detected by the SSD. [74].

The TKR is further designated into *front* and *back* sections. The *front* refers to the first 12 layers of tungsten which are 0.095 mm or a total of 0.36 X_0 thick [74]. The *back* refers to the bottom 4 layers of of tungsten which are 0.72 mm or a total of 0.72 X_0 thick [74]. The purpose of this design is to ensure both good direction reconstruction and high γ-ray conversion efficiency. Additionally the *back* tungsten layers help limit the amount of back-splash electrons and positrons propagating back into the TKR and therefore ruining the direction reconstruction. The bottom two TKR planes do not contain tungsten foil because the TKR trigger requires three successive hits. Therefore any event converting in the last two layers would not trigger [72]. Table 3.4 shows the properties of the TKR.

The total depth of the TKR at normal incidence is $\sim 1.0\ X_0$, meaning that about 63% of γ-ray events pair produce in the TKR. Using the X-Y position and Z position of each plane, the TKR is able to measure propagation of the electron-positron pair and reconstruct the incident γ-ray direction by finding the best track. The best track is longest, straightest, and that which carries the most momentum. Further description of the TKR design can be found in [74].

In the context of cosmic-ray experiments, the TKR has two important purposes. The first is an independent charge measurement of the incident cosmic-ray. This can be done by measuring the signal in the TKR which will be related to the energy deposition in the silicon via ionization. As with the ACD, ionization is charge dependent therefore the signal in the TKR can be used to discriminate between different cosmic-ray species. The reconstructed direction is used in the construction of other variables which depend on the incident direction of the cosmic ray. Direction reconstruction is important because the path-length of the cosmic ray through the LAT to correct the energy deposition in the ACD and reconstruct the energy in the CAL. Since cosmic rays do not pair produce, they leave long straight tracks through the entire TKR which can be easily reconstructed. However, low energy electrons induced from ionization can create false tracks. Therefore it is important to have a proper understanding of direction reconstruction.

3.1.4 Triggers and Filters

Because of the high rate of cosmic-ray triggers and wide variety of energies the LAT detects, it is necessary to have several different trigger schemes and different on-board event filters to reduce the amount of data volume to down-link to the ground [72].

Each subsystem provides separate triggers shown below:

- `TKR`: Three consecutive hits in the X-Y silicon layers have signal above threshold, calibrated to 0.25 MIPs, in a tower.
- `CAL_LO`: When any signal in any CAL crystal is above 100 MeV.
- `CAL_HI`: When any signal in any CAL crystal is above 1 GeV.
- `VETO`: When signal in an ACD tile associated with TKR towers is above the veto threshold of 0.45 MIPs.
- `CNO`: When the signal in any ACD tile is above 25 MIPs, which indicates the traversal of a cosmic-ray ion in the ACD.

Three additional triggers, for a total of 8 triggers, are defined and not used in flight. The last trigger is called `PERIODIC`, which runs at 2 Hz. These events are used for the diagnosis and calibration of LAT subsystems.

Eng.	`PER`	`CAL_HI`	`CAL_LO`	`TKR`	`VETO`	`CNO`	Prescale	Rate[Hz]
3	1	×	×	×	×	×	0	2
4	0	×	1	1	1	1	0	200
5	0	×	×	×	×	1	250	5
6	0	1	×	×	×	0	0	100
7	0	0	×	1	0	0	0	1500
8	0	0	1	0	0	0	0	400
9	0	0	1	1	1	0	0	700
10	0	0	0	1	1	0	50	100

Table 3.5: Definition of standard trigger engines where: 1 - required, 0 - excluded, and × - either [72].

These 8 triggers are mapped to all 256 possible combinations on to trigger engines. Triggers are allowed to open a request which opens a trigger window. If the trigger conditions are satisfied then a global trigger is issued and event acquisition is started [72]. The trigger engines are scalable such that a prescale value can be required for the number of valid trigger requests necessary to send a global trigger. Table 3.5 shows the different trigger engines.

Standard engines 4 and 6 are the most important for cosmic-ray measurements. Engine 4 requires at least `CAL_LO`, three hits in a row in the TKR, and signal in the ACD above 25 MIPs. Engine 6 requires high energy signal in CAL and signal below 25 MIPs in the ACD.

Additionally filters are implemented on-board due to the high rate of events and the limited bandwidth for down-link to the ground [72]. There are three on-board event filters for the LAT:

- `GAMMA` filter: designed to accept γ-rays.
- `HI_PASS` filter: any event with deposited energy > 20 GeV in the CAL is down-linked.
- `DIAGNOSTIC` filter: uses 2 Hz of `PERIODIC` triggers and unbiased sample of all triggers with no filters.

Because of the `GAMMA` filter, the event rate for cosmic rays is heavily reduced. Therefore it becomes necessary to use `HI_PASS` and `DIAGNOSTIC` filters for cosmic-ray studies. The `HI_PASS` filter is used predominantly for high energy cosmic-ray analyses and sets the minimum energy for the proton analysis to 54 GeV as seen in § 6.6. The `DIAGNOSTIC` filter is used for low energy cosmic-ray analyses since fluxes for low energy cosmic rays are significantly higher and therefore the 2 Hz trigger is not an overt issue. `DIAGNOSTIC` electrons were used in the determination of the absolute energy scale and associated uncertainty described in § 5.2.4 and § 6.8.3. A triggering event causes an amount of dead-time in order read the information from each subsystem. Dead-time can also come from time the LAT is not taking data during passage through the South Atlantic Anomaly (SAA), a region of higher than normal charge particle flux due to changes in Earth's magnetic field lines, and during calibration runs. This means the LAT has two time scales for triggered events, an elapsed-time and a live-time. Elapsed-time is defined as the start of the mission to the current time. Live-time is the amount of dead-time subtracted from the elapsed-time in the LAT. One such measure of live-time is `GltGemLiveTime` which measures the amount of time when the LAT is accepting triggers and is used in calculating event rates as described later in § 6.2.

3.2 Pass 8

Pass 8 encompasses ground-up redevelopment of the LAT event simulation and reconstruction software. Previous event simulation and reconstruction software, Pass 6 and Pass 7, were designed and calibrated prior to launch and several limitations in the reconstruction software were discovered. Using lessons learned in first few years of flight, limitations of the reconstruction and simulations as well as moving almost all calibrations to in-flight measurements, Pass 8 has significantly increased the quantity and quality of the γ-ray data collected by the LAT. Special attention was made to eliminating simultaneous events which fall within trigger windows known as 'ghosts'. Event collection and readout takes $\sim 25\mu$s and in that time a simultaneous low energy cosmic ray can readout with recorded data for a primary event [69]. 'Ghosts' inadvertently veto γ-ray events during reconstruction and thereby lower acceptance. To simulate these 'ghost' events, `DIAGNOSTIC` events are overlaid on top of simulated data and the sum of simulated data and overlay data is reconstructed. Therefore the the effect of 'ghosts' can be appropriately modeled to calculate an accurate acceptance and to recover some events previously excluded from analysis. The switchover from Pass 7 to Pass 8 software was June

24, 2015. Pass 8 improves the γ-ray acceptance, energy resolution, PSF of the LAT and increases the possible energy range down to 10 MeV and up to 1 TeV.

During Pass 8 development, GEANT4 was updated from v8.0p01 to v9.4p01. GEANT4 is a toolkit for the simulation of particles through matter, predominantly used in the area of particle physics [75]. Detailed models of detectors can be built and interactions from various particles can be simulated using the Monte-Carlo method via GEANT4. GEANT4 is used to produce the all-particle background simulation and the dedicated particle simulations, used in this analysis and described in § 3.3. GEANT4 v9.4p01 has wider range of hadronic physics lists, improvements due to LHC results, and better handling of multiple scattering events. These improvements from GEANT4 directly benefit a proton spectral measurement in the form of better estimations of the response of the LAT to protons. In this section we will discuss the improvements via Pass 8 in the ACD, CAL, and TKR reconstruction software.

3.2.1 ACD Reconstruction

When a charged particle interacts with an ACD tile, it deposits energy via ionization. The energy deposition is then converted to light through absorption, florescence, and phosphorescence transitions shown in Figure 3.6. The scintillation light is proportional to the amount of energy deposited. This minuscule amount of light is then converted to photo-electrons in the dual PMT readout for each ACD tile and then converted to pulse height amplitude (PHA) via the FREE board electronics chain. Each PMT has two readouts, a low and high gain range to measure energy

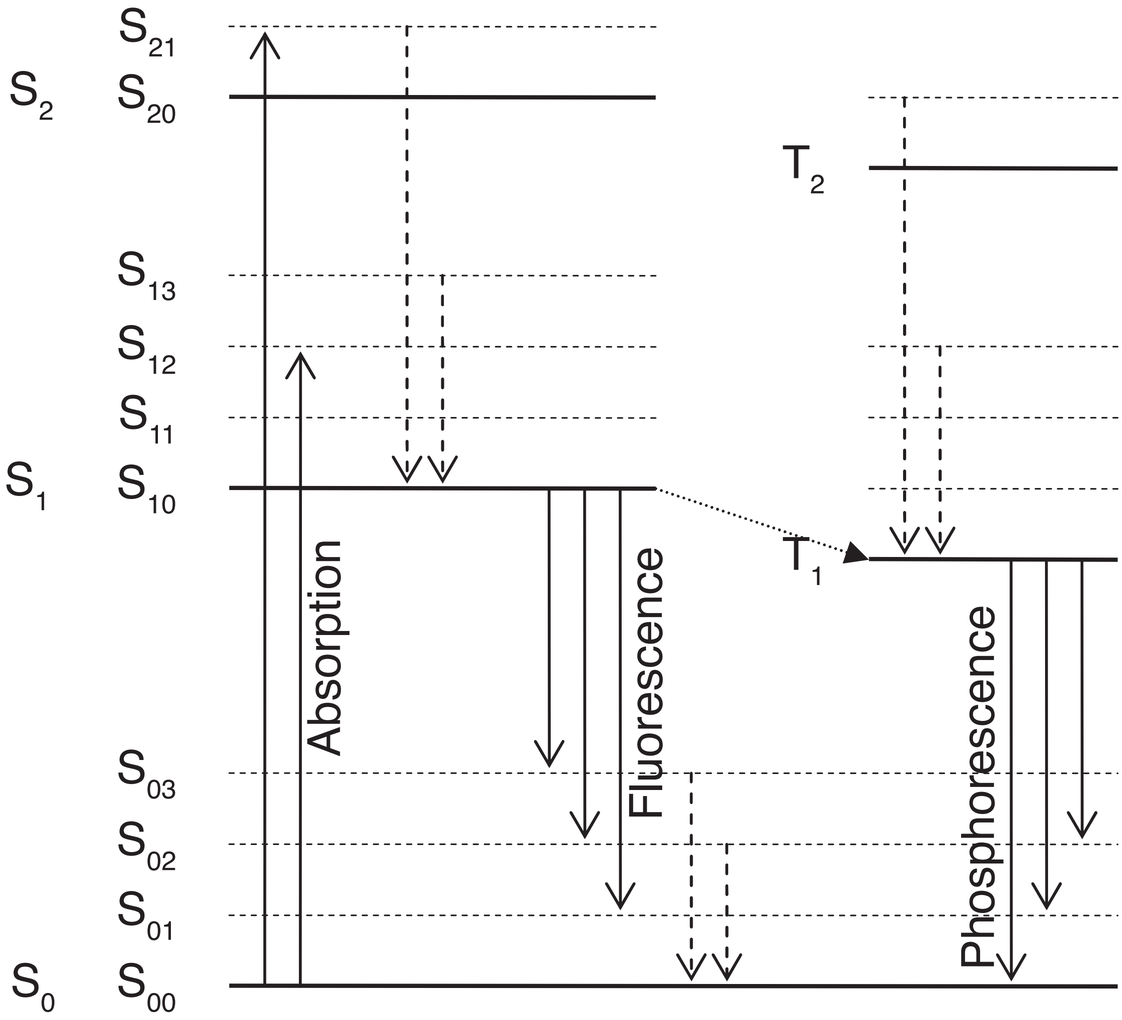

Figure 3.6: The absorption, florescence, and phosphorescence energy transitions for light emission in polyvinyltoluene (PVT). Radiative (solid lines) and non-radiative transitions (dashed line) are shown [76].

deposition from protons or electrons and ions respectively. While the low range is highly linear in response to signal, the high range saturates near 2000 PHA thereby degrading the signal deposited from cosmic-ray ions with $Z \geq 8$.

PHA is an uncalibrated signal from each PMT and is converted to physical units of minimum ionizing particles (MIP) via a lookup table of PMT pedestals and gains. Pedestals and gains are measured via `DIAGNOSTIC` flight data. For the low and high range of each PMT, equations 3.1 and 3.2 show the conversion to MIPs.

$$S(\text{MIP}) = \frac{S(\text{PHA}) - PED_{LOW}}{GAIN_{LOW} - PED_{LOW}} \tag{3.1}$$

$$S(\text{MIP}) = \frac{SAT(\text{PHA})(S(\text{PHA}) - PED_{HI})}{GAIN_{HI} \times (SAT(\text{PHA}) - S(\text{PHA}) + PED_{HI})} \tag{3.2}$$

S(PHA) is the signal in PHA and SAT(PHA) is the high range saturation typical near 2000 PHA. Through extensive testing of polyvinyltoluene (PVT), one MIP is equivalent to 1.9 MeV [71]. The signal in each PMT is averaged to measure the total energy deposited in each tile.

Once the energy in each tile is calculated, the energy deposition across the ACD can be associated with a direction from the TKR or CAL. The distance of closest approach (DOCA) is found for each tile from either the TKR or CAL direction and the tile with the smallest DOCA is determined to be the tile associated with the reconstructed direction. Previous versions of the LAT reconstruction code only used TKR directions but Pass 8 included CAL directions with ACD tile direction associations. These direction and ACD tile associations are incredibly powerful in particle discrimination since γ-rays do not deposit energy in the ACD while charged particles will deposit energy. If the deposited energy in the ACD tile is above 1 MeV, then the tile triggers a veto. Both TKR and CAL direction ACD tile associations are used in § 4.4 to measure the charge of incident cosmic rays and can reduce contamination associated with non-proton cosmic rays.

3.2.2 CAL Reconstruction

The CAL's reconstruction starts with the conversion of analog-to-digital conversion (ADC) values from each of the crystals' diodes to physical energy in units of MeV. Using dedicated calibrations for each crystal, generated from cosmic-ray ion flight data and beam-test data, energy is measured from each diode on both ends of the crystal. The energy deposited in each crystal is determined from the average of the energy measured by each diode pair on the end of said crystal. Additionally the position of the energy deposited is found by taking the ratio of the energy by each end of the crystal as seen in Figure 3.7. This produces a set of energy depositions with a three dimensional position for each energy deposition. It should be noted that if the energy deposition is too heavily one sided the longitudinal position measurement degrades. CAL crystals also saturate at 70 GeV and handling the saturation effect is one the improvements of Pass 8 over previous data reconstructions.

A large improvement to the CAL reconstruction in Pass 8 is the new clustering algorithms. In previous LAT reconstruction software, for a single event all crystals were included in direction and energy reconstruction. The general idea is to use the minimum spanning tree (MST) of the energy-weighted three dimension phase-space distribution of crystals and find any clusters associated, with either lower energy incident cosmic rays or low energy delta-rays far from the main cluster of crystals. MSTs are well studied and easily solvable and often implemented in other high energy physics experiments. The threshold to split the MST is energy dependent, being larger at lower energies when a γ-ray shower can be sparse and smaller at

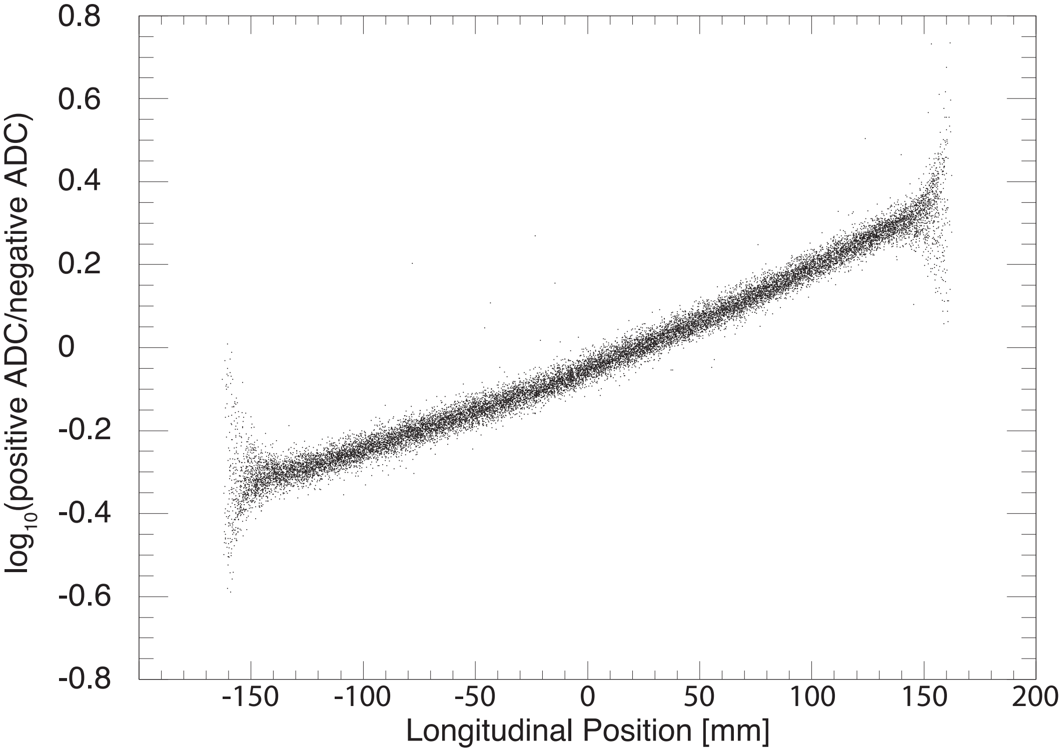

Figure 3.7: The light asymmetry calibration used for determining the longitudinal position along a CAL crystal of an energy deposition. If the energy deposition is too heavily one sided the longitudinal position measurement degrades [69].

higher energies when a γ-ray shower is more narrow. Clustering can directly improve reconstruction of proton showers by separating the narrow electromagnetic core and wide hadronic halo of the proton-induced shower. This can improve CAL direction reconstruction and energy estimation of the electromagnetic core as discussed in § 5.4.

After clustering, the directions can be found for each cluster. CAL directions are found by performing an energy weighted moment analysis. This is the same moment analysis as the previous version but with improvements described later.

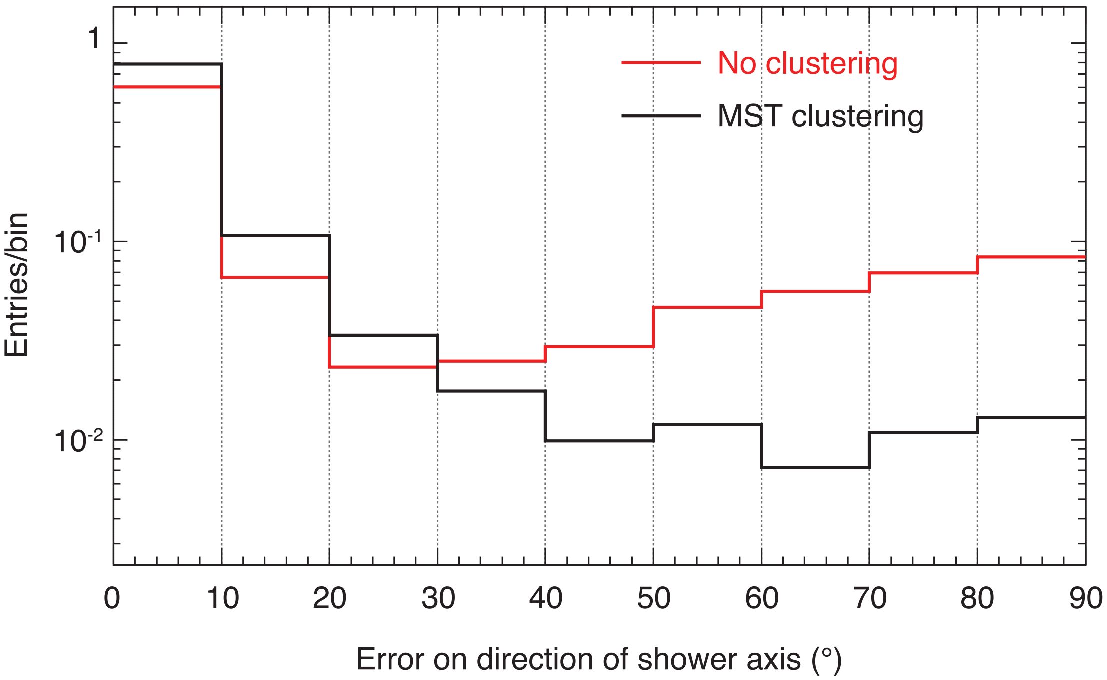

Figure 3.8: The improvement of the CAL direction from the MST clustering algorithm for Monte-Carlo γ-rays [77].

The centroid position for each cluster is found by using

$$\vec{r_c} = \left(\sum_{i=1}^{n} E_i \ \vec{r_i}\right) / \left(\sum_{i=1}^{n} \vec{r_i}\right) \tag{3.3}$$

where $\vec{r_i}$ is the position of each crystal and E_i is the energy of each crystal. Then the inertia tensor is found using

$$\begin{aligned}
I_{xx} &= \sum_{i=1}^{n} E_i(y_i^2 + z_i^2) && (3.4)\\
I_{yy} &= \sum_{i=1}^{n} E_i(x_i^2 + z_i^2) && (3.5)\\
I_{zz} &= \sum_{i=1}^{n} E_i(x_i^2 + y_i^2) && (3.6)\\
I_{xy} &= I_{yx} = -\sum_{i=1}^{n} E_i x_i y_i && (3.7)\\
I_{xz} &= I_{zx} = -\sum_{i=1}^{n} E_i x_i z_i && (3.8)\\
I_{yz} &= I_{zy} = -\sum_{i=1}^{n} E_i y_i z_i && (3.9)
\end{aligned}$$

and diagonalizing the associated inertia tensor to determine the CAL direction. We can also see the improvement to CAL direction using the clustering algorithm in Figure 3.8.

Distant crystals from the main cluster can bias the direction and centroid position as well as the transverse and longitudinal width of the showers. Therefore, the entire moment analysis process is iterated upon by removing crystals far from the primary axis until the difference between the directions for each iteration reaches a threshold. This iterative method is new to Pass 8 and vastly improves the data/MC agreement for `CalTransRms` and `Cal1LongRms`, improving CAL direction reconstruction for all types of particles. Once completed, the direction is found from the final inertia tensor and the eigenvalues of the inertia tensors are related to the width of the transverse and longitudinal directions using:

$$\texttt{CalTransRms} = \sqrt{(\lambda_1) / \sum_{i=1}^{n} E_i} \tag{3.10}$$

$$\texttt{CalLongRms} = \sqrt{(\lambda_0 + \lambda_2) / 2 \sum_{i=1}^{n} E_i} \tag{3.11}$$

where λ_0, λ_1, λ_2 are the eigenvalues of the inertia tensor assuming the primary axis of the shower is the eigenvalue with the smallest value.

Once the clusters and momentum analyses are finalized, the energy reconstruction is performed as described in § 5.2, which accounts for energy leakage and instrumental effects.

3.2.3 TKR Reconstruction

TKR data is digital with no analog to digital conversion such as in the ACD or CAL. Therefore a time over threshold (ToT) method is used to detect signal from the SSDs in the TKR. Figure 3.9 shows the basic idea, the amount of voltage over a defined threshold, 0.25 MIPs for each SSD, is found as a function of time. The width of the distribution is found from threshold crossings determining how much energy was deposited in each SSD. This value is normalized using in-flight `DIAGNOSTIC` events into values of MIPs. Since ionization is the method of energy deposition, ToT should scale with charge of the incident cosmic ray. This allows us to use ToT as an additional and independent measure of charge in the LAT as discussed in § 4.2. This method has some drawbacks since ToT response is less linear than the ACD but is still effective at removing helium and other ions. Therefore,

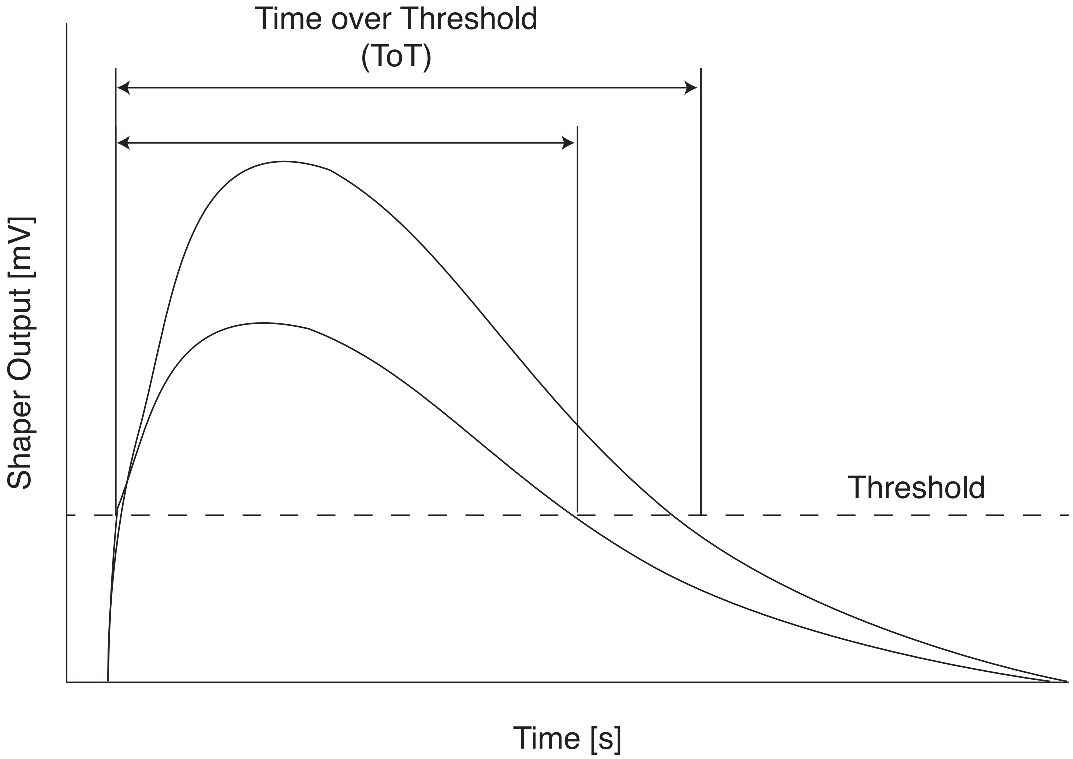

Figure 3.9: The time over threshold (ToT) measurement of digital signal from the TKR SSDs where the threshold is set to 0.25 MIPs. Two different ToT measurements are shown to illustrate the limitations of ToT as a proxy for pulse height and shape.

ToT is unable to distinguish between individual cosmic-ray ion species. Hits are determined by the X-Y position on each TKR plane in each tower which creates a three dimensional distribution of locations in the TKR.

A new method of track finding was developed around tree based algorithms. Vector links are formed by associated hits with adjacent layers i the TKR, these vector links are then linked themselves, requiring at least two adjacent vector links below the first element, across the TKR to form a track candidate. Track candidates are added to a list of all tracks and sorted by longest, straightest, and using a Kalman filter fit which uses all information about the vector links to predict the best track.

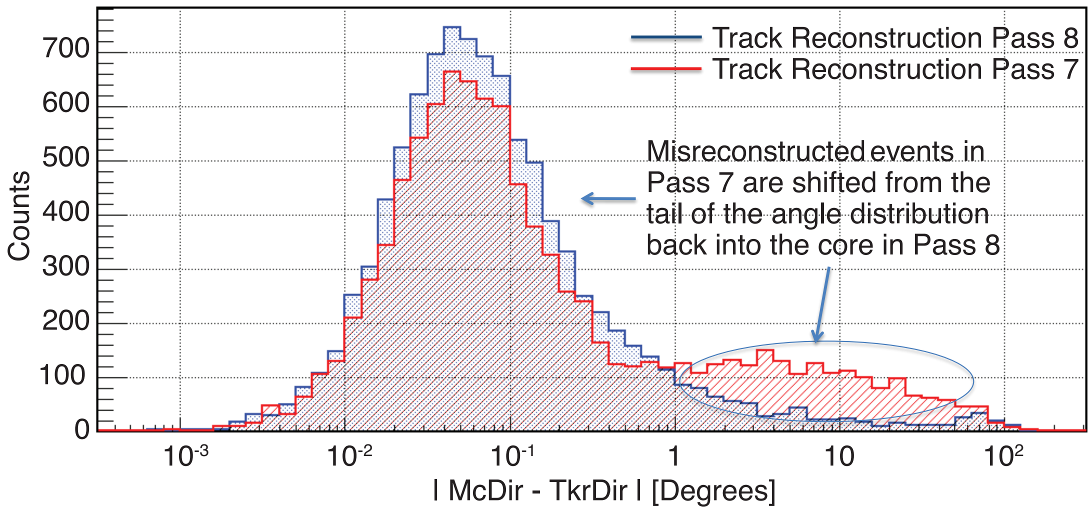

Figure 3.10: Improvement to the track reconstruction comparing Pass 7 to Pass 8. Plot is generated from Monte-Carlo 50 GeV γ-rays showing the clear reduction the tails of mis-reconstructed directions distribution [78].

The first entry of the list is considered the best track.

The improvement to track finding is most evident at energies above 1 GeV as can be seen in Figure 3.10. There is a general reduction of mis-reconstructed events which reduces the tails of the distribution of the difference between TKR directions and MC directions. In the context of cosmic-ray studies, improving the direction reconstruction at high energies allows for better charge separation and for the acceptance since we require a well reconstructed direction in our event selection discussed in § 6.1.

3.3 GEANT4 Monte-Carlo Simulations

Three sets of simulations are used in this analysis: the all-particle background simulation, dedicated proton simulations, and dedicated electron simulations. Each simulation is used for different purposes and are vitally important in the understanding of the LAT's interaction for cosmic rays. Additionally, each simulation is generated using GEANT4 9.4.p04 in combination with a detailed model of the entire *Fermi* spacecraft [75].

Figure 3.11 shows the basic schema for MC particle event generation. An event is set on a sphere from the center of the LAT, with the directions defined in Figure 3.2, with a 30 m radius. A disk of 6 m^2 area is produced tangential to said point on the sphere and the particle is fired at the LAT with the generated directions, energy, and particle type. The angular range of the sphere is dictated by the specific simulations summarized in Table 3.6 but is typically either 4π sr or 2π sr.

There are two types of simulations, a 'standard' simulation and a 'flux' simulation. In the 'standard' simulation, a specific number of events are generated per run, which sets the stop condition. In the 'flux' simulation a particle flux and generation time is specified, and average number of events generated is dependent on the particle flux, generation time, and angular distribution, where the stop condition is set by the simulation time. The 'standard' simulation is ideal for generation of instrument response and the 'flux' simulation is typically used for background studies but each can be used interchangeably if one is careful about the generation conditions.

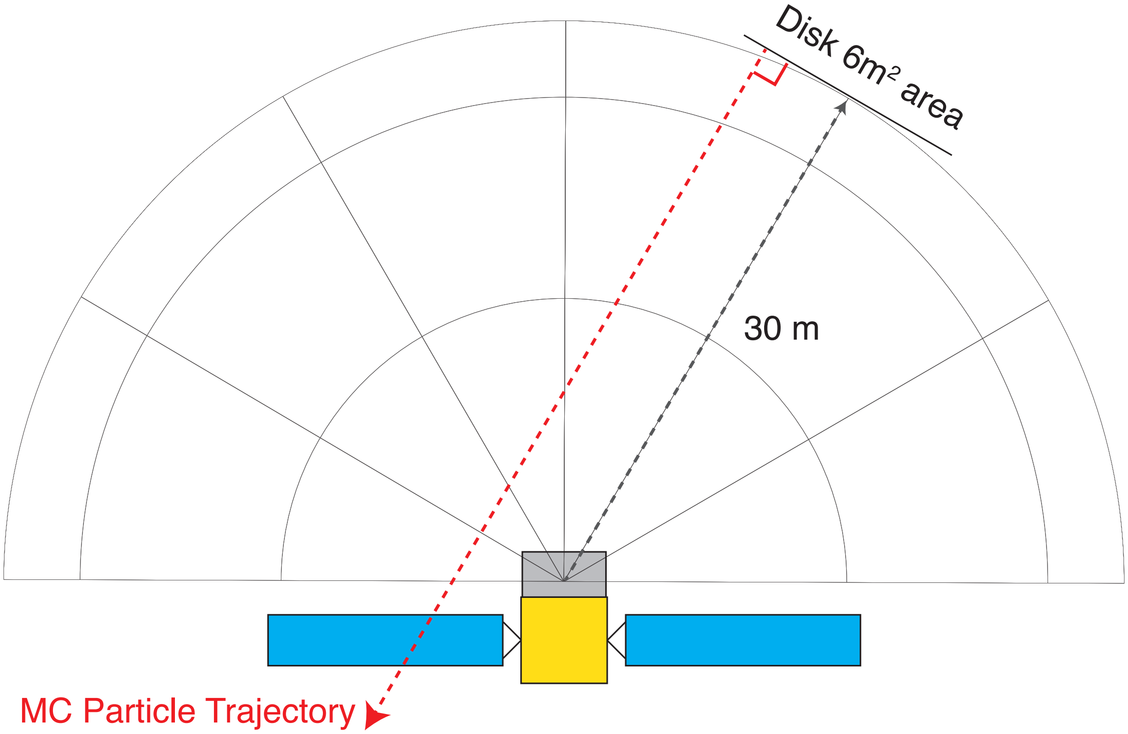

Figure 3.11: A simple demonstration of how Monte-Carlo particles are simulated with *FGST* using GEANT4. Particles are generated with a particle type, energy, and direction, and then generated on a disk of 6m^2 tangent to a sphere of 30 m radius from the center of the LAT.

Table 3.6 shows the parameters for each Monte-Carlo simulation used in this analysis. We will now give a brief description of each type of simulation.

3.3.1 All-Particle Background Simulation

The all-particle background simulation (BKG) uses realistic fluxes of different cosmic-ray spectra and Earth albedo γ-rays with data taken from *AMS-01*, *BESS*, and *TS93* [79–82]. The species of primary cosmic-rays simulated include electrons, positrons, protons, helium, and ions ranging from lithium to iron. Additionally, the all particle background simulations uses real spacecraft pointing information

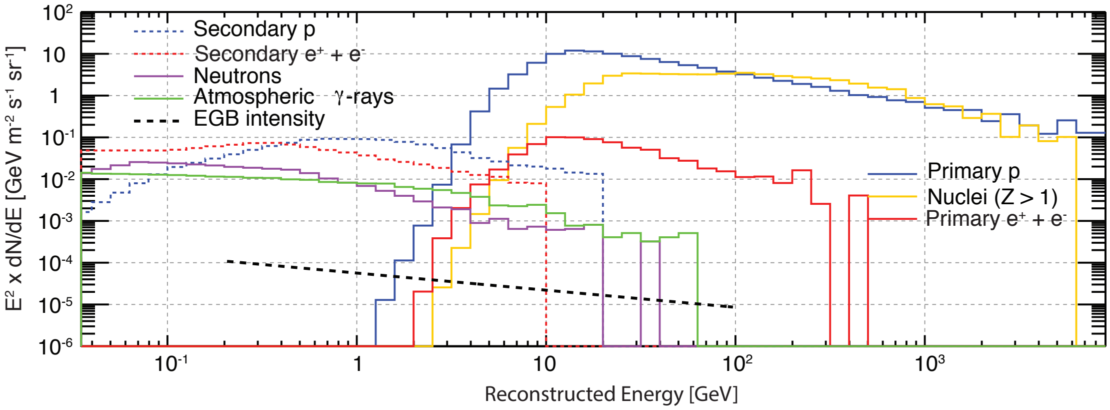

Figure 3.12: The space environment from the *Fermi* all-particle background simulation including sources from primary cosmic-ray, albedo γ-rays from the Earth's limb, and secondary particles [72].

and International Geomagnetic Reference Field (IGRF) parameterization of Earth's magnetic field in order to account for the geomagnetic environment which the BKG simulation will sample. All primary cosmic-ray species are simulated with a 4π sr angular distribution with a minimum energy of 40% of the geomagnetic cutoff rigidity calculated at a specific point in orbit using flight spacecraft pointing information. The maximum energy is dependent on the particle species: electrons and positrons extend to 1 TeV, protons extended to 10 TeV, helium extends to 10 TeV/nucleon, and ions with a charge above 2 extend to 50 GeV/nucleon. Secondary electrons, positrons, γ-rays, protons, and neutrons from interactions with Earth's atmosphere are also simulated with the same characteristics as primary particles but their generated energies typically do not extend above a few GeV. The total simulated live-time for this BKG simulation is 8.15 days. Live-time is defined as the amount of time in each orbit the LAT is actively taking data. It should be noted that while realistic fluxes are used for the generating distributions of BKG simulations, helium and ions (Z > 2) simulated with GEANT4 under-represent the number of interacting particles when compared to flight data. These discrepancies can be corrected by scaling the event rate for helium and ions from the simulation to that of flight data.

3.3.2 Proton Simulation

The dedicated proton simulation generates protons from 4 GeV to 20 TeV over a 4π sr angular distribution with $\gamma = -1.5$ spectral index. Each proton simulation is run with a particle flux of 1×10^{-5} particles/(m^2 s sr) over 5×10^6 seconds which corresponds to a simulated 57 days of proton data which represents a full orbital period of the LAT. A full orbital period is defined as the amount of time it takes the LAT to fully sample the entirety of Earth's Geomagnetic environment. Actual LAT orbital pointing files are used in the generation of simulated protons. This translates to, on average, 3769.91 generated events per run. A run is a single instance of GEANT4 simulation and total simulations have on the order of 10^6 runs. Overlay events are included to simulate 'ghost' events.

Dedicated proton simulations use `QGSP_BERT_EPAX` as the standard physics list for hadronic simulations. `QGSP` refers to Quark Gluon string model of initial proton interaction with precompound spallation framework, `BERT` is the Bertini cascade model, and `EPAX` is a custom simulation package to the LAT to improve simulations of heavier ions [83–85]. Over 6.6×10^9 protons were generated for the dedicated proton simulation. The dedicated proton simulation is used to estimate the LAT's response to protons in the form of acceptances, energy resolutions, and response matrices. Several different physics lists for GEANT4 hadronic simulations were simulated to test systematic uncertainties associated with the energy measurement and GEANT4 which are described in full in § 6.8.2. We can also use the dedicated proton simulation for data/Monte-Carlo comparisons by reweighing the true energy to that of the primary cosmic-ray proton spectrum and computing a fake live-time by making comparisons to the BKG simulation.

3.3.3 Electron Simulation

The dedicated electron simulation generates electrons from 10 GeV to 10 TeV over 2π sr angular distribution with $\gamma = -1$ spectral index. In contrast to the proton simulation, the electron simulation generates exactly 200 events with no associated flux or generation time. Electron simulations are generated with the standard GEANT4 electromagnetic package with inclusion of multiple scattering and the Landau-Pomeranchuk-Migdal effect for very high energy electromagnetic showers. Over 1.5×10^7 events were generated for the dedicated electron simulation. The dedicated electron simulation is used to estimate the residual electron contamination and in the background subtraction when reweighted to a realistic spectrum with a fake live-time and for use in data/MC comparisons. More information on the use of the electron simulations can be found in § 6.4.

Simulation Name	Particle	Energy Range	$\cos\theta$ Range	Spectral Index	Comment
allHEE10G10T-v20r09p09-OVL6p2	e^-	10 GeV - 20 TeV	0.0 - 1.0	-1.0	Used to estimate residual contamination
allPro-20r09p09-OVL6p2-4G20T	p^+	4 GeV - 20 TeV	-1.0 - 1.0	-1.5	Used for production of instrument response objects
allPro-200909-OVL6p2-QBBC	p^+	4 GeV - 20 TeV	0.0 - 1.0	-1.5	Produced with QBBC physics list and used to estimate systematic errors
allPro-200909-OVL6p2-FTFP˙BERT	p^+	4 GeV - 20 TeV	0.0 - 1.0	-1.5	Produced with FTFP˙BERT physics list and used to estimate systematic errors
allPro-200909-OVL6p2-QGS˙BIC	p^+	4 GeV - 20 TeV	0.0 - 1.0	-1.5	Produced with QGS˙BIC physics list and used to estimate systematic errors

Table 3.6: The summary of Monte-Carlo simulations used in the cosmic-ray proton spectral analysis.

Chapter 4: Charge Measurement

To measure the cosmic-ray proton spectrum, one needs to be able to distinguish between different cosmic-ray species. While charge resolution is highly dependent on the desired cosmic-ray measurement, the LAT has to be able to distinguish protons from helium and nuclei, where nuclei in the context of this thesis are defined as $Z > 2$. For this measurement the main source of contamination is associated with other cosmic-ray species. Despite the natural abundances of cosmic-ray species shown in Chapter 2, the LAT has a very different response to individual species. As can be seen in Figure 3.12 and § 3.3, cosmic-ray helium and nuclei interact at a rate equivalent to or greater than that of protons. This produces the dominate contamination source for protons and these events need to be removed, since cosmic-ray helium and nuclei will have different response in the LAT than protons. With the fact that cosmic-ray nuclei are poorly simulated with GEANT4, the response in the LAT is not well known and therefore difficult to include in the spectral reconstruction. Therefore we need to remove as many as possible cosmic-ray helium and nuclei before moving onto any stage of spectral reconstitution. Two LAT subsystems, the ACD and the TKR, distinguish between different cosmic-ray species. Both are able to independently measure charge via ionization.

4.1 Ionization

Ionization is the primary energy loss mechanism for heavy charged particles, Z $\geq$ 2, of moderate energy, GeV energy range, in material. The process occurs when a heavy charged particle scatters off of the electron shell of an atom. The scattering transfers energy to the electron, exciting said electron, and the primary particle loses energy in the interaction. Typically the energy loss is small compared to the total kinetic energy of the primary particle.

When the primary particle with a charge z and mass M interacts with the electron shell, it is through Rutherford Scattering:

$$\frac{d\sigma}{d\Omega} = \left[\frac{ze^2}{2\mu v^2 \sin^2\left(\frac{\theta}{2}\right)}\right]^2 \tag{4.1}$$

where v is the velocity of the primary particle and μ is the center of mass of the system [86]. Figure 4.1 shows the basic example of classical Rutherford scattering. In the case of ionization, where the primary particle is much more massive and has much more energy than the electron shell, the deflection angle θ will be small. In this derivation, we have to consider relativistic effects since the energy of the primary particle and energy transfered to electrons within the electron shell are well above their respective rest masses. We find the quantum mechanical version of 4.1 by accounting for effects from the spin state of the electron and in terms of the kinetic energy T, the energy lost is:

$$\frac{d\Omega}{dT} = \frac{2\pi z^2 e^4}{m_e c^2 \beta^2 T^2}\left(1 - \beta^2 \frac{T}{T_{max}}\right) \tag{4.2}$$

Where T_{max} is the maximum energy that can be deposited to the electron in the

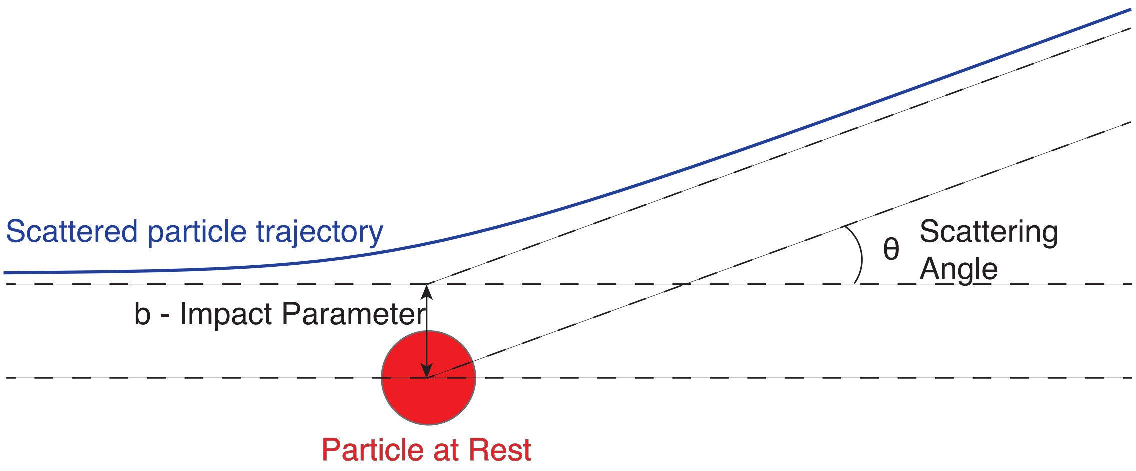

Figure 4.1: A simple illustration of Rutherford scattering of a charged particle off another charged particle at rest. θ is the scattering angle and b is the impact parameter.

electron shell. When a particle passes through material, it passes through N_A/A and interacts with Z electrons per unit density. Integrating Equation 4.2 to find the total energy deposited per unit length gives [87]:

$$\frac{dE}{dx} = \frac{N_A Z}{A}\int_I^{T_{max}} \frac{2\pi z^2 e^4}{m_e c^2 \beta^2 T^2}\left(1-\beta^2\frac{T}{T_{max}}\right) dT \tag{4.3}$$

$$= \frac{2\pi N_A z^2 Z e^4}{m_e c^2 \beta^2}\left(\ln\left[\frac{T_{max}}{I}\right]-\beta^2\right) \tag{4.4}$$

The I term is the minimum energy passed onto the electron. Since electrons are part of the electron shell, their energies are discretized, therefore the minimum energy is a function of the orbital electrons and the atom from which the primary particle is scattering. This derivation is a good approximation but a few other terms are required to properly calculate the average energy loss due to ionization [88].

The complete average energy loss over a distance dx is described by the Bethe

Bloch equation shown in 4.5 [34, 87].

$$-\left\langle \frac{dE}{dx} \right\rangle = \frac{4\pi N_A z^2 Z e^4}{m_e c^2 \beta^2} \frac{1}{\beta^2} \left[\frac{1}{2} \ln \frac{2 m_e c^2 \beta^2 \gamma^2 T_{max}}{I^2} - \beta^2 - \frac{\delta(\beta\gamma)}{2} \right] \tag{4.5}$$

T_{max}, as stated earlier, is the maximum energy transferred in a single collision with the electron shell, defined as:

$$T_{max} = \frac{2 m_e c^2 \beta^2 \gamma^2}{1 + 2\gamma m_e / M + (m_e/M)^2}. \tag{4.6}$$

The units of Equation 4.5 are MeV cm^2/g. There are a number of important features to note about Equation 4.5. First, it scales with the charge of the primary particle, z^2, which means that the higher the charge of the particle the more energy it will transfer into the electron shell. Second if the mass of the primary particle is $M \gg 2\gamma m_e$ then $T_{max} \approx 2 m_e c^2 \gamma^2 \beta^2$, which means Equation 4.6 and therefore Equation 4.5 have a small dependence on the mass of the primary particle. In the case of the LAT and a helium cosmic ray, the mass of the helium nucleus would only start to impact this estimation at energies above 5 TeV. The final feature of note can be easily seen in Figure 4.2.

At low energies, ionization is dominated by the $1/\beta^2$ term until it reaches a minimum after the relativistic effects start to increase. As energy increases there is a slow rise in the energy loss above the point of minimum ionization. If a particle traverses enough material without inelastic scattering, the particle will eventually lose enough energy and fall into this minimum ionization dip. Particles with energy or momentum near this minimum are called minimum ionizing particles or MIPs. MIPs are good for normalization of signal, for instance a proton will have energy loss of 1 MIP while a helium will have an energy loss of 4 MIPs. For instance, in the case

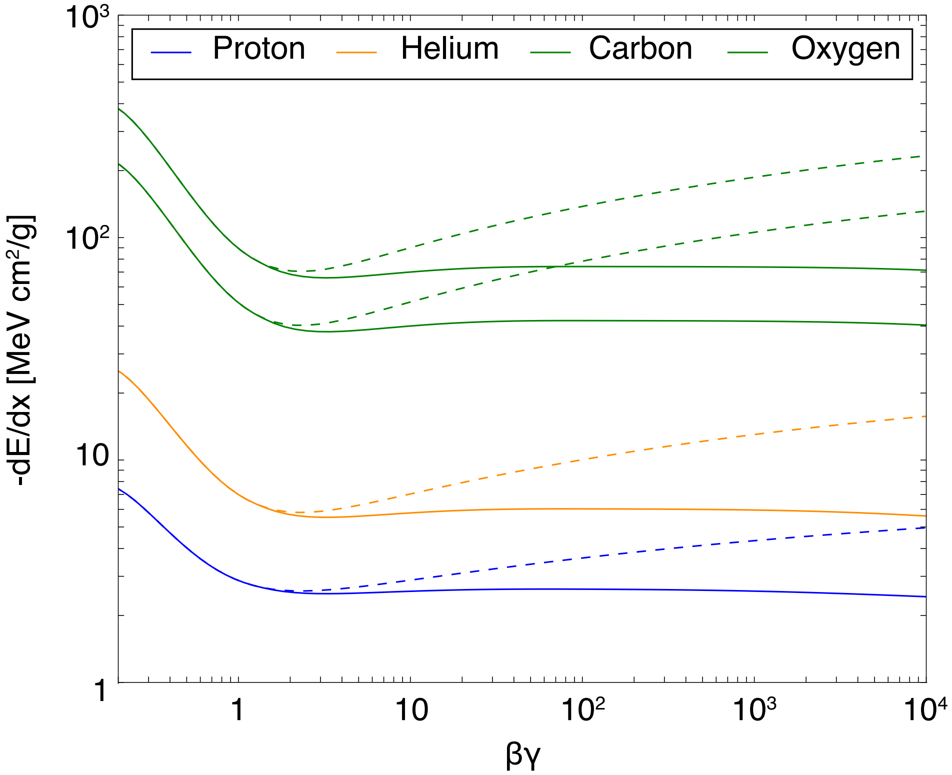

Figure 4.2: Energy loss due to ionization of protons (blue), helium (orange), carbon (green), and oxygen (green) in polyvinyltoluene (PVT). The solid lines show the ionization curves with density corrections and the dashed lines without density corrections [89, 90].

of an ACD tile composed of PVT, the minimum ionization is 2.0 MeV/cm [90]. This idea is demonstrated in § 3.2.1 where before conversion to MeV, signal in the ACD is in units of MIPs. The I term in Equation 4.5 refers to the mean excitation energy of the electron shell. The mean excitation energies are experimentally measured quantities and highly dependent on the atom and the electron shell orbits. The $\delta(\beta\gamma)$ term is a density correction term due to polarization of the medium at large primary particle energies [34, 89].

While Equation 4.5 describes the mean energy deposited due to ionization, the distribution of energy deposited at a single energy is called the straggling energy.

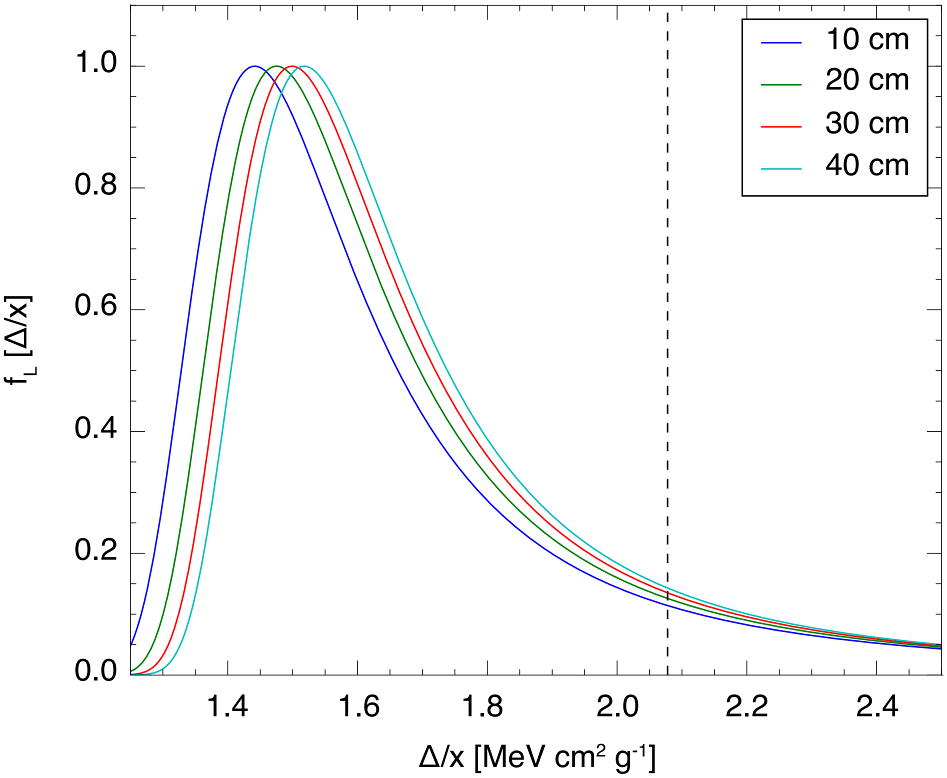

Figure 4.3: The straggling energy loss due to ionization of 100 GeV protons in PVT for various widths in units for MeV cm^2/g . The straggling energy loss is estimated with a Landau distribution and normalized set to 1.0. The black line represents the mean energy loss due to ionization as determined by Equation 4.5 [90].

$$P_L(\lambda) = \frac{1}{2\pi i}\int_{c-i\infty}^{c+i\infty} e^{s\log s+\lambda s} ds \tag{4.7}$$

$$= \frac{1}{\pi}\int_{0}^{\infty} e^{-t\log t-\lambda t}\sin(\pi t)dt \tag{4.8}$$

The distribution of energy loss can be described by a Landau distribution [91]: where Equation 4.8 is a complex integral and the evaluated contour integral. The Landau distribution is applicable when $\langle E_{Ion}\rangle / T_{max} < 0.01$, which means physically that the energy deposited via ionization is less than 1% the maximum energy that can be deposited to the electron shell. In terms of the straggling energy, using Equation

4.8, we define ξ:

$$\xi = \frac{4\pi N_A r_e^2 m_e c^2}{2} \left\langle \frac{Z}{A} \right\rangle \frac{x}{\beta^2} \tag{4.9}$$

where x is the width of the detector in $\mathrm{g/cm^2}$ and $\left\langle \frac{Z}{A} \right\rangle$ is the average average of the atomic number divided by the atomic mass of the detector material. Finally, we define the straggling function as:

$$\begin{aligned} f_L(x, \Delta) &= \frac{\phi(\lambda)}{\xi} && (4.10) \\ \lambda &= \frac{1}{xi}(\Delta - \langle\Delta\rangle) - \beta^2 - \ln\left(\frac{\langle\Delta\rangle}{I}\right) - 1 - C_E && (4.11) \end{aligned}$$

where Δ is the energy deposited, $\langle\Delta\rangle$ is the average energy deposited determined from Equation 4.5, and C_E is the Euler Constant [91]. We can see the straggling energy loss distribution in figure 4.3 for 100 GeV protons in PVT and various widths and the mean energy shown the black dotted line. Clearly the most probable energy deposition is shifted from the mean of the distribution with a long tail comprised of high energy delta-rays [34]. We also see the width of material traversed changes the most probable value of the straggling function, therefore with detectors with a non-negligible width, like the ACD, it is necessary to correct for the different path-lengths of the deposited energy.

This gives a picture where energy loss due to ionization is dominated by the energy and charge of the primary particle. The total energy loss due to ionization is clearly also dependent on the total amount of material traversed. With the basic idea of ionization established, we can now explain how the TKR and ACD measure charge.

4.2 Measuring Charge with the TKR

When a charged particle interacts with the silicon strips in the TKR it will deposit energy via ionization. We can use this ionization energy to determine the incident charge of the primary cosmic ray since the amount of energy deposited scales as a function of z as seen in Equation 4.5 and Figure 4.2. As described in § 3.1.3, the TKR is composed of interwoven layers of silicon strip charge detectors with tungsten converting foils. Each strip silicon strip is 400 μm deep, meaning the amount of energy deposited is very small [69]. The physical quantity used in the proton analysis is the ToT of the signal in the TKR described in § 3.2.3. ToT is the temporal width of the signal in the TKR over a predetermined threshold from atmospheric muon and beam-line calibrations. ToT is calibrated into units of MIPs using in flight cosmic-ray calibrations [72].

`Tkr1ToTTrAve` was determined to have the best energy resolution and therefore the best variable to measure charge of the primary cosmic ray. `Tkr1ToTTrAve` is the path length-corrected average ToT for the hits on the best track, excluding largest and smallest ToT measured. The charge resolution for `Tkr1ToTTrAve` can be seen in Figure 4.4 where the peaks and widths are fit using a normal distribution. Figure 4.4 shows separation between protons and helium, although long tails exist, but the TKR has limited charge resolution for ion, with $Z > 2$ since the TKR is optimized for sensitive particle tracking and not charge measurement. Saturation due to the nature of ToT measurement causes poor charge resolution for higher charge ions. The long tails of each cosmic-ray species also complicates charge separation and

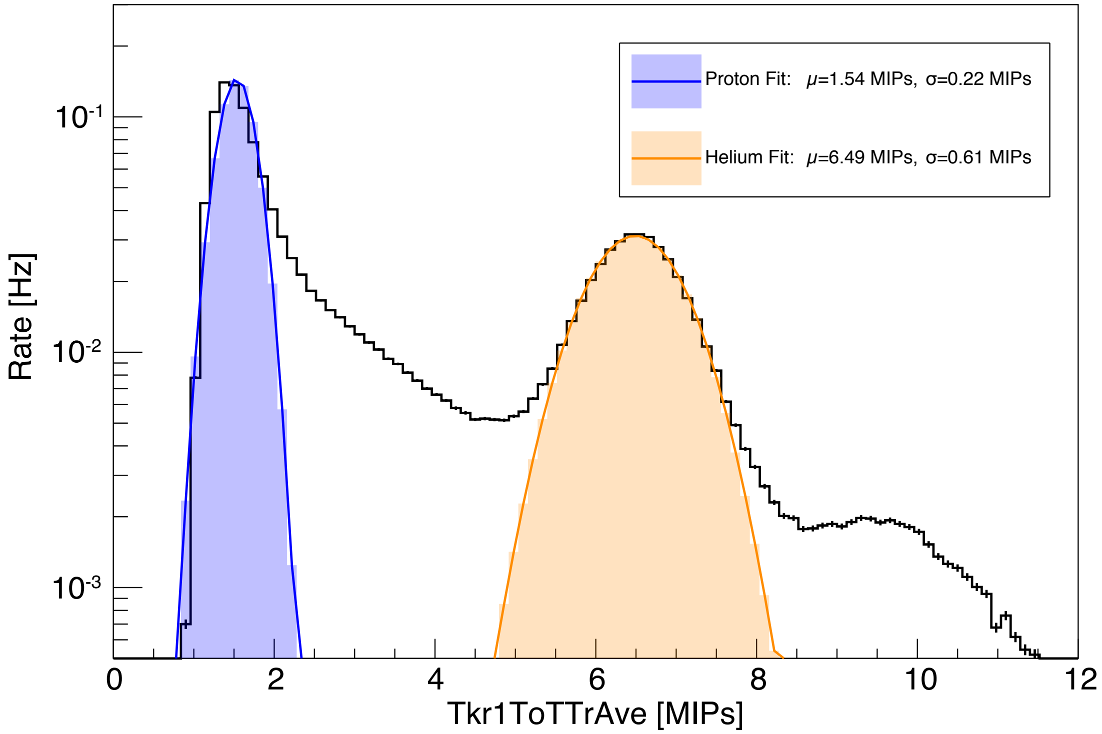

Figure 4.4: The different cosmic-ray population as seen with `Tkr1ToTTrAve`, in units of MIPs, from LAT flight data. Each peak is fit using a Normal distribution where blue is the proton peak and orange is the helium peak. Additionally, the values of the most probable value and width of the fit Normal distributions are show for each species. The offset of the proton and helium peaks from expected value, 1 MIP and 4 MIP respectively, is is due to the limitations of the ToT method of measuring TKR signal and associated calibrations described in § 3.2.3.

could lead to either ion contamination or signal reduction of protons.

Clearly, using the TKR alone is not enough to precisely measure the charge of primary cosmic-rays. In order to increase the charge resolution of the LAT overall, we can use an independent charge measurement via the ACD. Combined, the TKR and ACD can provide a precise charge measurement and efficiently reduce the proton contamination to negligible amounts.

4.3 Measuring Charge with the ACD

We can use the energy deposited in the ACD as a tracer for the charge of the cosmic ray. Since energy is deposited in the ACD via ionization, as described above, the amount of deposited energy will trace the charge of the cosmic ray. There are several energy variables produced from the Pass 8 ACD reconstruction and we use `Acd2Tkr1TileActDistEnergy` [92]. `Acd2Tkr1TileActDistEnergy` is the energy deposited in the tile which corresponds to the intersection of the best track from the TKR divided by the width of the tile to correct for the difference of widths between top and side tiles. We use the single tile because lower energy cosmic-rays, which have a higher flux, can interact with the LAT nearly simultaneously. These lower energy cosmic-rays are called ghosts described in § 3.2. Ghosts can deposit energy in the ACD but the TKR reconstruction filters out the ghost tracks ensuring the best track is associated with the higher energy event [92]. If the entire energy of the ACD was used, the ghost events would add energy to the measurement of the primary event, essentially skewing the result away from the expected ionization energy deposition. Figure 4.5 shows the energy distribution for `Acd2Tkr1TileActDistEnergy` from flight data where the different peaks refer to the different cosmic-ray populations. We can clearly see several cosmic ray species in `Acd2Tkr1TileActDistEnergy`, specifically protons, helium, carbon, and oxygen, although there is still overlap between protons and helium, the largest source of contamination in our analysis.

Once we have established that `Acd2Tkr1TileActDistEnergy` is the best ACD

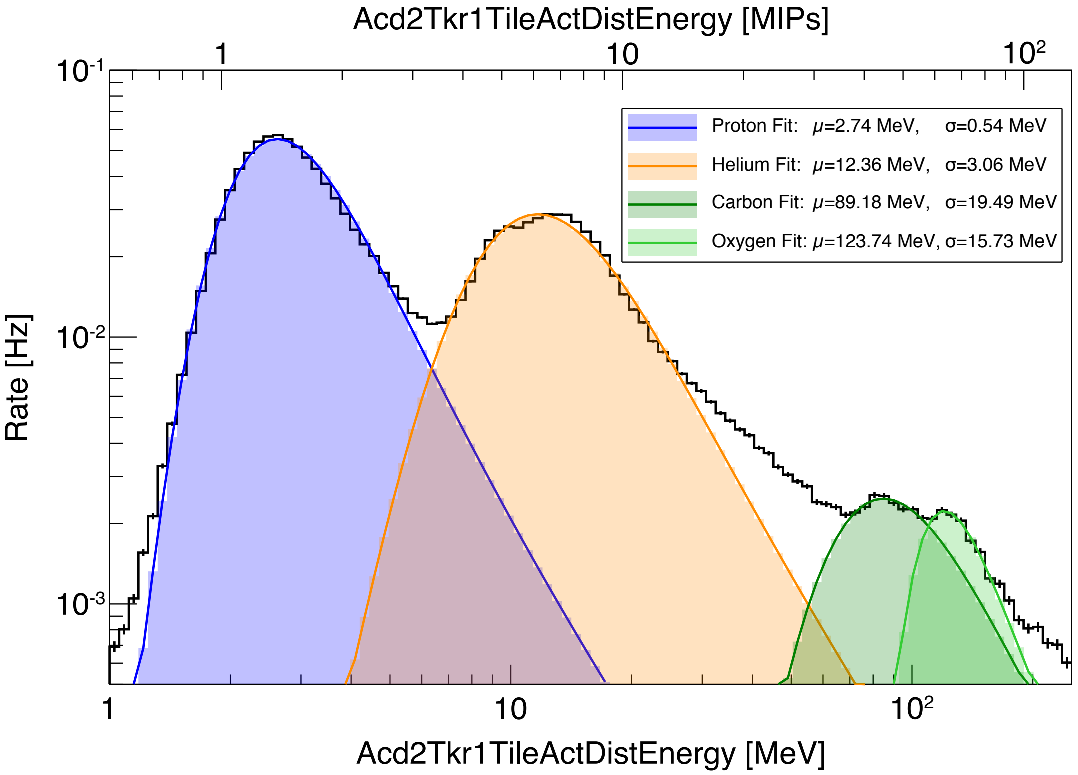

Figure 4.5: The different cosmic-ray population as seen with `Acd2Tkr1TileActDistEnergy`, in units of MeV, in LAT flight data. Each peak is fit using a Landau distribution described in Equation 4.8 where blue is the proton peak, orange is the helium peak, and green are the carbon and oxygen peak. Additionally the values of the most probable value and width of the fit Landau distribution are shown for each species.

energy variable, we have to account for the different path lengths of primary particle through the ACD tiles [69]. Remember that `Acd2Tkr1TileActDistEnergy` only accounts for the width of the tile, not necessarily the total distance traveled in the tile. As stated in § 3.1.1, the ACD tiles have non-negligible width, and the path length through the ACD tiles will change how much energy is deposited from the primary particle via ionization into each tile. To path length correct the energy deposition in the ACD, we use the best track from the TKR

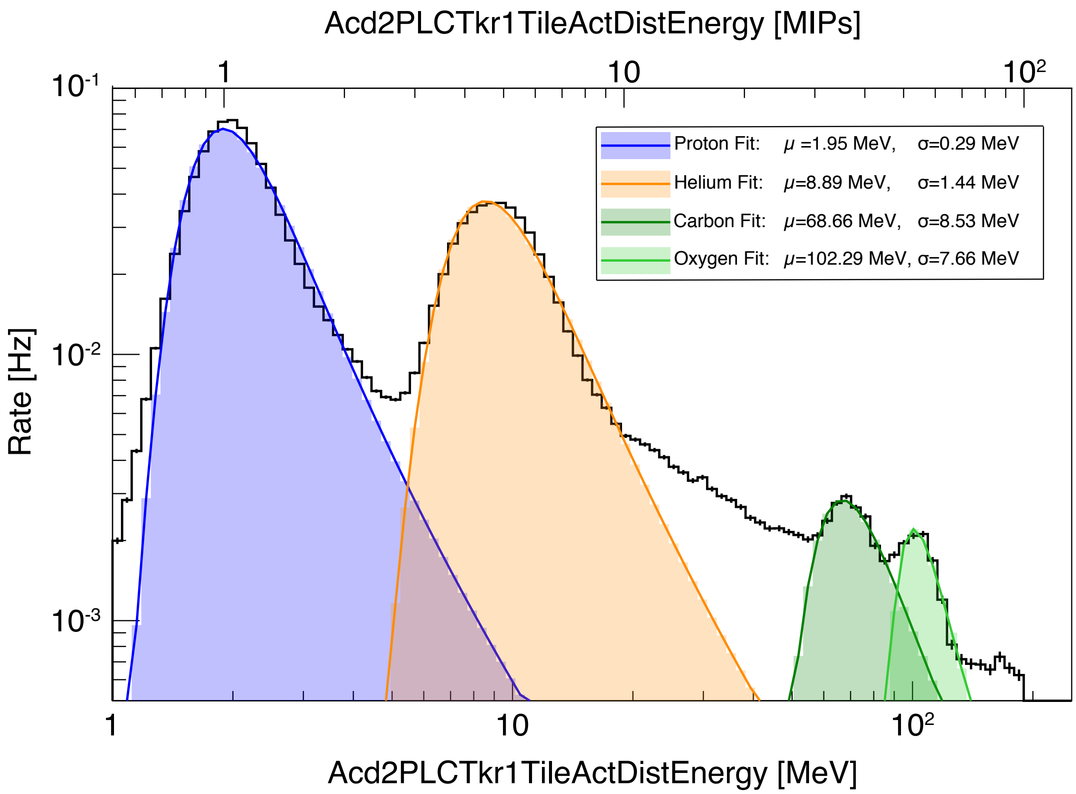

Figure 4.6: The different cosmic-ray population as seen with `Acd2PLCTkr1TileActDistEnergy`, in units of MeV, in LAT flight data. Each peak is fit using a Landau distribution described in Equation 4.8 where blue is the proton peak, orange is the helium peak, and green are the carbon and oxygen peak. Additionally the values of the most probable value and width of the fit Landau distribution are shown for each species.

and determine which face of the LAT the primary cosmic ray enters and then multiply `Acd2Tkr1TileActDistEnergy` by the cosine direction from the respective face direction in local coordinates. We define a new variable for the path length corrected deposited energy in the ACD called `Acd2PLCTkr1TileActDistEnergy`. Figure 4.6 shows the improvement to the charge resolution for different cosmic-ray populations using `Acd2PLCTkr1TileActDistEnergy`. Path length correcting `Acd2Tkr1TileActDistEnergy` reduces the width of each cosmic-ray species by a factor of 2.0. This allows for better charge separation and reduction of contamination from nuclei in the proton signal. We also see the most probable value for each cosmic-ray population in Figure 4.6 follow the z^2 dependence described in Equation 4.5 and shown in Figure 4.2. The z^2 dependence begins to break down for oxygen due to high range saturation of the ACD's PMTs described in § 3.1.1. This saturation effect limits the quality of individual cosmic-ray measurements for nuclei with charges greater than oxygen. Further changes can be made to improve the charge resolution for higher z nuclei by better accounting for the ACD saturation effects [72]. These improvements are described in Chapter 8 and allow for further separation of cosmic-ray secondaries like boron from carbon.

As we can clearly see, the ACD can provide charge measurement with enough charge resolution to separate and reduce the nuclei contamination of the proton signal. Without nuclei filtering, cosmic-ray helium and nuclei give a residual contamination of nearly 50% of the data sample as can be seen in Figure 3.12. We can use the TKR charge measurement, described in § 4.2, with the ACD charge measurement to create a cut to reduce nuclei contamination of the proton signal to below 1%.

4.4 Ion Filtering

To remove nuclei from our proton signal we developed two cuts: `CUT_NUCLEI_LOOSE` and `CUT_NUCLEI_TIGHT`. `CUT_NUCLEI_LOOSE` is used to remove the bulk of helium and other nuclei from the proton signal. `CUT_NUCLEI_TIGHT` is more specialized in removing residual nuclei and nuclei that enter from the bottom of the LAT and/or do not deposit energy via ionization in the TKR. We should note before diving into the specific cuts, note that these cuts are to remove helium and nuclei from the flight data which are the largest source of contamination for this proton analysis. Because of the nature of energy deposition via ionization, namely that ionization is proportional to z^2, the cuts will have little effect on the residual electron contamination. Fortunately, as established in Chapter 2, the cosmic-ray electron flux is much smaller than the cosmic-ray proton flux so we expect to have a low residual electron contamination.

4.4.1 Loose Nuclei Cut

The intention of the loose nuclei cut is to coarsely remove helium and nuclei from the data sample while leaving the proton population, and incidentally the electron and positron populations, as untouched as possible. We developed this cut by using the BKG simulations discussed in § 3.3 and two variables, `Acd2PLCTkr1TileActDistEnergy` and `Tkr1ToTTrAve`, discussed above and validate the cut using flight data. Looking at the residual contamination contours for `Tkr1ToTTrAve` versus `Acd2PLCTkr1TileActDistEnergy` in Figure 4.7 we can see the clear delineation between the different cosmic-ray populations. We establish a two dimensional polygon, noted with the black dotted line, that defines `CUT_NUCLEI_LOOSE`. All events that fall within the polygon are kept and all events that fall outside the polygon are removed. In terms of actual values, `CUT_NUCLEI_LOOSE` is:

```
CUT_NUCLEI_LOOSE = Tkr1ToTTrAve > 0.75 && Tkr1ToTTrAve < 7.0
&& (237.0/250.0 - 16.0*Tkr1ToTTrAve/250.0)
> log10(Acd2PLCTkr1TileActDistEnergy) &&
(-149.0/500.0 + 32.0*Tkr1ToTTrAve/500.0)
< log10(Acd2PLCTkr1TileActDistEnergy)
```

We can estimate the signal efficiency and rejection power to be 92.1% and 95.2% using BKG simulations. Clearly this cut is good at removing helium and nuclei while leaving the proton population and we can see in Figure 4.8 similar behaviors when applied to flight data.

Since we know the BKG simulation is not perfect, we need to check the cut against flight data to ensure we see similar behavior. In Figure 4.7 we see similar behavior in the positions of the peaks for the different populations while the event rates are clearly different; for instance, flight data helium has a higher event rate than in the simulations. This is mostly due to the fact that ionization is a fairly simple physical process to simulate but particle showers from nuclei are difficult involving nuclear, particle, and quantum chromodynamic (QCD) processes therefore the event rate is very difficult to reproduce via simulations. Since the positions of the peaks are the same, `CUT_NUCLEI_LOOSE` is still an effective method of removing helium and nuclei from our data set. There is still contamination from helium and nuclei that had less `Acd2PLCTkr1TileActDistEnergy` and develop `CUT_NUCLEI_TIGHT` to remove any residual helium and nuclei.

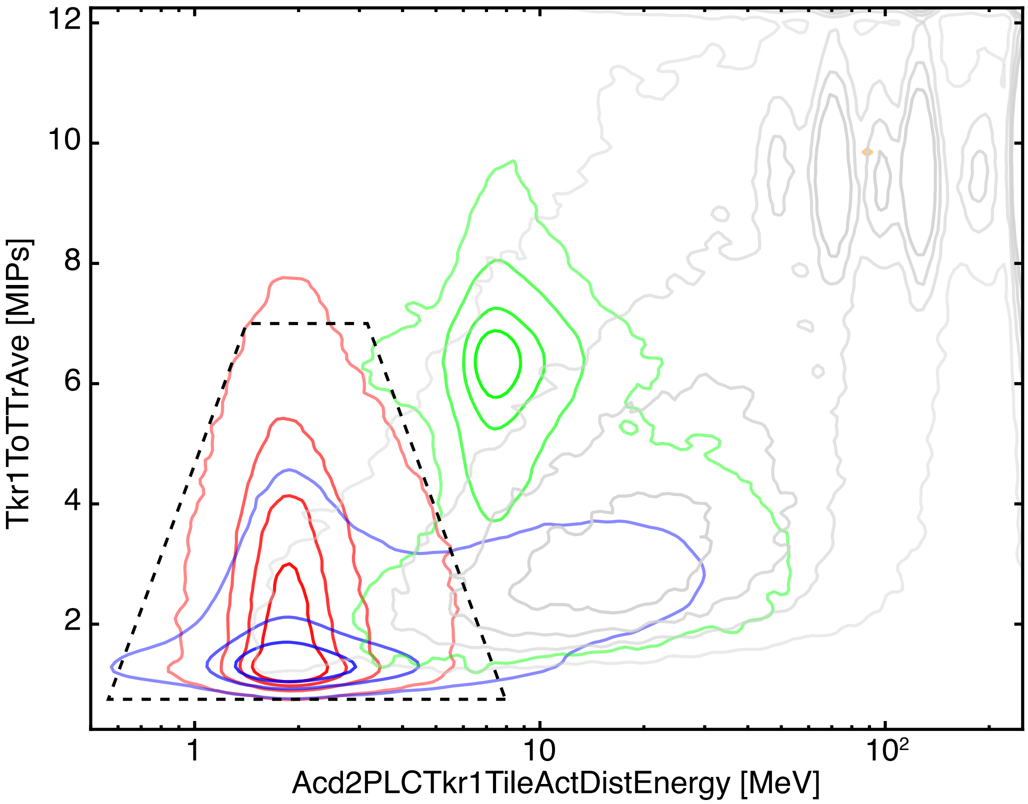

Figure 4.7: The containment contours for normalized event rate of different cosmic-ray populations for `Acd2PLCTkr1TileActDistEnergy` [MeV] versus `Tkr1ToTTrAve` [MIPs] from BKG simulation. The contours show 95%, 75%, 50%, and 25% percentile for the different cosmic-ray populations: electrons (red), protons (blue), helium (green), and nuclei (gray). The z-axis is normalized to event rate. Additionally, the polygon which defines `CUT_NUCLEI_LOOSE` is shown with the dotted black line. The density plots for flight data and BKG simulations are shown in Figure 4.8.

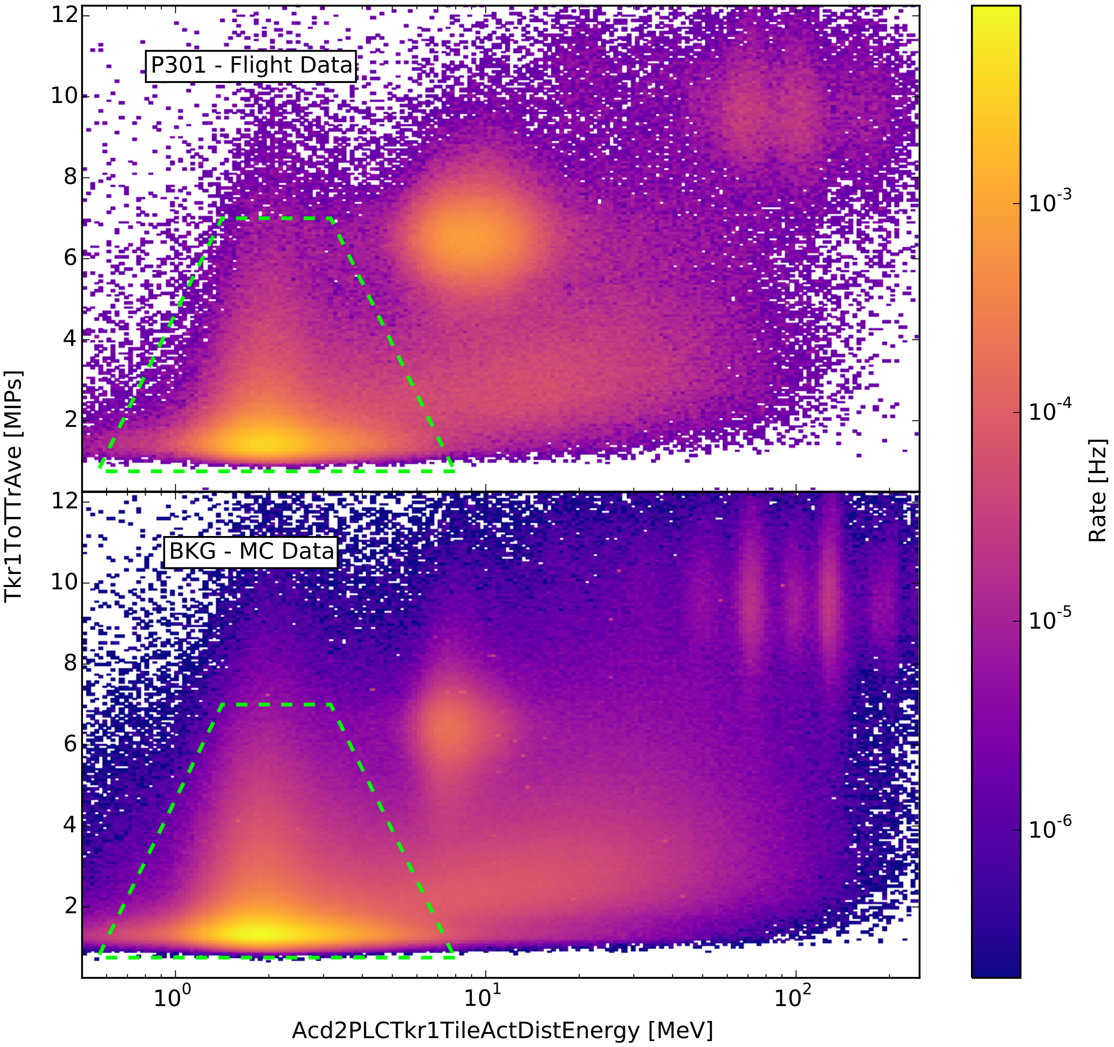

Figure 4.8: The density plot for normalized event rate of all cosmic-ray populations for `Acd2PLCTkr1TileActDistEnergy` [MeV] versus `Tkr1ToTTrAve` [MIPs] from the flight data and BKG simulation. The Z-axis is normalized to event rate. We can see the BKG simulation underestimates the event rate for for helium and nuclei but is able to reproduce the positions of the different cosmic-ray populations in the `Acd2PLCTkr1TileActDistEnergy` versus `Tkr1ToTTrAve` phase-space. Additionally, the polygon which defines `CUT_NUCLEI_LOOSE` is shown with the dotted green line.

4.4.2 Tight Nuclei Cut

A population of helium and nuclei events remain after using `CUT_NUCLEI_LOOSE`. The majority of these events have large incidence angles or enter through the bottom of the LAT. These events also have a poor direction reconstruction from the TKR due to not actually leaving an ionization track within the TKR. We can use the CAL reconstructed direction in place of the TKR direction. The CAL is able to reconstruct the direction of particles by calculating the moment of inertia tensor of the particle shower and using the longest axis of the moment of inertia tensor as the direction of the cosmic-ray. Several ACD variables are produced using the CAL direction instead of the TKR direction. One such variable is `Acd2Cal1TriggerEnergy15` which is the energy deposited in the ACD in a 15° cone using the CAL direction as reconstructed direction for tiles with a veto.

An issue arises due to the the top-down reconstruction preference of Pass 8. All events reconstructed in Pass 8 are assumed to enter from the top and exit through the bottom. The direction of bottom entering helium and nuclei can be misreconstructed by 180°. Despite this fact we can still use `Acd2Cal1TriggerEnergy15` because instead of measuring the ionization due incident cosmic-ray in the ACD, `Acd2Cal1TriggerEnergy15` will measure ionization and energy deposits in the ACD from daughter particles of the hadronic shower as it escapes the CAL and propagates through the TKR and ACD. `Acd2Cal1TriggerEnergy15` cannot be used for charge measurements or particle identification but can be used a simple veto for detecting these back-entering helium and nuclei. As we see in Figure 4.9, the majority

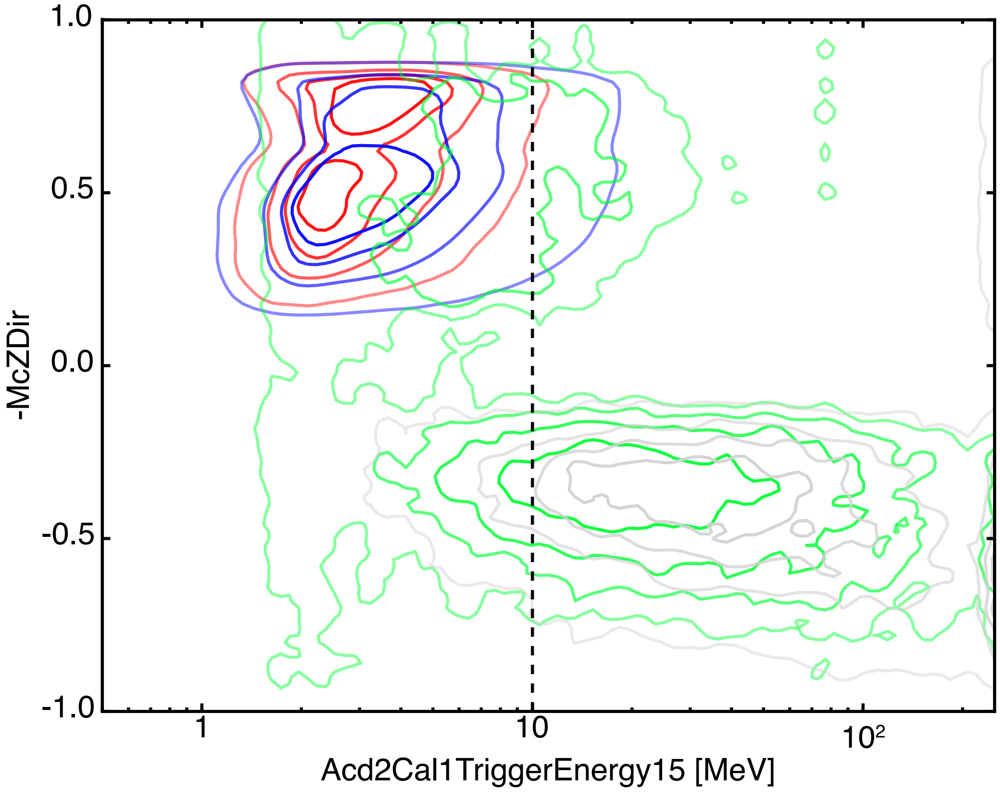

Figure 4.9: The containment contours for normalized event rate of different cosmic-ray populations for `Acd2Cal1TriggerEnergy15` [MeV] versus `McZDir` from BKG simulation. The contours show 95%, 75%, 50%, and 25% percentile for the different cosmic-ray populations: electrons (red), protons (blue), helium (green), and nuclei (gray). The Z-axis is normalized to event rate. Additionally, the polygon which defines `CUT_NUCLEI_TIGHT` is shown with the dotted black line.

of the helium and nuclei after `CUT_NUCLEI_LOOSE` are bottom entering events and `Acd2Cal1TriggerEnergy15` can be used to remove these bottom entering events from the data. `McZDir` is the Z component of the simulated direction and McZDir < 0 are top entering events and McZDir > 0 are bottom entering events. We define `CUT_NUCLEI_TIGHT` as:

```
CUT_NUCLEI_TIGHT = Acd2Cal1TriggerEnergy15 < 10
```

We can estimate the signal efficiency and rejection power to be 96.8% and 63.2% using BKG simulations. `CUT_NUCLEI_TIGHT` has lower rejection power than `CUT_NUCLEI_LOOSE` but since `CUT_NUCLEI_LOOSE` removes the bulk of helium and nuclei, the combination of the two cuts leaves a pure sample of protons with little residual contamination.

4.5 Residual Cosmic-Ray Contamination

Using the BKG simulations as a starting point we can combine `CUT_NUCLEI_LOOSE` and `CUT_NUCLEI_TIGHT` to estimate the signal efficiency and rejection power as 85.2% and 98.8%. It should be noted that the proton event rate is high enough that an 85.2% signal efficiency is sufficient for this analysis. To estimate the residual helium and nuclei contamination we need to correct the BKG simulation using flight data to adjust the rate for helium and nuclei. Unfortunately, there are few variables of merit that have not been cut on that can effectively trace the charge of incident cosmic-rays. We can measure that the BKG number of helium and nuclei events left in the BKG simulation is around 20,000 events. This means that we cannot correct the BKG event rate after applying `CUT_NUCLEI_LOOSE` and `CUT_NUCLEI_TIGHT` but

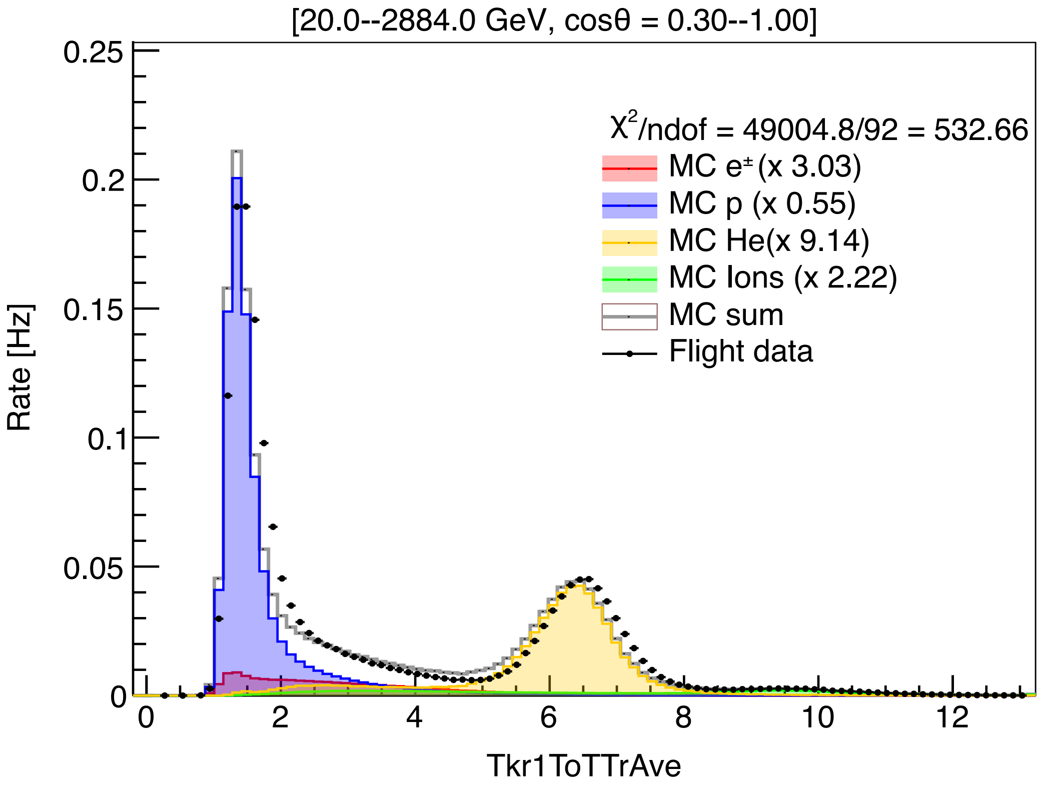

Figure 4.10: Data/MC agreement for Tkr1ToTTrAve from BKG simulations. Electrons and positrons (red), protons (blue), helium (orange), and nuclei (green), fit to flight data (black) without either `CUT_NUCLEI_LOOSE` or `CUT_NUCLEI_TIGHT` cut applied. The χ^2 is poor but this is an known issue with the BKG simulations.

we can estimate the correction factors for helium and nuclei event rates before applying `CUT_NUCLEI_LOOSE` and `CUT_NUCLEI_TIGHT` and then apply corrections after the cuts and estimate the residual contamination.

From Figure 4.10 we can estimate the correction factors for helium and nuclei event rates as 9.0 and 2.0 respectively. We use these correction factors in the estimation of the residual proton contaminations for helium and nuclei in Figure 4.11.

Figure 4.11 shows that the electron contamination dominates over both the

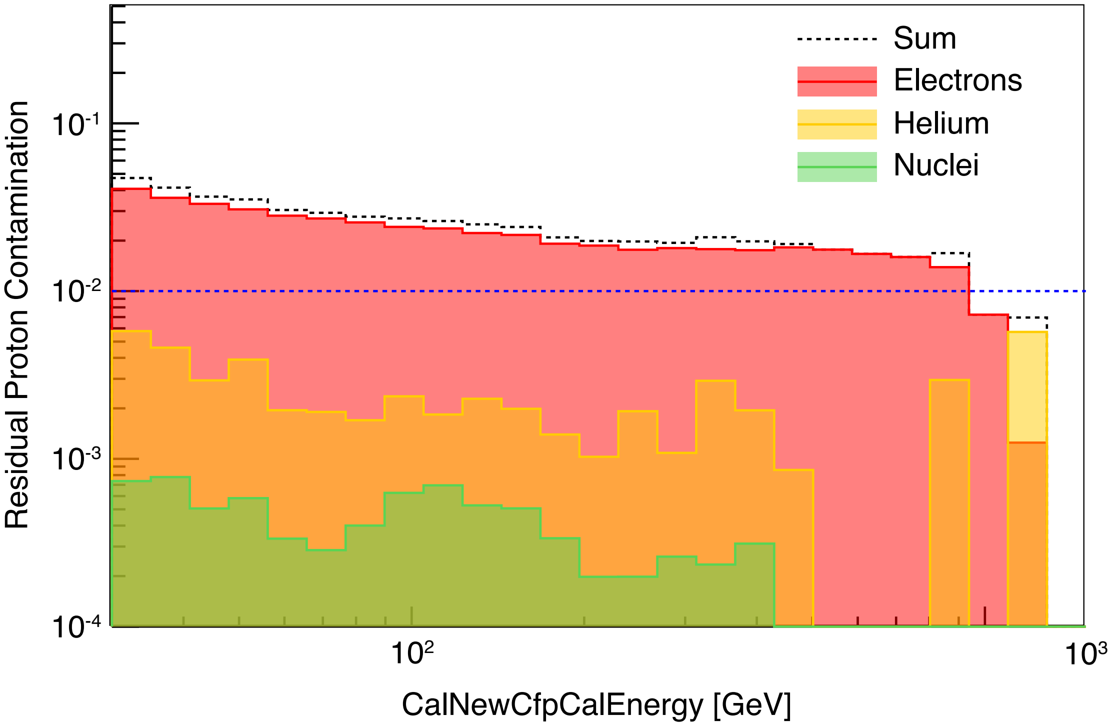

Figure 4.11: Residual contamination of protons due to electrons (red), helium (orange), nuclei (green) and the sum (black) using the BKG simulations. The event rate for helium and nuclei are corrected using comparisons to flight data. The blue dashed line shows 1% residual contamination.

helium contamination and nuclei contamination. Electron contamination is largest at lower energies then tends to decrease as energy increases, but never exceeds more than 4% while the helium and nuclei contamination is well below 1%. The reduction of residual contamination as proton energy increases is beneficial since probing higher energies of the cosmic-ray proton spectrum is more interesting. Clearly the combination of `CUT_NUCLEI_LOOSE` and `CUT_NUCLEI_TIGHT` reduce the most significant amount of helium and nuclei contamination but the electron contamination remains. This is not unexpected since we know ionization deposits energy proportional to z^2 and as established in Chapter 2, cosmic-ray electrons have a much lower flux than cosmic-ray protons so the residual electron contamination is low enough to proceed with the analysis. Further analysis of the residual electron and positron contamination in reference to spectral reconstruction is shown in § 6.4. In the proceeding chapters, the helium and nuclei contamination is considered negligible and only the electron contamination will be the only considered source of contamination.

Chapter 5: Energy Measurements in the *Fermi*-LAT

Without a proper understanding of energy deposition and hadronic shower evolution in the LAT, a spectral measurement would be impossible. Therefore, the energy measurement for proton interactions within the LAT is critical to measuring the cosmic-ray proton spectrum. We must first establish how different particles interact and deposit energy within the LAT and the fundamental physics of electromagnetic and hadronic showers. Secondly, we describe how the LAT's Pass 8 software estimates energy for electrons and γ-rays from deposited energy in the calorimeter via a parameterization and profile fit method. Finally, we explain how we estimate the energy for protons using knowledge of hadronic showers and electromagnetic showers with the Pass 8 reconstruction and simulation software.

5.1 Electromagnetic Showers

Electromagnetic showers are considerably less complicated than hadronic showers. Only two well understood interactions are required to describe the entirety of electromagnetic showers–specifically bremsstrahlung for electrons and positrons, and pair production for photons. Consequently, electromagnetic showers are easily parameterized, modeled, and simulated even to TeV energies.

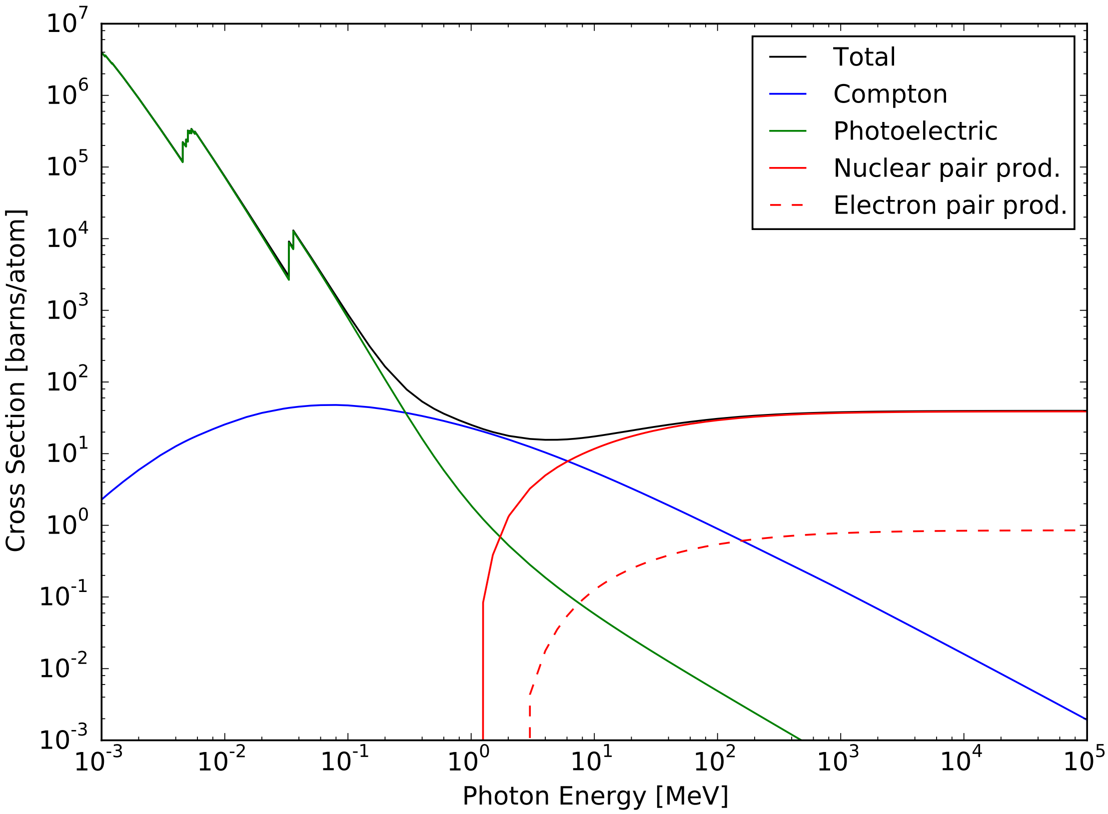

Figure 5.1: Photon cross-section as a function of energy in Cesium Iodide (CsI). Cross-section are in units of barns (10^{-24} cm^{2}) per atom and photon energy in units of MeV. The black line shows the total cross-section, the blue line shows the cross-section from Compton scattering, the green line show the cross-section from the photoelectric effect, the red solid line shows cross-section from nuclear pair production, and the red dashed line shows cross-section from electron shell pair production. Nuclear pair production dominates other processes above energies of 10 MeV [93].

The total cross-section and contributions from different physical processes of photons in carbon can be seen in Figure 5.1. At lower energies–typically below ∼10 MeV–the photoelectric effect, Rayleigh scattering and Compton scattering dominate. Above ∼10 MeV, pair production begins to dominate [34].

When a high energy photon undergoes pair-production, an electron-positron pair is created with an average kinetic energy given in Equation 5.1.

$$E_k = \frac{1}{2}(E_\gamma - 2m_ec^2) \tag{5.1}$$

The daughter electron and positron then lose energy via bremsstrahlung creating daughter photons. Energy loss via bremsstrahlung is estimated in a general form in Equation 5.2.

$$-\frac{dE}{dx} = 4\alpha N_A \frac{Z^2}{A} z^2 \left(\frac{1}{4\pi\epsilon_0 \frac{e^2}{Mc^2}} \right)^2 E \ln\left(\frac{183}{Z^{1/3}} \right) \tag{5.2}$$

It should be noted that because of the inverse mass squared of Equation 5.2 that lower mass particles, such as electrons and positrons, proportionally lose much more energy via bremsstrahlung than heavier particles such as protons and nuclei.

If these daughter photons have more than 10 MeV energy then they will undergo pair production, therefore creating more electron-positron pairs. This process continues until electrons drop below the critical energy to undergo bremsstrahlung or the daughter photons' interaction is no longer dominated by pair production. The critical energy is defined as when energy loss for electrons and positrons by bremsstrahlung and ionization are equal and is dependent on the material being traversed. Figure 5.2 shows the crossover point, the critical energy, for ionization and bremsstrahlung for an electron in CsI. The critical energy for CsI is measured to be 11.17 MeV. This is the basic process of an electromagnetic shower. A toy model is shown in Figure 5.3. It should be noted this toy model works well for the beginning of the shower to the maximum, but breaks down after the maximum number of particles created known as the shower maximum. If the incident particle is an electron or positron, it will undergo the same process, omitting the first step.

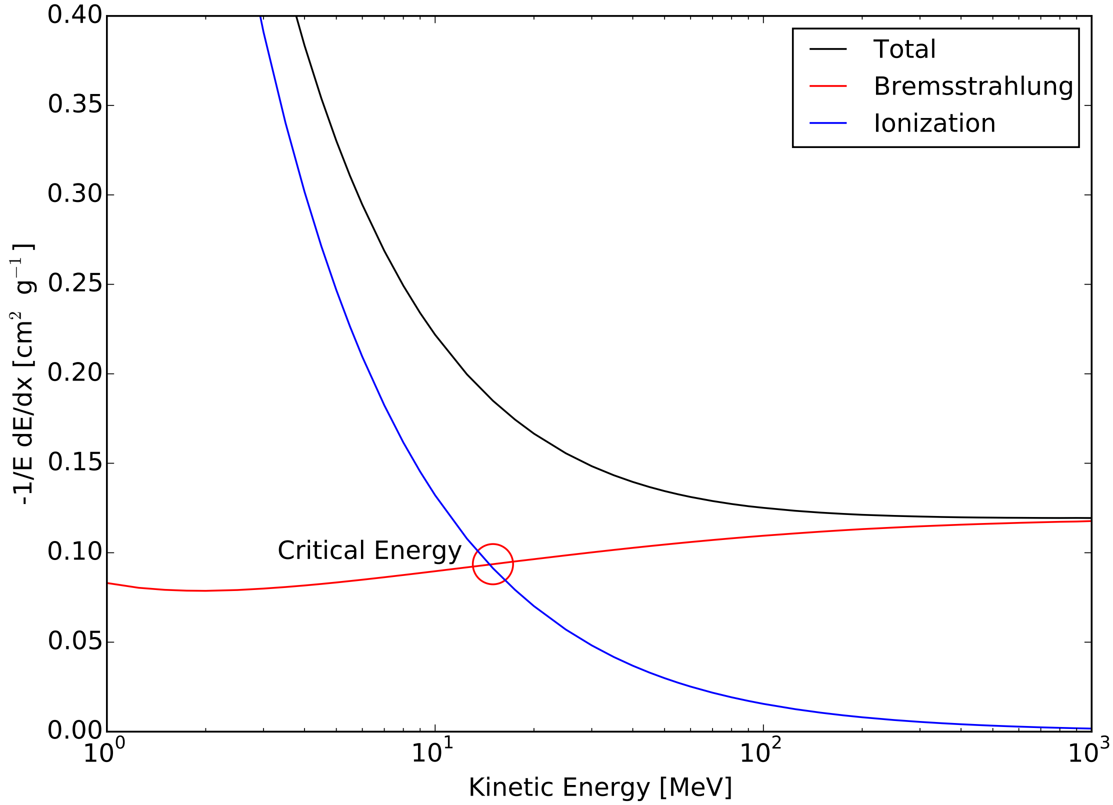

Figure 5.2: The fractional energy lost per X_0 of electrons and positrons in cesium iodide. Ionization (blue) dominates below 11 MeV while bremsstrahlung (red) dominates above 11 MeV. The Critical energy E_C is defined when energy loss due to ionization is equal to that of bremsstrahlung. For cesium iodide, E_C is measured to be 11.17 MeV. [94]

Electromagnetic showers are easily parameterized since a entirety of the incident particle's energy is converted into the shower. Therefore there is almost no missing energy and low stochasticity. The characteristic length traveled by electrons and positrons is defined as the radiation length (X_0). X_0 is dependent on the material and can be estimated by Equation 5.3 where Z and A are the atomic number of weight of the material [34].

$$X_0(g/cm^2) \approx \frac{716\ \mathrm{g/cm^2}\ A}{Z(Z+1)\ln(287/\sqrt{Z})} \tag{5.3}$$

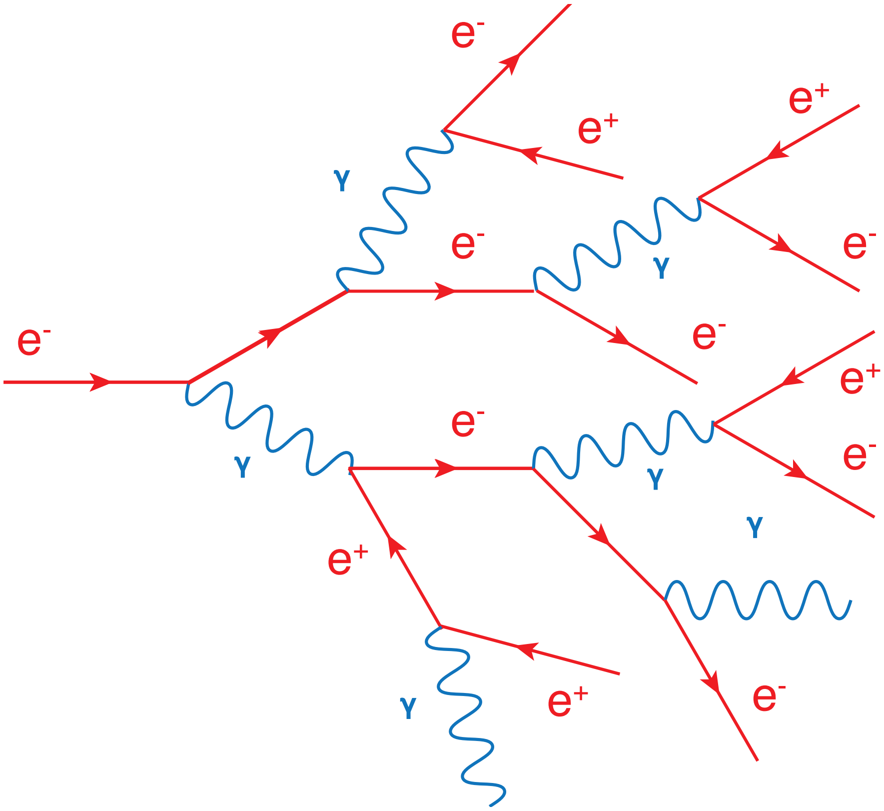

Figure 5.3: Toy visualization of an electromagnetic shower demonstrating pair production, $e^{\pm} \rightarrow \gamma\gamma$, and bremsstrahlung, $e^{\pm} + \gamma \rightarrow e^{\pm} + \gamma$.

For instance the CAL, composed of CsI(Tl) crystals, has a X_0 of 1.85 cm (§ 3.1.2). Continuing the toy model gives more insight into properties of electromagnetic showers. Since electromagnetic showers are an exponential process, the energy after crossing a length x of material can be estimated as:

$$E(x) = E_0 \; e^{-x/X_0} \tag{5.4}$$

where E_0 is the incident energy of the particle. The electron loses half of its energy after $X_0 \ln(2)$ amount of material is traversed and particle creation ceases when $E < E_c$. Therefore, the depth at which the maximum number of particles is created is:

$$x_{max} = X_0 \ln\left(\frac{E_0}{E_c}\right) + C_j \tag{5.5}$$

where C$_j$ = -0.5 of electron induced shower and C$_j$ = 0.5 for γ induced showers.

A more accurate form of the energy as a function of depth can be parameterized by the longitudinal profile seen in Equation 5.6 [95].

$$\frac{dE}{dt} = E_0 \; b \; \frac{(b \; t)^{a-1} e^{-bt}}{\Gamma(a)} \tag{5.6}$$

Where $t = x/X_0$ and Γ is the Gamma Function. The maximum of the shower is found to be $t_{max} = (a-1)/b$ and combining with Equation 5.5 results in Equation 5.7 [34, 95].

$$t_{max} = (a-1)/b = \ln(E_0/E_c) + C_j \tag{5.7}$$

This demonstrates the logarithmic energy dependence on the length of the shower and higher energy showers require more material. The longitudinal profile for electrons and γ-rays for several different energies can be seen in Figures 5.4 and 5.5. For instance, the CAL is 8.6 X$_0$ at normal incidence (§ 3.1.2), therefore there is enough material to capture the beginning and the maximum of an electromagnetic shower to TeV energies.

The transverse shower size is dominated by multiple coulomb scatterings of the electrons and positrons as they travel away from the primary axis of the shower. This behavior can be parameterized as seen in Equation 5.8 [96].

$$\frac{1}{dE(t)} \frac{dE(t,r)}{dr} = p \frac{2rR_C^2}{(r^2 + R_C^2)^2} + (1-p) \frac{2rR_T^2}{(r^2 + R_T^2)^2} \tag{5.8}$$

where r is the distance from the shower axis normalized to R_M, the Moliere radius, which is also the characterized length scale of the transverse shower. R_C and R_T are

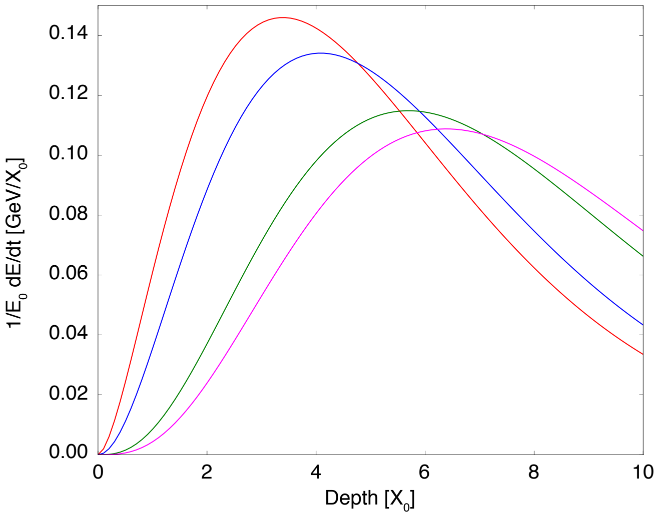

Figure 5.4: Longitudinal profile for 50 GeV(red), 100 GeV(blue), 500 GeV(green), and 1 TeV(magenta) electrons. The b parameters in Equation 5.6 are assumed to be b = 0.5, and E$_C$ = 1 MeV purely for illustrative purposes.

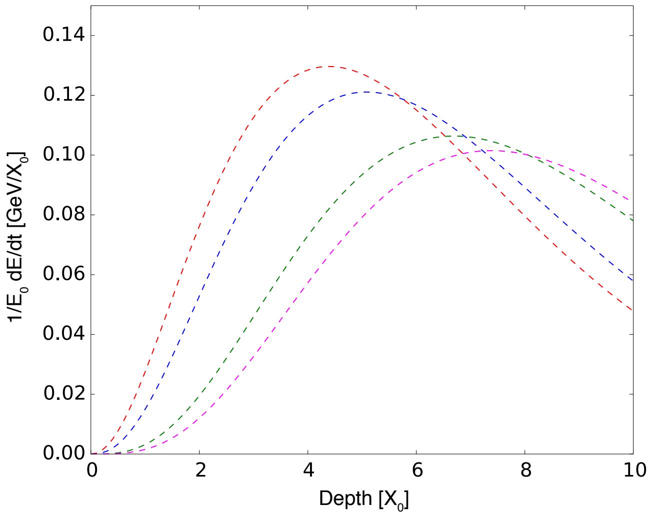

Figure 5.5: Longitudinal profile for 50 GeV(red), 100 GeV(blue), 500 GeV(green), and 1 TeV(magenta) γ-rays. The b parameters are equation 5.6 is assumed to be b = 0.5, and E$_C$ = 1 MeV purely for illustrative purposes.

length scales to determine the core and tail of the transverse shower and p is a weight term. A Moliere radius can be estimated as $R_M \approx X_0 E_s/E_c$ where $E_s \approx MeV$ and E_C is the critical energy [34]. A characteristic of the transverse profile is that as the shower evolves beyond the longitudinal maximum, the transverse size increases. 90% of the shower is contained within a single Moliere radius.

In summary, electromagnetic showers are characterized by their near complete conversion of incident particle energy into the shower, low stochasticity, simple parameterization by a few free parameters, short longitudinal and narrow transverse profile. This allows us the lay the groundwork for understanding how the LAT measures the energy of incoming γ-rays and any direct cosmic-ray measurements.

5.2 LAT Energy Measurement

After the reconstruction of measured quantities in each subsystem described in § 3.2, one has to interpret the data in order to reconstruct the physical properties of the original γ-ray. Since the CAL has a limited size, 8.6 X_0 deep at normal incidence and ∼17.2 X_0 deep at 60° off axis, the entire shower will not be contained– especially at energies above a few GeV and increasingly so as energy increases. Additionally, the box geometry of the LAT and CAL modules creates gaps and causes leakage if the shower passes by the edge of the CAL. One can find a simple estimate of this effect in Figure 5.5. Therefore, one cannot sum up the total energy deposited in the CAL and expect that sum to accurately reflect the true energy of the incident γ-ray. Additionally, because the LAT covers wide angular phase space, the energy reconstructed depends on both energy deposition in the CAL and the incident direction, measured either by the TKR or CAL, in order to properly account for gaps and geometric effects within the LAT.

There are two methods that estimate the incident energy of γ-rays, the parametric method described in § 5.2.1 and a longitudinal profile fit method described in § 5.2.2. These methods are performed independently and later the best energy is chosen to produce an event by event energy estimate of the incident γ-ray.

5.2.1 Parametric Method

The parametric method is used to estimate the energy of the incident γ-ray below energies of a few GeV of the LAT. At energies below 1 GeV, the photon interacts with enough material in the TKR such that the shower begins well before the interaction with the CAL. In many cases, the CAL catches the tail end of the shower, making an energy measurement difficult since the energy deposited in the CAL is only a fraction of the total shower and misses the maximum of the shower which is crucial to fit the shower profile since information in the shower tail is indistinguishable from low energy or high energy showers. The parametric method takes in several key types of information and returns an energy estimate. These key types of information include leakage corrections, position corrections, and total energy recorded in the TKR and CAL. A longitudinal profile fit is then performed using Equation 5.6 once the maximum of the shower is located either in the TKR or CAL. This works–despite the shower not being completely contained in the CAL–

because as described in § 3.1.3 the TKR is basically a thin sampling calorimeter. The result is then tuned using the GEANT4 low energy Monte-Carlo γ-rays [92].

While this method works to a certain degree at lower energies, at higher energies another method is implemented when the shower has much more containment in the CAL.

5.2.2 Profile Fit Method

The profile fit method is used to estimate the energy of the incident γ-ray above a few GeV and therefore is critical to the understanding of the proton spectral measurement which begins at 50 GeV. Electromagnetic showers in this energy range tend to be well developed and energy deposition in individual crystals allows for detailed modeling of shower development in both the longitudinal and transverse direction from the shower axis. Complications to this method arise due to gaps between the towers and layers of the calorimeter and saturation of individual CAL crystals. If a shower falls heavily in the gap between towers or layers, there is significantly less information available to measure the profile of the electromagnetic shower, therefore a detailed understanding of the location of the gaps is required. Crystal saturation occurs when more than 70 GeV is deposited in a crystal. This typically occurs in the core of the electromagnetic shower because, as was discussed in § 5.1, electromagnetic showers tend to be narrow. Because the CAL crystal no longer accurately reflects the energy deposition, the core of the shower and therefore the amplitude of the longitudinal profile will underestimate the incident energy of the γ-ray. To solve this, modeling of the transverse shower allows for a more accurate estimated amplitude of the longitudinal profile at that point in the shower development.

Using Equation 5.6 as the model for longitudinal development of electromagnetic showers, one can decompose the **a** and **b** parameters via principle component analysis into two new variables which are uncorrelated:

$$S_0 = \ln a \cos\psi + b \sin\psi \tag{5.9}$$

$$S_1 = -\ln a \sin\psi + b \cos\psi \tag{5.10}$$

This is done due to the fact that **a** and **b** are heavily correlated and a is approximately a log normal distribution [92]. **a** and **b** distributions are determined with GEANT4 Monte-Carlo simulations of CsI(Tl) and *psi* is determined to be 0.5 using the same simulations. This produces S_0 and S_1 which are uncorrelated and both normal distributions. To normalize S_0 and S_1 to be used in Equation 5.12, subtract the mean at the energy and divide by the RMS at the energy.

$$s_i = \frac{S_i - \mu_{S_i}(E)}{\sigma_{S_i}(E)} \tag{5.11}$$

Using Equation 5.8 as the model for transverse development of electromagnetic showers, one measures R_C and R_T for CsI(Tl) using GEANT4 Monte-Carlo simulations and stored in a look-up table for LAT energies.

Using the models of shower development described above, the predicted energy in each layer $e_{p,i}$ is calculated to find S_0 and S_1 which are transformed back to **a** and **b** and then integrated across the entire longitudinal profile to find the incident

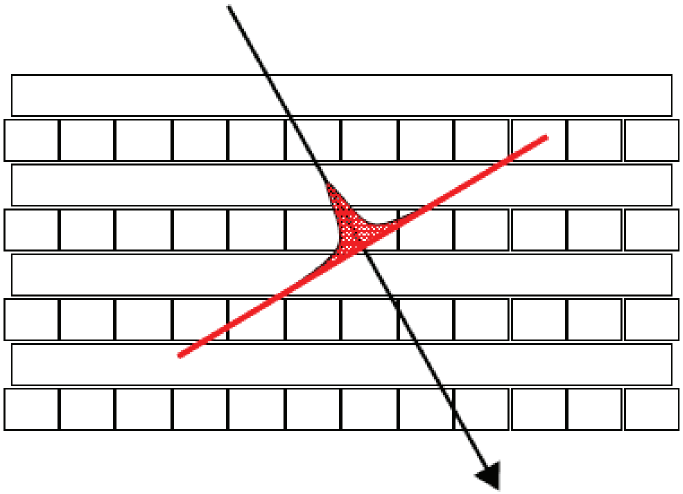

Figure 5.6: The Profile Fit method at one step in calculating predicted deposited energy in the CAL. Shown is the XZ projection where the red lines represent the extent of the shower in longitudinal and radial directions the black arrow represents the longitudinal axis of the shower. [92]

γ-ray energy. A direction is required to estimate $e_{p,i}$; an energy is calculated for both TKR direction § 3.2.3 and CAL direction § 3.2.2. More specifically, once an axis has been established it is divided into $X_0/10$ steps, along each step the depth is calculated in terms of X_0 and disk of radius 3 R_M is defined perpendicular the axis. An example of this disk and shower can be seen in Figure 5.6. The energy deposited in each layer from this disk is calculated according to Equations 5.6 and 5.8. This process continues until no more active CAL material is within this computed disk. Then finally, deposited energy is summed up for each layer and $e_{p,i}$ is computed. The difference between the predicted energies in each layer and measured energies in each layer, $e_{m,i}$ is minimized. Additionally, saturated crystals have been be treated separately and removed from $e_{m,i}$. The χ^2 that is minimized is described as:

$$\chi^2(E) = \sum_{i=1}^{8} \left(\frac{e_{m,i} - e_{p,i}}{\delta e(E)} \right)^2 + \sum_{k=1}^{n_{sat}} \left(\frac{max(0, e_{m,k} - e_{p,k})}{\delta e(E)} \right)^2 + s_0^2(E) + s_1^2(E) \quad (5.12)$$

where $\delta e(E)$ is the error of the longitudinal profile fit estimated from GEANT4 Monte-Carlo simulations [92].

$$\delta e(E) = 0.17 \times \exp\left(-\frac{\log_{10} E}{1.38} \right) \times \max(e_{m,i}) \quad (5.13)$$

The profile method is the backbone for estimating the energy of γ-rays above a few GeV. The handling of off-axis events, saturated crystals, inactive material in the CAL, and energy leakage provides an accurate estimation energy for γ-ray events.

5.2.3 Combining Energy Estimates

From the two methods described in § 5.2.1 and § 5.2.2 the best energy estimator is chosen to produce a single energy which compasses the entire energy range of the LAT for γ-rays. The sum of deposited energy from all crystals in the CAL, called `CalEnergyRaw`, at 1 GeV, the layer which the γ-ray converted into an electron-positron pair, and the event incidence angle are used to determine the crossover energy between the parameterized energy and profile fit energy on an event by event basis. Below the crossover energy the parameterized energy is used and above the crossover energy the profile fit energy is used.

The resultant energy resolution is shown in Figure 5.7. The profile fit method provides a good energy resolution of $\sigma E/E < 10\%$ from 1 GeV to 1 TeV. Above 1

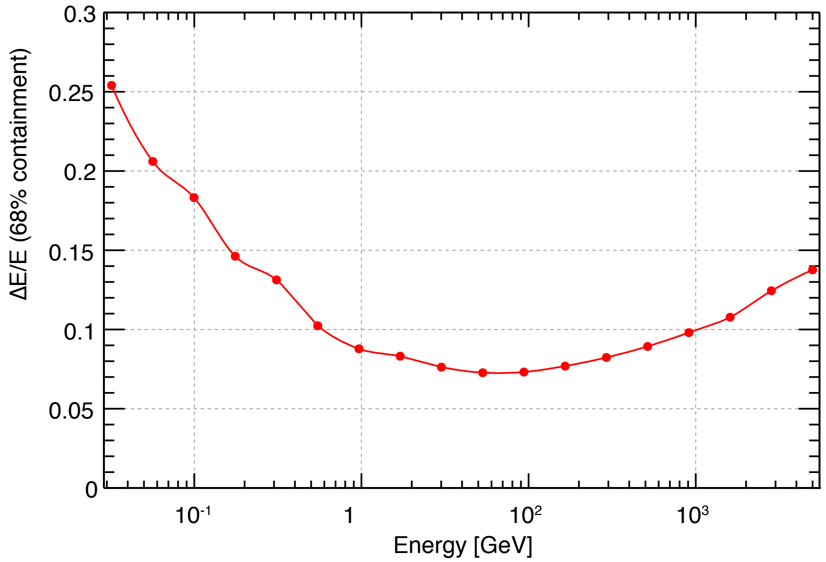

Figure 5.7: The Pass 8 68% confidence energy resolution for γ-rays in the LAT. The energy resolution is determined using dedicated γ-ray simulations using GEANT4 [97].

TeV the energy resolution begins to climb due to effects of greater shower leakage, CAL crystal saturation, and deterioration of direction reconstruction.

5.2.4 Absolute Energy Scale

We need to determine the absolute energy scale that should be applied to the reconstructed energy in order to ensure the accuracy of the reconstructed energy. The typical way to estimate the absolute energy scale is through beam-line studies. Using mono-energetic electrons at different energies and incident angle, the absolute energy scale is merely the difference between the mean of the reconstructed energy and the beam energy. The absolute energy scale involves both response of CAL crystals and accuracy of energy reconstruction. The absolute energy scale and associated uncertainties were measured on ground through beam-test data and the

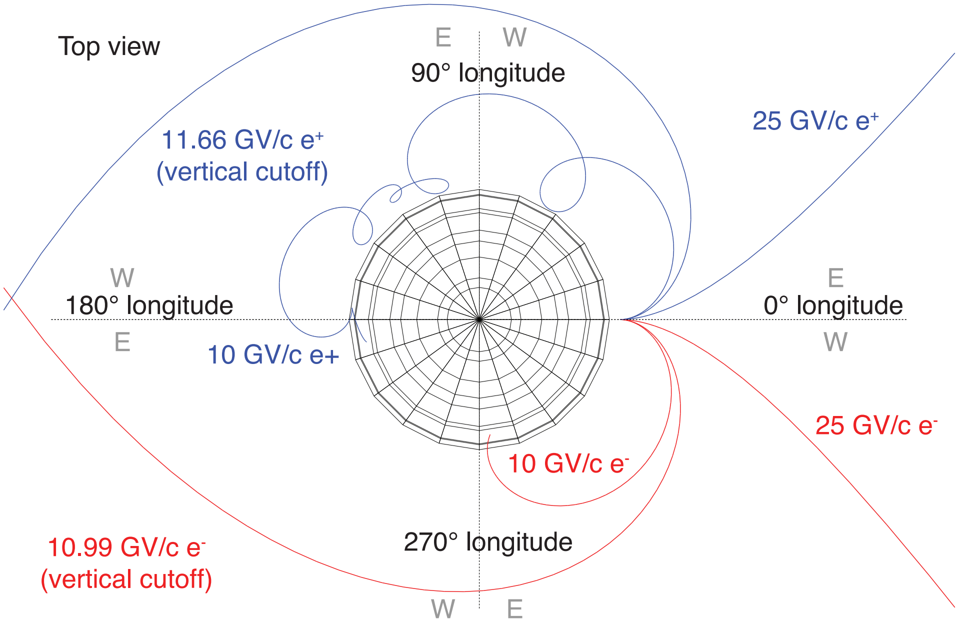

Figure 5.8: Illustration of electrons and positrons traced through Earth's magnetic field. The different energy electrons and positrons show the different interactions with Earth's magnetosphere, wherein the vertical geomagnetic rigidity cutoff is the trajectory for which electrons and positrons are determined to be primary or secondary. [98].

calibration unit (CU), described in § 6.8.2, but was not a representation of the whole LAT and it is therefore desirable to measure it in-flight. Additionally, it is important to understand the LAT's response for spectral studies of various γ-ray sources.

One can use the geomagnetic rigidity cutoff as a well known spectral cutoff with low energy electrons to estimate the absolute energy scale. One issue with using the geomagnetic rigidity cutoff are secondary electrons and positrons from cosmic-ray interactions with the Earth Limb. To estimate the fraction of the primary electrons and positrons to secondary electrons and positrons, tracer code implemented with models of the Earth's geomagnetic environment is needed to determine the allowed and forbidden regions for primary electrons and positrons [98] [99, 100]. The tracer code is run in reverse, given a particle of certain energy and trajectory, it is determined whether the particle could have originated from inside or outside the magnetosphere. Figure 5.8 shows the how the tracer code uses Earth's magnetic field to determine the minimum energy required for an electron or positron to originate as a primary cosmic-ray or from interactions in the Earth's limb. Once the fraction of primary electrons and positrons is found, flight data using the `DIAGNOSTIC` filter, an unbiased sample of events described in § 3.1.4, and a counts spectrum is measured in bins of McIlwain L. McIlwain L is a measure of the geomagnetic field lines which cross the geomagnetic equator at an altitude measured in Earth radii. The spectrum is then fit using Equation 5.14 and the energy cutoff, E_C, is found for the different bins of McIlwain L [98].

$$\frac{dN(E)}{dE} = \frac{cE^{-\Gamma}}{1 + (E/E_C)^{-6}} \tag{5.14}$$

The fit to the counts spectrum and measurement of E_C for a single bin of McIlwain L is shown in Figure 5.9. Once E_C has been measured by the LAT, it is then compared to the measurements given by the IGRF [100]. The mean offset across McIlwain L gives the absolute energy scale. For Pass 8, when using cosmic-ray electrons and positrons, this absolute energy scale has been at -3.7% [101]. The absolute energy scale should be applied to any energy measurement made by the LAT, including the cosmic-ray proton spectral measurement, as it is merely a measure of the offset of the reconstructed energy to the true energy.

While the energy measurement of the LAT works very well for γ-rays and elec-

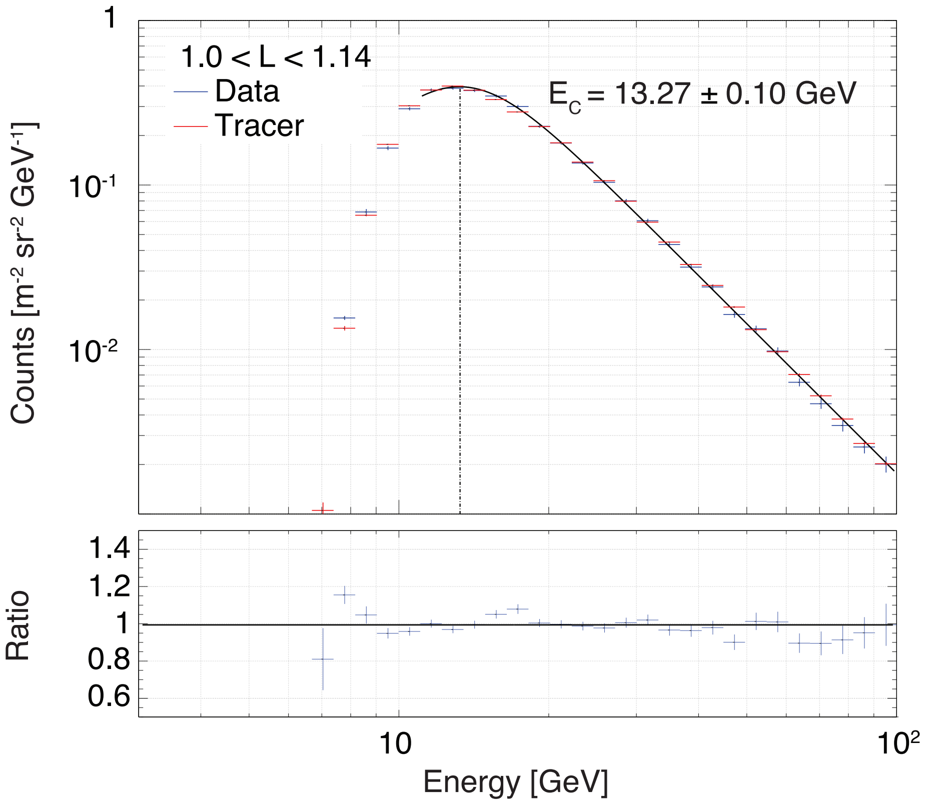

Figure 5.9: The geomagnetic cutoff for a single bin of McIlwain L of $1.0 < L < 1.14$ for electrons and positrons comparing flight data and tracer data [98].

trons, hadrons have a different response in the LAT due to fundamental differences in particle and shower physics.

5.3 Hadronic Showers

Hadronic showers are far more complicated than electromagnetic showers. Several different physical processes govern hadronic showers including: ionization, elastic hadronic scattering, inelastic hadronic scattering, nuclear de-excitation, production of unstable particles such as pions, and intrinsic energy loss from low cross-section particles like neutrons and neutrinos. Elastic and inelastic hadronic scattering are strong interactions which are difficult to calculate especially at energies above 100 GeV. Inelastic scatter dominates the proton-proton cross-section above a few GeV as seen in Figure 5.10. Finally, hadronic showers are more stochastic than electromagnetic showers because of the different interaction channels listed above. Despite these complications, toy models of hadronic showers can help in understanding these complex systems.

When an hadron first interacts with a material, it will undergo ionization energy loss as described in § 4.1 and Equation 4.5. Bremsstrahlung is not a major source of energy for protons since they are 1837 more massive than electrons and bremsstrahlung inversely depends on mass as seen in 5.2. The hadron will continue on its original trajectory, losing energy via ionization until the hadron interacts with a nuclei in the detector. If the hadronic scatters inelastically, a shower of daughter particles are produced through nuclear processes such as excitation, evaporations, and spallation. Figure 5.12 shows a toy example of an hadronic shower. Particles created through the primary interaction include charged and neutral pions, protons, neutrons, and also spallation nuclei from the original nucleus. Neutral pions decay with a lifetime of 8.4×10^{-17} seconds into two γ-rays each carrying half of the energy of the original neutral pion. These γ-rays then undergo the same processes as with electromagnetic showers creating an electromagnetic shower component of the larger hadronic shower. This creates a 'one way street' where energy is transferred from hadronic processes into electromagnetic processes through π^0 production and decay. On average, about 1/3 of the incident proton energy is converted into the electromagnetic component. Charged pions decay with a lifetime of 2.6×10^{-8}

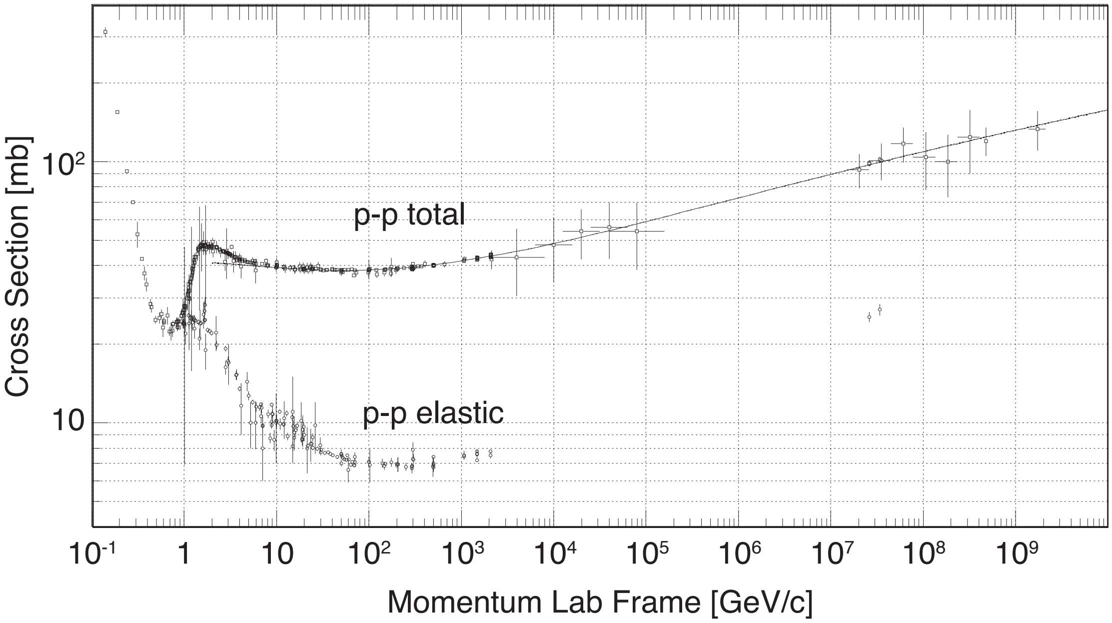

Figure 5.10: Total and elastic scattering cross-section for proton-proton interactions. This shows that inelastic scattering dominates above a momentum of 1 GeV. [34]

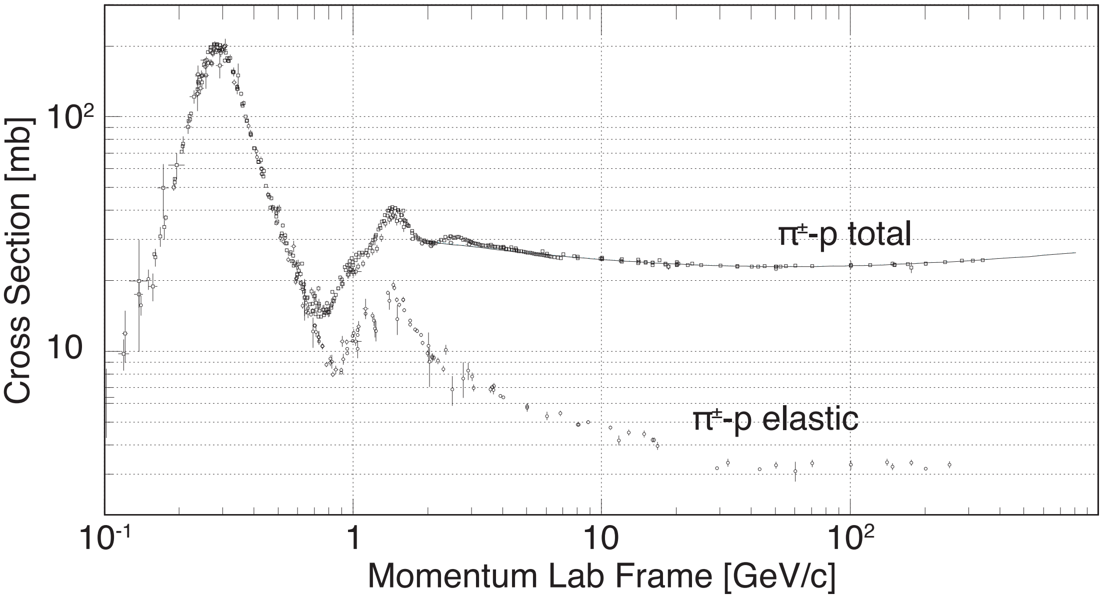

Figure 5.11: Total and elastic scattering cross-section for $\pi^{\pm}$-proton interactions. This shows that inelastic scattering dominates above a momentum 1 GeV. [34]

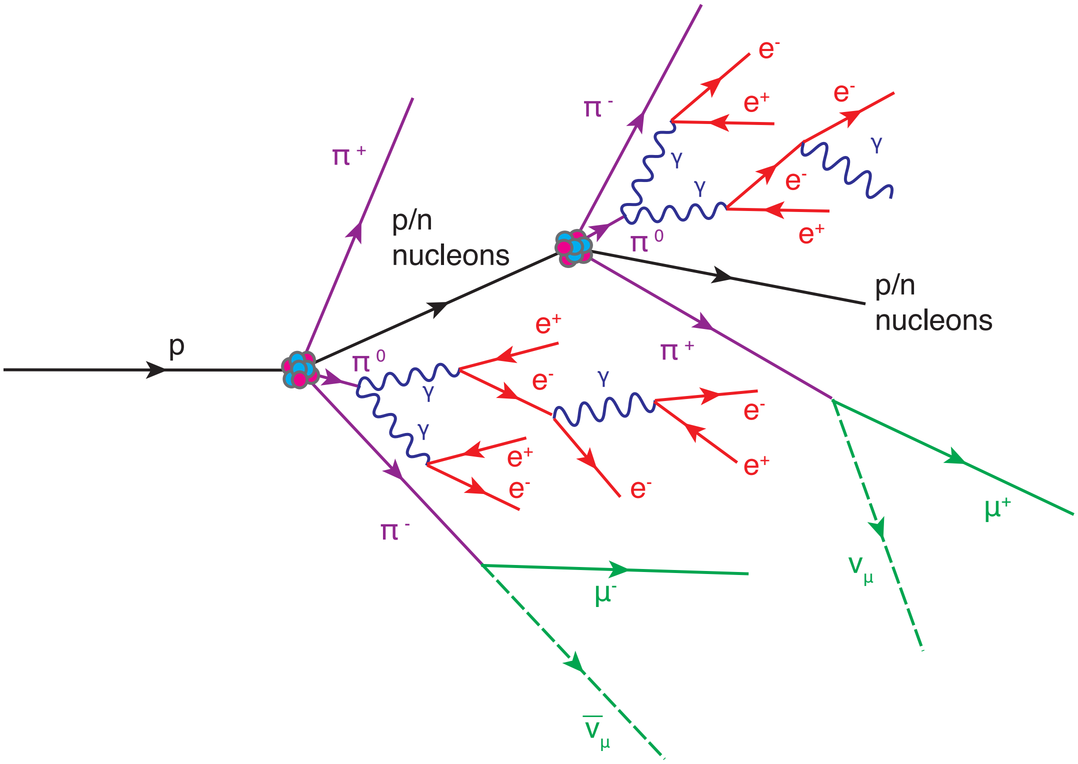

Figure 5.12: Toy visualization of an hadronic shower demonstrating the two components. The electromagnetic component with the same physics as described in § 5.1 and the non-EM component from $\pi^{\pm}$s, μs, protons, neutrons and nucleons.

seconds into muon and neutrino pairs. Muons will loose energy mostly via ionization due to their larger mass and neutrinos cross-section is so low they will likely not interact at all. Muons create a ‘visible’ channel through ionization energy losses but ionization is mostly energy independent and therefore is difficult to correlate back the original energy of the incident hadron. On average, about 1/3 of the incident proton energy is lost due to ionization of daughter particles such as muons and protons. Neutrinos creates an ‘invisible’ channel where particles carry their fraction of energy away from the shower and is almost impossible to measure. Only about 1% energy of the hadronic shower is transfered to neutrinos. The final 1/3 of incident proton energy is converted into invisible non-EM energy through binding energy and nuclear breakup. Daughter protons and neutrons will start the process over further propagating the hadronic shower till their energy falls below 1 GeV and their interactions are no longer dominated by inelastic scattering.

The distribution of the types of particles created in an hadronic shower can be seen in Figure 5.13 for simulated 100 GeV protons interacting the with the LAT. This gives us a view into deeper shower physics of hadronic showers in the LAT. We see a distribution of protons, neutrons, γ-rays, $e^{\pm}$s, $\pi^{\pm}$s, and π^0s as was discussed in the toy model. The majority of protons and neutrons created have low kinetic energies of only a few GeV and therefore are unlikely to interact via inelastic scattering. The majority γ-rays are too low energy to pair produce but γ-ray with energy above around 10 MeV will pair-produce to contribute to the electromagnetic fraction of the hadronic shower. Electron and positron interaction is dominated by ionization and the photoelectric effect below 10 MeV. Electrons and positrons with energy above 10 MeV will interact via bremsstrahlung and contribute to the electromagnetic fraction of the hadronic shower. Higher energy $\pi^{\pm}$s will be dominated by inelastic scattering and potentially further the shower as seen in Figure 5.11.

These processes describe a multicomponent particle shower with an electromagnetic and hadronic fraction. The electromagnetic (EM) fraction, composed of γ-rays decayed from π^0s, will create a core of the shower in the transverse shower axis and dominates the early longitudinal component of the shower. The hadronic fraction composed of $\pi^{\pm}$s will create a halo in the transverse shower axis and will dominate the later longitudinal component of the shower. The final component is

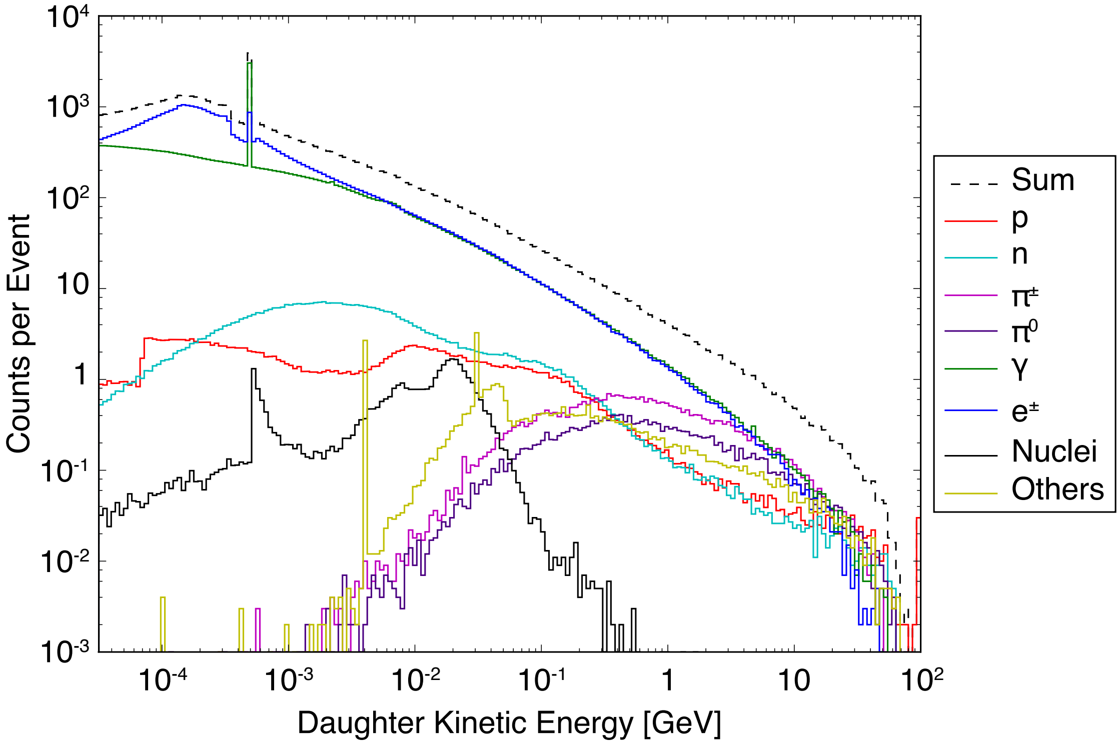

Figure 5.13: The kinetic energy and particle distribution of daughters produced with a simulated 100 GeV proton showering in the LAT, using 10^3 events and normalizing by event count. The full shower tree is simulated using GEANT4 with a minimum cut off kinetic energy of 0.5 MeV.

comprised of 'invisible' energy due to neutrinos, which do not interact with active detector material, and other low cross-section particles.

The fraction of the EM, hadronic, and invisible energies are highly dependent on the calorimeter's material, design, and size. The length scale that governs hadronic interactions, the nuclear interaction length λ_i, is longer than the X_0 for the same material. Comparisons of radiation lengths can be seen in Table 5.1,

$$\lambda_i = \frac{A}{N_A\ \rho\ \sigma_{inel}} \approx 35A^{1/3}\ (g/cm^2) \tag{5.15}$$

where λ_i is determined by Equation 5.15. N_A is Avogadro's Number, ρ is the density

Material	X_0 (cm)	X_0 (g/cm^2)	λ_i (cm)	λ_i (g/cm^2)
CsI(Tl)	1.860	8.39	38.04	171.5
Copper	1.436	12.86	15.32	137.3
Iron	1.757	13.84	16.77	132.1

Table 5.1: Radiation lengths (X_0) and nuclear interaction lengths (λ_i) for different materials.

of the material, and σ_{inel} is the inelastic cross-section for the material. Hadronic showers are typically much longer than electromagnetic showers of equivalent energy. Therefore it is necessary to have much more material and depth to capture an entire hadronic shower.

In a similar fashion to § 5.1, one can parameterize the average longitudinal hadronic shower development as shown in Equation 5.16 [102].

$$\frac{dE(x)}{dx} = k \left[w \left(\frac{x}{X_0} \right)^{a-1} e^{-b\frac{x}{X_0}} + (1-w) \left(\frac{x}{\lambda_I} \right)^{a-1} e^{-d\frac{x}{\lambda_I}} \right] \tag{5.16}$$

The first term refers to the EM component and the second term refers to the non-EM component. The w is a weighting factor between the EM and non-EM component; a, b, and d are free parameters depending on the shower and calorimeter with the potential of being energy dependent. Integrating from 0 to ∞ gives the total energy of the particle.

$$E_0 = \int_0^\infty \frac{dE(x)}{dx} dx \tag{5.17}$$

Therefore we can find the normalization to be:

$$k = \frac{E_0 (b\ d)^a}{\Gamma[a](w\ d^a\ X_0 + (1-w)\ b^a\ \lambda_i)}\ . \tag{5.18}$$

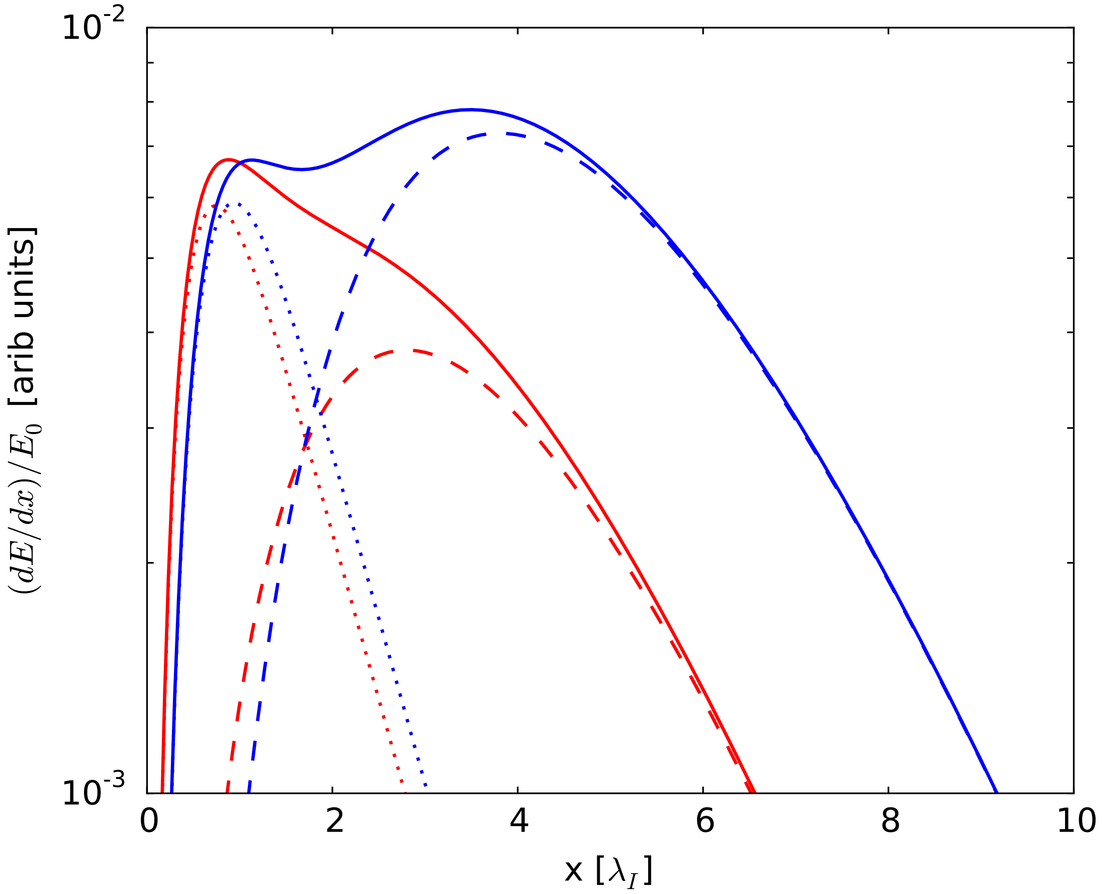

Figure 5.14: Average longitudinal profiles for hadronic showers in CsI. Red lines are 100 GeV protons and blue lines are 1 TeV protons. The dashed lines are the EM component and the dotted lines are the non-EM component. [103]

Figure 5.14 shows the average longitudinal development of hadronic showers in a CsI calorimeter. The EM component dominates the early portion of the shower and increases with energy. In late shower, the non-EM component begins to dominate after a few nuclear interaction lengths. It should be noted that Equation 5.18 describes the average longitudinal shower profile large variations in energy deposition and traverse size can occur from event to event.

Due to the myriad of particle production channels in a proton inelastic scat-

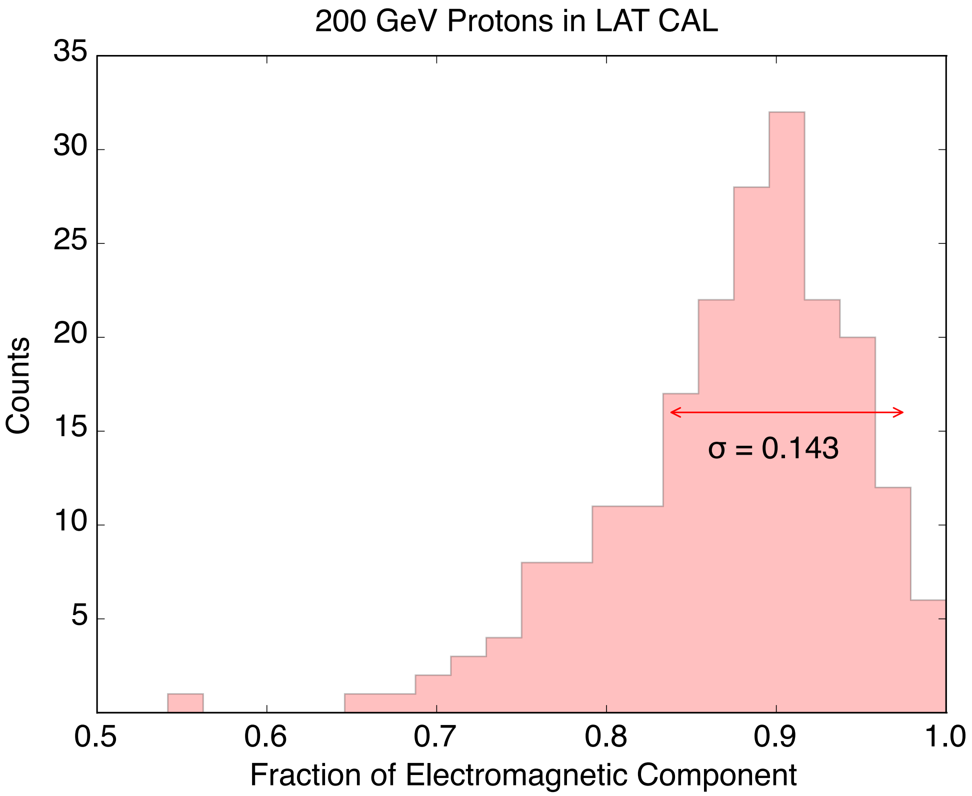

Figure 5.15: The EM fraction of a 200 GeV proton induced shower showing the natural stochasticity of hadronic showers. These events are taken from GEANT4 simulations described in § 3.3.

tering event, the number of π^0 and $\pi^{\pm}$s will vary greatly from event to event which creates a large stochasticity from hadronic shower to hadronic shower. Therefore, the EM and hadronic fractions also vary greatly between different hadronic showers–even at the same energy. The effect can be seen in Figure 5.15 where the EM fraction of 200 GeV protons on the LAT's CAL vary from 0.7 to 1.0. This stochasticity suggests a need for a larger hadronic calorimeter than comparative EM calorimeters.

$$\frac{dE}{dr} = \frac{B_1}{r} e^{-\frac{r}{\lambda_1}} + \frac{B_2}{r} e^{-\frac{r^2}{\lambda_2^2}} \tag{5.19}$$

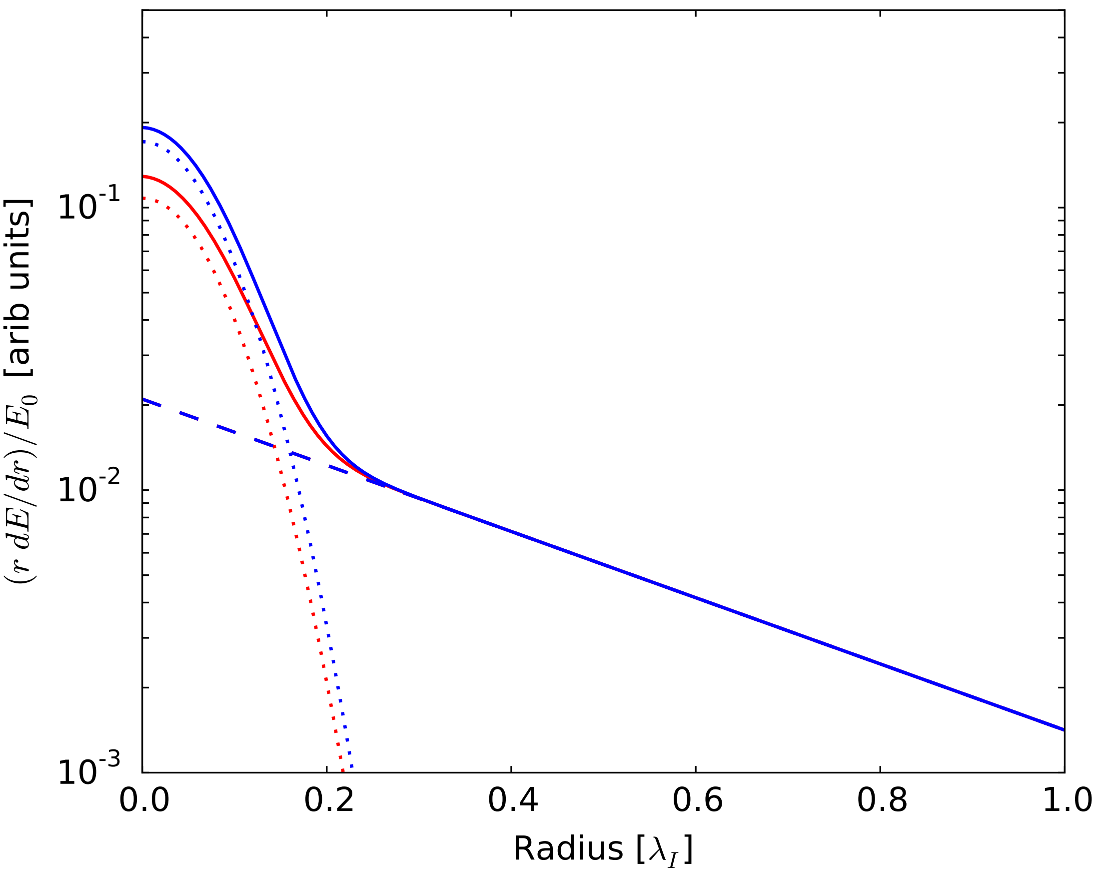

Figure 5.16: The average transverse profiles for hadronic showers in CsI. Red lines are 100 GeV protons and blue lines are 1 TeV protons. The dashed lines are the EM component, the dotted lines are the non-EM component, and the solid lines are the sum of the two components. Each component has been scaled by Energy E_0. [104]

Additionally, the average transverse development of hadronic showers can be parameterized. In a similar vein to the average longitudinal development, the transverse development is characterized by a two component mode of an EM core and an hadronic halo [104].

Using values from D. Acosta [104], Figure 5.16 shows the two components and how the EM component dominates near the shower axis while the non-EM component produces an extension beyond $0.5\lambda_i$. 95% of the transverse shower is contained within 1 λ_i. Hadronic showers are much wider than an electromagnetic shower whose width is determined by the Moliere radius as shown in Equation 5.8. This is useful for particle identification as shown previously in Chapter 4, but can lead to leakage of the non-EM component if the calorimeter is not wide enough.

In summary, hadronic showers are far more complicated than electromagnetic showers. Hadronic showers involve processes of electromagnetic showers and strong/nuclear processes producing a different spectrum of daughter particles including electrons, positrons, γ-rays, π^0s, $\pi^{\pm}$s, protons, neutrons, and other mesons and baryons. Generally, they have an EM core with an hadronic component which extends in both the longitudinal and transverse directions. The EM core is generated from π^0s for which the main decay channel is two γ-rays. This creates a 'one way street' that removes energy from the shower. The fraction of energy deposited from the EM component increases with energy and is highly dependent on the design, material, and size of the calorimeter. Hadronic showers are longer and wider than electromagnetic showers with increased stochasticity from event to event due to fluctuations in particle production from strong processes. These differences necessitate that hadronic calorimeters are much larger than electromagnetic showers to capture the entire shower development, especially the hadronic tails. With this knowledge we can develop a strategy to estimate the response of the CAL to proton-induced showers to make an accurate energy estimate for hadronic showers in order to measure the proton spectrum.

5.4 Measuring the Energy of Hadronic Showers in the LAT

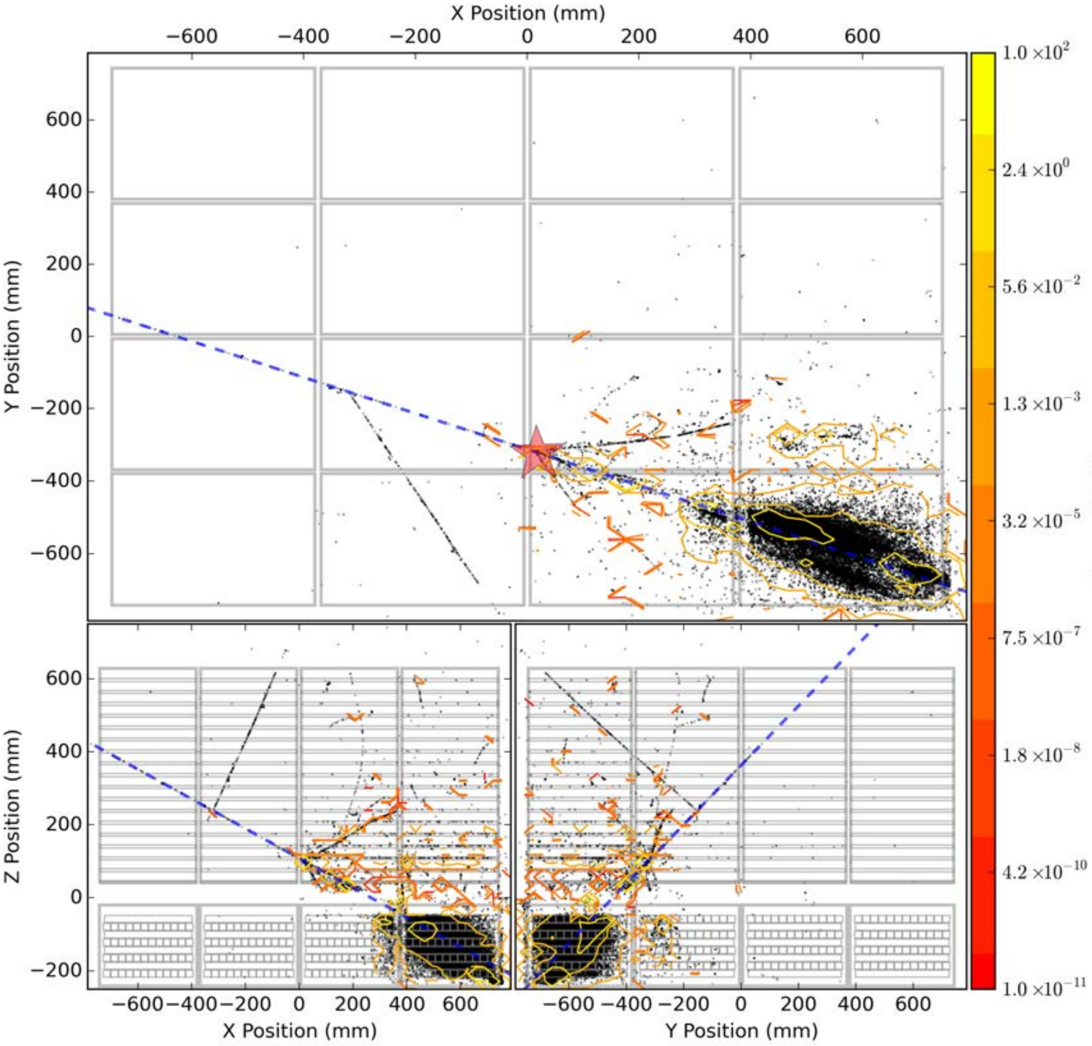

Figure 5.17: An hadronic shower in the LAT induced by a single 100 GeV proton from GEANT4 simulations [75]. Each black dot represents a daughter particle's starting position; the yellow and red contours show the energy density of the shower; the blue line is the incident direction of the proton; and the gray outline show the detector locations of the LAT's TKR and CAL; and finally the red star represents the beginning of the hadronic shower. The full shower tree is simulated using GEANT4 with a minimum cut off kinetic energy of 0.5 MeV.

We can start thinking about how the LAT measures the energy of hadronic showers by looking at the topology of an hadronic shower in the LAT. Figure 5.17 shows all of the daughter particles created from a 100 GeV proton showering in the LAT taken from the GEANT4 simulations described in § 3.3. Many of the expected behaviors described in § 5.3 are present including many particles created at the first point of inelastic scattering, a halo of low energy particles away from the shower core, and a dense core of mostly electrons and γ-rays along the shower axis containing most of the shower energy. The distribution of daughter particles is in line with Figure 5.13, dominated by low energy γ-rays and electrons but with a substantial fraction of heavier mesons and baryons. How this translates to deposited energy is very dependent on the calorimeter. In the case of the CAL, the particle distribution for daughters that deposit energy in the CAL's crystals is demonstrated in Figure 5.18. This is very different distribution than what is seen in Figure 5.13. Protons deposit a large amount of energy, but since the number count of protons in the particle distribution is low, the total fraction of deposited energy is low. Despite a larger fraction of neutrons compared to protons, they deposit very little energy in the CAL. Conversely, electrons deposit the majority of energy for these showers. This indicates that the majority of deposited energy is attributed to the EM fraction of the hadronic shower described in § 5.3. The strategy for measuring the energy of the incident proton is highly dependent on the calorimeter that is used to measure the hadronic shower.

As was established in § 3.1.2, the CAL is only $\sim 0.5\lambda_i$ at normal incidence and at horizontal incidence is closer to $\sim 3\lambda_i$–well under a typical hadronic calorimeter depth of $20\lambda_i$. Additionally, because the CAL is a homogeneous electromagnetic

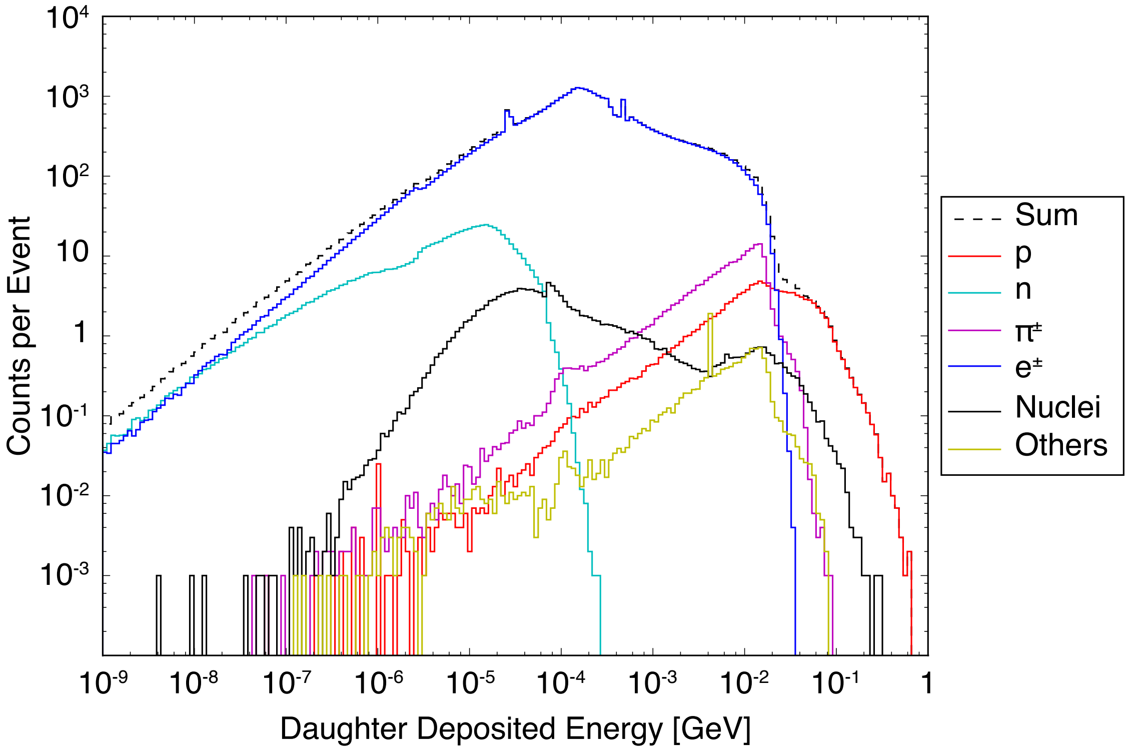

Figure 5.18: The particle distribution of particles which deposit energy in the CAL for 100 GeV proton induced hadronic showers, using 10^3 events and normalizing by event count. The full shower tree is simulated using GEANT4 with a minimum cutoff kinetic energy of 0.5 MeV.

calorimeter designed to accurately measure the energy of γ-rays, there is little hope of either capturing the entire development of an hadronic shower or being able to accurately measure the energy deposited by the non-EM component. Figure 5.15 and 5.19 shows the energy deposited in the CAL that comes from the EM component of the proton induced hadronic showers across several energies. Over 90% of the energy is from this EM component and the fraction increases as energy increases. This is due to two reasons: CsI(Tl) has a poor response to protons/neutrons which are typically used to measure the non-EM fraction and, as stated previously, the CAL under the best circumstances is too shallow to induce further hadronic cas-

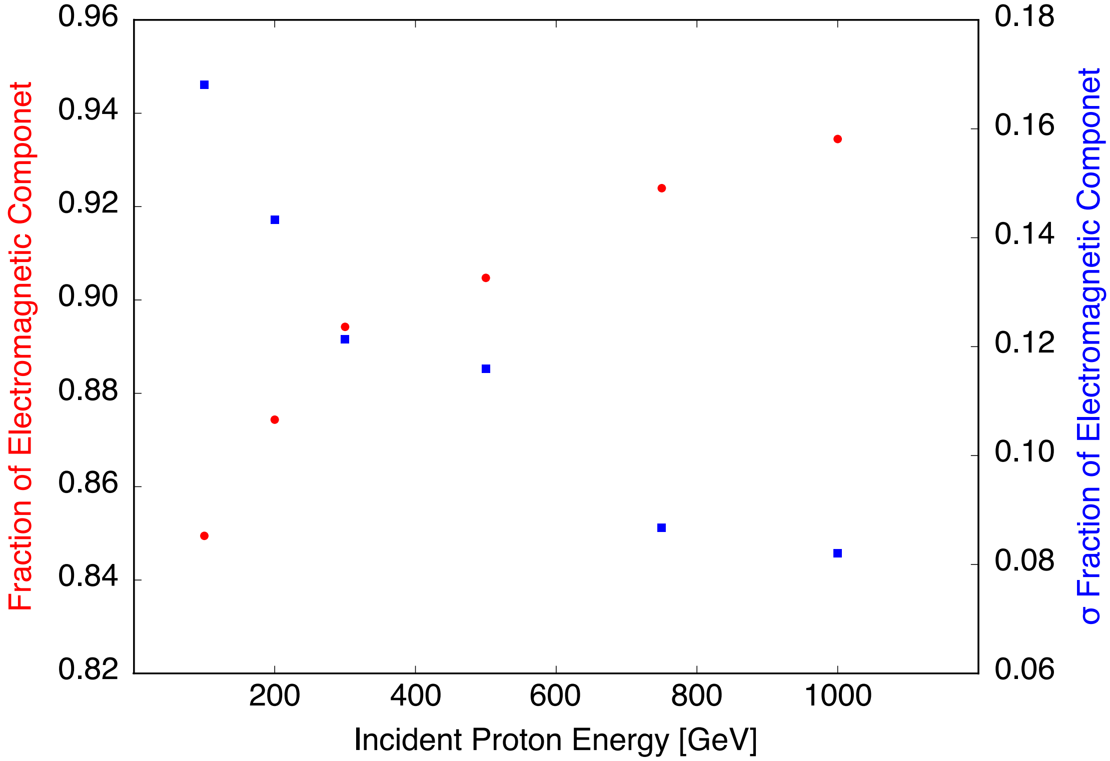

Figure 5.19: The EM fraction of the energy deposited from a proton-induced shower in the LAT versus proton incident energy from GEANT4 simulations.

cades. This is in agreement with § 5.3 where we learned that the EM fraction of hadronic showers increases as incident particle energy increases.

Additionally, shower leakage becomes problematic as incident proton energy increases. Because of the LAT's geometry, shower containment of not only the non-EM component but the important EM fraction decreases as energy increases, putting a fundamental limit on the highest energy measurable by the CAL. Shower leakage corrections can be estimated using profile fitting of Equation 5.16 and a version of the method described in § 5.2.2, although these methods are limited the maximum of the EM component is not contained within the CAL.

Despite all of these limitations, an energy measurements can still be made by the CAL. As was stated in § 5.3, an average 1/3 of the incident proton energy is converted into the EM fraction of the hadronic shower. Since the CAL is predominantly measuring the EM fraction of the hadronic shower, the energy measurement is limited by the natural stochasticity of π^0 production during proton inelastic scattering. While Figure 5.7 shows an energy resolution ∼ 10-15%, for the reason stated above, that the proton energy resolution is larger than that of electrons or γ-rays of the same energy. To counteract this effect, we actively select a class of proton events which begin showering early in the LAT, either in the bottom of the TKR or the top of the CAL and with a large energy deposit in the CAL. These two cuts on the data are: `CalEnergyRaw > 20000` and `TkrTree1ThickRLnNodes < 10` respectively called `CUT_MINIMAL_RAW_ENERGY` and `QUAL_CUT_THICKNODES`. `CalEnergyRaw` refers to the raw energy deposited in the CAL reconstructed on a crystal level as explained in § 3.2.2. We want this amount to be greater than 20 GeV which ensures the proton has inelastically scattered is above the `HI_PASS` filter threshold described in Chapter 3. `Tkr1Tree1ThickRLnNodes` refers to the number of nodes found by the tree based track finder algorithm per X_0 in the bottom and thicker layers of the tungsten foil in the TKR, which is analogous to the number of electrons and positrons or hits in the TKR in the bottom half. `QUAL_CUT_THICKNODES` has two tasks, minimizing ‘back-splash’ of electrons and positrons back into the TKR and away from the CAL, reducing energy leakage and selecting on protons that do not begin showering too high in the TKR, thereby reducing the measurement of the EM fraction of the hadronic shower.

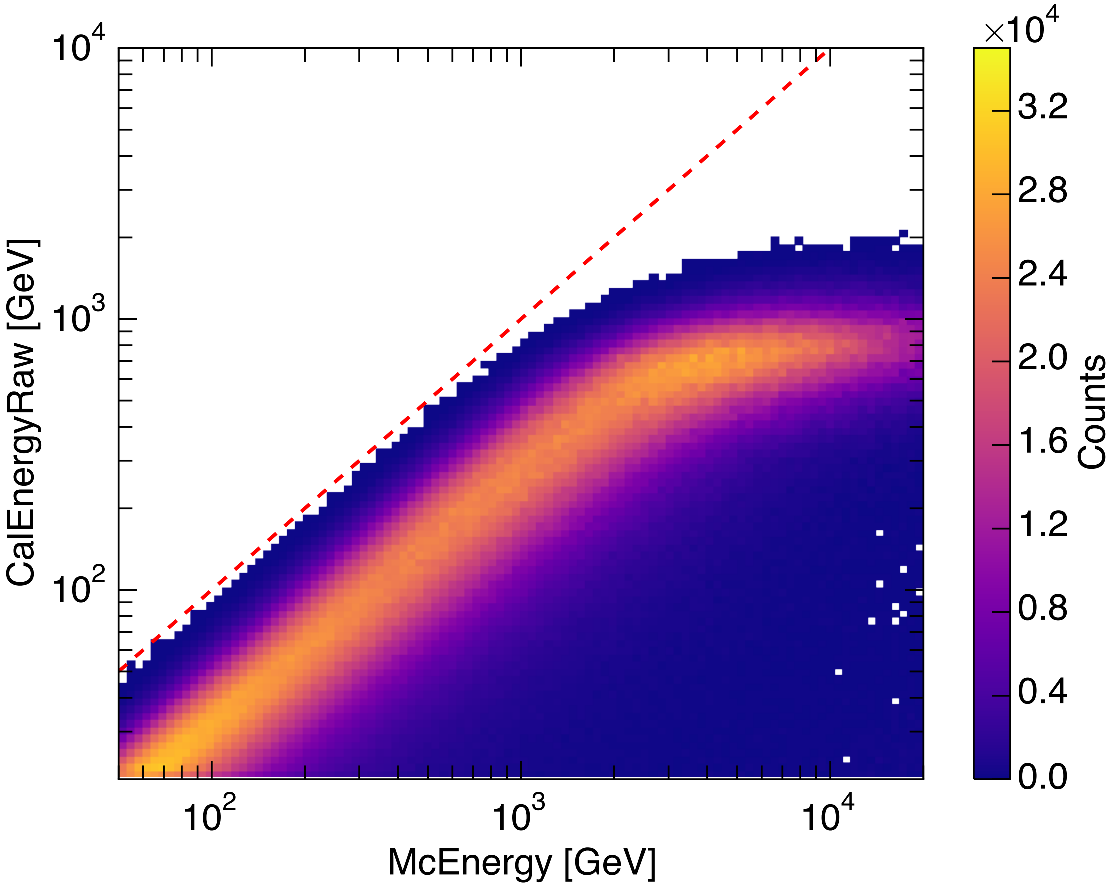

Figure 5.20: `CalEnergyRaw` versus `McEnergy` for protons from GEANT4 Monte-Carlo simulations. The simulations are run from 4 GeV to 20 TeV and cover a 4π sr solid angle. The red dashed line represents when `CalEnergyRaw` = `McEnergy`.

It is not enough to just use `CalEnergyRaw` as the energy measurement, we need to correct for geometry effects, inactive material, and energy leakage out of the CAL. Figure 5.20 shows how `CalEnergyRaw` traces the incident proton energy from GEANT4 simulations. We see a wide distribution of `CalEnergyRaw` with a mean of roughly 1/3 the incident proton energy. There is an obvious non-linearity at high energies where geometry effects due to gaps between CAL modules and leakage is an important issue.

Once we have an hadronic shower with a large EM fraction that begins close to the top of the CAL, we use the established profile fitter for γ-rays and electrons, described in § 5.2.2, to estimate the energy of the EM fraction. The energy estimator used is called `CalNewCfpCalEnergy` which uses the CAL direction, determined from a 3D moment analysis of the shower, as the measured shower axis. The reason for using the CAL direction instead of the TKR direction is because above an incident energy of 1 TeV, 'back-splash' of low energy electrons from the CAL into the TKR becomes an irreducible problem, thereby degrading the direction reconstruction from the TKR. Using the CAL direction solves this issue and ensures the quality of the energy reconstruction above 1 TeV. The profile fitter counteracts issues of shower leakage out of the CAL and shower propagation through non-detector material in the CAL and is essentially using Equation 5.16 with a $w \approx 1$. This gives a better estimate for the EM component of the hadronic shower. We apply cuts to the data based on the quality of the energy reconstruction, specifically to variables defined in Equation 5.10. When fitting the profile, S_0 and S_1 are given an acceptable range from -5 to 5. Events with S_0 and S_1 at ±5.0 have poor energy reconstruction. We remove these events with `(CalNewCfpPar0 < 4.999 && CalNewCfpPar1 > -4.999)` called `CUT_SATURATED_PARAMS` and `(CalNewCfpCalPar0 < 4.999 && CalNewCfpCalPar1 > -4.999)` called `CUT_SATURATED_CAL_PARAMS`.

We developed two additional data cuts to deal with the pernicious effect of leakage of the hadronic shower out of the CAL. The first cut requires the proton event must have a long path length through active material in the CAL of at least 20 cm using the cut `Tkr1LengthInCal > 200.0` called `QUAL_CUT_Len200`.

`Tkr1LengthInCal` estimates the geometric path length through the CAL using the best track determined from the TKR reconstitution algorithms, subtracting the amount the track that passes through gaps and non-detector material in the CAL. This cut translates to a minimum path length of 0.5 λ_i and has the effect of removing normal incidence events limiting the angular distribution to $0.9 > \cos(\theta) > 0.3$, where the minimum is determined by the maximum incidence angle where the TKR can determine a direction. We are also ensuring better shower development and

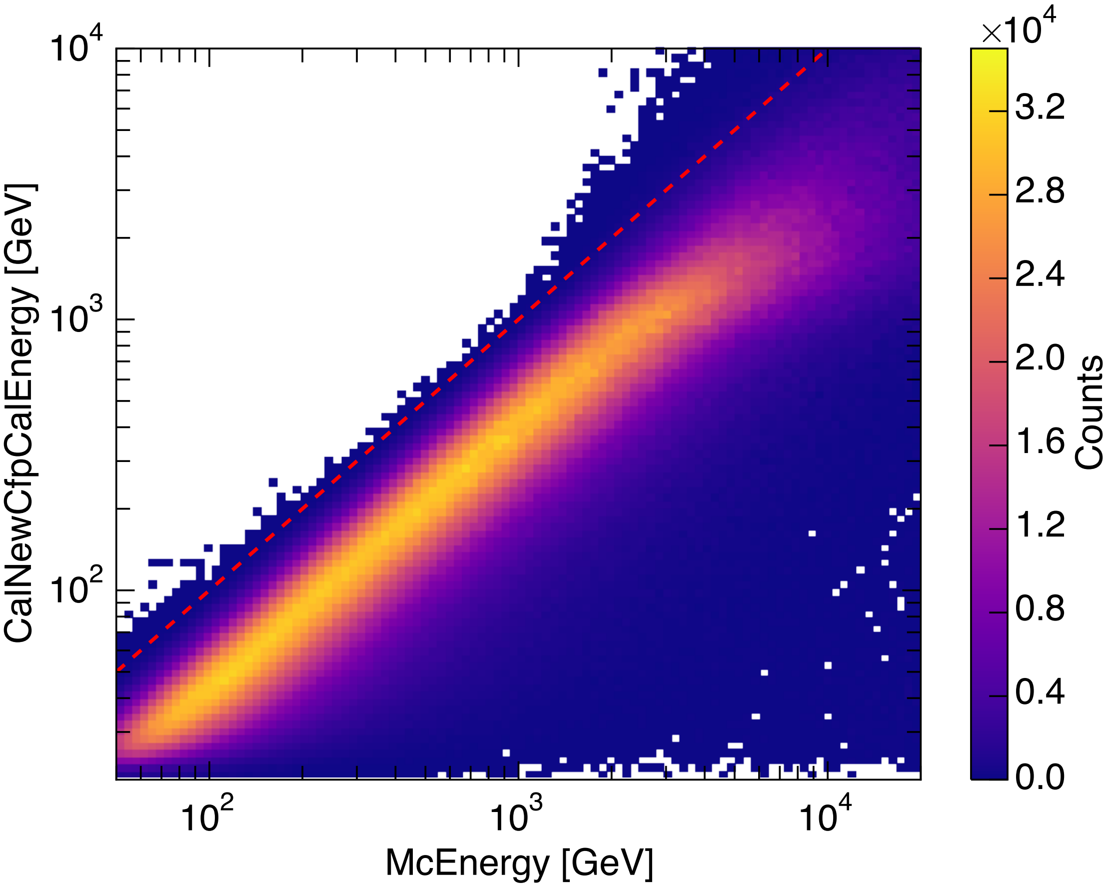

Figure 5.21: `CalNewCfpCalEnergy` versus `McEnergy` for protons from GEANT4 Monte-Carlo simulations. The simulations are run from 4 GeV to 20 TeV and cover a 4π sr angular distribution. The red dashed line represents when `CalNewCfpCalEnergy` = `McEnergy`.

reducing leakage of the hadronic shower out of the CAL. The final cut we use is `CalLeakCorr > 0.25` called `QUAL_CUT_LEAKCORR25` where `CalLeakCorr` is an attempt to characterize the fraction of the shower that leaks out of the CAL but using the profile fitter. We require that proton events have less than 25% leakage in the CAL. `CalLeakCorr` is only an estimate and tends to underestimate the fraction of shower leakage for hadronic showers because of the difference in physics between electromagnetic showers. It also accounts for shower the fraction of shower that falls in the gaps between CAL modules.

We can see the results of these cuts and the profile fitter in Figure 5.21, which shows the comparison between `McEnergy` and `CalNewCfpCalEnergy`. When compared to Figure 5.20, we see a more linear response. Additionally, leakage effects at energies above 1 TeV have been reduced. We can cover the large range of energies from $\sim$ 50 GeV to $\sim$ 5 TeV. Eventually, above $\sim$ 5 TeV the compensation for leakage begins to break down as there is not enough information on the shower contained in the CAL to effectively use the profile fitter. This systematic limitation, in contrast to statistical limitations, sets the maximum energy we can measure. Using `CalNewCfpCalEnergy` over `CalEnergyRaw` is a clear improvement, but we still have to deal with a large energy resolution due to the stochastic nature of hadronic showers and the fact that we are only measuring the EM fraction of the total shower. Figure 5.21 is essentially the response matrix that will be used to unfold the true particle spectrum in Chapter 6.

Estimating the energy resolution for protons in the LAT is a bit different than the usual method implemented by similar detectors. `CalNewCfpCapEnergy` will not

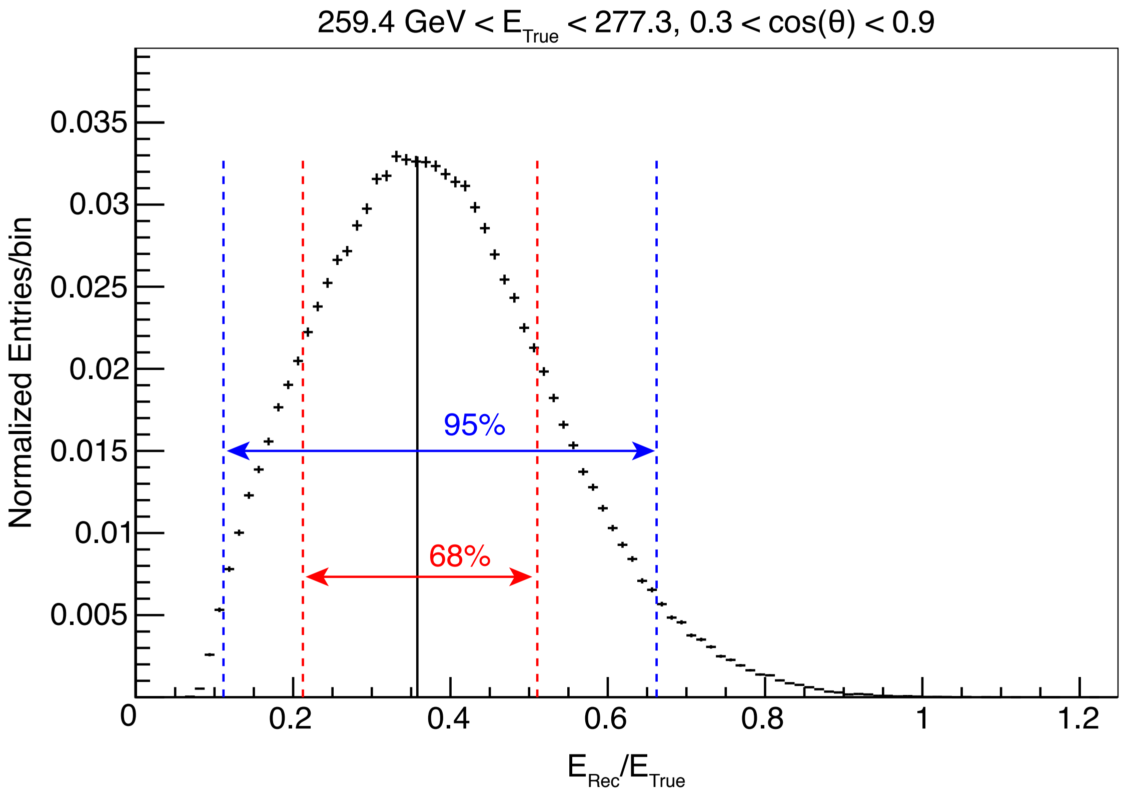

Figure 5.22: The distribution of `CalNewCfpCalEnergy/McEnergy` for a single bin in `McEnergy`. The red and blues lines represent 68% and 95% confidence interval respectively. This distribution is used to estimate the energy resolution of the LAT for protons, and is generated using GEANT4 Monte-Carlo simulations.

reconstruct the total incident energy of the cosmic ray proton and significant bias is introduced. This bias can be seen in Figure 5.22 where the peak of the energy dispersion distribution is located at ~ 0.4; typically this peak should be located near 1.0 in other detectors. Additionally, the energy dispersion distribution is asymmetric with a long tail towards high energy reconstruction. To estimate the energy resolution, one finds the energy dispersion distribution for each bin in `McEnergy` and calculates the cumulative distribution function (CDF). With the CDF, we find the mode and the 68% and 95% confidence intervals, and then divide the confidence intervals by

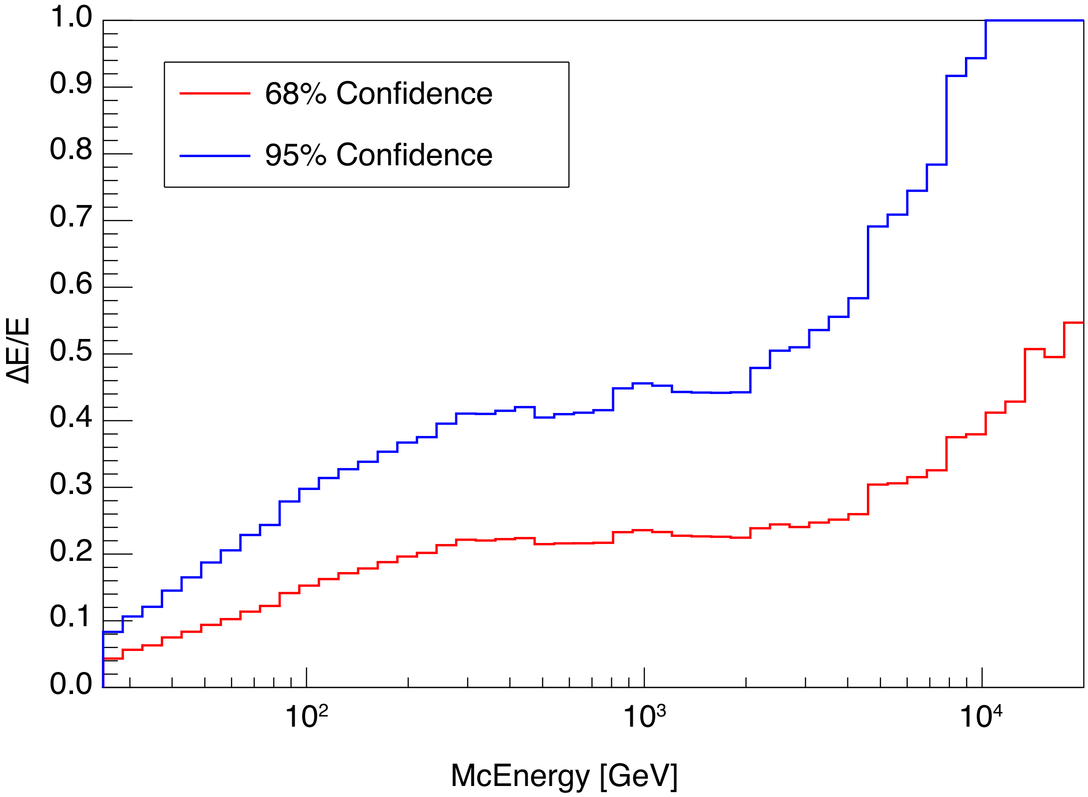

Figure 5.23: The LAT 68% (red) and 95% (blue) proton energy resolution, using all of the energy measurement cuts and using `CalNewCfpCalEnergy` as the energy estimator from GEANT4 Monte-Carlo simulations.

the mode–thereby re-centering the confidence interval around 1.0. These re-centered 68% and 95% confidence intervals is the estimated energy resolution for protons in the LAT seen in Figure 5.23. It should be noted that the energy range in Figure 5.23 is determined by the energy range of the proton simulations described in § 3.3 and does not represent the final energy range of this analysis. The 68% confidence interval is around 20% for a large range of incident proton energies and increases sharply above a few TeV to 70%. For the 95% confidence interval, the asymmetry in the Figure 5.22 becomes apparent with energy resolution of around 40% from 40 GeV to 2 TeV and then again rising sharply to 100% energy resolution at 10

TeV. Therefore, the largest energy of incident cosmic-ray protons that the LAT can confidently measure is 10 TeV. Above 10 TeV, there is not enough information on the hadronic shower contained within the LAT's CAL and natural stochasticity of hadronic showers does not allow for the estimate of the incident proton's energy. As stated in § 3.1.4 the `HI_PASS` limits the minimum energy is around 50 GeV. Together this sets the energy range of this cosmic-ray proton analysis from 50 GeV to 10 TeV. Additionally, the estimated energy resolution shown in Figure 5.23 is important because it is used to determine true energy binning when unfolding the true spectrum in Chapter 6.

In summary, despite significant challenges of using the CAL, an electromagnetic homogeneous calorimeter not designed for such a purpose, we can still estimate the energy of cosmic-ray protons. Using the Pass 8 profile fitting method described in § 5.2.2, we estimate the EM fraction of the proton induced hadronic shower correction for effects from energy leakage and shower development through inactive material. We developed a set of cuts on the data which further reduces events with large shower leakage, poor energy reconstruction, and the start of shower too high in the TKR. With all of these efforts we estimate the cosmic-ray protons' incident energy from 50 GeV to 10 TeV with a 68% confidence energy resolution ranging from 20% to 40%. Using this energy measurement of cosmic-ray protons we can begin to develop the spectral analysis and measure the cosmic-ray proton spectrum.

Chapter 6: Spectral Analysis

The goal of the spectral analysis is to produce a differential energy spectrum from flight data across the LAT energy range and to estimate largest systematic uncertainties associated with this analysis. The first step in our spectral analysis is to establish our event selection using the cuts developed in Chapter 4 and Chapter 5 to produce a data set of well reconstructed cosmic-ray protons with low residual contamination and large EM fraction of the resultant hadronic shower from both GEANT4 Monte-Carlo simulations and flight data. Using GEANT4 Monte-Carlo simulations described in § 3.3 we produce instrument response functions (IRFs) such as the acceptance, contamination, and response matrix. The next step is to extract the differential energy spectrum via unfolding the true counts spectrum from the flight data using the response matrix and then using the acceptance and contamination to correct for instrumental effects. Because of the limitations of the LAT when measuring hadronic showers and the fact that our IRFs are estimated using simulations, we need to understand the associated systematic uncertainties with regards to the acceptance, energy estimation, and GEANT4 Monte-Carlo simulations. These systematic uncertainties are then integrated into the measured spectrum with the statistical uncertainties for the final results of the LAT cosmic-ray proton spectral measurement. We then fit the measured spectrum including both statistical and systematic uncertainties using a broken power-law and pose three astrophysical interpretations for the spectral fit.

6.1 Event Selection

Using the knowledge developed in Chapter 4 and Chapter 5 we develop an event selection to build data sets from GEANT4 Monte-Carlo simulations and flight data to use in our spectral reconstruction. These data sets will contain protons with a well reconstructed direction from both the TKR and CAL, low residual contamination from other cosmic-ray populations, and an accurate energy estimation with a large EM fraction of the hadronic shower. The majority of events passing the `HI_PASS` filter are cosmic rays and, combined with the large flux for cosmic-ray protons over 7 years of flight, produce a large data set with very low statistical uncertainties across the entire LAT energy range. Figure 6.1 shows the number of integrated counts over the LAT energy for cosmic-ray protons. The proton flux used is fit from *AMS-02* using a broken power-law model extended to 10 TeV. The counts are calculated using 7 years of elapsed time with an average 75% live-time fraction and acceptance values ranging from 2.0 m^2 sr to 0.1 m^2 sr. The acceptance is a measure of the instrument's efficiency in detecting particles over an area (m^2) and solid angle (sr). An event selection with an acceptance of 0.1 m^2 sr produces over 10,000 events at the highest energies and therefore statistical uncertainties are around 1%, which are well below systematic uncertainties. We can therefore select

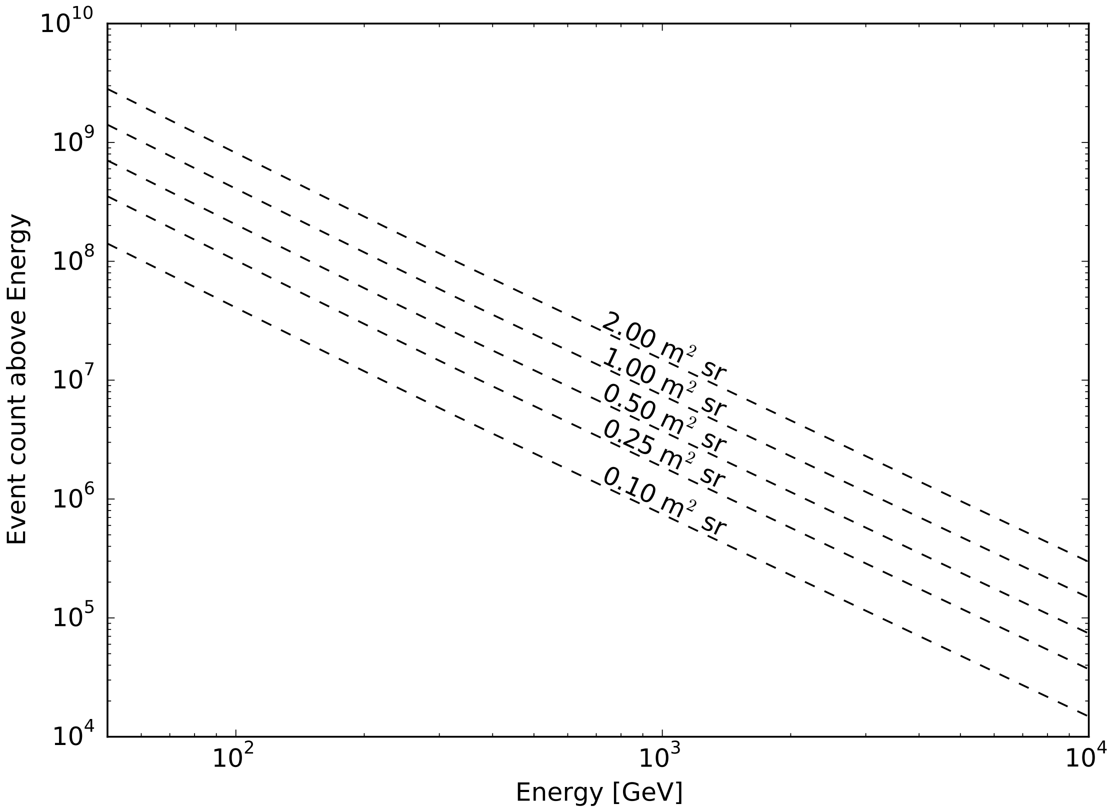

Figure 6.1: The integral counts for different values of acceptance, ranging from 2.0 m^2 sr to 0.1 m^2 sr, from 50 GeV to 10 TeV. The cosmic-ray proton flux is measured from a fit from *AMS-02* data, shown in Figure 7.1, and extended to 10 TeV. We also assume 7 years of elapsed time with 75% live-time fraction [5].

a small subset of protons with desirable event topologies that improve the energy resolution and still reconstruct the cosmic-ray proton spectrum. All variables and cuts are described in Appendix I and Appendix II.

The first set of cuts require the event has triggered and passes the `HI_PASS` filter. This cut is defined as:

```
CUT_TRIGGER_FILTER =
(GltGemSummary&0x20) == 0 && (GltGemSummary&0x40) == 0
&& FswGamState == 0
```

where the first and second term require no periodic or solicited triggers and the last term requires the `GAMMA` filter not activated. Together these cuts ensure the event has passed the `HI_PASS` filter.

The second set of cuts require a track to be found and at least 20 GeV energy deposited in the CAL. This cut is defined by

```
CUT_TRACK_ENERGY = TkrNumTracks > 0 && CalEnergyRaw > 20000.
```

The third set of cuts requires that the track is well reconstructed and is defined by

```
CUT_TRACK_RECON = WP8CTPSFTail > 0.5 && CalTrackAngle < 0.3.
```

`WP8CTPSFTail` is a multivariate classifier variable which is trained on simulations where signal is defined as a well reconstructed track such that the difference between TKR and MC directions is under 1 degree. `CalTrackAngle` is the difference between the CAL direction and the TKR direction and we require the CAL direction and TKR direction to have good agreement; with a difference under 20° degrees.

We then apply the final set of cuts defined in Chapter 4 and Chapter 5 which are designed to remove nuclei and improve energy resolution. We can see the results of successive cuts on the proton acceptance in Figure 6.2, using the same acceptance calculation described in § 6.3. Clearly the well reconstructed direction and improved

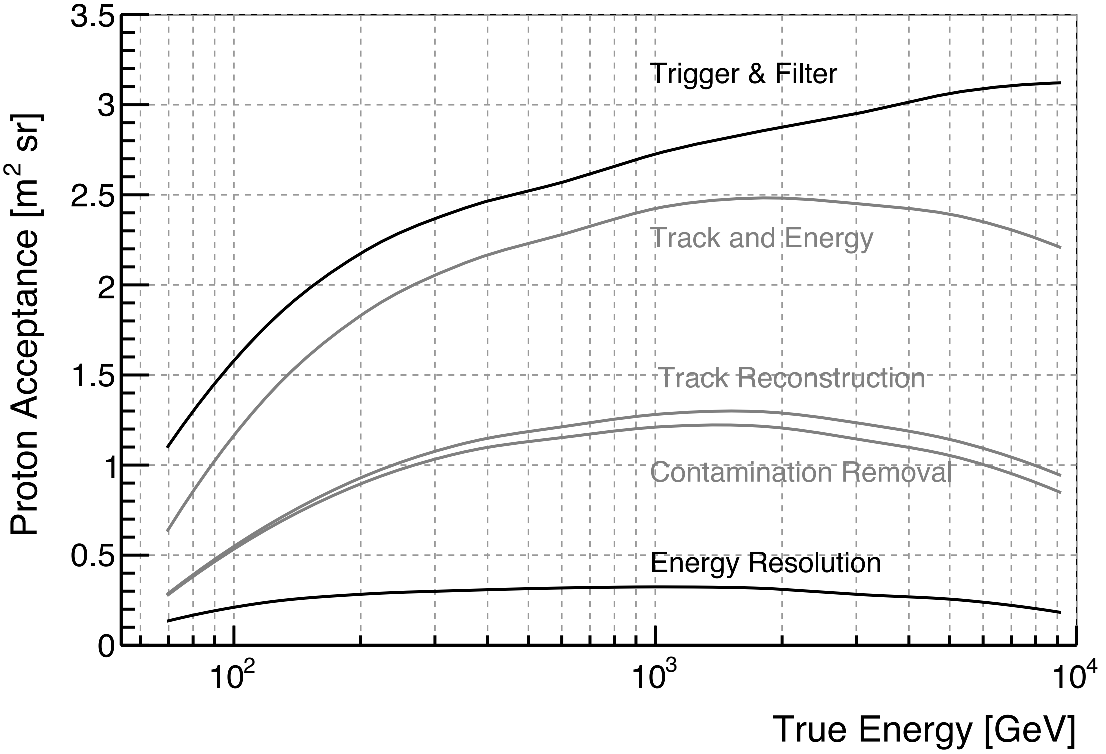

Figure 6.2: The change in the acceptance from successive cuts from the event selection including trigger, track and energy, minimum distance, direction reconstruction, and energy resolution cuts.

energy resolution cuts have the largest effect on the acceptance. Despite the large reduction in the acceptance, the cosmic-ray proton flux is high enough to have more than enough events to measure the proton spectrum. We find 183,769,600 events after the proton event selection. This is a large enough sample such that statistical uncertainties fall below 3% across all energy bins and the measurement is dominated by systematic uncertainty. We also developed this event selection to maintain a flat acceptance across as much true energy as possible in order to improve sensitive to any spectral features.

6.2 Event Rate

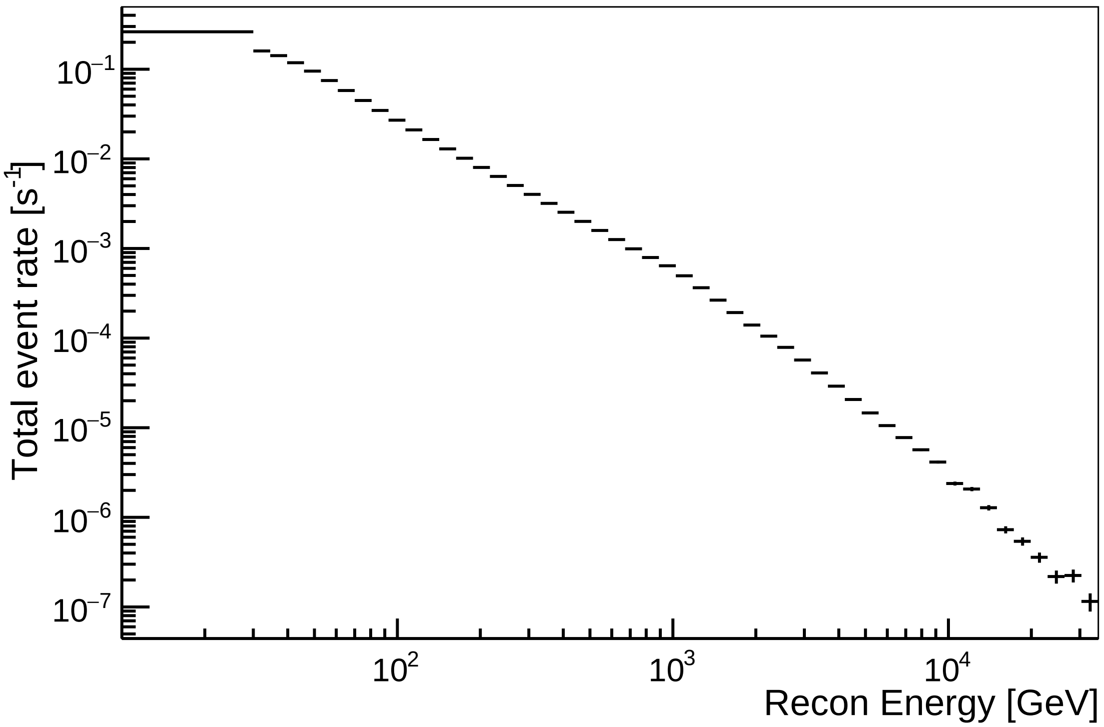

Figure 6.3: The proton event rate in 50 bins of reconstructed energy from 30 GeV to 35 TeV with an underflow bin from 10 GeV - 30 GeV using 7 years of flight data with a measured live-time of 5.22 years.

To build the event rate, we use 7 years of flight data from August 4, 2008 to July 30, 2015. The reconstructed energy binning covers from 30 GeV to 35 TeV to encompass the entire energy range with an additional underflow bin from 10 GeV to 30 GeV, which is not used in the spectral reconstruction. It is beneficial to reconstruct an event rate because the background subtraction can be calculated in event rate and therefore there is no dependence of the live-time. To convert from a counts spectrum to an event rate, we need to calculate the live-time of this dataset.

To calculate the live-time, we use a variable called `GltGemLiveTime` which is measured using the *Fermi* on-board clock in units of 'ticks' from the start of the mission. The live-time of the LAT is described in § 3.1.4. Each tick is 50 ns long. We measure the difference between the maximum and minimum `GltGemLiveTime` for each run, multiply that value by 50 ns and add up the sum to find the total live-time of the dataset. We find a total live-time of 5.22 years for the entire 7 years of flight data. Figure 6.3 shows an example event rate used for this analysis.

6.3 Instrument Acceptance

The acceptance is a measure of the instrument's efficiency in detecting particles over an area (m^2) and solid angle (sr). We use dedicated proton simulations calibrated with beam-line and flight data to estimate the acceptance. As stated in § 3.3, each proton simulation runs from 4 GeV to 20 TeV over 4π sr, with a spectral index of -1.5, a counts flux of 1×10^{-5} particles/(m^2 s sr) over 5×10^6 seconds. This translates to, on average, 3769.91 generated events per run, as shown in Equation 6.1.

$$(1 \times 10^{-5}/(\mathrm{m}^2\ \mathrm{s}\ \mathrm{sr}))\ \times\ (4\pi\ \mathrm{sr})\ \times\ (6\ \mathrm{m}^2)\ \times\ (5 \times 10^6\ \mathrm{s}) = 3769.91 \tag{6.1}$$

We calculate the acceptance by finding the ratio of the number of events that pass our cuts and the number of events generated for each bin in true energy (essentially the efficiency of the event selection) multiplied by the generation area and solid angle.

$$A_i = A_{Gen} \times \Omega_{Gen} \times \frac{N_{Pass,i}}{N_{Gen,i}} \tag{6.2}$$

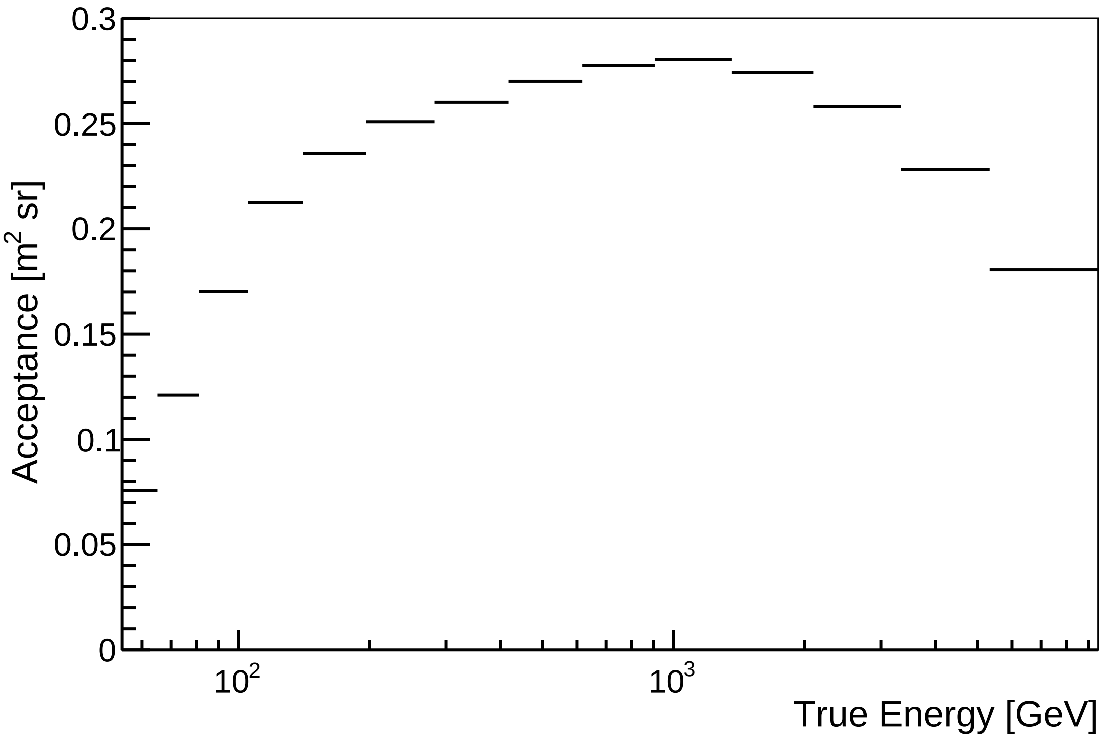

Figure 6.4: The proton acceptance, in units of m^2 sr, for the LAT. The acceptance is used to correct for instrumental effects and is important in reconstructing differential energy flux. The acceptance is estimated over the true energy.

where A_i is the acceptance for bin i, A_{Gen} is the generated area of 6 m^2, Ω_{Gen} is generated solid angle in sr, $N_{Pass,i}$ is the number of events that pass the event selection in bin i, and $N_{Gen,i}$ is the number of events generated in bin i. To find the number of generated events per bin in terms of the dedicated proton simulation, we integrate the counts spectrum from the minimum energy, $E_{i,min}$, to the maximum energy, $E_{i,max}$, for that bin.

$$Q_{Gen,i} = \int_{E_{i,min}}^{E_{i,max}} E^{-\gamma} dE = \frac{(E_{i,min}E_{i,max})^{-\gamma}(E_{i,max}E_{i,min}^{\gamma} - E_{i,min}E_{i,max}^{\gamma})}{1-\gamma} \tag{6.3}$$

$Q_{Gen,i}$ is the particle flux for bin i in units of counts per m^2 s sr. Relating $Q_{Gen,i}$ to $N_{Gen,i}$ can be done with Equation 6.4.

$$N_{Gen,i} = Q_{Gen,i} \times A_{gen} \times \Omega_{gen} \times F_{gen} \times t_{gen} \tag{6.4}$$

From this we can simplify Equation 6.2 to:

$$A_i = \frac{N_{Pass,i}\ (\gamma - 1)}{F_{gen}\ t_{gen}\ (E_{i,min}E_{i,max})^{-\gamma}(E_{i,max}E^{\gamma}_{i,min} - E_{i,min}E^{\gamma}_{i,max})} \tag{6.5}$$

where F_{gen} is the generation particle flux in counts per m^2 s sr, t_{gen} is the generation time, γ is the generation spectral index, $E_{i,min}$ is the minimum energy for bin i, $E_{i,max}$ is the maximum energy for bin i, and $N_{Pass,i}$ is the number of events that pass the event selection.

Using Equation 6.5, we can find the acceptance for each bin in true energy. Figure 6.4 shows the result of the acceptance calculation using the true energy binning from 5.23. We see an acceptance of 0.08 m^2 sr in the lowest energy bin, due to event rate loss from the `HI_PASS` filter. The `HI_PASS` operates on `CalEnergyRaw` and not the true energy of the proton effectively shifting minimum energy from 20 GeV to 54 GeV. The acceptance rises to a maximum acceptance of 0.28 m^2 sr at 1 TeV and then falling to 0.16 m^2 sr at 9.5 TeV, which is caused by loss of events passing containment cuts described in § 5.4. This acceptance will be used in the calculation of differential energy flux J_E in § 6.5.

6.4 Residual Contamination

The residual contamination is dominated by cosmic-ray electrons as shown earlier in Figure 4.11. Figure 4.11 is produced using the BKG simulation for which

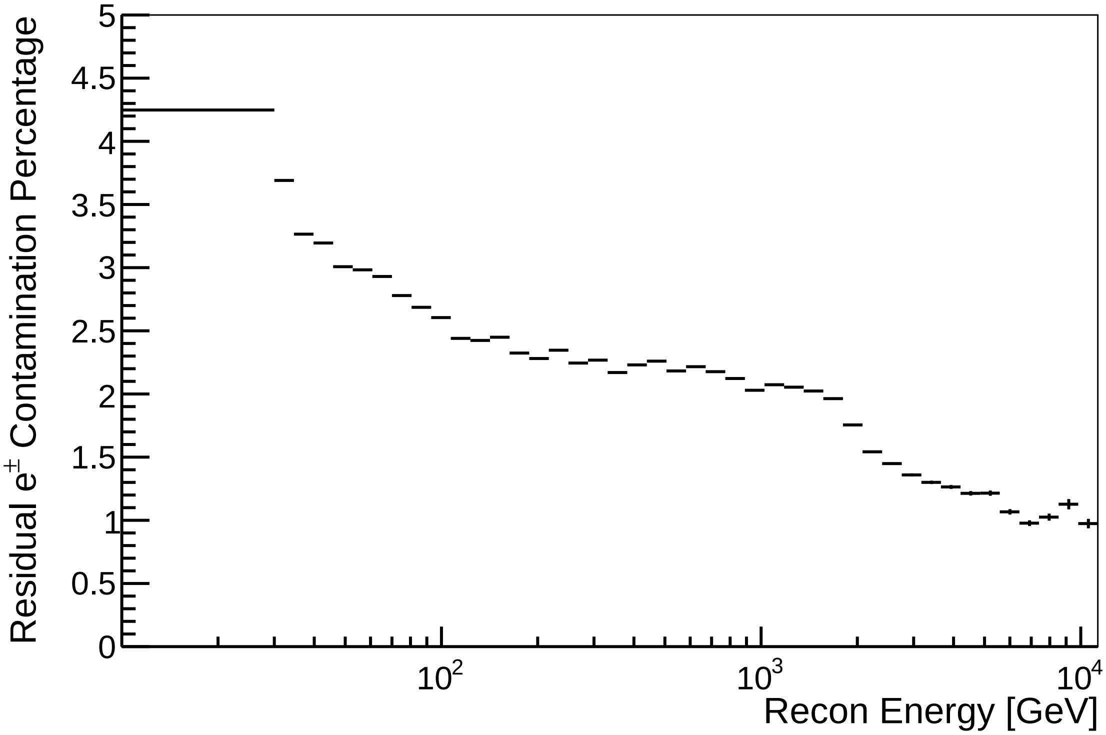

Figure 6.5: The residual contamination of the proton data due to electrons. Estimated using proton and electron simulations weighted to realistic cosmic-ray spectra. The residual contamination is estimated over the reconstructed energy.

electrons are only simulated to 1 TeV. To find the contamination beyond 1 TeV, we used the dedicated electron simulation for which electrons are simulated to 10 TeV. Using the electron + positron spectrum measured by *AMS-02*, a power-law with a spectral index of $\gamma = -3.170$, we weight the dedicated electron simulation in order to create a realistic spectrum [105]. We compute an electron estimated live-time estimate for the electrons and, by comparing the weighted event rate to the BKG simulation, we can create an electron event rate in reconstructed energy space from 30 GeV to 20 TeV. The same procedure is applied to protons. Using the proton spectrum measured by *AMS-02*, a broken power-law with a primary spectral index γ = -2.849, a break at $E_B = 336$ GeV, and break index of $\Delta\gamma = 0.133$, we weigh the dedicated proton simulation in order to create a realistic spectrum [5]. We compute a proton estimated live-time estimate for the electrons and by comparing the weighted event rate to the BKG simulation, we can create a proton event rate in reconstructed energy space from 30 GeV to 20 TeV. Both of the simulated cosmic-ray spectra assume a temporally static spectrum because we are above energies which would be effected by solar modulation.

To find the residual electron contamination shown in Figure 6.5, we apply the event selection to both proton and electron Monte-Carlo simulations and simply take the ratio between the simulated proton and electron event rates. The residual contamination is largest at lower energies, reaching almost 4% but falls to 2% at 1 TeV in reconstructed energy, due to the difference in spectral indices between the cosmic-ray proton and electron spectra. Systematic uncertainty associated with the electron contamination could be computed, but since contamination is much lower than any other uncertainty discussed in § 6.8, it can be effectively ignored. The contamination is low enough, below systematic uncertainties associated with acceptance and energy estimation discussed in § 6.8, and therefore not a dominant contribution to the total uncertainty measurement.

6.5 Spectral Reconstruction

Because the LAT's CAL energy deposition from cosmic-ray protons is dominated by the EM component of the hadronic shower, the reconstructed energy will have a significant bias from the true energy as seen in Figure 5.22. Because of this and the wide energy resolution seen in Figure 5.23, we are unable to measure a spectrum on an event-by-event basis as is typically done in other cosmic-ray experiments [1–4]. We reconstruct the cosmic-ray proton spectrum on a statistical basis by unfolding the true energy counts spectrum from a reconstructed energy counts spectrum via a response matrix and the unfolding software TUnfold.

6.5.1 The Inverse Problem

The inverse problem is a well studied class of statistical problems. Let us assume one wants to find an underlying physical quantity by convolving a model through a detector's response matrix, resulting in a measurement. To find the physical quantities, the naive assumption would be to invert the response matrix, and apply to measurements to find the physical quantities, but this assumption is flawed as will be discussed. Given an observable quantity ν_i for bin i with N bins correlated with a true quantity μ_j for bin j with M bins, we can use a response matrix R_{ij}, which translates the observable quantity to the true quantity, shown in Equation 6.6 [106]. It is assumed that the observed quantity and the response matrix are known to a degree where statistical uncertainties are negligible but the true quantity is unknown.

$$\nu_i = \sum_{j=1}^{M} R_{ij}\ \mu_j \tag{6.6}$$

where the response matrix element R_{ij} is

$$\begin{aligned} R_{ij} &= \frac{P(\text{observed in bin i and true in bin j})}{P(\text{true value in bin j})} \\ &= P(\text{observed in bin i} \mid \text{true in bin j}) \end{aligned} \tag{6.7}$$

The response matrix with element R_{ij} is the probability that an event will be found with the observed quantity in bin i given the true value was in bin j [106, 107]. The response matrix includes true events which are not observed by a detector. This generalized form has the benefit that there are no assumptions on the true quantity distribution. It should also be noted that N and M do not have to be equal; the response matrix does not have be a square matrix. Summing over the observable index i, one can have a measure of the average efficiency in true energy:

$$\sum_{i=1}^{N} R_{ij} \equiv \epsilon_j \tag{6.8}$$

The efficiency is essentially the acceptance described in § 6.3 without angular information included. Additionally, this form can be extended to multiple observed quantities but for this generalization we are assuming one observed quantity primarily because for the cosmic-ray proton spectral measurement we only use one observed quantity, the reconstructed energy.

To include a background for the observed quantity, one simply amends Equation 6.6 to be

$$\nu_i = \sum_{j=1}^{M} R_{ij}\ \mu_j + \beta_i \tag{6.9}$$

where β_i uses the binning of the observed quantity [106, 107]. One background is included in this generalization, but in principle multiple backgrounds can be included.

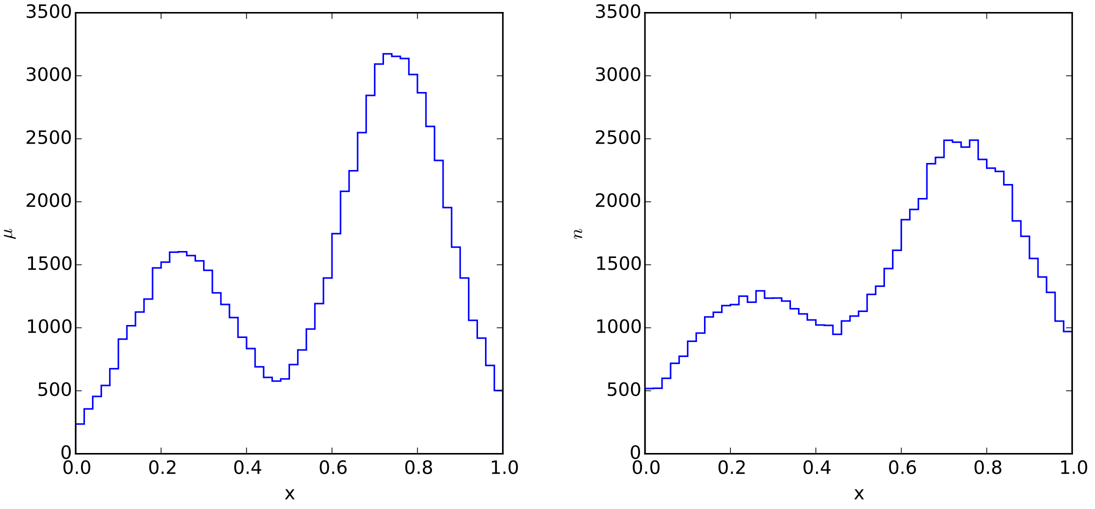

(a) True Distribution μ

(b) Data Distribution n

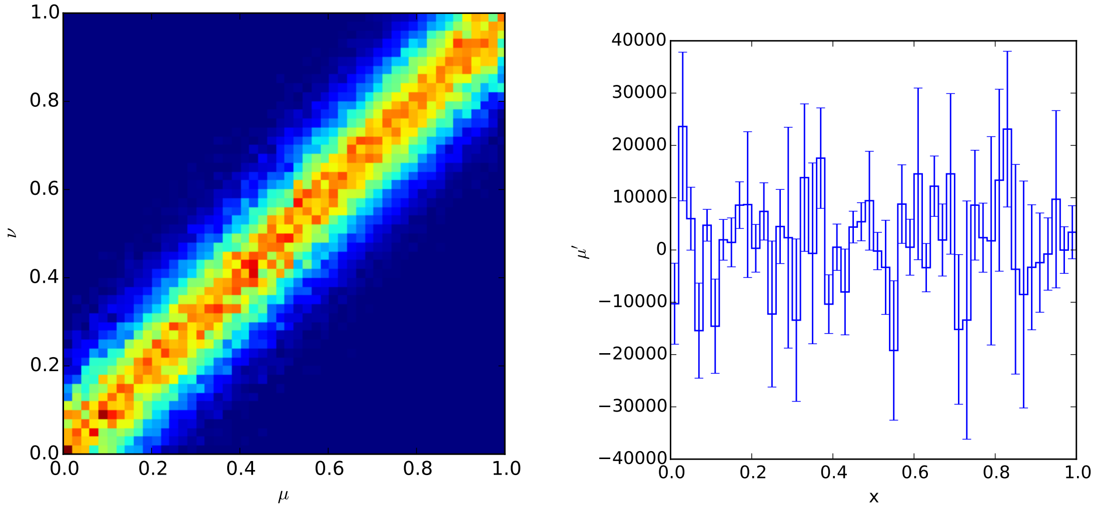

(c) Response Matrix

(d) Unfolded Distribution $\mu' = R^{-1}\nu$

Figure 6.6: A toy model of unfolding by finding the true distribution μ' by inverting the response matrix R and taking the dot product with the observed distribution ν. Using a double Gaussian function as the true distribution and adding noise into the response matrix with a Gaussian distribution with $\mu = 0$ and $\sigma = 0.2$.

Typically R_{ij} and β_i are determined from either calibration of the detector or Monte-Carlo simulations. In the case of the LAT, the response matrix is found using dedicated proton and electron Monte-Carlo simulations which have been calibrated using beam-test data prior to launch, described in § 6.8. The background estimation is described above in § 6.4. We can generalize even further by using vector forms for ν_i, μ_j, R_{ij}, and β_i where:

$$\vec{\nu} = R\vec{\mu} + \vec{\beta} \tag{6.10}$$

A seemingly obvious solution to finding $\vec{\mu}$ is to invert R such that:

$$\vec{\mu}' = R^{-1}(\vec{\nu} - \vec{\beta}) \tag{6.11}$$

making the assumption that $M = N$. It is important to propagate the statistical uncertainty associated with the observed quantity, even if it is small. Defining V_{ij} and U_{ij} as the covariance matrices of the observed $\vec{\nu}$ and true distributions $\vec{\mu}$ as such:

$$U_{ij} = \sum_{k=1}^{N} (R^{-1})_{ik}(R^{-1})_{jk}\nu_k \tag{6.12}$$

We can develop a simple example to examine whether inverting the response matrix is sound. Creating a true distribution, Figure 6.6(a), a data distribution, Figure 6.6(b), and response matrix linking the true and measured distributions, 6.6(c), we can use Equation 6.11 to find the 'unfolded' distribution μ'. The data distribution n is generated through a different set of random variables than the response matrix and the true distribution. The unfolded data distribution, Figure 6.6(d) clearly shows that using Equation 6.11 does not recover the true distribution. This happens because the inverted response matrix exacerbates small structures present in the data distributions. Since the data distribution is generated from a different set of random numbers, small statistical fluctuations exist and the inverted response matrix artificially blows up these fluctuations as is evident in 6.6(d). Additionally, inverting the response matrix is unfavorable because it requires $N = M$ and the response matrix to be not singular. These requirements are atypical in most detectors, further disfavoring inverting the response matrix to find the true distribution [106, 108, 109]. Therefore a more careful treatment needs to be considered. Two such methods are forward folding and unfolding–each with their own benefits and drawbacks.

6.5.2 Forward Folding

One solution to the inverse problem is forward folding. Using the same notation as the previous section, we can define a χ^2 as a function of the measured data, n, the response matrix, R_{ij}, and the true distribution, μ_i, and the inverse of the covariance matrix of the data,$\text{cov}[n_i, n_j]^{-1}$, and any background, β_i:

$$\chi^2(\vec{\mu}) = \sum_{i,j=1}^{N} \left((R_{ij}\mu_i + \beta_i) - n_i\right) \text{cov}[n_i, n_j]^{-1} \left((R_{ij}\mu_j + \beta_j) - n_j\right). \tag{6.13}$$

Equation 6.13 essentially minimizes the differences between the measured data and the true distribution folded through the response matrix. The minimization can be done with the least-squared methods, for example MINUIT [110, 111]. In order to find the true spectrum, we have to account for instrument effects from the acceptance of the detector. Assuming that μ takes the form of

$$\mu_i = A_i \times \Phi_i(q) \times \Delta(x_i) \tag{6.14}$$

Name	Functional Form	No. of Free Parameters
Power-law	$N_0\left(\frac{E}{E_0}\right)^{\gamma}$	3
Broken Power-law	$N_0\begin{cases}(E/E_b)^{\gamma_1}, & E < E_b\\ (E/E_b)^{\gamma_2}, & E > E_b\end{cases}$	4
Smoothly Broken Power-law	$N_0\left(\frac{E}{E_0}\right)^{\gamma_1}\left(1+\frac{E}{E_b}^{\frac{\gamma_1-\gamma_2}{\beta}}\right)^{-\beta}$	6

Table 6.1: Table of example spectral models commonly used in high-energy astrophysics. The name of the function, functional form, and number of free parameters are shown.

where

$$\Phi_i(q) = \frac{\int \Phi(x,q)dx}{\Delta x_i}. \tag{6.15}$$

A_i is the acceptance, $\Phi_i(q)$ is the intrinsic distribution before instrumental effects, and x_i is the true quantity, for instance the energy of the cosmic-ray [112, 113]. $\Phi(x,q)$ takes an assumed functional form with parameters q and 6.1 shows a few examples of different functional forms typically used in high-energy astrophysics.

Forward folding is a robust method for determining the true distribution from an observed distribution. With no regularization, forward folding does not introduce any uncertainty into the reconstruction [113]. The formulation is simple enough for one to build their own forward folding algorithm and to check errors and performance of the algorithm.

Unfortunately, forward folding has a number of drawbacks. Forward folding does not ‘unfold’ the spectrum but merely finds the best parameters of the model which recreate the measured distribution. Of course using the fitted parameters with the model can give the true distribution. Forward folding is dependent on whether the true distribution can be easily modeled. If the true distribution is complicated, unknown, or requires many free parameters, fitting can be difficult [112, 113]. In the case of the cosmic-ray proton spectrum, the behavior of the spectrum above a few TeV is not well constrained by other cosmic-ray measurements [1–5]. We do not want to lose sensitivity to any unknown spectral features by using a model that would not include said spectral features. To include any unknown features would require many free parameters with far more complicated models of Galactic propagation, re-acceleration, diffusion, or interactions. Therefore we would like a method that is as model independent as possible. The most common method is unfolding.

6.5.3 Unfolding

As seen previously, inverting the response matrix leads to large variations in the ‘unfolded’ distribution. One method to correct this is to impose a measure of smoothness on the estimation of the true distribution called regularization. Using the χ^2 from Equation 6.13 developed in the forward folding section, there exists a phase-space of possible true distributions with agreement between observed distributions and measured data [106, 108]. This acceptable phase space is defined by

$$\chi^2(\vec{\mu}) \leq \chi^2_{min} + \Delta\chi^2. \tag{6.16}$$

We also need to define a regularization function, $S(\mu)$, which is a measure of the smoothness of the unfolded distribution. Using a Lagrange multiplier, we can combine Equation 6.16 and the regularization function and find

$$\mathcal{L} = \chi^2(\vec{\mu}) + \alpha S(\vec{\mu}) + \lambda \left[n_{tot} - \sum_{i=1}^{N} \nu_i \right] \tag{6.17}$$

where α is known as the regularization parameter, λ is a Lagrange multiplier and the final term is used to ensure the unfolded distribution has the same number of entries as the data distribution [107, 114].

There are several choices for the regularization function $S(\mu)$ including Tikhonov, maximum entropy, or cross-entropy [115–117]. For this analysis we use Tikhonov regularization because it is common in unfolding steeply falling spectra and is the method used in our preferred software tool for performing unfolding. [114]. This analysis uses the software package TUnfold included in CERN's ROOT particle physics software to perform unfolding. TUnfold is ideal for our needs for several reasons. It is already included in ROOT, it has a robust choice of settings accounting for complex binning configurations, choice of regularization terms, propagation of statistical and systematic uncertainties, and simple integration with ROOT's native data products [110].

Tikhonov regularization has the regularization function take the form of

$$S(f(y)) = -\int \left(\frac{d^k f(y)}{dy^k} \right)^2 dy. \tag{6.18}$$

Essentially, it forces the unfolded distribution to be smoothed in terms of the derivative, curvature, or change of curvature. For the discretized case, $S(\vec{\mu})$ takes the form of

$$S(\vec{\mu}) = \begin{cases} -\sum_{i=1}^{M-1} (\mu_i - \mu_{i+1})^2, & k = 1 \\ \\ -\sum_{i=1}^{M-2} (-\mu_i + 2\mu_{i+1} - \mu_{i+2})^2, & k = 2 \\ \\ -\sum_{i=1}^{M-3} (-\mu_i + 3\mu_{i+1} - 3\mu_{i+2} + \mu_{i+3})^2, & k = 3 \end{cases} \tag{6.19}$$

where k=1 refers to the derivative, k=2 refers to the curvature, and k=3 refers to the change of curvature [115]. TUnfold uses Tikhonov regularization with the least squared minimization and two methods for choice of regularization strength: L-curve scan and minimizing global correlation coefficients [108, 114].

The L-curve scan method finds the maximum between $L_x = \log_{10} \chi^2$ from Equation 6.13 and $L_y = \log_{10} S(\vec{\mu})/\alpha$. L_x test the agreement between the observed distribution with the data and L_y test the agreement of the regularization. Unfolding is repeated over different values of $\log_{10} \alpha$, thus creating a curve of L_x versus L_y. The point of maximum curvature is found and determined to be the optimal choice of α [114, 118].

The minimizing global correlation coefficients method uses the data covariance matrix, $\mathrm{cov}[n_i, n_i]$, and defines the global correlation coefficient:

$$\rho_i = \sqrt{1 - \frac{1}{(\mathrm{cov}[n_i, n_i]^{-1})(\mathrm{cov}[n_i, n_i])}} \,. \tag{6.20}$$

Either the maximum or average correlation is minimized with the entire covariance matrix with and without systematic uncertainties. Unfolding is repeated over different values of $\log_{10}\alpha$, thus a creating curve of global coefficients; the point of minimum curvature is found and determined to be the optimal choice of α [114].

Many more details on unfolding can be found in [106].

6.6 Response Matrix

The response matrix is used to translate between measured signal and true signal. We produce the response matrix using dedicated proton simulations by creating a two dimensional histogram of the reconstructed energy versus the true energy. In order to account for statistical effects of different samples, we normalize the number of events in each bin which pass our event selection by the acceptance normalization described in Equation 6.5.

The binning of the response matrix for reconstructed energy is 50 logarithmic bins from 30 GeV to 35 TeV with an additional bin from 10 GeV to 30 GeV– an underflow bin. The reconstructed energy binning is engineered to encompass the entire range of reconstructed energy for protons. The binning of the response matrix for true energy is determined from the energy resolution. The minimum energy is determined by the `HI_PASS` filter and the `CalEnergyRaw > 20000` cut and the mean true energy for protons with `CalEnergyRaw` of 20 GeV. The average true energy for events with a `CalEnergyRaw` of 20 GeV is 54 GeV, therefore we should avoid reconstructing events with true energy below 54 GeV. The maximum energy is found when the 95% containment energy resolution reaches 100% at 9.5 TeV.

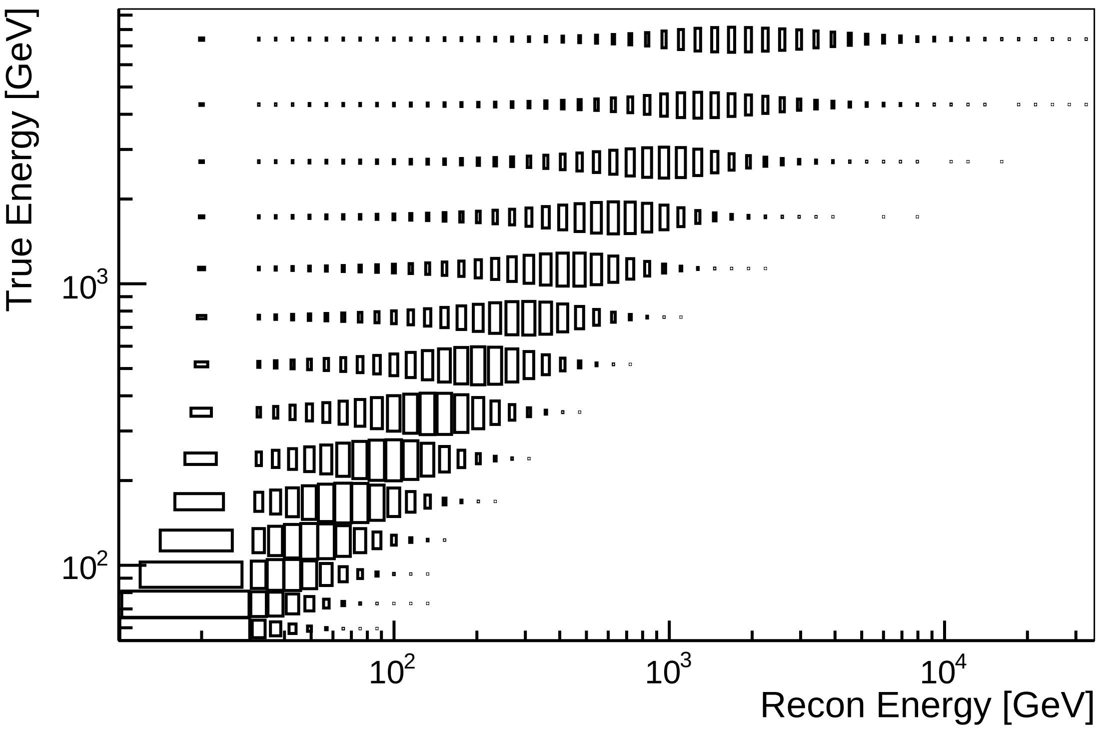

Figure 6.7: The response of the LAT to protons. The response matrix is used in to unfold flight data from reconstructed energy to true energy. The reconstructed energy binning is set to 50 bins from 30 GeV to 35 TeV and the true energy binning is determined from the energy resolution shown in Figure 5.23 ranging from 54 GeV to 9.5 TeV.

The response matrix for protons with the binning described above is shown in Figure 6.7. The response matrix contains information about energy resolution and acceptance. It is used in the following sections to convert the event rate from reconstructed energy to true energy. With the choice of unfolding established and the response matrix estimated, we can combine all of the instrument response functions and build the cosmic-ray proton spectrum.

6.7 Building the Spectrum

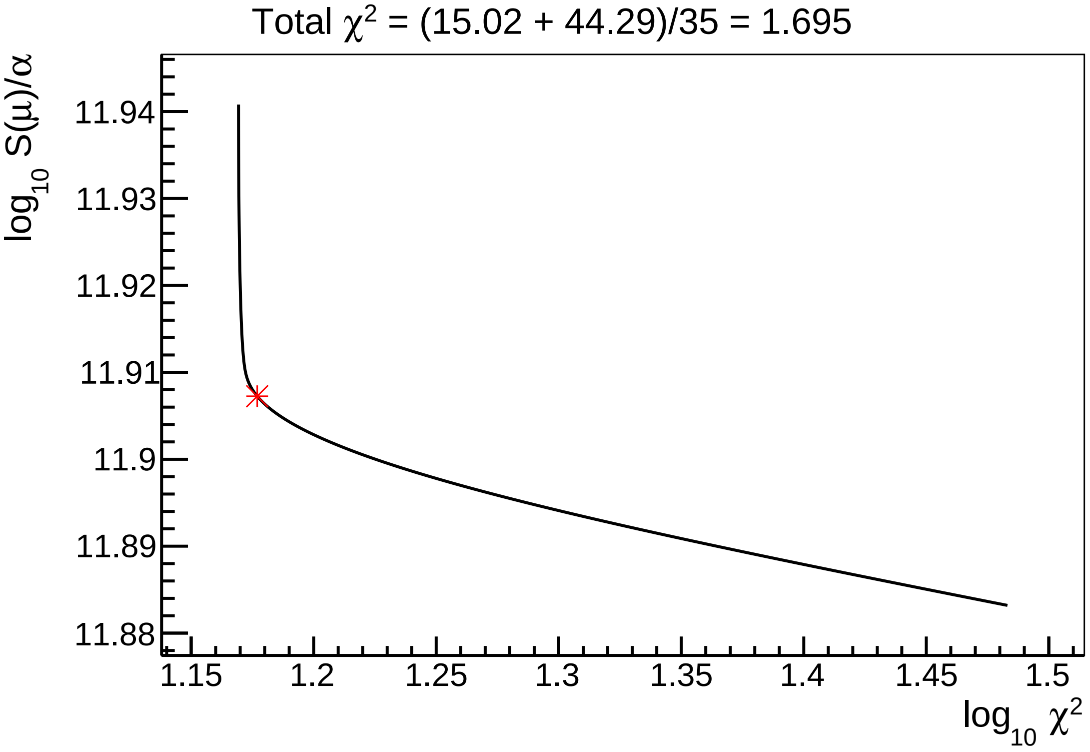

Figure 6.8: The LCurve scan of $\log_{10}\chi^2$ versus $\log_{10} S(\vec{\mu})/\alpha$ for unfolding the cosmic-ray proton spectrum. The optimal choice should be at the point of maximum curvature in the LCurve and is shown by the red marker. The total χ^2 is the sum of the χ^2 from Equation 6.13 and χ^2 associated with the regularization divided by the degrees of freedom $N_{D.O.F.}$ = M - N - 1 = 50 - 14 - 1 = 35.

To build the cosmic-ray proton spectrum, we use all of the data and instrument response products established in the previous sections. First we unfold the event rate using TUnfold and the Tikhonov regularization with k=1. We use k=1 because we expect a smooth spectrum with little curvature and, therefore k=2 will not be able to properly regularize the unfolded distribution. This is shown because when using k=2 the total χ^2 is significantly worse than when using a k=1 regularization.

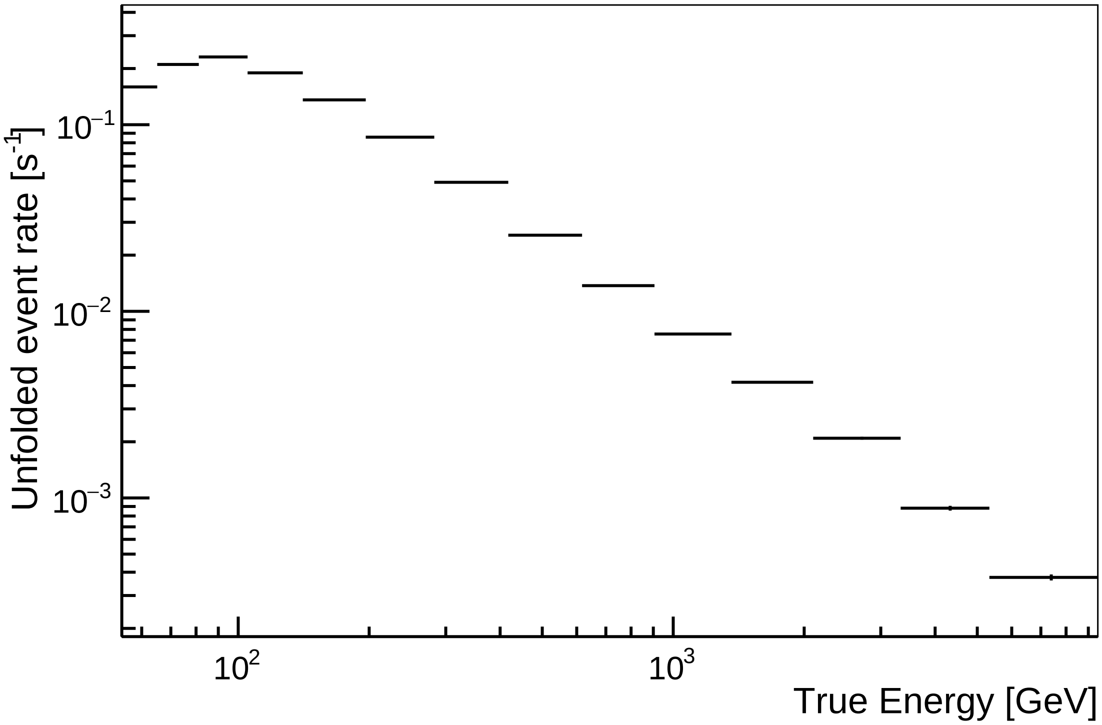

Figure 6.9: The unfolded event rate in true energy using TUnfold and Tikhonov regularization of k=1 from 54 GeV to 9.5 TeV using 7 years of flight data.

This corresponds to `kRegModeDerivative` in TUnfold [114].

We find our strength of regularization using the LCurve scan method and find the resultant LCurve seen in Figure 6.8. The LCurve scan method successfully finds the point of maximum curvature and produces a total reduced $\chi^2 = 1.695$ which is the sum of the χ^2 from Equation 6.13 equaling 15.02, and χ^2 associated with the regularization equaling 44.29, divided by the degrees of freedom $N_{D.O.F.}$ = M - N - 1 = 50 - 14 - 1 = 35. We also use `kDensityModeBinWidth` to account for the non-standard true energy binning derived from the proton energy resolution We set `axisSteeringMode = 'None'` in order to not introduce biases associated with designating a specific underflow bin in reconstructed energy.

To find the differential energy flux once the unfolded event rate is found one simply uses

$$J_{E,i} = \frac{N_i}{A_i \Delta E_i} \tag{6.21}$$

where N_i is the event rate, A_i is the acceptance, ΔE_i is the width of the energy bin all for bin number i. Because of the steeply falling spectrum of J_E, it is useful to multiply the spectrum by $E^{2.7}$ to visually enhance spectral features which might otherwise be difficult to observe. E_i for bin i is found for each bin by taking the geometric mean, $E_i = \sqrt{E_{i,min} \times E_{i,max}}$. This is to ensure agreement of the energy scaling for other measurements from *CREAM-1*, *AMS-02*, *PAMELA*, *BESS-TeV*, and *ATIC* taken from the supremely useful cosmic-ray database [1–5, 119].

Once we have established how to build the cosmic-ray proton spectrum we need to estimate the systematic uncertainties associated with the spectrum.

6.8 Systematic Uncertainties

The estimate of systematic uncertainties is crucial since this analysis is systematics dominated due to the limitations of the LAT for measuring the incident energy of cosmic ray protons. We study two sources of systematic uncertainties believed to be dominant: systematic uncertainties in the acceptance and systematic uncertainties from the energy estimation. Since the energy estimation, characterized by the response matrix, and the acceptance are both generated from GEANT4 Monte-Carlo simulations, both systematic uncertainties can be related to general uncertainty associated with GEANT4 hadronic models.

We use three methods to probe the systematic uncertainties associated with the acceptance and energy estimation: constant signal scanning efficiency, uncertainties associated with the GEANT4 hadronic interaction and shower models, and the absolute energy scale uncertainties. The constant signal efficiency method used as the main probe for uncertainties associated with the acceptance, is performed by selecting different subsets which probe the stability of the spectral measurement as a function of the path length in the CAL. Using the path length in the CAL, this method can also be used to probe energy estimation uncertainties through stability of the evolution of the EM and hadronic components of a cosmic-ray proton induced shower. We use alternative physics lists of hadron simulations in GEANT4 to probe the energy estimation. These alternative physics lists have different models for shower development, primary interactions, cascade, and spallation, and therefore will produce alternative response matrices and effective area. Each alternative physics list will produce different deposited energy and therefore alternate response matrices and acceptances which are used to unfold flight data. The final significant systematic we include is the uncertainty from the absolute energy scaling derived from the *Fermi*-LAT cosmic-ray electron analysis which also tests the uncertainty associated with the energy estimation. The combination of these systematic uncertainties is used to constrain any spectral features and interpretations with the measured cosmic-ray proton spectrum as discussed in Chapter 7.

6.8.1 Constant Signal Efficiency Uncertainty

The acceptance is estimated from the GEANT4 simulations. We need a method to test the stability of the measured cosmic-ray proton spectrum, checking the reproducibility of the measured spectrum for subsets with different acceptances, event rates, and contaminations. To do so, we use a method called constant signal efficiency. We produce energy dependent quantiles of the path length of the proton shower in the CAL using `Tkr1LengthInCal`. `Tkr1LengthInCal` is used since it is a smooth variable across different energies that provides changes in the acceptance and improvement in the energy resolution as `Tkr1LengthInCal` increases. This is the same variable used in § 5.4 to improve the energy resolution ensuring that events have at least 0.5 λ_i in the CAL. `Tkr1LengthInCal` is calculated from the geometric path determined by the best track from the TKR and subtracting any distance that falls within the gaps of the CAL.

`Tkr1LengthInCal` is used for a number of reasons. Firstly, `Tkr1LengthInCal` probes the shower development through interactions with different amounts of active material. This probe has the beneficial secondary effect of testing the energy resolution. As more material is traversed, the energy resolution of the LAT for protons should increase, because more of the EM component of the hadronic shower is contained within the CAL. Secondly, `Tkr1LengthInCal` probes GEANT4's simulation of hadronic shower development in the CAL and how it varies through different amounts of material. Thirdly, `Tkr1LengthInCal` probes the LAT model in GEANT4. We can see how well the LAT is modeled by looking at different

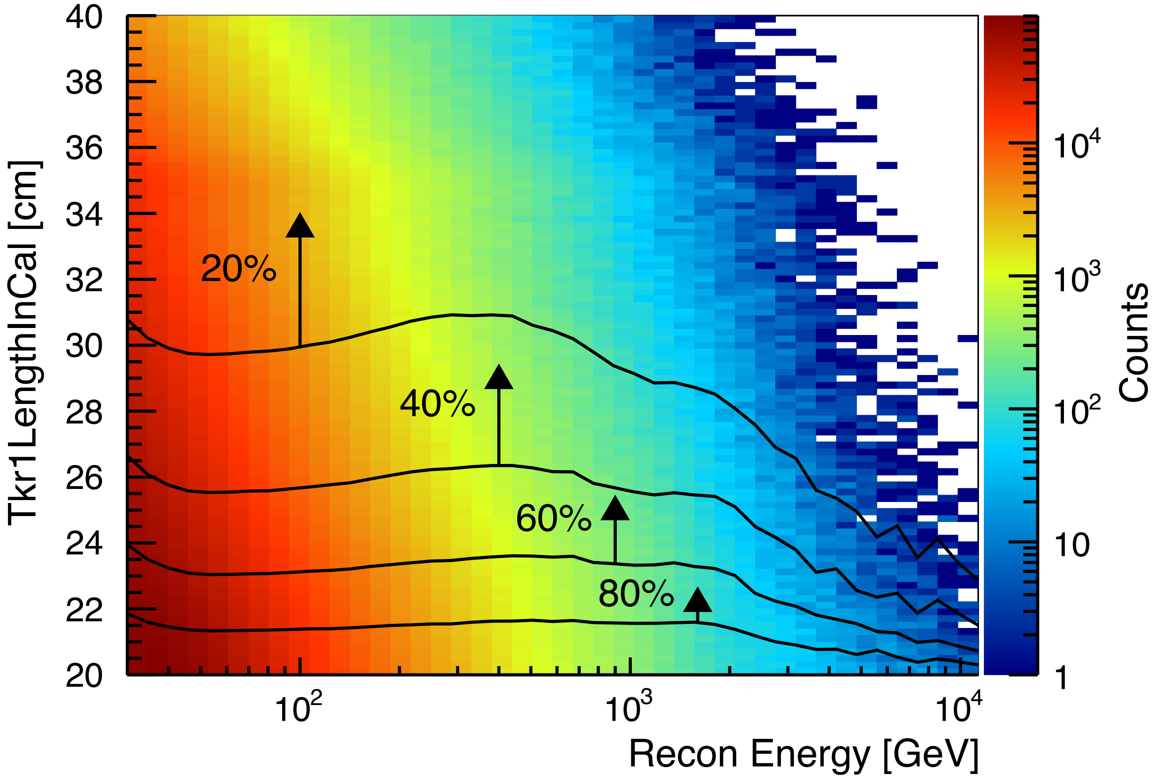

Figure 6.10: The energy dependent 80%, 60%, 40%, and 20% quantiles for `Tkr1LengthInCal` of events in the CAL. Each successive energy dependent quantile cut remove shorter and shorter path length events.

cross-sections of paths through the LAT.

We scan over seven energy dependent quantiles ranging from 90% to 30%, removing lower path length events with each cut. For each quantile, we produce an event rate from flight data, acceptance, contamination, and a response matrix using the same methods as described in § 6.3, § 6.4, § 6.5 respectively. To produce the cut for each signal efficiency, using one year of flight data we find the corresponding quantile value for each reconstructed energy. Using the values of `Tkr1LengthInCal` for each energy bin, we develop a spline cut which encompasses the desired phase-

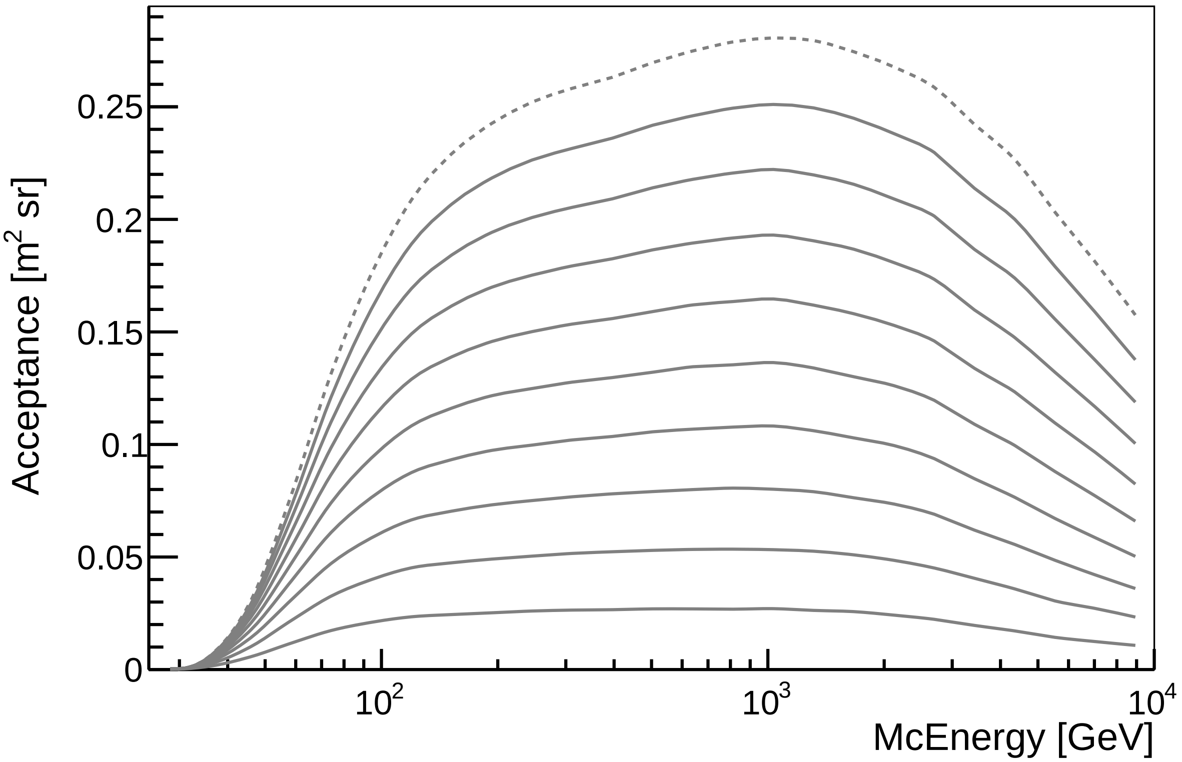

Figure 6.11: The acceptance, with units of m^2 sr, for each constant signal efficiency cut from 90% efficiency to 10% efficiency shown by the solid gray lines. The dotted gray line corresponds to 100% signal efficiency or no cut on the data.

space. Figure 6.10 shows constant signal efficiency cuts used in this method. Figure 6.11 and 6.12 show acceptances and residual electron contamination produced from each scanning efficiency cut used in the spectral reconstruction for each quantile. We see the expected behavior in Figures 6.11 and 6.12, where the acceptance is reduced 10% by each successive cut while the residual electron contamination remains constant around 2-3%. We produce a spectrum for each constant signal efficiency using the same spectral reconstruction and unfolding method described in § 6.5 with the same energy binning in reconstructed and true energy used to unfold the proton

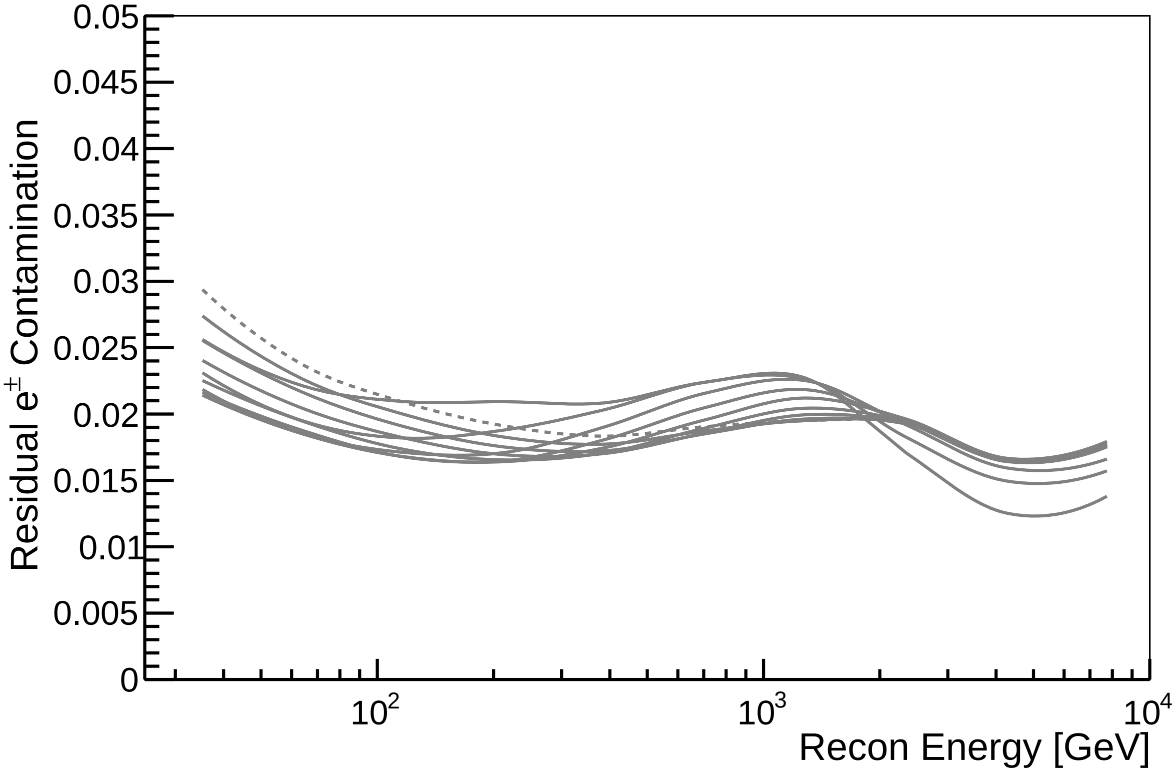

Figure 6.12: The residual electron contamination for each constant signal efficiency cut from 90% efficiency to 10% efficiency shown by the solid gray lines. The dotted gray line corresponds to 100% signal efficiency or no cut on the data. The change in the trend is most likely due to the spectral break observed in Figure 6.18 and the increased counts of protons but unchanging cosmic-ray electron spectrum.

spectrum without the constant signal efficiency method.

Once the spectra for each constant signal efficiency is unfolded, the maximum variation for each energy bin is found and set as the error from the constant signal efficiency. Statistical and other systematic errors are not considered in this measurement and are added in quadrature later to find the total systematic uncertainty of the cosmic-ray proton spectrum. We can see in figure 6.16 the uncertainty from the constant signal efficiency is only a few percent until 1 TeV and rises to 5%. This is a small contribution of the overall systematic uncertainty compared to uncertainties from GEANT4 and the absolute energy scale. The spectrum is very stable when cutting on `Tkr1LengthInCal` for events through the instrument. This tells us that we have a good understanding of our acceptance, how our standard physics simulation in GEANT4 models hadronic shower development, and the model of our instrument in GEANT4. We do not have a trend in our spectral results that correlates with the fraction of shower containment or relative EM hadronic shower component ratios.

6.8.2 GEANT4 Uncertainty

The energy resolution response matrix, used in unfolding the true energy spectrum, and effective area are all determined from the GEANT4 proton simulations. We need to understand the uncertainties in the quality of these simulations. Particle accelerators and detectors have observed, through data/Monte-Carlo comparisons, limitations of the GEANT4 hadronic simulations. These studies show that the current GEANT4 precision for response is within a few percent, and event-by-event fluctuations are well reproduced, but longitudinal shower shape is overestimated around 5%, and transverse shape is overestimated around 10% [120–122]. In order to test the quality of the GEANT4 simulations we can use alternative physics lists for the generation of protons. These alternative physics lists have different models for shower development, primary interactions, cascade, and spallation, and therefore will produce alternative response matrices and effective area. We can use these different response matrices and effective areas in the unfolding of the flight data. When

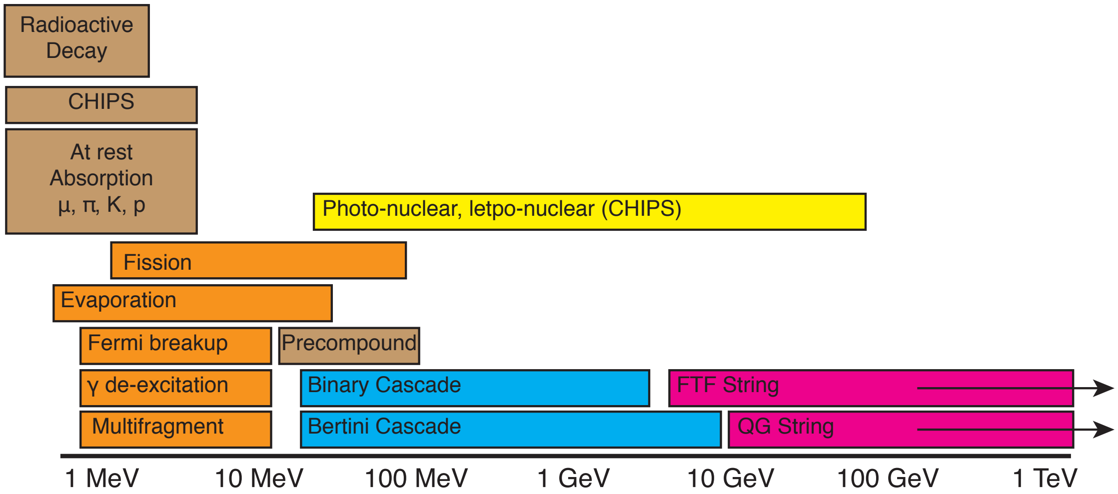

Figure 6.13: The different configurations that build GEANT4 physics lists for hadron simulations. A physics list needs to cover the entire energy range of the simulation [75].

compared to the unfolded result of the standard physics lists described in § 3.3, this gives an estimate of the uncertainties for the different physics lists in GEANT4. The alternative physics lists alter the energy deposition, and therefore are able to probe the systematic uncertainties associated with the energy estimation.

The available number of physics lists used in testing is limited due to the version of GEANT4 used in the Pass 8 Event simulation and reconstruction package and degeneracy of physics lists. Pass 8 uses GEANT4 9.4.p04 and, of the available physics lists, only `QBBC` and `QGS_BIC` demonstrate enough differences from the standard list of `QGSP_BERT_EPAX` to be considered. Figure 6.13 shows the energy range for the different models used to build a physics list for hadronic simulations.

`QBBC` uses the Quark-Gluon-String model for the primary interaction above 20 GeV, a combination of the Bertini cascade and Binary Cascade models below 20 GeV, and the Chiral Invariant Phase Space (CHIPS) model to model nuclear de-excitation from 10 MeV to 100 GeV. CHIPS is an alternative to the Precompound model used in the standard physics list for Pass 8 and is an important test of particle production from the primary interaction of the simulated proton with LAT [83, 84, 123, 124].

`QGS_BIC` uses the Quark-Gluon-String model for the primary interaction above 20 GeV, the Binary cascade model below 20 GeV, and does not include an additional model for nuclear de-excitation such as CHIPS or Precompound. This physics list tests the dependence of the GEANT4 simulations on nuclear de-excitation and the differences between the Bertini cascade and Binary Cascade models [83, 123].

We additionally tested the `FTFP_BERT` physics list. The only difference between `FTFP_BERT` and `QGSP_BERT_EPAX` is the use of the Fritiof (`FTF`) as the model of the primary interaction, instead of the Quark-Gluon-String model [84, 85, 125]. `FTF` models have undergone rapid development in recent years but since we are using GEATN4 9.4.p04, which was released in 2011, the viability of the `FTF` models was questionable. At the time of release, QGS models were considered the best reproduction of collider physics experiments and were the preferred models for ATLAS, CMS, and LHCb [126–128]. These experiments use the Large Hadron Collider (LHC) which is a proton-proton particle collider with a center of mass energy of 7 TeV at the time of evaluation for the GEANT4 physics lists. To answer the question of the viability the alternative physics lists, including `FTF` models, we looked at data/MC agreement between beam-test data reprocessed with Pass 8.

Prior to launch, a calibration unit (CU) of the LAT underwent extensive beam-test studies at CERN and GSI, a German heavy ion accelerator, in order to calibrate

Beam-Test Run	Particle	Energy (GeV)	Incidence Angle	Number of Events
2237	p^+	20	0°	100211
2363	p^+	100	0°	37183
2364	p^+	100	45°	28128
2365	p^+	100	90°	24784
1775	p^+	150	0°	8958

Table 6.2: The summary of Beam-Test runs for protons including information of energy, incidence angles, and number of events triggered [129].

the triggers, estimate the response of the LAT to electrons, protons and nuclei, and decide and calibrate the best choice of physics lists to be used in GEANT4 [129]. The CU is composed of 3 CAL modules, 2 TKR modules and 5 ACD tiles and, because of these differences between the LAT, not all of the cuts can or should be applied to the beam-test data or simulations. Mono-energetic protons at specific interaction points give a unique probe to test the viability of the alternate physics to be used in the greater analysis of understanding these systematic errors. While many configurations were tested for electrons, as a proxy for γ-rays, only a few configurations were tested for protons as seen in Table 6.2. Additionally, the beam-test data has not been validated with Pass 8 and therefore we are limited to looking at fundamental variables not using reconstructed variables that are heavily dependent on Pass 8 reconstruction. Such variables include the total energy deposition in the CAL, `CalEnergyRaw`, and the energy deposition in each layer, `CalELayerN` where `N` refers to the layer number. We establish a set of similar cuts applied to beam-test and simulation data to ensure an interacting proton event within the CU. We require a track to be found, `TkrNumTracks` > 0, a minimal length in CAL, `EvtCalCsIRLn` > 4, agreement between the CAL and TKR reconstructed directions, `CalTrackAngle` < 0.3, and at least 1 GeV energy deposited in the CAL, `CalEnergyRaw` > 1000.

Using 100 GeV protons at normal incidence with the CU of the LAT, we can see the data/MC agreement between the standard physics lists in Figures 6.14 and 6.15. `QGSP_BERT_EPAX`, `QGS_BIC`, and `QBBC` all reproduce the data well, while `FTFP_BERT` underestimates the energy deposition as seen in Figure 6.14(d) and 6.15(d) across the different layers of the CAL and in the CAL as a whole. Because of this poor data/MC agreement for `FTF` based models and large underestimation of deposited energy, we have decided to not include any `FTF` based models in the estimation of the GEANT4 uncertainties.

For the production of the alternative physics list proton simulations, we use a similar configuration to that of the standard proton simulation described in § 3.3 and Table 3.6. Each alternative physics list covers from 4 GeV to 20 TeV with a spectral index of -1.5 and covers the top hemisphere of the LAT for angular distribution of 2π sr. The total number of generated events for each alternative physics list is 185×10^6. We produce alternate acceptances and response matrices for each alternate physics list. Using these alternate response objects, we unfold the flight data with the same settings and procedures as with the standard physics list,

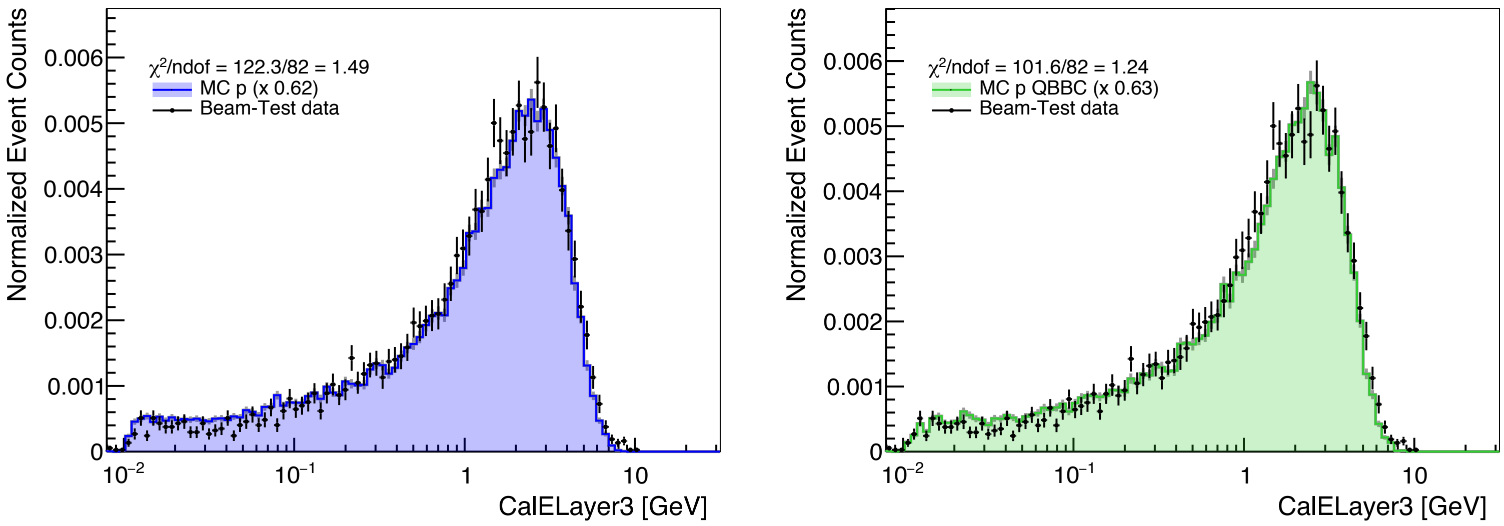

(a) Physics List - `QGSP_BERT_EPAX`

(b) Physics List - `QBBC`

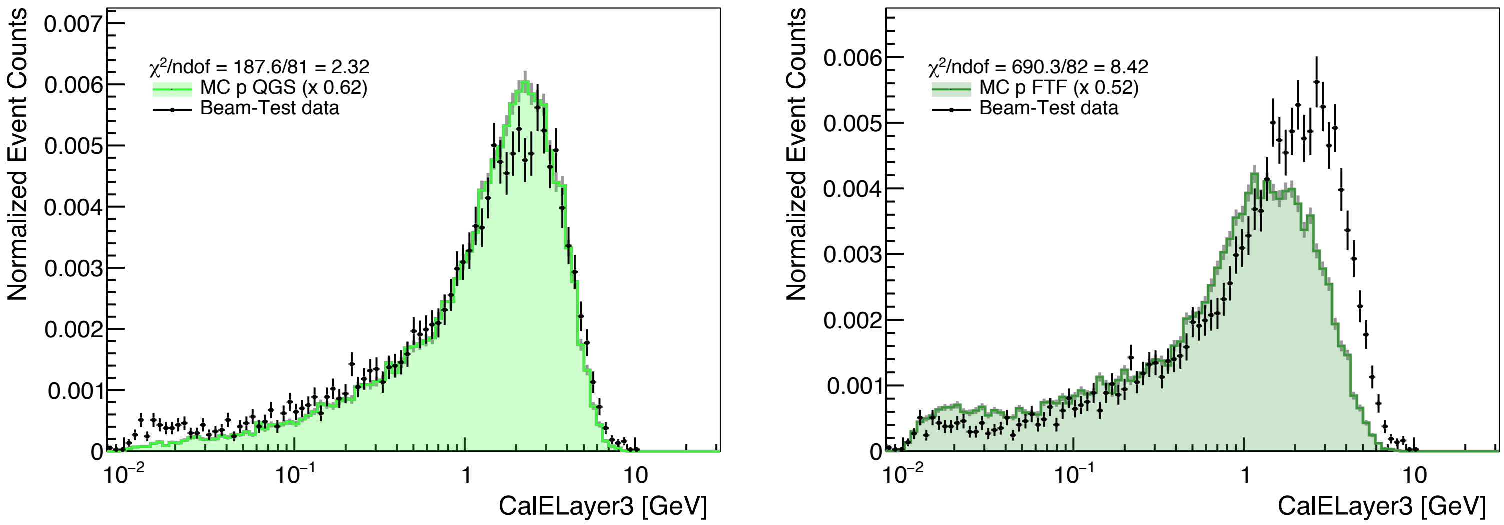

(c) Physics List - `QGS_BIC`

(d) Physics List - `FTFP_BERT`

Figure 6.14: Data/MC agreement for 100 GeV protons at normal incidence from the Beam-Test CU and simulated 100 GeV protons using various physics list for the energy deposited in the 3rd layer of the CAL.

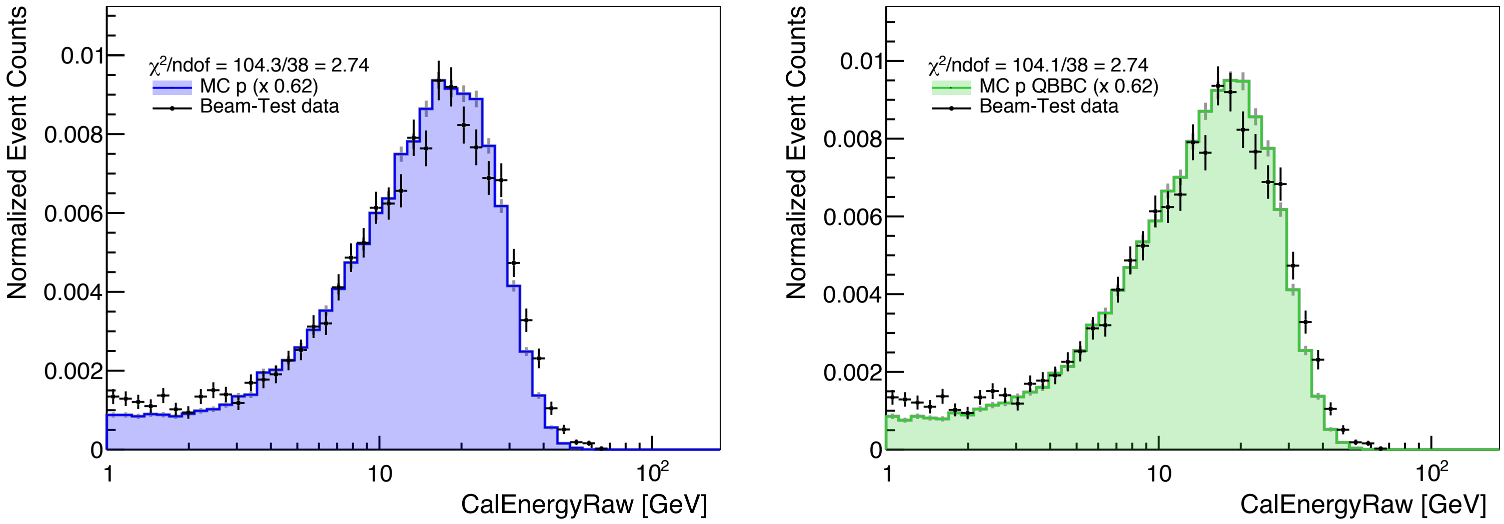

(a) Physics List - `QGSP_BERT_EPAX`

(b) Physics List - `QBBC`

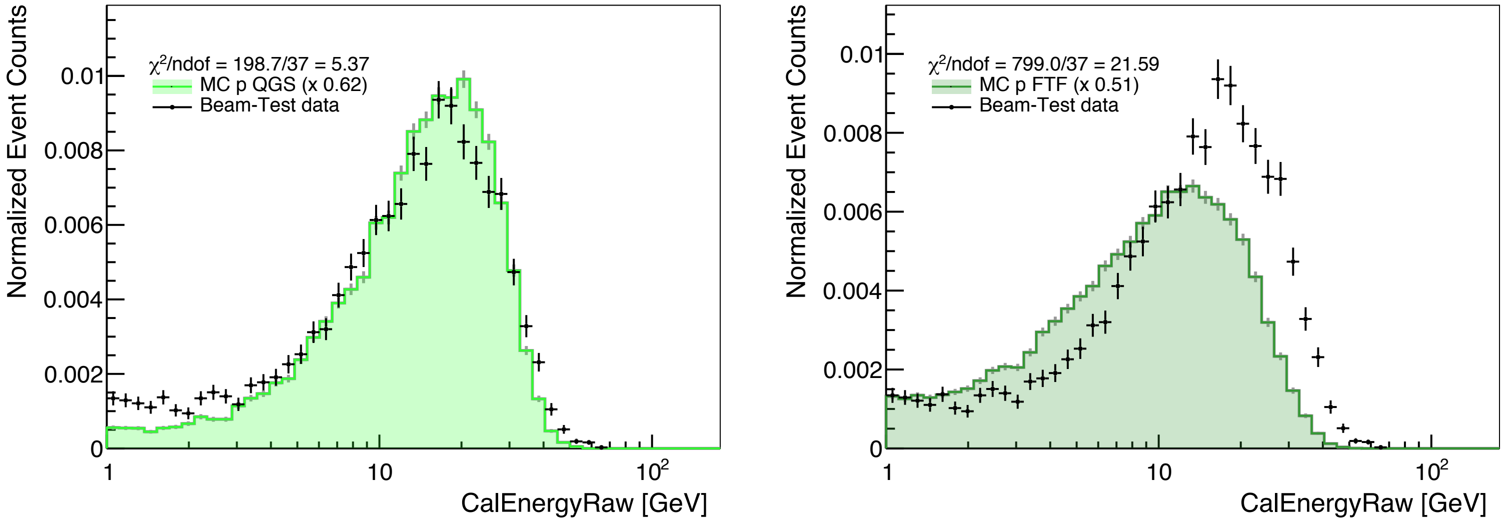

(c) Physics List - `QGS_BIC`

(d) Physics List - `FTFP_BERT`

Figure 6.15: Data/MC agreement for 100 GeV protons at normal incidence from the Beam-Test CU and simulated 100 GeV protons using various physics list for the energy deposited in the whole CAL.

as described in § 6.5. We use the maximum variation of each alternate spectra to set limits on systematic uncertainty for GEANT4. We then add the error set from each alternate spectrum in quadrature, ignoring statistical uncertainty, to find the total systematic uncertainty for GEANT4 and associated energy estimation. The combined systematic uncertainty for `QBBC` and `QGS_BIC` is shown in Figure 6.16. The estimated uncertainty is under 15% across the entire energy range with a minimum of 5% at 400 GeV. The uncertainty rises as energy rises, to 11% at a few TeV. We see this is the dominant source of systematic uncertainty across most of the energy of this analysis.

This estimation agrees well with other studies from collider experiments such as *CALICE* and other LHC experiments. These studies show that the current GEANT4 precision for response is within a few percent, event-by-event fluctuations are well reproduced, but longitudinal shower shape is overestimated around 5% and transverse shape is overestimated around 10% [120–122]. These combined effects will alter the energy reconstruction since the full profile method, described in § 5.2.2, depends on the shower geometry as well as energy deposition. The final systematic uncertainty is associated with the uncertainty of absolute energy scale described in § 5.2.4.

6.8.3 Absolute Energy Scale Uncertainty

As discussed in § 5.2.4, the absolute energy scale is a measure of accuracy of the reconstructed energy. The absolute energy scale has an associated systematic uncertainty which is related to how well the energy estimation is known. At energies around 10 GeV, the systematic uncertainty is related to uncertainties associated with using electrons and positrons in measuring E_C via the geomagnetic cutoff energy. Due to contamination from protons and nuclei as well as uncertainties in the electron acceptance, the uncertainty is estimated by the *Fermi* LAT Pass 8 electron spectrum group to be 2% at 10 GeV [101]. The absolute energy scale uncertainty is more difficult at TeV energies since one cannot rely on the geomagnetic rigidity cutoff. Once again using the result from the *Fermi* LAT Pass 8 electron spectrum group, one can probe the full profile fit method described in § 5.2.2. The data/MC agreement for the χ^2 from Equation 5.12 show a systematic shift of 0.13 corresponding to a layer energy bias of $2.2\delta E$. Using Equation 5.13, $2.2 \times 0.17 \times \exp(-\log_{10}(10^3)/1.38) = 4.2\%$. This results in a 4.2% bias in the reconstructed energy [101].

In summary, the absolute energy scale uncertainty is 2% at 10 GeV and 4% at 1 TeV. We estimate the uncertainty in the intermediate energies linearly in $\log_{10}(E)$. This uncertainty is associated with energy reconstruction and was determined from electrons. As stated in § 5.3, the LAT is predominantly measuring the EM component of proton induced hadronic showers and the EM fraction increases with incident proton energy, therefore this systematic uncertainty will effect the proton energy reconstruction on the same order as the electron energy reconstruction. Since the absolute energy scale uncertainty is associated with the reconstructed energy, it cannot be directly applied as an uncertainty to the final measurement and needs to be to included prior to unfolding. Using the same procedures established in § 6.5, we apply the error to the response matrix according to the reconstructed energy. This propagates the absolute energy scale uncertainty through the unfolding statistical uncertainty, which is then removed to find the absolute energy scale uncertainty in true energy space for the proton spectrum. As seen in Figure 6.16, the absolute energy scale uncertainty is 5% below 500 GeV and rises to 12% at a few TeV.

Including the absolute energy scale uncertainty can be considered a conservative addition to the total systematic uncertainty. Essentially the absolute energy scale uncertainty is an estimate of the systematic uncertainties associated with the energy estimation. The GEANT4 systematic uncertainty already encompasses this to a degree, since each alternate physics list changes the energy deposition and shower profile, altering the reconstructed energy. Because of this fact we are including the absolute energy scale uncertainty separately from the other systematic uncertainties as seen in Figure 6.18.

6.9 Results

Combining the spectral results from § 6.7 and the systematic uncertainties from § 6.8 we find the differential energy flux shown in Table 6.3 and Figure 6.18. Table 6.3 shows the energy range, unfolded background subtracted counts, and differential energy flux with statistical, separated, and total systematic uncertainties. Figure 6.18 shows the differential energy spectrum multiplied by $E^{2.7}$ in order to better see subtle spectral features. The red markers show the statistical uncertainties, the red shaded region shows the statistical and systematic uncertainties without absolute energy scale uncertainty, and the red dashed lines show the statistical and systematic uncertainties with absolute energy scale uncertainty. We can see the energy dependence of individual components of the of systematic uncer-

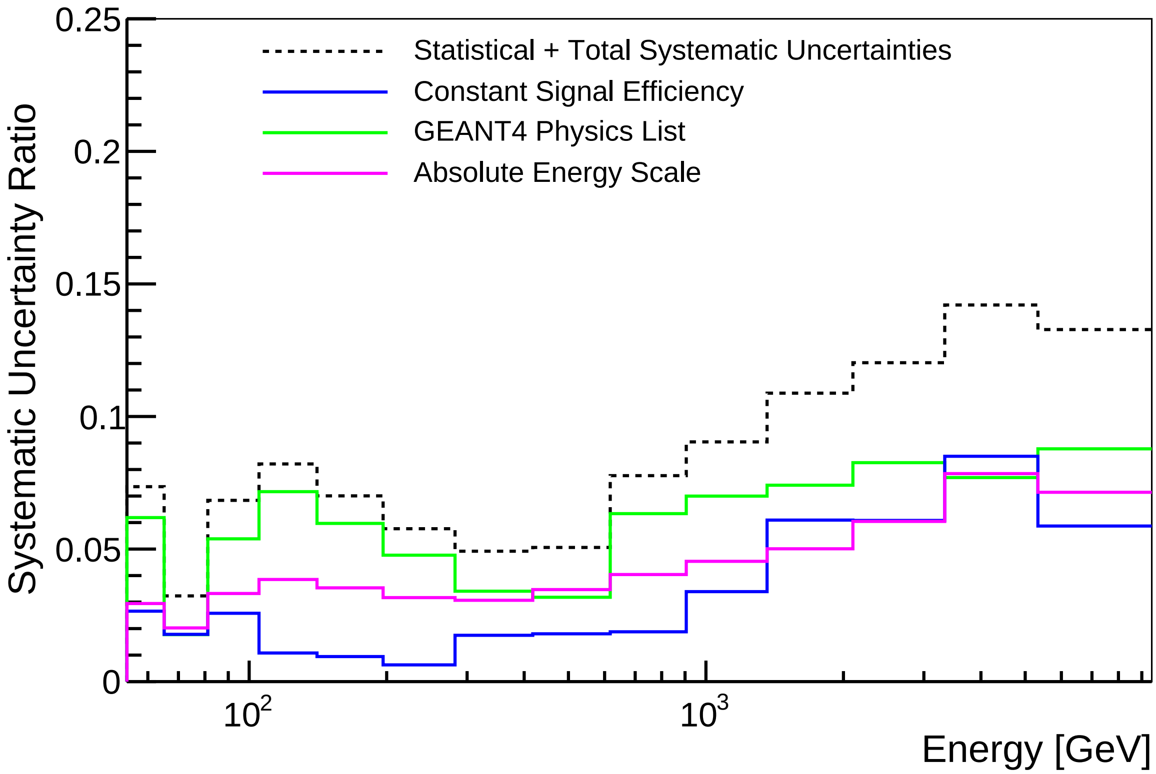

Figure 6.16: The ratio of each systematic uncertainty versus energy associated with the measured proton spectrum. Blue lines show the uncertainty from the scanning efficiency described in § 6.8.1. Green lines show the uncertainty from GEANT4 described in § 6.8.2. Magenta lines show the uncertainty from the absolute energy scaling described in § 6.8.3. The black dotted line is sum in quadrature of all systematic uncertainty and statistical uncertainty.

tainties in Figures 6.16 and 6.17. The constant signal efficiency uncertainty, which traces the systematic uncertainty associated with the acceptance, is low across most energies, reaching 5% at several TeV. The GEANT4 uncertainty, which traces the systematic uncertainty associated with the energy estimation, is the largest source of systematic uncertainty at around 10% across most energies. The absolute energy scale uncertainty, which also traces the uncertainty associated with the energy estimation, starts at 5% below 1 TeV and raises to around 10% above 1 TeV.

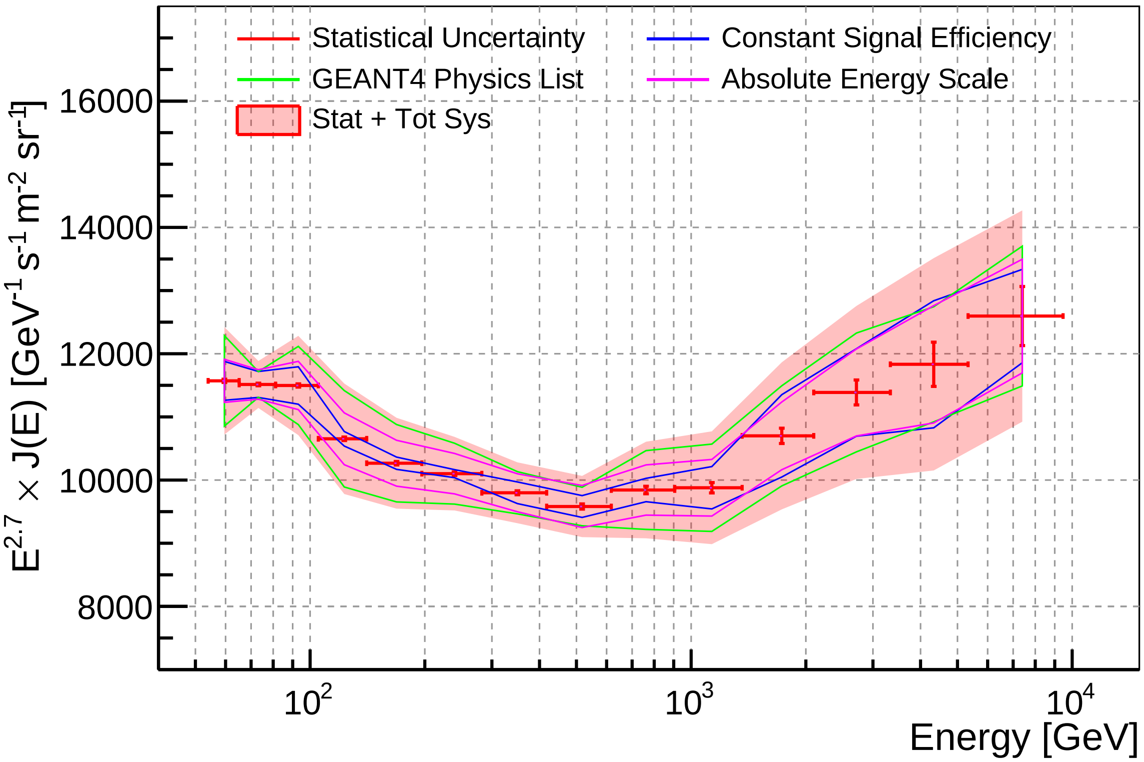

Figure 6.17: The measured proton spectrum from the *Fermi* LAT in units of GeV^{-1} s^{-1} m^{-2} sr^{-1} multiplied by E$^{2.7}$ using 7 years of flight data. Red markers show the statistical uncertainty. Blue show the uncertainty from the scanning efficiency described in § 6.8.1. Green shows the uncertainty from GEANT4 described in § 6.8.2, magenta shows the uncertainty from the absolute energy scaling described in § 6.8.3. The red shaded region shows the quadrature sum of statistical and all systematic uncertainties.

It should be noted that we have two measures of the energy estimation uncertainty from GEANT4 and absolute energy scale systematics. The overlap of these two systematics is not known and we maybe over accounting for the energy estimation uncertainty. Additionally, the absolute energy scale uncertainty was measured via electrons. While uncertainty should applicable to cosmic-ray protons, the absolute energy scale uncertainty has not been measured directly for protons. This is

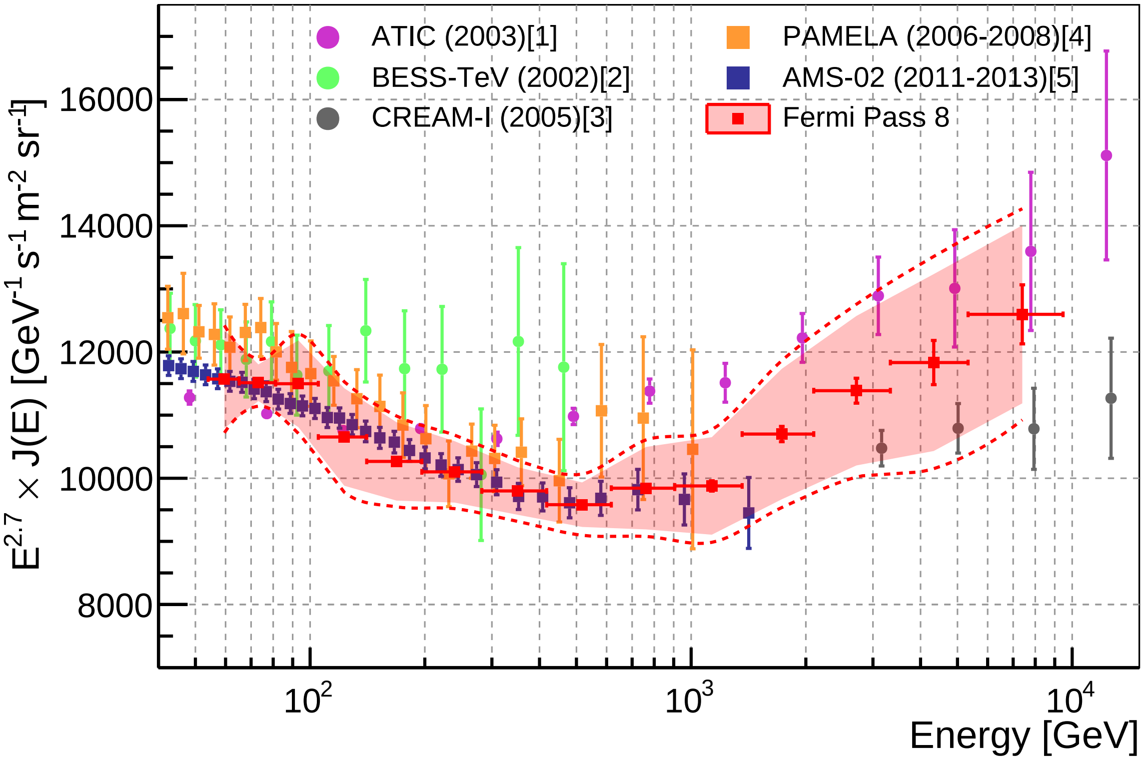

Figure 6.18: The measured proton spectrum from the *Fermi* LAT in units of GeV^{-1} s^{-1} m^{-2} sr^{-1} multiplied by E$^{2.7}$ using 7 years of flight data. The red markers show the statistical uncertainty. The red shaded region shows the sum of the statistical uncertainty, the constant scanning efficiency uncertainty (§ 6.8.1), and the GEANT4 uncertainty (§ 6.8.2). The red dashed lines includes absolute energy scale uncertainty (§ 6.8.3). Other measurements from *ATIC* [1], *BESS-TeV* [2], *CREAM-1* [3], *PAMELA* [4], and *AMS-02* [5] are shown for comparison.

one of the future tasks described in Chapter 8.

Therefore we conservatively present two different estimates of the total systematic uncertainties as seen in Figure 6.18: without the absolute energy scale uncertainty (red shaded region) and with the absolute energy scale uncertainty (red dashed lines). This measurement represents the first time a space-based measurement of the cosmic-ray proton spectrum has been able to extend to nearly 10 TeV and observe an energy range covered by both space-based and balloon-borne cosmic-ray experiments. The measured cosmic-ray proton spectrum overlaps with other *AMS-02* and *PAMELA* [4] and extends past the maximum energy measurement of *AMS-02* [5] and additionally overlaps with *ATIC* [1] and *CREAM-1* [3] measurements. The measurement is systematics dominated and is limited by the size of the CAL and its ability to contain and measure hadronic showers, and by the systematic uncertainties associated with GEANT4. Without major improvements to event reconstruction for protons and improvements in proton interactions models, future improvements to the systematic uncertainties associated with the energy estimation are limited.

Energy [GeV]	Unfolded Counts	J_E [GeV^{-1} s^{-1} m^{-2} sr^{-1}] ($\sigma_{stat} \pm \sigma_{scan} \pm \sigma_{G4} \pm \sigma_{AbsEne} \pm \sigma_{SysTot}$)
54.0 - 65.1	26,265,077	$1.89 \times (1 \pm 0.004 \pm 0.050 \pm 0.117 \pm 0.056 \pm 0.139) \times 10^{-1}$
65.1 - 81.2	34,658,545	$1.08 \times (1 \pm 0.002 \pm 0.019 \pm 0.019 \pm 0.022 \pm 0.035) \times 10^{-1}$
81.2 - 105.1	38,022,096	$5.67 \times (1 \pm 0.013 \pm 0.146 \pm 0.306 \pm 0.189 \pm 0.388) \times 10^{-2}$
105.1 - 140.8	31,250,118	$2.50 \times (1 \pm 0.007 \pm 0.027 \pm 0.179 \pm 0.096 \pm 0.205) \times 10^{-2}$
140.8 - 196.4	22,388,392	$1.04 \times (1 \pm 0.003 \pm 0.010 \pm 0.062 \pm 0.037 \pm 0.072) \times 10^{-2}$
196.4 - 282.3	14,128,481	$3.98 \times (1 \pm 0.011 \pm 0.025 \pm 0.190 \pm 0.126 \pm 0.229) \times 10^{-3}$
282.3 - 417.6	8,096,446	$1.40 \times (1 \pm 0.004 \pm 0.024 \pm 0.048 \pm 0.043 \pm 0.068) \times 10^{-3}$
417.6 - 617.2	4,215,046	$4.75 \times (1 \pm 0.020 \pm 0.086 \pm 0.151 \pm 0.165 \pm 0.239) \times 10^{-4}$
617.2 - 905.6	2,262,067	$1.71 \times (1 \pm 0.010 \pm 0.032 \pm 0.109 \pm 0.069 \pm 0.133) \times 10^{-4}$
905.6 - 1360.9	1,245,342	$5.92 \times (1 \pm 0.049 \pm 0.201 \pm 0.414 \pm 0.269 \pm 0.533) \times 10^{-5}$
1360.9 - 2097.6	686,724	$2.06 \times (1 \pm 0.023 \pm 0.126 \pm 0.153 \pm 0.103 \pm 0.223) \times 10^{-5}$
2097.6 - 3332.9	344,252	$6.55 \times (1 \pm 0.114 \pm 0.398 \pm 0.541 \pm 0.396 \pm 0.780) \times 10^{-6}$
3332.9 - 5330.7	145,217	$1.93 \times (1 \pm 0.057 \pm 0.164 \pm 0.149 \pm 0.152 \pm 0.269) \times 10^{-6}$
5330.7 - 9463.9	61,828	$5.03 \times (1 \pm 0.187 \pm 0.295 \pm 0.441 \pm 0.359 \pm 0.641) \times 10^{-7}$

Table 6.3: Number of unfolded counts after background subtraction and flux J_E in units of GeV^{-1} s^{-1} m^{-2} sr^{-1}, with its statistical and systematic errors (the constant signal efficiency, GEANT4, and absolute energy scale uncertainty) and summed systematic uncertainties.

Chapter 7: Interpretation

The basic predictions from § 2.3, § 2.4, and § 2.5 are that the source of Galactic cosmic-rays are evenly distributed over the entire Galactic disk, cosmic-ray acceleration produces a power-law spectrum with a single index, and the diffusive component in cosmic-ray propagation is also described by a power-law spectrum with a single index. These predictions use the assumptions of homogeneity of acceleration, propagation, and sources; isotropy of propagation and sources in the Galactic disk; and linearity of acceleration and propagation. The break in the cosmic-ray proton spectrum and observed breaks in other cosmic-ray species at ∼100 GeV cannot be explained with these models of acceleration, propagation, and sources of cosmic rays. We first fit the cosmic-ray spectrum measured with the *Fermi*-LAT with a power-law and broken power-law spectral form. Then we also fit the measurements from LAT in combination with the higher energy cosmic-ray measurements from *CREAM-1*. We examine each of the model components in detail and show how a new measurement of the cosmic-ray proton spectrum could be interpreted. The majority of these interpretations came out in response to *AMS-02* observations of a spectral break at ∼300 GeV [5]. I present a literature review of a set of interpretations which challenge the current cosmic-ray paradigm.

7.1 Spectral Fits

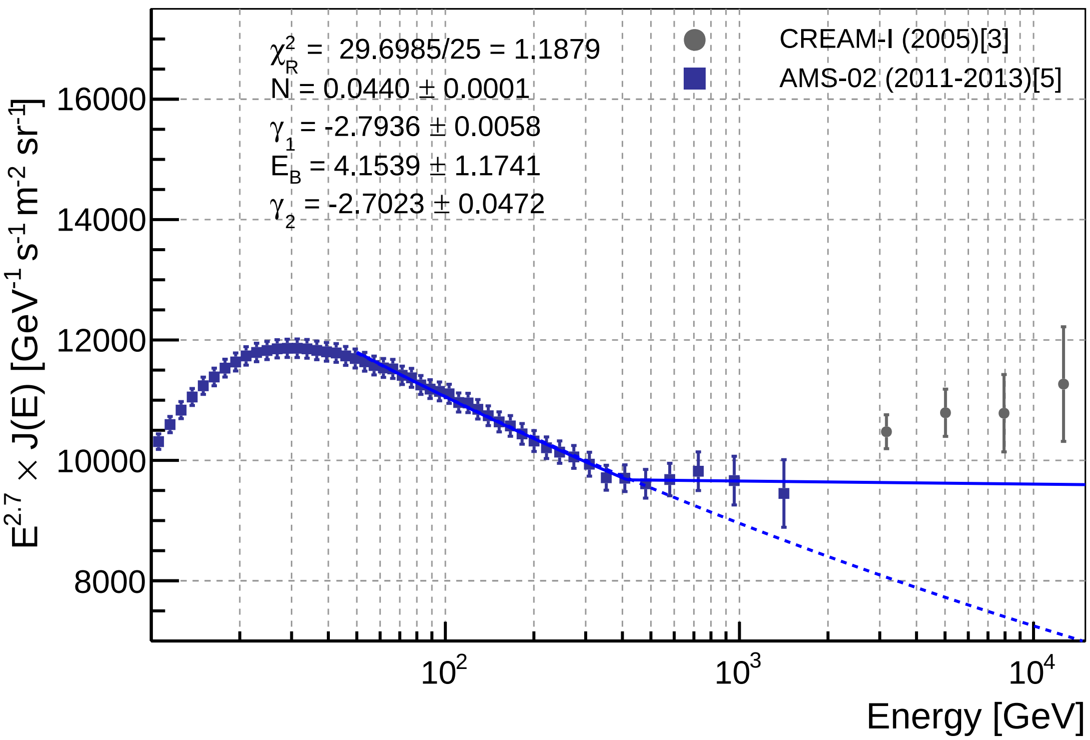

Figure 7.1: *AMS-02* proton spectrum fit with a broken power-law (blue sold line) defined in 6.1, and a power law (blue dashed line) defined in 6.1. *CREAM-1* data is shown for reference for higher energy measurements and not included in the fit. Broken power-law fit results and reduced χ^2 are shown on the figure. E_B is in units of 100 GeV.

The *Fermi*-LAT provides a single measurement from 54 GeV to 9.5 TeV which crosses the observed spectral break from *AMS-02*. This provides a probe for confirming the spectral break and measuring a possible second spectral index to energy ranges typically measured by balloon-borne experiments. The combined systematic uncertainties are too large to discern between *CREAM-1* and *ATIC* measurements but they show an intriguing change of the spectrum above 2 TeV. All following

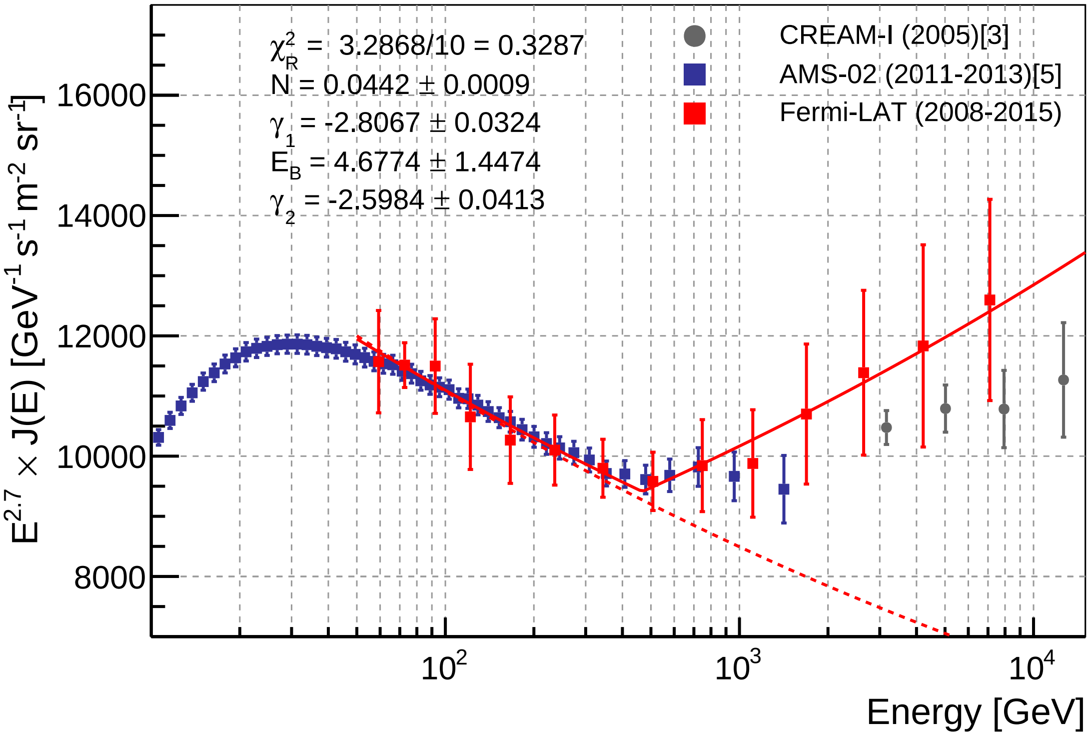

Figure 7.2: *Fermi*-LAT proton spectrum fit with a broken power-law (red sold line) defined in 6.1, and a power law (red dashed line) defined in 6.1. *CREAM-1* and *AMS-02* data is shown for reference and not included in the fit. Broken power-law fit results and reduced χ^2 are shown on the figure. E_B is in units of 100 GeV.

fits were performed using a χ^2 fit based in ROOT using the TMinuit minimizer over kinetic energy [110, 111]. All data is fit including statistical and systematics uncertainties. We fit the *Fermi*-LAT proton spectrum measurement and included systematic uncertainties with a power-law and broken power-law as seen in Figure 7.2. The dashed lines in Figures 7.1 and 7.2 represent fits with a power-law and does not fit the data in either data-set.

The original *AMS-02* cosmic-ray proton measurement was performed in rigidity instead of kinetic energy. We have to convert the energy and flux of kinetic

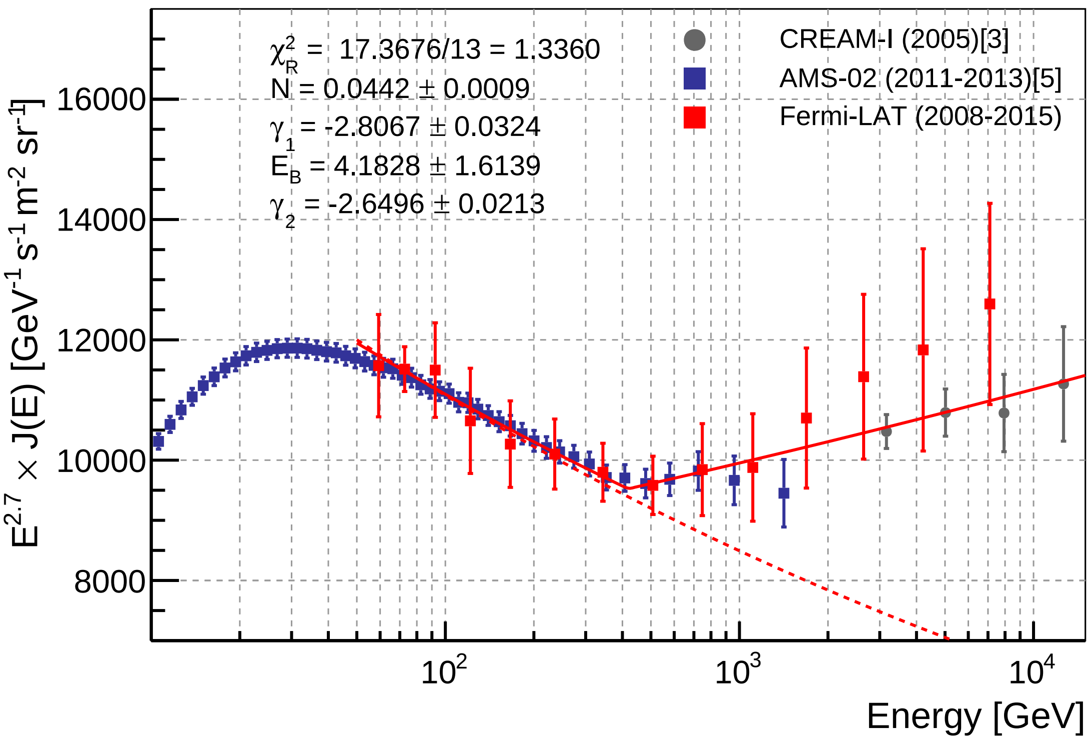

Figure 7.3: *Fermi*-LAT and *CREAM-1* proton spectrum fit with a broken power-law (red sold line) defined in 6.1, and a power law (red dashed line) defined in 6.1.*AMS-02* is shown for reference and not included in the fit. *CREAM-1* data is included in the fit to help constrain high end of the spectrum. Broken power-law fit results and reduced χ^2 are shown on the figure. E_B is in units of 100 GeV.

energy using Equation 2.1 and fit the data using the same method as was used for the *Fermi*-LAT spectral fit for consistency. It should be noted that extending the secondary index from *AMS-02* to 10 TeV does not agree with higher energy measurements from either *ATIC* or *CREAM-1* therefore, demonstrating the need for a single measurement to bridge the gap between space-based and balloon-borne measurements. We find a break at 467 ± 144 GeV, which falls within the uncertainties when performing the same fit with *AMS-02* data in Figure 7.1 with a break

Data	γ_1	E_B [GeV]	γ_2
AMS-02	-2.794 ± 0.006	415 ± 117	-2.702 ± 0.047
Fermi-LAT	-2.807 ± 0.032	467 ± 144	-2.598 ± 0.041
CREAM-1 and *Fermi*-LAT	-2.807 ± 0.032	418 ± 161	-2.650 ± 0.021

Table 7.1: Fit results using *Fermi*-LAT, *AMS-02*, and *CREAM-1* data with a broken power-law described in Table 6.1. The primary index, γ_1, energy break in GeV, E_B, and secondary index, γ_2, are shown with associated fitting errors. All data includes statistical and systematic uncertainties.

at 415 ± 117 GeV. *Fermi*-LAT results find a much larger secondary index than the *AMS-02* measurement, $\gamma_2 = -2.60 \pm 0.04$ for the LAT and $\gamma_2 = -2.70 \pm 0.05$ for *AMS-02*. This could be due to the fact that *AMS-02* extends to 1.8 TeV and therefore does not have enough high energy data to fully characterize the index of the spectral break.

We can also combine *Fermi*-LAT and *CREAM-1* measurements into a single spectral fit shown in Figure 7.3. We find a similar spectrum to with a secondary index of $\gamma_2 = -2.65 \pm 0.02$. Compared to *AMS-02*, with a secondary index of $\gamma_2 = -2.70 \pm 0.05$, the two measurements become consistent within uncertainties. This is to demonstrate consistencies between the *AMS-02* and *Fermi*-LAT measurements when considering balloon-borne measurements. The summary of the different combinations of fits is shown in Table 7.1.

7.2 Source Injection

The first assumption is that the source injection of cosmic rays is described by a power-law spectrum with a single spectral index across the entire range of energies for Galactic cosmic rays. We know from observations that the emission from SNRs evolves in time and that they can be broken into two rough categories, young and old SNRs. The acceleration of cosmic rays at those sites must also evolve with time. It is interesting to consider what impact that should have on the Galactic cosmic rays. In the case of a single SNR, the highest energy cosmic rays are believed to be accelerated and escape from a SNR earlier because of the faster shock velocity and more turbulent magnetic field in the shock-front. This would imply that low energy cosmic rays escape later and have a lower energy due to adiabatic expansion of the shock front [68]. Therefore, including a temporal component in the spectrum of cosmic rays inside the SNR would be

$$\frac{dN}{dE} \propto t^{\beta} E^{\gamma+1} \tag{7.1}$$

where the maximum energy accelerated is

$$E_{max} \propto t^{-\alpha} \tag{7.2}$$

and α and β can be related to the injection spectrum of cosmic rays by

$$\gamma_{inj} = \gamma + \frac{\beta}{\alpha}. \tag{7.3}$$

γ can also have a direct rigidity dependence since it can be related to the Mach

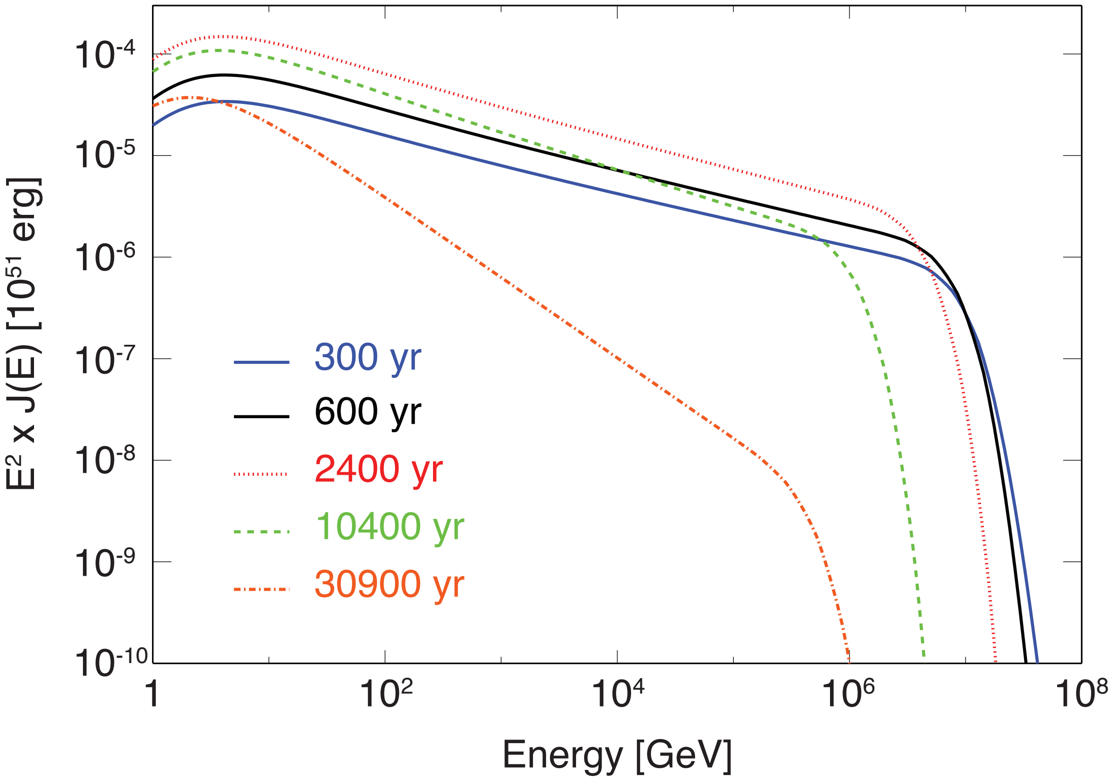

Figure 7.4: The instantaneous cosmic-ray spectrum generated via first order Fermi acceleration from 300, 600, 2400, 10400, and 30900 year old SNR. For the shock environment $\eta \approx 2.5 \times 10^{-3}$ where η represents the fraction of the particles crossing the shock-injected in the acceleration process [130]

number through an approximated form of 2.11 to be

$$\gamma = \frac{\mathcal{M}^2 + 3}{\mathcal{M}^2 - 1}. \tag{7.4}$$

For a young SNR, when $\mathcal{M}$ is large, $\gamma = 1$, but for an old SNR , when M is smaller, $\gamma > 1$. This produces a spectrum where low energy cosmic rays have a steeper spectrum than high energy cosmic rays producing a break in the observed spectrum. Figure 7.4 shows the temporal evolution of the instantaneous cosmic-ray spectrum for different age SNRs. As the age of a SNR increases, the cosmic-ray injection spectrum steepens, the flux of low energy particles in the in 100s of GeV and TeV energy increase, and the maximum energy decreases.

Additionally, the time dependence of the shock front makes observations of the hadronic component difficult. Shock fronts have two phases: ejecta-dominated and Sedov-Taylor phase. Maximum energy can only increase during the ejecta dominated phase. During the Sedov-Taylor phase, the maximum energy decreases because the shock slows and particles with higher energy than the maximum energy escape. The cross over between the ejecta dominated and Sedov-Taylor phase is typically $\sim 10^3$ years. This creates a situation where the highest energy cosmic rays are accelerated in young shocks during a very narrow time window and escape in the Sedov-Taylor phase. To observe the maximally accelerated cosmic-rays, γ-ray observations need to observe a SNR near the cross over between the two phases or observe locally dense regions called Molecular Clouds near SNRs for γ-ray excesses from cosmic-ray interactions.

The temporal acceleration dependent interpretation attempts to include a temporal dependence of cosmic-ray acceleration under the simple assumptions described above. γ-ray observations do not offer a complete view into cosmic-ray acceleration. A catalog of SNRs observed by the *Fermi*-LAT can be found in the Fermi-LAT Supernova Remnant Catalog [67]. Three recent observations of SNRs have measured hadronic contributions from π_0 production in IC 443, W44, and W51. The temporal acceleration dependent interpretation is difficult to test with γ-ray observations since they probe a subset of cosmic-ray acceleration in Galactic SNRs but do not offer a complete connection to the injected cosmic rays. This would be difficult to

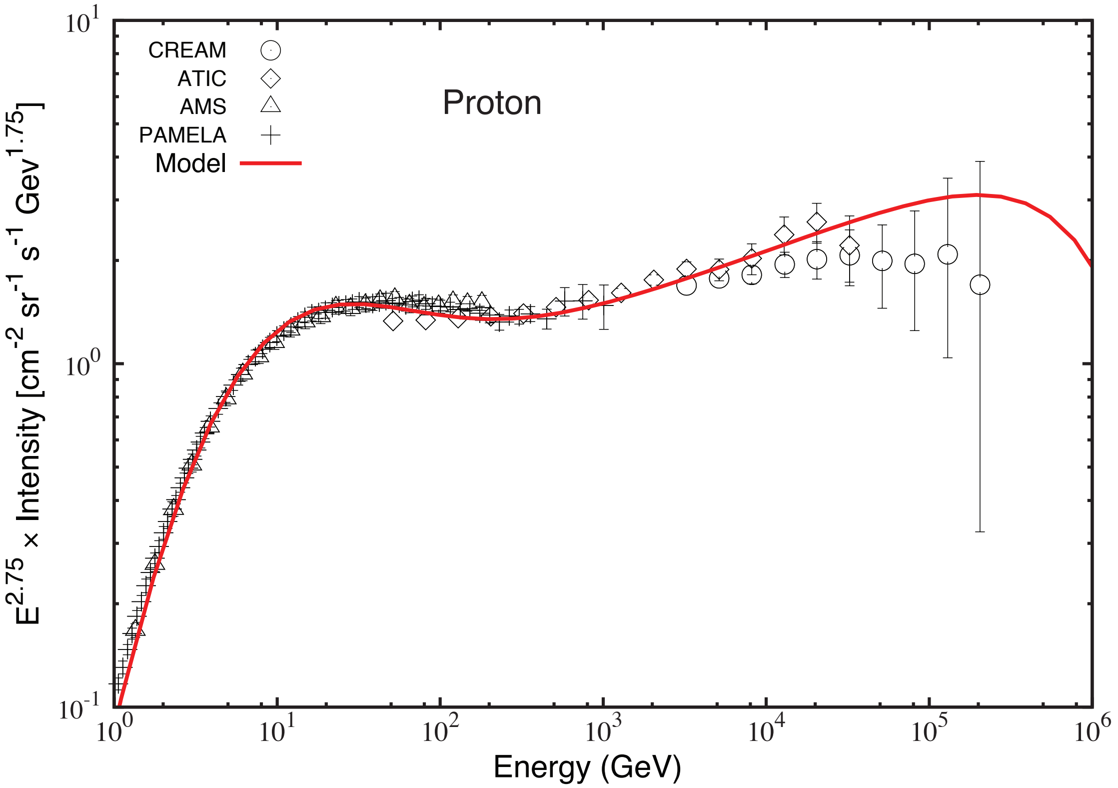

Figure 7.5: Proton spectrum fit with model including cosmic-ray re-acceleration from weak and old SNR shocks using *CREAM-1*, *ATIC*,*PAMELA*, and *AMS-01* data. The model shows a break at ∼100 GeV [131].

test with young SNRs where the EM component dominates over the hadronic component and therefore the models including both EM and hadronic components tend to not be able to definitively separate contributions from either model. Interpreting the cosmic-ray observations requires a more complete and integrated picture than γ-ray observations alone. One consequence of the temporal acceleration dependent interpretation that can be measured by direct cosmic-ray measurements is that the break should appear in every cosmic-ray species at the same rigidity since there is no explicit dependence on charge or mass of the accelerated cosmic ray [68].

Another possible interpretation associated with cosmic-ray acceleration is the re-acceleration of cosmic rays from old SNRs shock fronts [131]. Old SNRs shock fronts are much larger than their young counterparts, and therefore it is possible that an additional component of re-acceleration is needed as described in § 2.5.2. Normal re-acceleration of cosmic rays via second order Fermi accelerations from interactions with the ISM produces a small change in the observed proton spectrum and would be constant over the entire observed spectrum. Re-acceleration from older weaker shocks would have a larger effect on low energy cosmic rays, as discussed earlier, since old and weak shocks would produce a steeper spectrum for low energy cosmic rays. Results can be seen in Figure 7.5 where a spectral break can be recreated in the proton spectrum at ∼100 GeV. One consequence of both of these interpretations is that these spectral breaks would be generated in all cosmic-ray species at the same rigidity since there is no dependence on the charge or mass of the cosmic-ray. This gives some predictive power and additional theoretical constraints from looking at different cosmic-ray species. Recent measurements of cosmic-ray helium from *AMS-02* show a break in the helium spectrum at the same rigidity which is promising for this interpretation [28]. The *Fermi*-LAT proton cosmic-ray spectrum measurement could put constraints on the population of old weak SNRs. This can be used to enhance our understanding of cosmic-ray acceleration from older SNRs in a way that would be difficult for γ-ray observations.

7.3 Propagation

The second assumption is that diffusion of cosmic rays is described by a power-law spectrum with a single spectral index and is homogeneous across the entire Galactic disk and halo. This would produce a single offset across the entire energy range as described in § 2.5.1. One possible change to diffusion is through inclusion of self-generating magnetic field turbulence in the ISM [132]. 'Normal' diffusion occurs from cosmic rays interacting with the turbulent magnetic field present in the Galactic spiral arms, but self-generating turbulence can occur at lower energies and dominates over Galactic magnetic turbulence. This is done by adding a self-generating term to the diffusion term of Equation 2.22 as

$$\nabla \cdot (D_i \nabla \mathcal{N}_i) \rightarrow \nabla \cdot (D_i \nabla \mathcal{N}_i) + \Gamma_{CR} \mathcal{N}_i \tag{7.5}$$

where Γ_{CR} is defined as the generation of wave power through cosmic ray streaming instability

$$\Gamma_{CR} = \frac{16\pi^2}{3} \frac{v_A}{k \mathcal{W}_i B_0^2} \sum_j \left[p^4 v(p) \frac{\partial \mathcal{N}_j}{\partial z} \right]_{p = Z_j e B_0 / kc} \tag{7.6}$$

where i is the individual cosmic-ray species, j is summed over all cosmic ray species, B_0 is the Galactic magnetic field strength, z is the height from the center of the disk, v_A the Alfven velocity of the ISM, k is the wave number of the cosmic ray, p is the momentum of the cosmic ray, and $\mathcal{W}$ is the wave power spectrum of all cosmic ray species. This will generate a steeper diffusive component at low energies thereby producing a break at a ∼100 GeV [132].

A second possible interpretation considers using a two halo model and height-

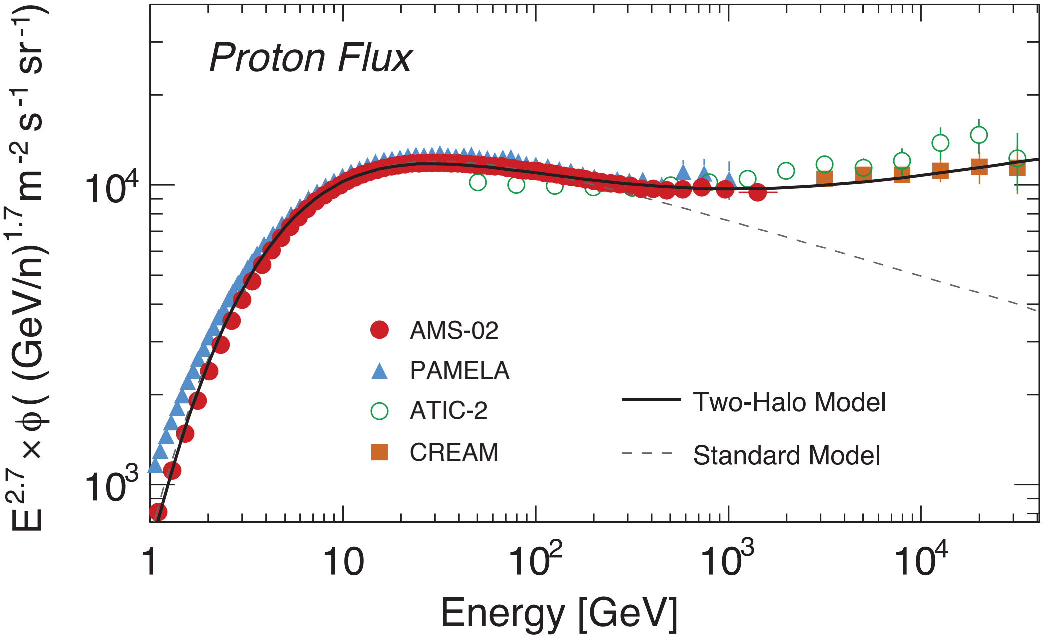

Figure 7.6: Proton cosmic-ray spectrum fit using a two halo model for cosmic-ray diffusion showing evidence for a break in the spectrum at ∼100 GeV. The standard model shown with the dashed line and two halo model shown with sold line using data from *CREAM-1*, *PAMELA*, *ATIC*, and *AMS-02* [133].

dependent spectral index of cosmic-ray diffusion [133]. This model has two halos with different diffusion properties where the first halo is dominated by contributions from the turbulent disk and the second halo is dominated by contributions from the self-generated cosmic-ray turbulence described above. Additionally the spectral index of the diffusion coefficient is allowed to be a function of height from the disk as a simple piecewise function of $\delta_i = 0.15$ and $\delta_o = 0.75$. For standard diffusion models, a halo single diffusion coefficient typically has a value of $\delta = 0.55$. Propagating a standard injection spectrum of cosmic rays through this model can create a spectral break at ∼100 GeV as seen in Figure 7.6. A standard single halo model cannot reproduce the break. Evidence for spatial dependence of cosmic-ray diffusion can be seen through diffuse γ-ray observations near and off the Galactic disk [134, 135]. These alternative propagation models can easily recreate the observed spectral breaks seen in several cosmic-ray species but fail to address the difference between the proton-helium ratio seen by *AMS-02* and massively under-produce the cosmic-ray positron flux observed by several experiments [28, 133]. The *Fermi*-LAT cosmic-ray proton spectrum measurement does limit the effects of self-generating cosmic rays in both the Galactic disk and the two component halo model. This has the effect of an increase of the energy range in which self-generating cosmic-ray turbulence has a dominant effect.

7.4 Source Distribution

The last assumption is based on an isotropic distribution of cosmic-ray accelerators throughout the Galactic disk. An interpretation can be made by examining large scale anisotropy of cosmic rays to find a constraint on the distance and age of a local SNR [136]. Assuming a local SNR with magnetic field strength typically seen in old SNRs, $\sim 0.3\mu$G, dipole measurements of cosmic-ray anisotropy from 100 GeV to 10 PeV can be fit with a 2 Myr old SNR within 200 pc with a maximum acceleration energy greater than 1 PeV. This local SNR is able to produce not only a spectral break at few 100 GeV but also account for the TeV anisotropy observations [136]. This interpretation also accounts for the positron and anti-proton excess observed by *AMS-02* and other cosmic-ray detectors [137]. Additionally, a

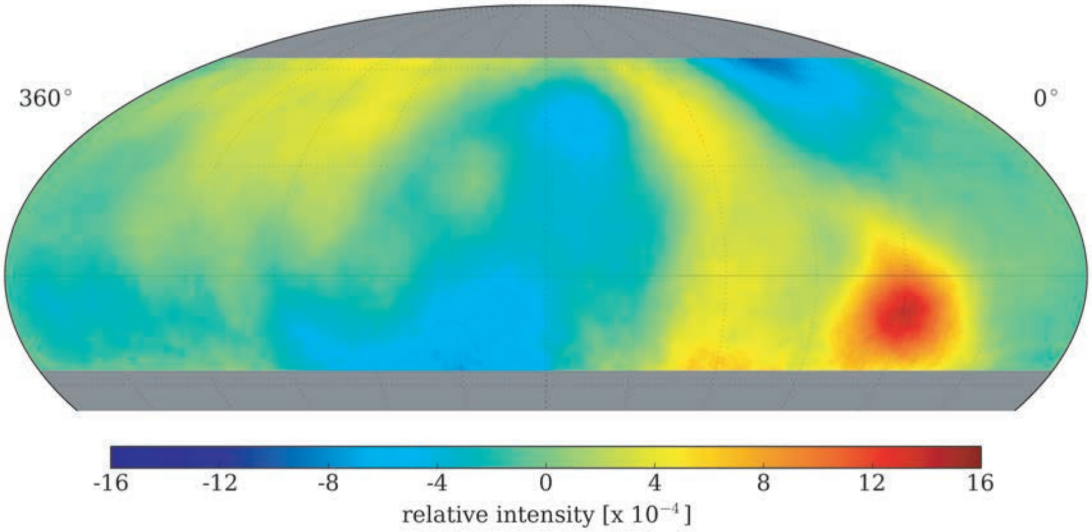

Figure 7.7: All particle cosmic-ray anisotropy measured by *HAWC* above $\sim$ 2 TeV in units of relative intensity [31].

local source does not require any changes to cosmic-ray propagation. Such a SNR would be large, over 100 degrees across the entire sky, and difficult to observe in either radio or γ-ray energy bands and difficult to disentangle from Galactic diffuse measurements. A number of candidates exist, such as SNRs associated with Vela and Geminga, which both have an estimated distance of around 250 pc. A single 2 Myr old SNR would be impossible to observe via current γ-ray observations. γ-ray emission would be extremely faint and low energy, near 70 MeV, which is on the lower end of the *Fermi*-LAT energy range. Additional local features exist like Loop 1 and the Local Bubble which are probable features from an old SNR. The spectral break could also result from a distribution of local old SNRs which the γ-ray diffusive measurements could help explain.

An alternative interpretation is to examine an ensemble of local cosmic-ray

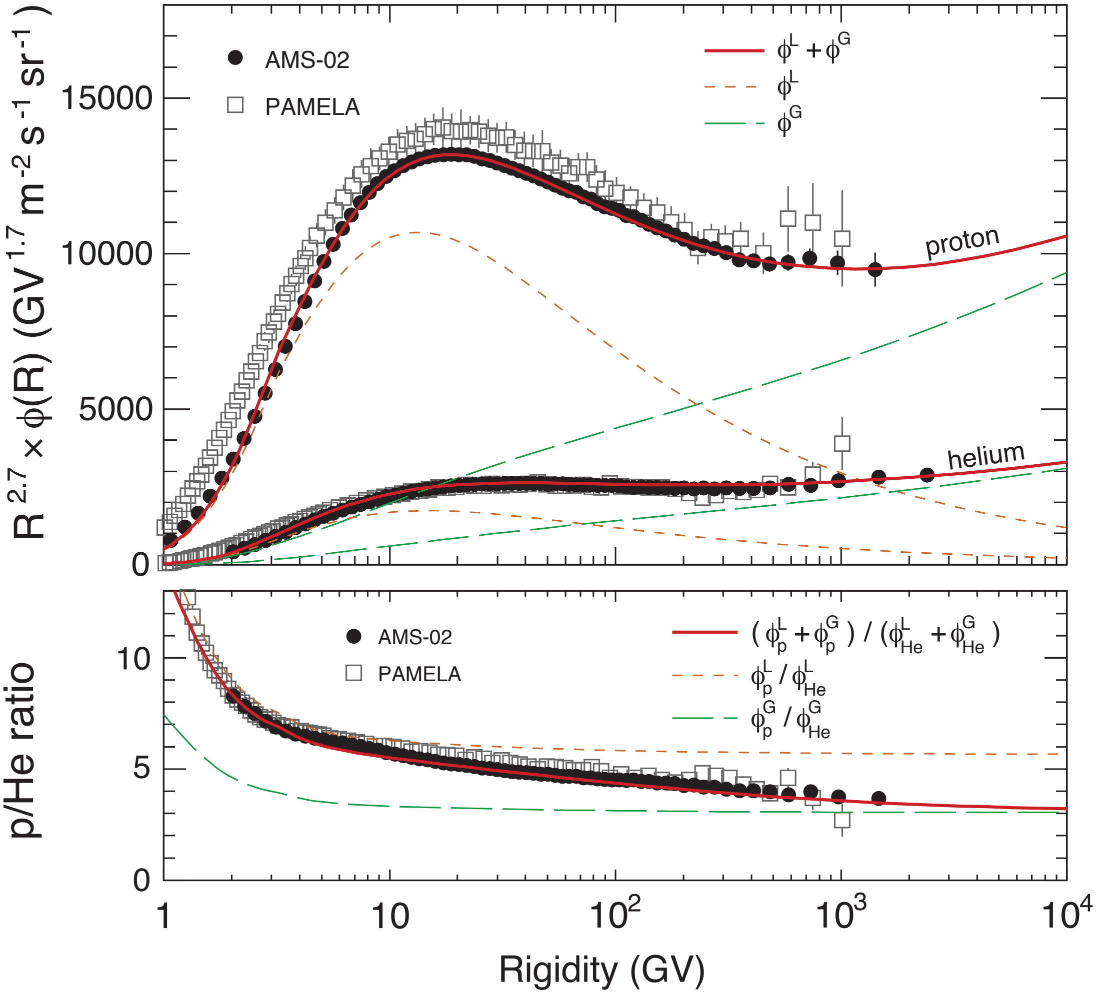

Figure 7.8: The cosmic-ray proton and helium spectra measured in rigidity by *AMS-02* modeled with a two component flux distribution. The first component refers to local old SNR and the second component refers to a Galactic ensemble of SNRs. Proton and helium spectra are fit with the same distribution parameters. The ratio between proton and helium cosmic rays is also shown [138].

accelerators. Recent observations shown in Figure 7.7 at TeV energies from ground based all-particle measurements have shown that cosmic rays do not arrive in an isotropic distribution but have large scale features on the order of 10^{-3} of relative intensity [29–31]. Since these cosmic rays fall within the energy range of Galactic cosmic-rays, one interpretation is an ensemble of local sources of cosmic rays within a few 100 pc and, therefore, have not traversed enough through the Galaxy to have their directions randomized through interactions with Galactic magnetic fields.

Using two distributions of cosmic-ray accelerators, the first being an ensemble of local and old SNRs with weak shocks and the second being an ensemble of Galactic SNRs, one can generate and propagate cosmic rays through the standard propagation equation [138]. The accelerator distributions are defined in terms of rigidity, $\mathcal{R}$, with

$$Q_i = Y_i \times (\mathcal{R}/\mathcal{R}_0)^{-\nu} e^{-\mathcal{R}/\mathcal{R}_{max}} \tag{7.7}$$

where i determines the cosmic-ray species, Q is the source term, Y is the normalization term ,$\mathcal{R}_0 = 4GV$, ν is the spectral index of the source distribution, and $\mathcal{R}_{max}$ is the maximum possible accelerator rigidity set to 5 PV. As stated previously in § 7.2, old SNRs will have a lower Mach number and therefore a larger spectral index for low energy cosmic rays, therefore the spectral index for a local SNR is $\nu = -2.6$ and for the Galactic SNR ensemble $\nu = -2.1$. The results of this model are shown in Figure 7.8. For higher rigidities the observed proton spectra has a predicted spectral index of $\gamma^G = \nu^G - \delta = -2.6$ [138]. This value is within the error from the broken power-law fits to the *Fermi*-LAT cosmic-ray spectrum measurement seen in Figures 7.2 and 7.3. Such a distribution of SNRs or objects would be ideal candidates for a new class of wide field low energy γ-ray observatories such as the proposed *ComPair* [139] and *e-ASTROGAM* [140]. The *Fermi*-LAT provides a single measurement from 54 GeV to 9.5 TeV which crosses the energy range of the multi-component distribution of local SNRs and Galactic ensemble of SNR.

All alternative interpretations discussed in § 7.2, § 7.3, and § 7.4 can reproduce the break in the proton spectrum observed by the *Fermi*-LAT but these interpretations do not exist in a vacuum. Any changes that are made to the proton spectrum need to be calculated and propagated through all cosmic-ray species and potential γ-ray observations. Among all alternative interpretations, I prefer the source distribution interpretation. It not only provides the observed spectral break in cosmic-ray protons, it can reproduce spectral breaks seen in other species and the observed cosmic-ray ratios, which is difficult for other models changing cosmic-ray acceleration. Cosmic-ray electron and positron ratios are also well reproduced, which is difficult for scenarios such as re-acceleration and propagation. Additionally, it provides a possible explanation for the large scale cosmic-ray anisotropy observed in TeV energies by ground based cosmic-ray observatories. Finally, a local distribution of cosmic-ray accelerators can potentially be confirmed through diffusive γ-ray observations in diffusive γ-ray observations.

7.5 Future of Interpretations

The cosmic-ray proton spectrum provides a rich opportunity for the exploration of the cosmic-ray paradigm in acceleration, propagation, and origins. Alternative interpretations need to be taken in context with other cosmic-ray measurements such as primary-primary ratios, secondary-primary ratios, and anti-matter measurements. Source injection interpretations can be constrained through additional γ-ray SNR observations. SNR populations could studied with sub-degree point spread function with, MeV γ-ray observatories to determine the hadronic fraction of total observed γ-ray flux. Propagation interpretations can be constrained through further primary to secondary cosmic-ray ratio and observations of cosmic-ray electrons. Further *AMS-02* measurements and future cosmic-ray observatories: *DAMPE* [141], *CALET* [142], and *ISS-CREAM* [143], can extend primary to secondary ratios to higher energies and confirm or exclude predicted behavior. Source distribution interpretations can be explored through diffuse γ-ray observations. A local ensemble of accelerators would emit large scale low energy γ-rays with possibly distinguishable signals for diffuse γ-ray produced through cosmic-ray interactions. This ensemble could be resolved through future γ-ray studies.

The *Fermi*-LAT and its ability to measure the cosmic-ray proton spectrum to beyond 1 TeV allows for the detection of spectral break independently from other observations. This provides a conformation of an overall consistency among current measurements with different observational techniques. The *Fermi*-LAT also provides an opportunity to observe physical features of the Galaxy which are difficult or impossible to detect with other methods. The *Fermi*-LAT proton spectrum measurement establishes a foundation for other cosmic-ray measurements to be performed with the LAT, such as a dedicated proton anisotropy measurement or studies with other cosmic-ray species, as discussed in Chapter 8.

Chapter 8: Future of LAT Cosmic-ray Studies

The spectral analysis and associated event selection creates opportunities to perform new cosmic-ray observations with Fermi. Two such possibilities are cosmic-ray proton anisotropy and cosmic-ray ion measurements.

8.1 Proton Anisotropy Studies

One such observation is an all-sky proton cosmic-ray anisotropy measurement. Recent measurements from *HAWC* [31], *IceCube* [30], and *TIBET III* [144] of TeV energy all particle cosmic-rays have shown a significant spatial anisotropy in the cosmic-ray flux, as seen in Figure 7.7. Such a measurement requires a very large set of data but fortunately does not require a good energy resolution. Therefore, we could relax the event selection cuts to increase event rate. As shown in Figure 6.2, removing the energy resolution cuts and relaxing the track reconstruction cuts could potentially increase the proton acceptance to over 2 m^2 sr. The *Fermi*-LAT is currently the only detector able to perform an all-sky space-based proton only anisotropy measurement. With the larger proton acceptance over seven years of flight data, the *Fermi*-LAT could measure an estimated 1×10^9 events.

8.2 Cosmic-ray Ion Studies

The spectral analysis also enables the spectral measurement of cosmic-ray ions such as boron and carbon. The boron-carbon ratio is a standard secondary to primary ratio measurement since boron is predominantly secondary cosmic rays. Boron is not the end product of stellar nucleosynthesis or a significant result of Big Bang nucleosynthesis, therefore understanding boron in relation to carbon provides a powerful probe for cosmic-ray propagation. The energy dependence of the boron-carbon ratio goes as $\mathcal{N}_B/\mathcal{N}_C \quad \propto \quad E^{\delta}$ where $\delta \sim -0.6$. This is a direct result of diffusion in cosmic ray propagation. At higher energies, the data decreases in quality, thus the power-law index begins to vary from -0.3 to -0.8 due to imprecise measurements.

Figure 8.1 shows several previous experiments' measurements, both balloon-borne and satellite, of the boron-carbon ratio. The LAT has several advantages over previous satellite and balloon-borne experiments. It is above the atmosphere thus, unlike balloon-borne experiments, the LAT has little residual atmospheric contamination. Atmospheric contamination becomes very important at high energies; carbon cosmic rays begin to spallate in the atmosphere creating atmospheric boron. Atmospheric boron is indistinguishable from stellar boron. The magnitude of the effect on B:C is still relativity unknown since the magnitude of atmospheric boron contamination is unknown at high energies. The LAT also has the advantage of having a large geometric factor, mostly due to its long lifetime, thus, statistical uncertainty in the LAT measurement should be low.

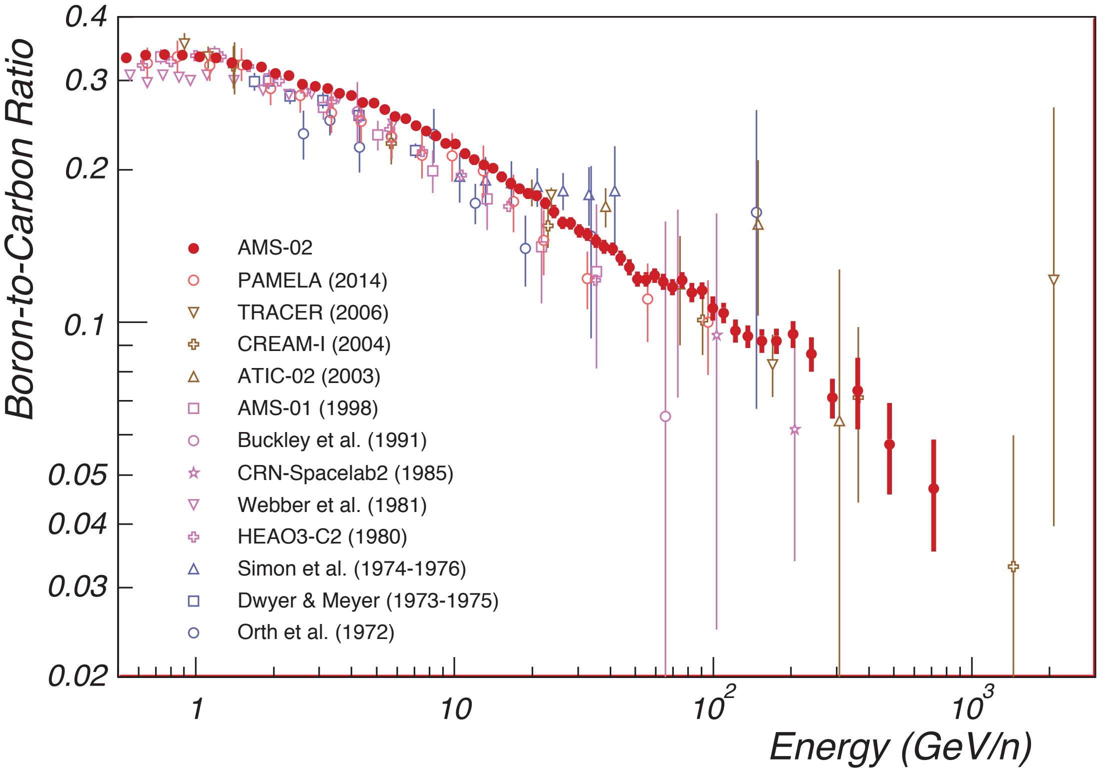

Figure 8.1: The boron to carbon vs kinetic energy per nucleon [GeV/nuc] from 0.5 GeV/nuc to 2 TeV/nuc for many different cosmic-ray measurements [48].

To measure the boron-carbon ratio, we need to measure charge and energy of heavy cosmic rays. We want to use the ACD's high range as independently as possible to measure charge of heavy cosmic rays. While the ACD is an excellent charge detector with a 99.97% particle detection efficiency, under current calibrations it has very poor charge resolution [71]. Improving calibrations should improve charge resolution. We call the method to improve the charge resolution the Flattening method.

The basic idea is to use a series of cuts to skim cosmic-ray ions from the data. We can alter the charge cuts shown in Chapter 4 to select on cosmic-ray ions

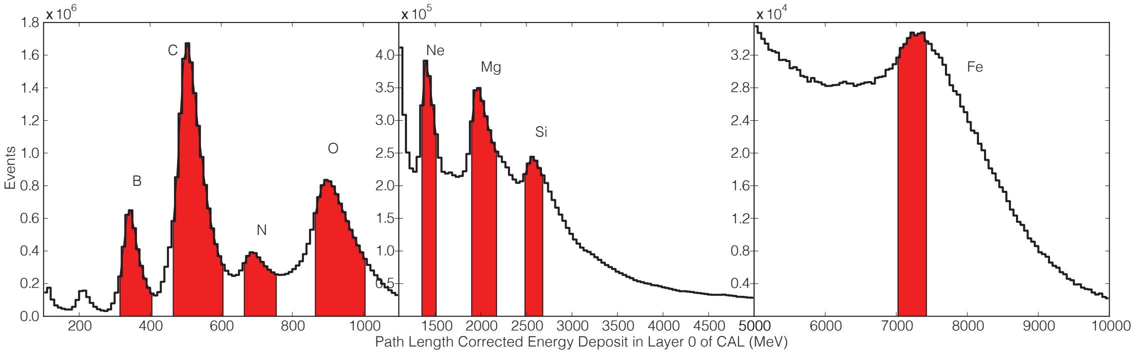

Figure 8.2: Path length corrected energy deposition in the 0th layer of the CAL. Red areas indicate selection used for calibration sample.

instead of removal. We then measure the charge of the cosmic ray ions using the CAL and split the data up according to their element. Individual CAL crystals have very good energy resolution, as seen in Figure 8.2. This data subset is called the calibration subset. The calibration needs to be as uniform as possible: single element, mono-energetic, and well reconstructed. Each element is binned according to the position of the track intersection in the ACD. We fit the ACD signal in each bin for all elements with a Gaussian distribution. ACD signal is recorded in pulse height amplitude, PHA, which has been pedestal subtracted and path length corrected. The fitted peaks are used to create a response map for each element and each PMT. Once we have a response map of the ACD for each element, we take the average of the peaks over the 'pixels' for each element. We then find the flattening corrections necessary to align each 'pixel' of each element to the average peak for that element. Once we have the flattening corrections, we apply those corrections to the ACD signal in the entire heavy cosmic ray data set.

To build the calibration set of data we use the CAL to find the charge of cosmic-ray ions. We want each element to deposit energy consistent with its minimum ionizing value in the zeroth layer of the CAL. This ensures that the events selected for each element are at the same energy. We use the CAL to select on charge initially since the CAL has a much better charge resolution than the ACD. This creates a uniform mono-energetic sample of heavy cosmic rays for that specific element. We select on the energy deposition for each element in the zeroth layer of the CAL. We can see in Figure 8.2 eight distinguishable elements in the heavy cosmic ray data: boron, carbon, nitrogen, oxygen, neon, magnesium, silicon, and iron. Once we have our calibration sample for each element, we can begin to calculate the flattening corrections.

The next step is to bin the calibration data based on the intersection of the best track with the ACD. Each bin, or ‘pixel’, has a number of events and we fit the distribution of events with a Gaussian distribution. Figure 8.3 shows a single ‘pixel’ fitted with a Gaussian distribution. We record the peak, width, and associated errors of the Gaussian fit for each ‘pixel’. Each PMT is treated separately to account for potential unknown electronic factors. The process is repeated for all ‘pixels’ and each calibration element. The minimum ‘pixel’ size is based on error in the track reconstruction. We determine the ‘pixel’ size by the number of events in each ‘pixel’. Each ‘pixel’ needs enough events to be well fit with a Gaussian distribution.

Once we have fitted all bins for all elements, we have a response map for the whole ACD for each heavy cosmic-ray element. Pixelization reveals in Figure 8.5(a) the non- uniformity within and between tiles. The ACD measures a different signal for a carbon cosmic ray depending on the location of cosmic ray ion entering the

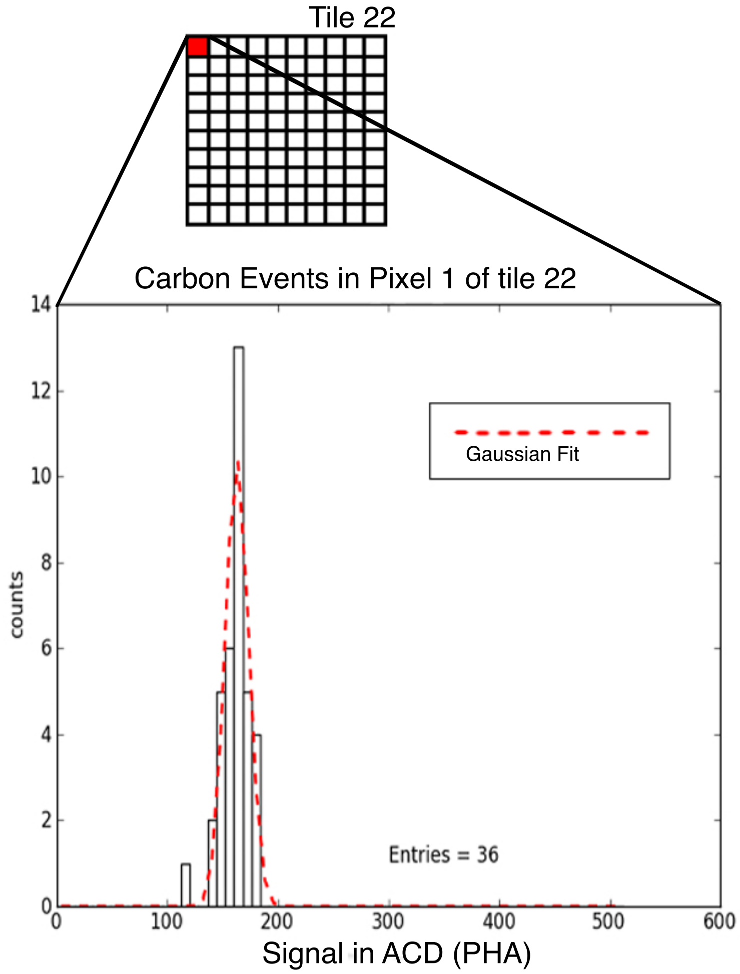

Figure 8.3: Events and a Gaussian fit for the carbon event distribution in a single pixel of tile 22 of the ACD.

LAT. The Flattening method intends to make the signal in the ACD uniform with respect to individual elements. A uniform signal across the ACD should improve the ACD's charge resolution.

Next, we flatten the ACD's response and improve uniformity. Once the response map for each calibration element and each PMT is created, we can flatten the response of the ACD. First, we find the average signal over all 'pixels' for each heavy cosmic ray element and each PMT. We then plot the signal for each element

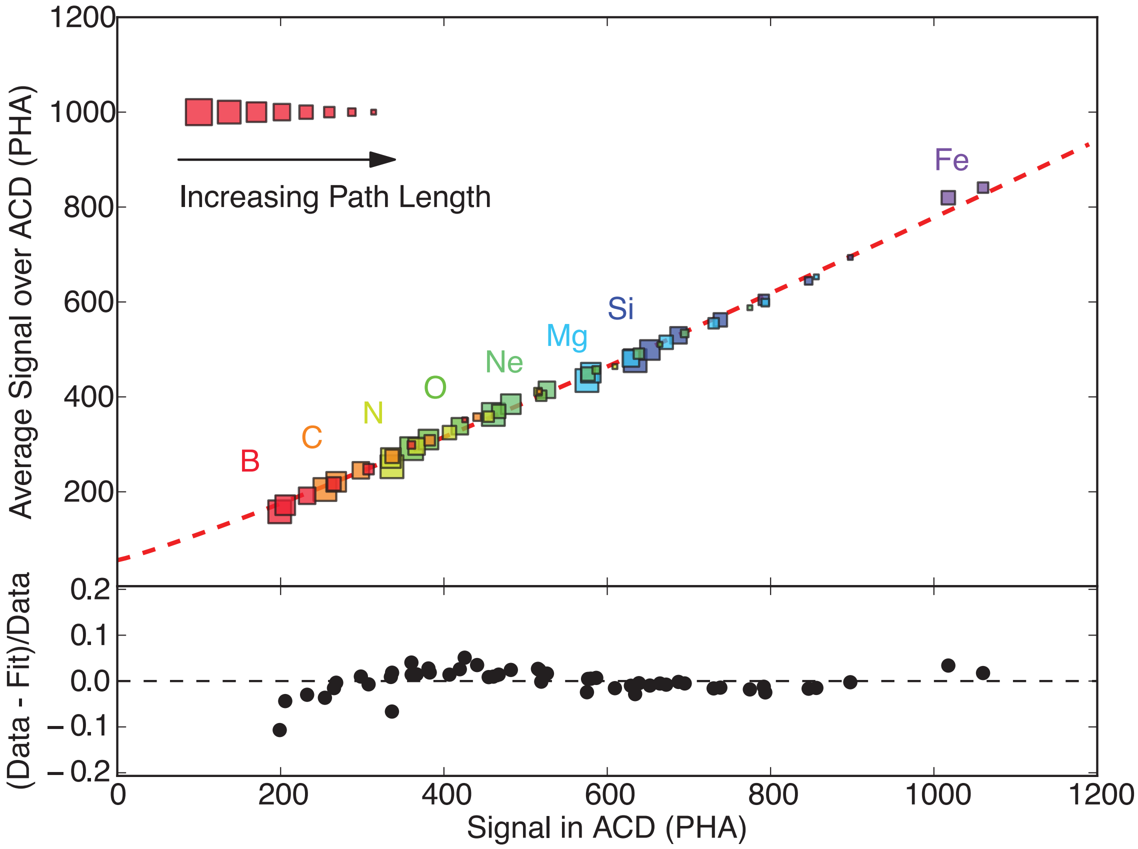

Figure 8.4: The top plot shows the fit to find the flattening correction for a single pixel in the ACD. The bottom plot shows the relative residuals for the fit

from a 'pixel' vs the average signal for each element for all 'pixels'. We fit the plot with the second order polynomial:

$$S_{flat}(\mathrm{PHA}) = a_i + b_i S(\mathrm{PHA}) + c_i S(\mathrm{PHA})^2 \tag{8.1}$$

This function aligns the signal in each 'pixel' to the average signal over all 'pixels'. Each 'pixel' has three unique coefficients. We can see the fit for a single 'pixel' and the associated flattening corrections in Figure 8.4. Applying these corrections to the ACD signal will produce a uniform signal in the ACD for each cosmic-ray species. Applying these flattening corrections to the entire cosmic ray ion data set gives us

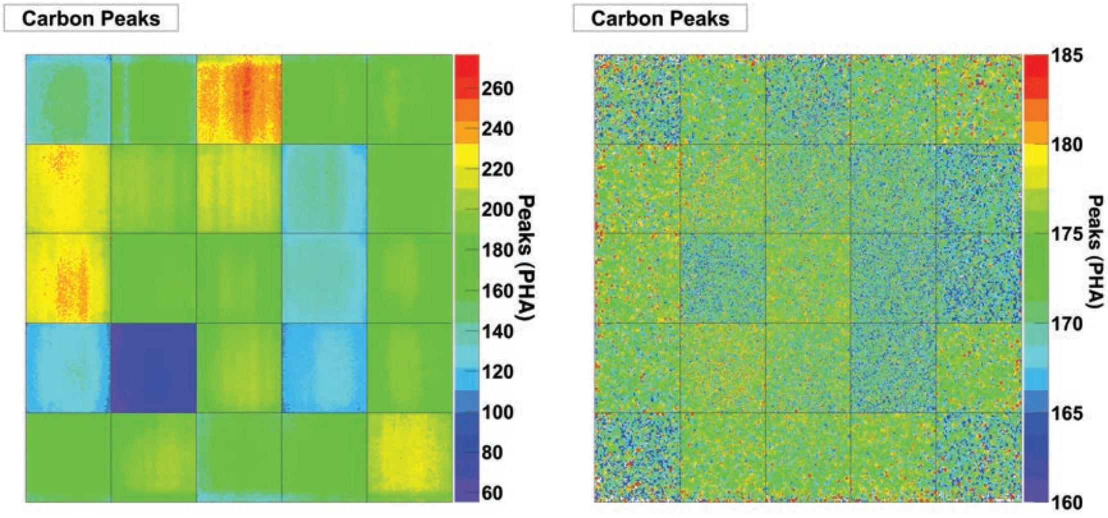

(a) Carbon peak in PHA not flattened (b) Carbon peak in PHA flattened

Figure 8.5: Carbon peaks in PHA before and after applying the flattening algorithm.

the cosmic ray ion data set with flattened ACD signal.

Taking the set of carbon calibration events from the new flattened data and making the response maps with the same method done with Figure 8.5(a) gives Figure 8.5(b). There are certain irregular 'pixels'; these are mostly likely due to poor fitting of the flattening corrections or poor peak fitting.

Figure 8.6 shows improvement to the charge resolution in the ACD across all detected cosmic-ray species. Clearly, flattening the response has improved ACD's charge resolution. Carbon, oxygen, and iron peaks become more refined after flattening. Additional peaks of neon, magnesium, and silicon appear where there was no evidence of such before flattening. We also see boron and nitrogen shoulders from their more dominant primaries. The apparent boron peak in the unflattened data is not actually boron but is due to the large range of carbon signal in the ACD. There

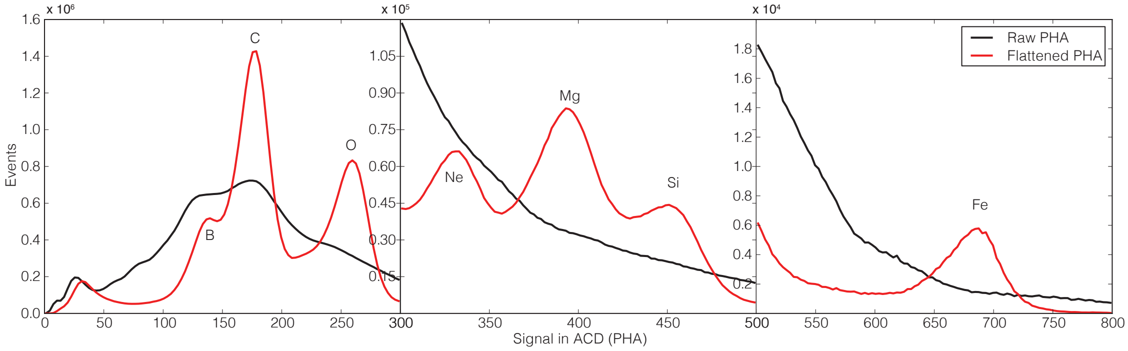

Figure 8.6: Shows the signal in the ACD with various methods of flattening. Black represents the unflattened signal. Red represents the flattened signal with pixelized data.

is a similar affect with iron. There appear to be several sources in the unflattened data, but in reality, this just demonstrates the range in PHA that iron spans in the unflattened data. We can now use the ACD as a charge selector for cosmic-ray ions.

One of the next major steps in cosmic-ray ion studies is estimating the response matrix and energy measurement for cosmic-ray ions. The proton analysis estimates the response and produces acceptance and response matrices using GEANT4 simulations discussed in Chapter 6. This cannot currently be done with cosmic-ray ions and GEANT4. As shown in Figure 4.10, GEANT4 has limited success in recreating the response for ions and because of this we cannot use current simulations to reconstruct the boron-carbon ratio. Alternative Monte-Carlo software can be used, such as FLUKA, which have been shown to better simulate hadrons at higher energies but this would require a major effort to implement FLUKA with the current *Fermi* software [145]. Limited beam-test studies were performed using low energy ions but there were not enough configurations at high enough energies to properly calibrate new Monte-Carlo simulations with the beam-test data.

Several new space-based cosmic-ray experiments have recently launched or will launch in the near future which will measure energies well beyond what is currently possible. They will also provide high precision measurements for multiple cosmic-ray species further elucidating the state of cosmic-ray physics.

8.3 Future Cosmic-ray Missions

Three new dedicated space based cosmic-ray missions have been launched or will launch in the near future, *DAMPE* [141], *CALET* [142], and *ISS-CREAM* [143]. *DAMPE* and *CALET* have very similar designs to the *Fermi*-LAT: large acceptance and field of view with a basic tracker and electromagnetic calorimeter, but have several key improvements over *Fermi*-LAT. Their calorimeters are much larger, both are over twice the depth of the CAL, and each features dedicated CCD charge detectors on the top of the respective instruments. *DAMPE* is a free flying satellite while *CALET* is on the International Space Station like *AMS-02*. *ISS-CREAM* is also attached to the International Space Station and has the benefits of several independent charge detectors and a hadronic calorimeter. Additionally, *DAMPE*, *CALET*, and *ISS-CREAM* each underwent extensive beam testing to measure the response of the instrument to leptons and hadrons therefore reducing the dependence on Monte-Carlo simulations for energy measurements and spectral reconstruction. These new detectors have an estimated energy range from several GeV to >10 TeV and in the case of *ISS-CREAM* to 100 TeV, but in order to build enough statistics for beyond 10 TeV measurements, years of data collection is required.

Direct measurements of the cosmic-ray proton spectrum are leading to improved understanding of our Galaxy, the physics of particle acceleration and, in combination with recent gamma-ray measurements, possible origins for cosmic rays.

Appendix I: Variables of Merit

Location for description of LAT variables of merit used in this analysis.

`Acd2Cal1TriggerEnergy15`: The energy deposited in the ACD tiles in a 15° cone with vetoes around the reconstructed direction from the CAL in units of MeV.

`Acd2Tkr1TileActDistEnergy`: The energy deposited in the ACD tile intersecting with the best track from the TKR and corrected for the different tile widths between the top and side LAT tiles in units of MeV.

`Cal1XDir`: The reconstructed direction of the moment of inertia tensor of the particle shower in the CAL cosine in the X direction of the particle.

`Cal1YDir`: The reconstructed direction of the moment of inertia tensor of the particle shower in the CAL cosine in the Y direction of the particle.

`Cal1ZDir`: The reconstructed direction of the moment of inertia tensor of the particle shower in the CAL cosine in the Z direction of the particle. Top is defined as `Cal1ZDir` > 0 and bottom as `Cal1ZDir` < 0.

`CalEnergyRaw`: The sum of the deposited energy in the CAL from all crystals in units of MeV.

`CalLeakCorr`: An estimation of the fraction of leakage of the shower out of the CAL assuming an electromagnetic shower.

`CalNewCfpCalPar0`: The first fit parameter from the profile fit method described in § 5.2.2 used in determining `CalNewCfpCalEnergy`.

`CalNewCfpCalPar1`: The second fit parameter from the profile fit method described in § 5.2.2 used in determining `CalNewCfpCalEnergy`.

`CalNewCfpCalEnergy`: The reconstructed energy using the profile fit method described in § 5.2.2 using the reconstructed direction from the CAL as the primary axis of the shower in units of MeV.

`CalNewCfpPar0`: The first fit parameter from the profile fit method described in § 5.2.2 used in determining `CalNewCfpEnergy`.

`CalNewCfpPar1`: The second fit parameter from the profile fit method described in § 5.2.2 used in determining `CalNewCfpEnergy`.

`CalNewCfpEnergy`: The reconstructed energy using the profile fit method described in § 5.2.2 using the best track from the TKR as the primary axis of the shower in units of MeV.

`CalTrackAngle`: The difference between the reconstructed TKR and CAL directions measured in radians.

`GltGemLiveTime`: The number of 50 ns ticks of the Fermi on-board clock from start of the mission.

`Tkr1LengthInCal`: The geometric path of the particle in the CAL, minus the distance traveled in gaps and non-active material, taken from the best track determined by the TKR in units of mm.

`Tkr1ToTTrAve`: The average time over threshold measurement for all hits in the tracker from a single event removing the largest and smallest time over threshold measurements in units of MIPs.

`Tkr1XDir`: The reconstructed direction cosine of the best track from the TKR in the X direction of the particle.

`Tkr1YDir`: The reconstructed direction cosine of the best track from the TKR in the Y direction of the particle.

`Tkr1ZDir`: The reconstructed direction cosine of the best track from the TKR in the Z direction of the particle. Top is defined as `Tkr1ZDir` < 0 and bottom as `Tkr1ZDir` > 0.

`TkrNumTracks`: The number of tracks found in TKR reconstruction.

`TkrTree1ThickRLnNodes`: The number of nodes in the thick layers of the TKR normalized the path-length in radiation lengths of material traversed.

`McEnergy`: The generated kinetic energy of the simulated particle in units of MeV.

`McXDir`: The generated direction cosine in the X direction of the simulated particle.

`McYDir`: The generated direction cosine in the Y direction of the simulated particle.

`McZDir`: The generated direction cosine in the Z direction of the simulated particle. Top is defined as `McZDir` < 0 and bottom as `McZDir` > 0.

`WP8CTPSFTail`: A multivariate classifier variable which trained on simulations where signal is defined as a well reconstructed track such that the difference between TKR directions and MC directions is under 1 degree.

Appendix II: List of Cuts

The specific cuts used in this analysis on variables of merit.

Trigger and Filter cuts.

```
CUT_TRIGGER_FILTER =
(GltGemSummary&0x20) == 0 && (GltGemSummary&0x40) == 0
&& FswGamState == 0
```

Track energy cuts.

```
CUT_TRACK_ENERGY = TkrNumTracks > 0 && CalEnergyRaw > 20000
```

TKR recon cuts.

```
CUT_TRACK_RECON = WP8CTPSFTail > 0.5 && CalTrackAngle < 0.3
```

Loose ion cut.

```
CUT_NUCLEI_LOOSE = Tkr1ToTTrAve > 0.75 && Tkr1ToTTrAve < 7.0 &&
(237.0/250.0 - 16.0*Tkr1ToTTrAve/250.0)
> log10(Acd2PLCTkr1TileActDistEnergy) &&
(-149.0/500.0 + 32.0*Tkr1ToTTrAve/500.0)
< log10(Acd2PLCTkr1TileActDistEnergy)
```

Tight ion cut.

```
CUT_NUCLEI_TIGHT = Acd2Cal1TriggerEnergy15 < 10
```

CAL Saturation Parameters cut.

```
CUT_SATURATED_CAL_PARAMS =

(CalNewCfpPar0 < 4.999 && CalNewCfpPar1 > -4.999) &&

(CalNewCfpCalPar0 < 4.999 && CalNewCfpCalPar1 > -4.999)
```

Path length in CAL cut.

```
QUAL_CUT_Len200 = Tkr1LengthInCal > 200.0
```

CAL Leakage cut.

```
QUAL_CUT_LEAKCORR25 = CalLeakCorr > 0.25
```

CAL shower and back-splash cut.

```
QUAL_CUT_THICKNODES = TkrTree1ThickRLnNodes < 10
```

Bibliography

[1] A. D. Panov et al. Energy spectra of abundant nuclei of primary cosmic rays from the data of atic-2 experiment: Final results. *Bulletin of the Russian Academy of Sciences: Physics*, 73(5):564–567, 2009.

[2] Y. Shikaze et al. Measurements of 0.2–20 gev/n cosmic-ray proton and helium spectra from 1997 through 2002 with the {BESS} spectrometer. *Astroparticle Physics*, 28(1):154 – 167, 2007.

[3] Y. S. Yoon et al. Cosmic-ray proton and helium spectra from the first cream flight. *The Astrophysical Journal*, 728(2):122, 2011.

[4] O. Adriani et al. Pamela measurements of cosmic-ray proton and helium spectra. *Science*, 332(6025):69–72, 2011.

[5] M. Aguilar et al. Precision measurement of the proton flux in primary cosmic rays from rigidity 1 gv to 1.8 tv with the alpha magnetic spectrometer on the international space station. *Phys. Rev. Lett.*, 114:171103, Apr 2015.

[6] M. G. Aartsen et al. Measurement of the cosmic ray energy spectrum with IceTop-73. *Phys. Rev.*, D88(4):042004, 2013.

[7] T. Antoni et al. KASCADE measurements of energy spectra for elemental groups of cosmic rays: Results and open problems. *Astropart. Phys.*, 24:1–25, 2005.

[8] M.A.K. Glasmacher et al. The cosmic ray energy spectrum between 10^{14} and 10^{16} ev. *Astroparticle Physics*, 10(4):291 – 302, 1999.

[9] A. Zech. A measurement of the uhecr spectrum with the hires fadc detector. *Nuclear Physics B - Proceedings Supplements*, 136:34 – 39, 2004.

[10] P. Abreu et al. The Pierre Auger Observatory I: The Cosmic Ray Energy Spectrum and Related Measurements. In *Proceedings, 32nd International Cosmic Ray Conference (ICRC 2011): Beijing, China, August 11-18, 2011*, 2011.

[11] J. D. Hunter. Matplotlib: A 2d graphics environment. *Computing In Science & Engineering*, 9(3):90–95, 2007.

[12] D. Pacini. La radiazione penetrante alla superficie ed in seno alle acque. *Il Nuovo Cimento (1911-1923)*, 3(1):93–100, 1912.

[13] V. F. Hess. Über Beobachtungen der durchdringenden Strahlung bei sieben Freiballonfahrten. *Physikalische Zeitschrift*, 13:1084–1091, November 1912.

[14] W. Kolhörster. Bemerkungen zu dem Referat des Herrn Kähler: #8222Die durchdringende Strahlung der Atmosphäre.“. *Naturwissenschaften*, 2:739–740, July 1914.

[15] R. A. Millikan and G. H. Cameron. The origin of the cosmic rays. *Phys. Rev.*, 32:533–557, Oct 1928.

[16] J. Clay, P.M. van Alphen, and C.G.'T Hooft. Results of the dutch cosmic ray expedition 1933. *Physica*, 1(7):829 – 838, 1934.

[17] P. Auger, P. Ehrenfest, R. Maze, J. Daudin, and R. A. Fréon. Extensive Cosmic-Ray Showers. *Reviews of Modern Physics*, 11:288–291, July 1939.

[18] P. Bassi, G. Clark, and B. Rossi. Distribution of Arrival Times of Air Shower Particles. *Physical Review*, 92:441–451, October 1953.

[19] Carl D. Anderson. The positive electron. *Phys. Rev.*, 43:491–494, Mar 1933.

[20] Seth H. Neddermeyer and Carl D. Anderson. Note on the nature of cosmic-ray particles. *Phys. Rev.*, 51:884–886, May 1937.

[21] C. M. G. Lattes, H. Muirhead, G. P. S. Occhialini, and C. F. Powell. Processes Involving Charged Mesons. *Nature*, 159:694–697, May 1947.

[22] G D Rochester and C C Butler. The penetrating particles in cosmic-ray showers: I. heavily-ionizing particles. *Proceedings of the Physical Society*, 61(4):307, 1948.

[23] P. S. Freier, E. P. Ney, and P. H. Fowler. Cosmic Rays and the Sunspot Cycle: Primary α-Particle Intensity at Sunspot Maximum. *Nature*, 181:1319–1321, May 1958.

[24] H. Aizu, Y. Fujimoto, S. Hasegawa, M. Koshiba, I. Mito, J. Nishimura, K. Yokoi, and M. Schein. Heavy Nuclei in the Primary Cosmic Radiation at Prince Albert, Canada. II. *Physical Review*, 121:1206–1218, February 1961.

[25] R. R. Daniel and S. A. Stephens. Electron Component of the Primary Cosmic Radiation at Energies greater than 15 GeV. *Physical Review Letters*, 15:769–772, November 1965.

[26] D. A. Bryant, T. L. Cline, U. D. Desai, and F. B. McDonald. Explorer 12 Observations of Solar Cosmic Rays and Energetic Storm Particles after the Solar Flare of September 28, 1961. *Journal of Geophysical Research*, 67:4983–5000, December 1962.

[27] E. C. Stone. A Measurement of the Primary Proton Flux from 10 to 130 Million Electron Volts. *Journal of Geophysical Research*, 69:3939–3945, October 1964.

[28] M. Aguilar, D. Aisa, B. Alpat, A. Alvino, G. Ambrosi, K. Andeen, L. Arruda, N. Attig, P. Azzarello, A. Bachlechner, and et al. Precision Measurement of the Helium Flux in Primary Cosmic Rays of Rigidities 1.9 GV to 3 TV with the Alpha Magnetic Spectrometer on the International Space Station. *Physical Review Letters*, 115(21):211101, November 2015.

[29] A. A. Abdo et al. The Large Scale Cosmic-Ray Anisotropy as Observed with Milagro. *Astrophys. J.*, 698:2121–2130, 2009.

[30] Paolo Desiati. Observation of TeV–PeV cosmic ray anisotropy with IceCube, IceTop and AMANDA. *Nucl. Instrum. Meth.*, A742:199–202, 2014.

[31] A. U. Abeysekara et al. Observation of Small-scale Anisotropy in the Arrival Direction Distribution of TeV Cosmic Rays with HAWC. *Astrophys. J.*, 796(2):108, 2014.

[32] M. Ackermann et al. Detection of the Characteristic Pion-Decay Signature in Supernova Remnants. *Science*, 339:807, 2013.

[33] T. Jogler and S. Funk. Revealing w51c as a cosmic ray source using fermi-lat data. *The Astrophysical Journal*, 816(2):100, 2016.

[34] K. A. Olive et al. Review of Particle Physics. *Chin. Phys.*, C38:090001, 2014.

[35] J A Simpson. Elemental and isotopic composition of the galactic cosmic rays. *Annual Review of Nuclear and Particle Science*, 33(1):323–382, 1983.

[36] K. R. Lang. *Astrophysical formulae.* 1999.

[37] T.K. Gaisser. *Cosmic Rays and Particle Physics.* Cambridge University Press, 1990.

[38] D. J. Bird, S. C. Corbato, H. Y. Dai, B. R. Dawson, J. W. Elbert, B. L. Emerson, K. D. Green, M. A. Huang, D. B. Kieda, M. Luo, S. Ko, C. G. Larsen, E. C. Loh, M. H. Salamon, J. D. Smith, P. Sokolsky, P. Sommers, J. K. K. Tang, and S. B. Thomas. The cosmic-ray energy spectrum observed by the Fly's Eye. *The Astrophysical Journal*, 424:491–502, March 1994.

[39] Enrico Fermi. On the origin of the cosmic radiation. *Phys. Rev.*, 75:1169–1174, Apr 1949.

[40] Leverett Davis. Modified fermi mechanism for the acceleration of cosmic rays. *Phys. Rev.*, 101:351–358, Jan 1956.

[41] Thomas K. Gaisser, Todor Stanev, and Serap Tilav. Cosmic Ray Energy Spectrum from Measurements of Air Showers. *Front. Phys.(Beijing)*, 8:748–758, 2013.

[42] H. S. Ahn et al. Energy spectra of cosmic-ray nuclei at high energies. *The Astrophysical Journal*, 707(1):593, 2009.

[43] O. Adriani et al. Pamela measurements of cosmic-ray proton and helium spectra. *Science*, 332(6025):69–72, 2011.

[44] A. M. Hillas. The Origin of Ultra-High-Energy Cosmic Rays. *ARA&A*, 22:425–444, 1984.

[45] Ray J. Protheroe. Effect of energy losses and interactions during diffusive shock acceleration: Applications to SNR, AGN and UHE cosmic rays. *Astropart. Phys.*, 21:415–431, 2004.

[46] V. L. Ginzburg and S. I. Syrovatskii. *The Origin of Cosmic Rays*. 1964.

[47] Y. Uchiyama, F. A. Aharonian, T. Tanaka, T. Takahashi, and Y. Maeda. Extremely fast acceleration of cosmic rays in a supernova remnant. *Nature*, 449:576–578, October 2007.

[48] A. Oliva. Precision Measurement of Boron to Carbon flux ratio in Cosmic Rays from 2 GV to 1.8 TV with the Alpha Magnetic Spectrometer on the International Space Station. In *Proceeings for The 34th International Cosmic Ray Conference*, volume ICRC2015, 2015.

[49] W. R. Binns et al. Observation of the 60fe nucleosynthesis-clock isotope in galactic cosmic rays. *Science*, 352(6286):677–680, 2016.

[50] Hans-Walter Rix and Jo Bovy. The Milky Way‘s stellar disk. *Astron. Astrophys. Rev.*, 21:61, 2013.

[51] A. W. Strong and I. V. Moskalenko. Propagation of cosmic-ray nucleons in the galaxy. *Astrophys. J.*, 509:212–228, 1998.

[52] Andrew W. Strong, Igor V. Moskalenko, and Vladimir S. Ptuskin. Cosmic-ray propagation and interactions in the Galaxy. *Ann. Rev. Nucl. Part. Sci.*, 57:285–327, 2007.

[53] M. Ackermann et al. Fermi large area telescope study of cosmic rays and the interstellar medium in nearby molecular clouds. *The Astrophysical Journal*, 755(1):22, 2012.

[54] M. Ackermann et al. Gamma-ray observations of the orion molecular clouds with the fermi large area telescope. *The Astrophysical Journal*, 756(1):4, 2012.

[55] R. Silberberg and C. H. Tsao. Spallation processes and nuclear interaction products of cosmic rays. *Physical Reports*, 191:351–408, August 1990.

[56] D. Müller, J. J. Connel, A. Decourchelle, R. Mewaldt, S. Reynolds, A. Strong, H. Völk, and M. Wiedenbeck. KEY MEASUREMENTS IN THE FUTURE - Working Group Report. *Space Science Reviews*, 99:353–373, October 2001.

[57] D. Breitschwerdt, J. F. McKenzie, and H. J. Voelk. Galactic winds. I - Cosmic ray and wave-driven winds from the Galaxy. *Astronomy and Astrophysics*, 245:79–98, May 1991.

[58] M. Su, T. R. Slatyer, and D. P. Finkbeiner. Giant Gamma-ray Bubbles from Fermi-LAT: Active Galactic Nucleus Activity or Bipolar Galactic Wind? *The Astrophysical Journal*, 724:1044–1082, December 2010.

[59] H. Nishino et al. Search for proton decay via $p \to e^+\pi^0$ and $p \to \mu^+\pi^0$ in a large water cherenkov detector. *Phys. Rev. Lett.*, 102:141801, Apr 2009.

[60] R. Cowsik and L. W. Wilson. The Nested Leaky-Box Model for Galactic Cosmic Rays. *International Cosmic Ray Conference*, 2:659, August 1975.

[61] A. W. Strong and I. V. Moskalenko. Models for galactic cosmic-ray propagation. *Advances in Space Research*, 27:717–726, 2001.

[62] F. Acero et al. Development of the model of galactic interstellar emission for standard point-source analysis of fermi large area telescope data. *The Astrophysical Journal Supplement Series*, 223(2):26, 2016.

[63] L. Maccione, C. Evoli, D. Gaggero, and D. Grasso. DRAGON: Galactic Cosmic Ray Diffusion Code. Astrophysics Source Code Library, June 2011.

[64] Katia M. Ferriere. The interstellar environment of our galaxy. *Rev. Mod. Phys.*, 73:1031–1066, 2001.

[65] Carmelo Evoli, Daniele Gaggero, Andrea Vittino, Giuseppe Di Bernardo, Mattia Di Mauro, Arianna Ligorini, Piero Ullio, and Dario Grasso. Cosmic-ray propagation with DRAGON2: I. numerical solver and astrophysical ingredients. 2016.

[66] M. N. Mazziotta, F. Cerutti, A. Ferrari, D. Gaggero, F. Loparco, and P. R. Sala. Production of secondary particles and nuclei in cosmic rays collisions with the interstellar gas using the FLUKA code. *Astropart. Phys.*, 81:21–38, 2016.

[67] F. Acero et al. The First Fermi LAT Supernova Remnant Catalog. *Astrophys. J. Suppl.*, 224(1):8, 2016.

[68] Yutaka Ohira, Norita Kawanaka, and Kunihito Ioka. Cosmic-ray hardenings in light of AMS-02 data. *Phys. Rev.*, D93(8):083001, 2016.

[69] W. B. Atwood, A. A. Abdo, M. Ackermann, W. Althouse, B. Anderson, M. Axelsson, L. Baldini, J. Ballet, D. L. Band, G. Barbiellini, and et al. The Large Area Telescope on the Fermi Gamma-Ray Space Telescope Mission. *ApJ*, 697:1071–1102, June 2009.

[70] A. A. Moiseev, J. F. Ormes, R. C. Hartman, T. E. Johnson, J. W. Mitchell, and D. J. Thompson. Observation and simulations of the backsplash effects in high-energy γ-ray telescopes containing a massive calorimeter. *Astroparticle Physics*, 22:275–283, November 2004.

[71] A. A. Moiseev, R. C. Hartman, J. F. Ormes, D. J. Thompson, M. J. Amato, T. E. Johnson, K. N. Segal, and D. A. Sheppard. The anti-coincidence detector for the GLAST large area telescope. *Astroparticle Physics*, 27:339–358, June 2007.

[72] M. Ackermann et al. The Fermi Large Area Telescope on Orbit: Event Classification, Instrument Response Functions, and Calibration. *ApJS*, 203:4, November 2012.

[73] J. E. Grove and W. N. Johnson. The calorimeter of the Fermi Large Area Telescope. In *Space Telescopes and Instrumentation 2010: Ultraviolet to Gamma Ray*, volume 7732 of *Proceedings of SPIE*, page 77320J, July 2010.

[74] W. B. Atwood et al. Design and initial tests of the Tracker-converter of the Gamma-ray Large Area Space Telescope. *Astroparticle Physics*, 28:422–434, December 2007.

[75] S. Agostinelli et al. GEANT4: A Simulation toolkit. *Nucl. Instrum. Meth.*, A506:250–303, 2003.

[76] K.D. Rakes. *Evaluating the Response of Polyvinyl Toluene Scintillators Used in Portal Detectors*. Biblioscholar, 2012.

[77] Carmelo Sgro. A minimum spanning tree clustering algorithm for the fermi lat calorimeter. In *2011 Fermi Symposium*, Rome, Italy, 2012.

[78] Tracy Usher. Performance of the track reconstruction for the fermi lat in pass 8. In *2012 Fermi Symposium*, Monterey, California, 2012.

[79] J. Alcaraz et al. Protons in near earth orbit. *Physics Letters B*, 472(1–2):215 – 226, 2000.

[80] T. Sanuki et al. Precise measurement of cosmic-ray proton and helium spectra with the bess spectrometer. *The Astrophysical Journal*, 545(2):1135, 2000.

[81] R. L. Golden et al. Measurement of the positron to electron ratio in the cosmic rays above 5 gev. *The Astrophysical Journal Letters*, 457(2):L103, 1996.

[82] W. R. Webber. *The Spectra of Cosmic Ray Nuclei $>$ 1 Gev/nuc — Implications for Acceleration and Propagation*, pages 25–45. Springer Netherlands, Dordrecht, 1983.

[83] G. Folger and J. P. Wellisch. String parton models in GEANT4. *eConf*, C0303241:MOMT007, 2003.

[84] Aatos Heikkinen, Nikita Stepanov, and Johannes Peter Wellisch. Bertini intranuclear cascade implementation in GEANT4. *eConf*, C0303241:MOMT008, 2003.

[85] Julia Yarba. Recent developments and validation of Geant4 hadronic physics. *J. Phys. Conf. Ser.*, 396:022060, 2012.

[86] Jerry B Marion. *Classical dynamics of particles and systems.* Academic Press, New York, NY, 1965.

[87] H. Bethe. Zur Theorie des Durchgangs schneller Korpuskularstrahlen durch Materie. *Annalen der Physik*, 397:325–400, 1930.

[88] John David Jackson. *Classical electrodynamics.* Wiley, New York, NY, 3rd ed. edition, 1999.

[89] R. M. Sternheimer. The density effect for the ionization loss in various materials. *Phys. Rev.*, 88:851–859, Nov 1952.

[90] James F. Ziegler. Comments on icru report no. 49: Stopping powers and ranges for protons and alpha particles. *Radiation Research*, 152(2):219–222, 1999.

[91] L. Landau. On the energy loss of fast particles by ionization. *J. Phys.(USSR)*, 8:201–205, 1944.

[92] P. Bruel and Fermi-LAT Collaboration. Gamma rays, electrons and positrons up to 3 TeV with the Fermi Gamma-ray Space Telescope. *Journal of Physics Conference Series*, 404(1):012033, December 2012.

[93] M. J. Berger, J. H. Hubbell, S. M. Seltzer, J. Chang, J. S. Coursey, R. Sukumar, D. S. Zucker, and K. Olsen. XCOM: Photon cross section database (version 1.5), 2010.

[94] M.A. Zucker M.J. Berger, J.S. Coursey and J. Chang. Stopping-power and range tables for electrons, protons, and helium ions, 2015.

[95] Egidio Longo and Ignazio Sestili. Monte carlo calculation of photon-initiated electromagnetic showers in lead glass. *Nuclear Instruments and Methods*, 128(2):283–307, October 1975.

[96] G. Grindhammer and S. Peters. The Parameterized Simulation of Electromagnetic Showers in Homogeneous and Sampling Calorimeters. *ArXiv High Energy Physics - Experiment e-prints*, January 2000.

[97] Fermi science support center: Pass 8 analysis and energy dispersion. http://fermi.gsfc.nasa.gov/ssc/data/analysis/documentation/Pass8_edisp_usage.html. Accessed: 2016-07-01.

[98] M. Ackermann et al. In-flight measurement of the absolute energy scale of the Fermi Large Area Telescope. *Astroparticle Physics*, 35:346–353, January 2012.

[99] D.F. Smart and M.A. Shea. A review of geomagnetic cutoff rigidities for earth-orbiting spacecraft. *Advances in Space Research*, 36(10):2012 – 2020, 2005. Solar Wind-Magnetosphere-Ionosphere Dynamics and Radiation Models.

[100] International Association of Geomagnetism and Working Group V-MOD. Aeronomy. International geomagnetic reference field: the eleventh generation. *Geophysical Journal International*, 183(3):1216–1230, 2010.

[101] M. Ackermann et al. Pass 8 Electron Spectrum. *PRL*, 2016.

[102] R. K. Bock, T. Hansl-Kozanecka, and T. P. Shah. Parametrization of the Longitudinal Development of Hadronic Showers in Sampling Calorimeters. *Nucl. Instrum. Meth.*, 186:533, 1981.

[103] Yu. A. Kulchitsky and V. B. Vinogradov. Analytical representation of the longitudinal hadronic shower development. *Nucl. Instrum. Meth.*, A413:484–486, 1998.

[104] D. Acosta et al. Lateral shower profiles in a lead/scintillating fiber calorimeter. *Nuclear Instruments and Methods in Physics Research A*, 316:184–201, June 1992.

[105] M. Aguilar et al. Precision measurement of the $(e^+ + e^-)$ flux in primary cosmic rays from 0.5 gev to 1 tev with the alpha magnetic spectrometer on the international space station. *Phys. Rev. Lett.*, 113:221102, Nov 2014.

[106] G. Cowan. *Statistical Data Analysis*. Oxford science publications. Clarendon Press, 1998.

[107] G. Cowan. A survey of unfolding methods for particle physics. *Conf. Proc.*, C0203181:248–257, 2002. [,248(2002)].

[108] Volker Blobel. An Unfolding method for high-energy physics experiments. In *Advanced Statistical Techniques in Particle Physics. Proceedings, Conference, Durham, UK, March 18-22, 2002*, pages 258–267, 2002.

[109] N. D. Gagunashvili. Parametric fitting of data obtained from detectors with finite resolution and limited acceptance. *Nucl. Instrum. Meth.*, A635:86–91, 2011.

[110] Rene Brun and Fons Rademakers. Root - an object oriented data analysis framework. In *AIHENP'96 Workshop, Lausane*, volume 389, pages 81–86, 1996.

[111] F James and M Roos. MINUIT: a system for function minimization and analysis of the parameter errors and corrections. *Comput. Phys. Commun.*, 10(CERN-DD-75-20):343–367. 38 p, Jul 1975.

[112] Goddard Space Flight Center. *XSPEC: an x-ray spectral fitting package user's guide for version 8.* NASA, Goddard Space Flight Center, 1994.

[113] J. Albert et al. Unfolding of differential energy spectra in the MAGIC experiment. *Nucl. Instrum. Meth.*, A583:494–506, 2007.

[114] Stefan Schmitt. TUnfold: an algorithm for correcting migration effects in high energy physics. *JINST*, 7:T10003, 2012.

[115] A. N. Tikhonov and V. Y. Arsenin. *Solutions of Ill-posed problems.* W.H. Winston, 1977.

[116] Claude E. Shannon. A Mathematical Theory of Communication. *The Bell System Technical Journal*, 27(3):379–423, 1948.

[117] E. T. Jaynes. Prior probabilities. *IEEE Transactions on Systems Science and Cybernetics*, 4(3):227–241, Sept 1968.

[118] P. C. Hansen. The l-curve and its use in the numerical treatment of inverse problems. In *in Computational Inverse Problems in Electrocardiology, ed. P. Johnston, Advances in Computational Bioengineering*, pages 119–142. WIT Press, 2000.

[119] D. Maurin, F. Melot, and R. Taillet. A database of charged cosmic rays. *Astron. Astrophys.*, 569:A32, 2014.

[120] Julia Yarba. Recent developments and validation of geant4 hadronic physics. *Journal of Physics: Conference Series*, 396(2):022060, 2012.

[121] Andrea Dotti. Simulation of Showers with Geant4. In *Proceedings, International Conference on Calorimetry for the High Energy Frontier (CHEF 2013): Paris, France, April 22-25, 2013*, pages 247–253, 2013.

[122] B. Bilki et al. Pion and proton showers in the CALICE scintillator-steel analogue hadron calorimeter. *JINST*, 10(04):P04014, 2015.

[123] G. Folger, V. N. Ivanchenko, and J. P. Wellisch. The Binary Cascade. *European Physical Journal A*, 21:407–417, September 2004.

[124] M. Kosov and D. Savin. New exclusive CHIPS-TPT algorithms for simulation of neutron-nuclear reactions. *J. Phys. Conf. Ser.*, 608(1):012050, 2015.

[125] V. V. Uzhinsky. The Fritiof (FTF) Model in Geant4. In *Proceedings, International Conference on Calorimetry for the High Energy Frontier (CHEF 2013): Paris, France, April 22-25, 2013*, pages 260–264, 2013.

[126] The ATLAS Collaboration. The atlas experiment at the cern large hadron collider. *Journal of Instrumentation*, 3(08):S08003, 2008.

[127] Stefan Piperov. Geant4 validation with CMS calorimeters test-beam data. In *Hadron collider physics. Proceedings, 19th Symposium, HCP2008, Galena, USA, May 27-31, 2008*, 2008.

[128] S. Easo, I. Belyaev, G. Corti, C. Jones, A. Papanestis, W. Pokorski, F. Ranjard, and P. Robbe. Simulation of lhcb rich detectors using geant4. *IEEE Transactions on Nuclear Science*, 52(5):1665–1668, Oct 2005.

[129] L. Baldini et al. Preliminary results of the lat calibration unit beam tests. *AIP Conference Proceedings*, 921(1), 2007.

[130] Damiano Caprioli. Cosmic-ray acceleration in supernova remnants: non-linear theory revised. *Journal of Cosmology and Astroparticle Physics*, 2012(07):038, 2012.

[131] Satyendra Thoudam and Jörg R. Hörandel. Cosmic-ray spectral anomaly at GeV-TeV energies as due to re-acceleration by weak shocks in the Galaxy. In *Proceedings, 33rd International Cosmic Ray Conference (ICRC2013): Rio de Janeiro, Brazil, July 2-9, 2013*, page 1022, 2013.

[132] Roberto Aloisio, Pasquale Blasi, and Pasquale Serpico. Nonlinear cosmic ray Galactic transport in the light of AMS-02 and Voyager data. *Astron. Astrophys.*, 583:A95, 2015.

[133] Nicola Tomassetti. Cosmic-ray protons, nuclei, electrons, and antiparticles under a two-halo scenario of diffusive propagation. *Phys. Rev.*, D92(8):081301, 2015.

[134] M. Ackermann et al. Fermi-lat observations of the diffuse γ-ray emission: Implications for cosmic rays and the interstellar medium. *The Astrophysical Journal*, 750(1):3, 2012.

[135] Daniele Gaggero, Alfredo Urbano, Mauro Valli, and Piero Ullio. Gamma-ray sky points to radial gradients in cosmic-ray transport. *Phys. Rev. D*, 91:083012, Apr 2015.

[136] V. Savchenko, M. Kachelrieß, and D. V. Semikoz. Imprint of a 2 Million Year old Source on the Cosmic-ray Anisotropy. *Astrophys. J.*, 809(2):L23, 2015.

[137] M. Aguilar et al. Electron and Positron Fluxes in Primary Cosmic Rays Measured with the Alpha Magnetic Spectrometer on the International Space Station. *Physical Review Letters*, 113(12):121102, September 2014.

[138] Nicola Tomassetti. Origin of the Proton-to-Helium Ratio Anomaly in Cosmic Rays. *Astrophys. J.*, 815:L1, 2015.

[139] A. A. Moiseev, M. Ajello, J. H. Buckley, R. Caputo, E. C. Ferrara, D. H. Hartmann, E. Hays, J. E. McEnery, J. W. Mitchell, R. Ojha, J. S. Perkins, J. L. Racusin, A. W. Smith, and D. J. Thompson. Compton-Pair Production Space Telescope (ComPair) for MeV Gamma-ray Astronomy. *ArXiv e-prints*, August 2015.

[140] V. Tatischeff et al. The e-ASTROGAM gamma-ray space mission. *ArXiv e-prints*, August 2016.

[141] J. Wu, J. Guo, J. Chang, and M. Cai. The DAMPE mission. In *41st COSPAR Scientific Assembly, abstracts from the meeting that was to be held 30 July - 7 August at the Istanbul Congress Center (ICC), Turkey, but was cancelled.*, volume 41 of *COSPAR Meeting*, July 2016.

[142] P. S. for the CALET Collaboration Marrocchesi. CALET on the ISS: a high energy astroparticle physics experiment. *Journal of Physics Conference Series*, 718(5):052023, May 2016.

[143] E. S. Seo et al. Cosmic Ray Energetics And Mass for the International Space Station (ISS-CREAM). *Advances in Space Research*, 53:1451–1455, May 2014.

[144] Tibet ASγ Collaboration. On Temporal Variations of the Multi-TeV Cosmic Ray Anisotropy Using the Tibet III Air Shower Array.

[145] G. Battistoni, F. Cerutti, A. Empl, A. Fassò, A. Ferrari, E. Gadioli, M. V. Garzelli, S. Muraro, M. Pelliccioni, L. S. Pinsky, J. Ranft, S. Roesler, P. R. Sala, and R. Villari. Hadronic models for cosmic ray physics: the FLUKA code. *Nuclear Physics B Proceedings Supplements*, 175:88–95, January 2008.